POLISH ACADEMY OF SCIENCES
COMMITTEE OF METALLURGY
INSTITUTE OF METALLURGY
AND MATERIALS SCIENCE

ARCHIVES OF METALLURGY AND MATERIALS

QUARTERLY

Volume 49 · Issue 2

WARSZAWA — KRAKÓW 2004

The Archives of Metallurgy and Materials is covered in the following Institute for Scientific Information® products: SciSearch (the Science Citation Index® — Expanded), Research Alert®, Materials Science Citation Index®, and Current Contents® / Engineering, Computing and Technology. Articles published in the Archives of Metallurgy and Materials are also indexed or abstracted by Cambridge Scientific Abstracts.

EDITORIAL ADDRESS
(University of Science and Technology).
M. Bitner al. Mickiewicza 30, AGH, paw. A-4, III p., pok. 312b
30-059 Kraków, Poland
Tel. +48 (12) 6173425
e-mail: archives@imim-pan.krakow.pl

Skład, łamanie druk i oprawa: Warszawska Drukarnia Naukowa PAN
Warszawa, ul. Śniadeckich 8, tel./fax 628-87-77

Ark. wyd. 20,5 Ark. druk. 16,5
Nakład: 250 egz.
Druk ukończono w 2004 r.

Special Issue

MCTM 2004

Summer School on Mass and Charge Transport in Materials July 13–17, 2004, Kraków, Poland

Guest Editors:

Dr. Elżbieta Bielańska

Dr. Maria Socjusz-Podosek

Professor Paweł Zięba

Polish Academy of Sciences
Institute of Metallurgy and Materials Science
Kraków, Poland

Editorial

The special issue of *Archives of Metallurgy and Materials* contains invited papers presented at the Summer School on Mass and Charge Transport in Materials, held in Kraków, Poland between 13 and 17 July 2004 as one of the actions of Centre of Excellence in *Nano- and Microscale Characterization and Development of Advanced Materials* – NAMAM, at the Institute of Metallurgy and Materials Science of the Polish Academy of Sciences.

The Summer School on Mass and Charge Transport in Materials (MCTM) was a forum for the presentation and discussion of recent achievements in the field of diffusive transport of matter in metals, alloys and ceramic materials. The MCTM School was intended mostly for postgraduate and Ph.D. students and other young scientists specializing in materials science and engineering, concentrated on some selected and more specific problems which are usually beyond the scope of regular courses in physical metallurgy. The participation at MCTM School gave them a fresh view of recent achievements and prospects for the future in such areas as: modeling and simulation of diffusion, grain boundary and interface diffusion, diffusion in intermetallics and thin layers, reactive diffusion, role of diffusion and charge transport in oxidation and corrosion processes as well as experimental techniques in diffusion studies.

The School attracted 51 participants, 25 from the host country and 26 from 9 countries all over the world (Austria, Denmark, France, Germany, Holland, Hungary, Israel, Russia, Ukraine) who presented 18 invited lectures and 12 poster contributions.

The Organizing Committee located the conference in Kraków, the ancient capital of Poland, a world renowned centre of culture, art and science which integrates the traditional aspects of Polish life with a modern, and forward looking approach to international collaboration and development. The venue (Kontrast Hotel) offered a pleasant ambience, ample space for the scientific programme, a good restaurant, and a high-quality accommodation for all participants and accompanying persons. The scientific agenda was completed by a social programme with such highlights as welcome reception, folklore evening and School dinner.

The success of the MCTM was a result of an effort made by many people. The list starts with the participants themselves who had worked hard for a long time before they came to Kraków to present so many interesting results. Valuable advice of the Scientific Committee members has to be acknowledged. We also appreciate the involvement of those who chaired the sessions or refereed the contributions in due time. Last but not least, the event would not have taken place without significant activity of all the members of the Local Organizing Committee from the Institute of Metallurgy and Materials Science of the Polish Academy of Sciences.

The publication of the invited lectures in a reviewed and archived journal will increase the scientific impact of the MCTM School. All authors can be considerably proud of the papers which have been accepted for publication. All the papers have been fully refereed, and they constitute a lasting contribution to *Archives of Metallurgy and Materials*.

We are most grateful for the financial support provided to the conference. The MCTM School was organized within 5th European Framework Programme – Accompanying Measures, Contract No.: G5MA-CT-2002-04048. We also appreciate very much the sponsorship of the Polish Committee for Scientific Research (Nr 62/E-88/SPB/5.PR UE/DZ 143/2003-2005).

Elżbieta Bielańska
Maria Socjusz-Podosek
Paweł Zięba, (*Guest Editors*)
Institute of Metallurgy and Materials Science
Polish Academy of Sciences
25, Reymonta Str., 30-059 Kraków, Poland

A R C H I V E S O F M E T A L L U R G Y A N D M A T E R I A L S
Volume 49 2004 Issue 2

M. DANIELEWSKI *

DIFFUSION IN MULTICOMPONENT SYSTEMS

DYFUZJA W UKŁADACH WIELOSKŁADNIKOWYCH

The key concepts (constitutive equations) for the mass flux and models of the diffusion in multicomponent systems are presented. The D a r k e n concept of separation of diffusion and drift flows, i.e. the postulate that the total mass flow is a sum of diffusion flux and translation is presented as the most promising model of mass transport. This is applied for the general case of diffusional transport in *r*-component solid solution. The equations of mass conservation, the appropriate expressions describing the fluxes (drift flux and diffusional flux) and momentum conservation equation allow a complete quantitative description of diffusional transport process. The equations describing the interdiffusion (mixing) in the general case where the components diffusivities vary with composition are presented. If certain assumptions and a quantitative condition are fulfilled, then there exists the unique solution of the D a r k e n interdiffusion problem. A condition for the "up-hill diffusion" in the three component mixture is given and a universal example of such effect is demonstrated. The phenomenology allows the quantitative data on the dynamics of the processes to be obtained within an interdiffusion zone.

Przedstawiono podstawowe równania konstytutywne wyrażające strumień masy w ośrodku ciągłym oraz metody opisu dyfuzji w wieloskładnikowych roztworach stałych. Jako najbardziej zaawansowaną i efektywną dla opisy dyfuzji w wieloskładnikowych roztworach stałych przedstawiono metodę D a r k e n a. Metoda ta jest oparta na postulacie, iż strumień masy w każdym ośrodku ciągłym, w szczególności w ciele stałym, można jednoznacznie rozdzielić na część dyfuzyjną i konwekcyjną (dryft). Omówiono zastosowanie metody D a r k e n a dla stopów wieloskładnikowych (jednofazowych roztworów stałych). W takich układach dla jednoznacznego opisu procesu dyfuzji (transportu) wystarczające są: równania zachowania masy dla każdego ze składników, równanie stanu oraz właściwe równanie(a) na strumień dyfuzji. Omówiono podstawowe zależności opisujące transport w ogólnym przypadku ośrodka, w którym ruchliwości składników są funkcją jego składu. Taki opis procesu (model) posiada jednoznaczne rozwiązanie. Omówiono teorie i przykłady tworzenia struktur dyfuzyjnych („up-hill diffusion") w układach trójskładnikowych. Omówiona metoda pozwala na opis dynamiki procesów transportu masy dla szerokiej gamy problemów fizyko-chemicznych.

* FACULTY OF MATERIALS AND CERAMICS, AGH UNIVERSITY OF SCIENCE AND TECHNOLOGY, 30-059 CRACOW, AL. MICKIEWICZA 30, POLAND

1. Introduction

The fundamental D a r k e n and W a g n e r equations assume that the partial molar volumes of the diffusing components are constant [1, 2] and equal [2]. The conservation of momentum is not included in all the models of interdiffusion [3, 4]. All the models of interdiffusion neglect the dynamics of the transport process [1–4] and can not be applied for two- and three-dimensional problems. Multicomponent systems are important in all areas of science. In rare cases the transport problems in such systems can be reduced to F i c k ' i a n diffusion[1]. The best example is tracer diffusion in multicomponent solid solution at equilibrium, e.g., ^{18}O in $(FeCr_2)^{16}O_4$.

Study of the diffusion in solids was initiated by Sir Roberts-Austen who discovered the diffusion of gold in solid lead in 1896. For a long time afterward, people believed that atomic diffusion occurred by a direct exchange mechanism or a ring mechanism in metallic crystals (Figure 1).

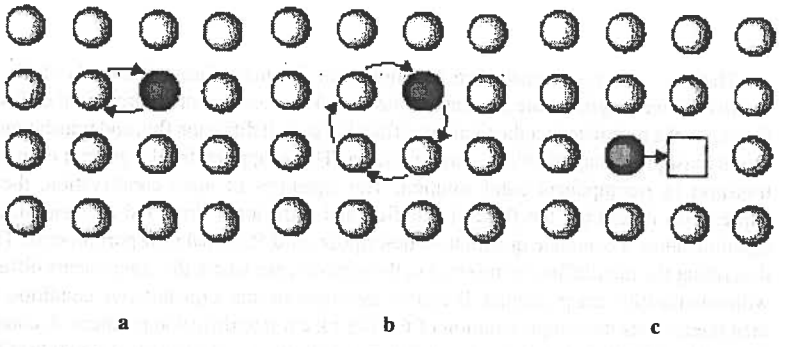

Fig. 1. The atomic diffusion mechanisms: a) a direct exchange mechanizm, b) ring mechanizm and c) vacancy mechanism

In 1947, Ernest K i r k e n d a l l reported the results of experiments on the interdiffusion between Cu and Zn. E r n e s t K i r k e n d a l l curiosity had led him toward the startling discovery he made while a graduate student at the University of Michigan. He developed a simple, elegant new technique utilizing diffusion 'couples' of dissimilar metals which demonstrated unequivocally that the individual component (atoms) in a solid alloy diffuse at different rates. The K i r k e n d a l l experiments proved that a) diffusion by direct interchange of atoms–the prevailing idea of the day–was incorrect and b) that a less-favored theory, the vacancy mechanism, must be correct. When K i r k e n d a l l first published the results of his doctoral thesis research on the rates of diffusion in a solid state in 1939, he was a graduate student. Later, as an instructor at Wayne State University, he repeated his experiment, publishing a second paper in 1942. His discovery had little impact on the scientific community at the time because the nation was embroiled in World War II. But, by 1946, K i r k e n d a l l, along with his student, Alice Smigelskas, had co-authored a third paper asserting that interdiffusion between copper and zinc in brass showed movement of

[1] Fick'ian diffusion means that the process can be adequately described by so called Fick's laws (1855).

the interface between the different phases due to high-temperature interdiffusion. This discovery–forever after known as the "K i r k e n d a l l Effect"–supported the idea that atomic diffusion occurs through vacancy exchange. That third paper was submitted to *Transactions of the AIME*, but publication was delayed for six months because a leading scientist at the time thought K i r k e n d a l l was wrong. The paper was finally published in 1947. Thus, all nowadays concepts were initiated in 1947 by S m i g e l s k a s and K i r k e n d a l l. They conducted an experiment studying the interdiffusion between Cu and Cu/Zn alloy. They inserted "insoluble" Mo wire markers at the Cu/alloy interface before diffusion annealing, Fig. 2.

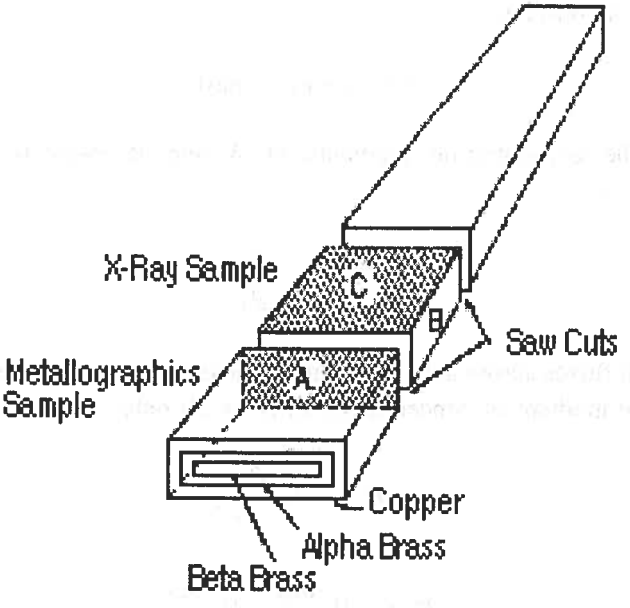

Fig. 2. A schematic of the specimen used by Kirkendall and Smigelskas.

After annealing, it was found that the distance between the markers had decreased. Alloy was "annihilated" and new formed in initial Cu layer (zone).

This experiment showed:

1. faster Zn out-diffusion than Cu diffusion in ($D_{Zn} > D_{Cu}$).
2. that there is no law of lattice site conservation during diffusion in solids
3. the drift process in binary alloy (movement of "inert markers" in solid metallic alloy).

This phenomenon has been known since then as the K i r k e n d a l l effect. It played a decisive role in the development of the solid-state diffusion theory. It shows the different independent intrinsic diffusion fluxes of the components *A* and *B*, which causes swelling (creation) of one part and shrinking (annihilation) of the other part of the couple, leading to the marker displacement. K i r k e n d a l l experiment was explained be a creation and dissolution of vacancies going on at different locations. However the key conclusion is that

one has to expect movement due to diffusion in solids. Once the solid is non uniform, mobilities are non negligible and differ from each other than vast number of phenomena can occur: Kirkendall shift (marker movement), Kirkendall-Frenkel voids might be formed, stress, deformation and/or cracking etc. The drift velocity [2] is a source of all whose effects. A more detailed analysis of the concepts of drift velocity, the choice of the proper reference frame for diffusion, as well as the other consequences of the proposed formalism have already been published [5, 6].

Let's analyze the Kirkendall experiment in more detail. Namely, in the manner postulated by Darken (1948). He assumed that the total concentration of the binary solid solution (alloy) is constant:

$$c = c_A + c_B = \text{const.} \tag{1}$$

Consequently the concentration gradients of A and B elements must be always equal and opposite

$$\frac{\partial c_A}{\partial x} = -\frac{\partial c_B}{\partial x} \tag{2}$$

and the diffusion fluxes across any given lattice plane (in internal reference frame) can be expressed by the gradient of concentration of A (or B) only:

$$J_A^d = -D_A \frac{\partial c_A}{\partial x}, \tag{3}$$

$$J_B^d = -D_B \frac{\partial c_B}{\partial x} = D_B \frac{\partial c_A}{\partial x} \tag{4}$$

where J_A^d, J_B^d, D_A and D_B denote the diffusion fluxes of elements A and B and their intrinsic diffusivities, Fig. 3.

Difference in the intrinsic diffusivities means that the fluxes of A and B atoms across a lattice plane (in internal reference frame) are different [1]. The motion of A and B atoms occurs by a vacancy moving in the opposite direction. Thus, the net flux of vacancies will be equal and opposite to sum of the both fluxes:

$$J_V^d = -J_A^d - J_B^d = D_A \frac{\partial c_A}{\partial x} - D_B \frac{\partial c_A}{\partial x} = (D_A - D_B) \frac{\partial c_A}{\partial x}. \tag{5}$$

[1] In a substitutional alloy, diffusion occurs often by a vacancy mechanism. Thus, the motion of an atom in one direction occurs by a vacancy moving in the opposite direction. The flux of vacancies during the diffusion process will be equal and opposite to the flux of diffusing atoms.

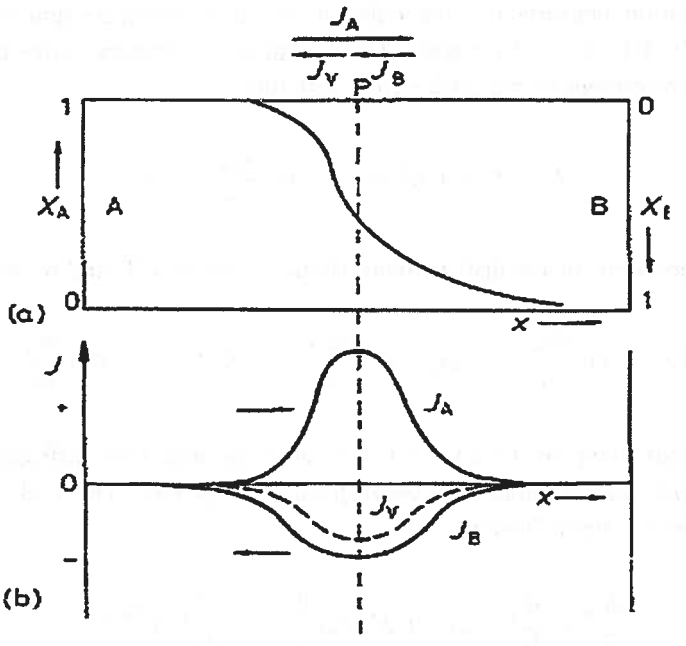

Fig. 3. The distribution of elements and fluxes in the binary diffusion couple, J_V denote the flux of vacancies: $J_A + J_B + J_V = 0$, e.g., in the substitutional alloy.

The difference in the intrinsic diffusivities A and B means there is a net flux of vacancies. However, the vacancy concentration depends on temperature only and must remain constant. It means that they are created on one side of the arbitrary cross-section, and annihilated on the other one. This may occur at dislocations, with dislocation motion acting as either a source or a sink of vacancies. The positive climb of a dislocation introduces a new lattice plane, and generates vacancies, while the negative climb of a dislocation absorbs vacancies and removes a lattice plane, i.e., lattice planes drift from one side of the interface to the other.

The lattice planes near the any cross-section in the diffusion zone move in a direction opposite to the local vacancy flux. This movement of lattice planes is local drift velocity for an external observer. Diffusion occurs (is defined) relatively to drifting lattice planes. Such explanation is a foundation of the D a r k e n model.

Darken model. In most diffusion experiments what is required is an effective diffusion coefficient. Coefficient that will allow computing diffusional profile (evolution of the system due to interdiffusion) using the already well developed mathematical methods (e.g., for the heat transport processes, the Fick'ian diffusion in a case of variable diffusivities etc.).

Consider the flux of atoms in infinite diffusional couple, i.e., thick enough to avoid the changes of concentration(s) at both its ends. For such a couple external reference frame is easily defined relatively to end of the specimen. In such a frame of reference the fluxes of

elements at a position measured relative to the end of the specimen are sum of the diffusion flux given e.g., by F i c k ' s I Law and defined relative to a drifting lattice plane, and the flux due to the movement of the lattice (the drift flux)

$$J_A = J_A^d + J_A(drift) = - D_A \frac{\partial c_A}{\partial x} + c_A \upsilon \tag{6}$$

Substituting expression for the drift velocity (lattice velocity [2]) and re-arranging gives

$$J_A = - D_A \frac{\partial c_A}{\partial x} + \frac{c_A}{c}(D_A - D_B)\frac{\partial c_A}{\partial x} = - (N_B D_A + N_A D_B)\frac{\partial c_A}{\partial x} \tag{7}$$

which is the equivalent of F i c k ' s I law with an effective diffusion coefficient $\tilde{D} = N_B D_A + N_A D_B$ that is called the *interdiffusion coefficient.* The Fick's 2nd law for D a r k e n model of interdiffusion

$$\frac{\partial c_A}{\partial t} = \frac{\partial}{\partial x}\left((N_B D_A + N_A D_B)\frac{\partial c_A}{\partial x}\right) = \frac{\partial}{\partial x}\left(\tilde{D}\frac{\partial c_A}{\partial x}\right) \tag{8}$$

is diffusion equation with variable diffusion coefficient (=interdiffusion coefficient). The model presented above describing interdiffusion in any kind of alloy (solid solution) is known as *D a r k e n ' s m o d e l.* Above equations can be solved to derive time–dependent variations in alloy composition, as was done previously for Fick's Second Law for interstitial diffusion. When the composition of an alloy approaches pure *A* or pure *B*, the interdiffusion coefficient approaches the diffusion coefficient of the solute.

Matano analysis. In majority of real systems a concentration dependence of the diffusion coefficients is observed. Moreover the interdiffusion in binary alloys can be transformed to diffusional problem with variable diffusivity. Solution of such problem can be used to analyze an experimentally measured concentration profile and determine the diffusion coefficient or the interdiffusion coefficient.

In such a case equation of mass conservation takes the form of the Fick's 2nd law

$$\frac{\partial c_i}{\partial t} = \frac{\partial}{\partial x}\left(D_i(c_i)\frac{\partial c_i}{\partial x}\right) \tag{9}$$

and can be solved using the B o l t z m a n method. Substituting for

$$\eta = \frac{x}{\sqrt{t}} \tag{10}$$

gives the ordinary differential equation

$$\frac{\eta}{2}\frac{\partial c_i}{\partial \eta} = -\frac{\partial}{\partial \eta}\left(D_i(c_i)\frac{\partial c_i}{\partial \eta}\right) \tag{11}$$

Integrating for infinite couple gives (providing grad(c) = 0 at $x = 0$)

$$\frac{1}{2}\int_0^{c_i}\eta\,\mathrm{d}c_i' = -\int_0^{c_i}\mathrm{d}\left(D_i(c_i)\frac{\partial c_i}{\partial \eta}\right) = -D_i(c_i)\frac{\partial c_i}{\partial \eta}\bigg|_{c_i} \tag{12}$$

and

$$D_i(c_i) = -\frac{1}{2}\frac{\partial \eta}{\partial c_i}\bigg|_{c_i}\int_0^{c_i}\eta\,\mathrm{d}c_i' = -\frac{1}{2t}\frac{\partial x}{\partial c_i}\bigg|_{c_i}\int_0^{c_i}x\,\mathrm{d}c_i' \tag{13}$$

From a measured diffusion profile $c_i(x)$ after annealing for some time t, this equation can be used to derive the diffusion coefficient for composition c_i.

The first step is to find the "M a t a n o p l a n e". It defines initial contact interface ($x = 0$) and can be found using the following condition

$$\int_0^{c_i}x\,\mathrm{d}c_i' = 0\,. \tag{14}$$

The above equation is equivalent of the statement that the areas above and below the $x = 0$ line are the same. The M a t a n o plane corresponds to the position of the lattice plane of the original contact interface at the beginning of the process ($t = 0$) since the amount of material which has diffused across this plane in either direction is the same. However, inert markers placed at the original position of the interface will have moved relative to the M a t a n o plane, due to the K i r k e n d a l l effect, i.e., the position of the initial contact interface is a function of time (parabolic for the binary infinite diffusional couple).

Once the M a t a n o plane has been defined, the diffusion coefficient at a certain composition can be computed from Eq. (13). It is the product of the area of the curve up to that composition, and the tangent at the same point, Fig. 4. This method allows complicated concentration-dependent diffusion coefficients to be calculated quite simply from straightforward diffusion couple experiments. Its limitations are due to non-uniqueness of the M a t a n o interface (multiple interfaces were often observed for ternary and higher alloys) and due to infinite geometry.

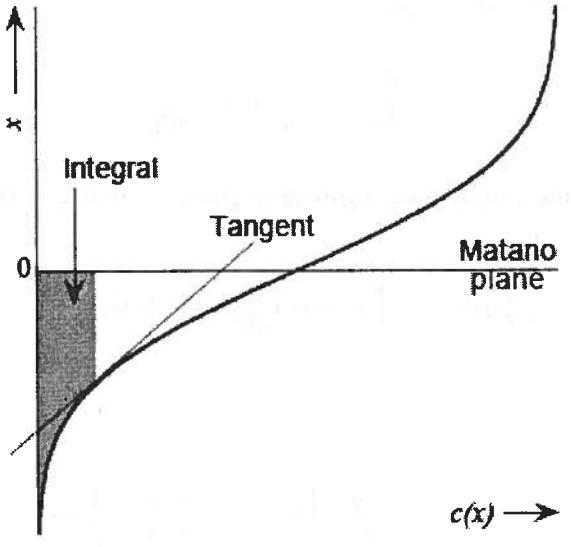

Fig. 4. Schema showing the Matano interface on diffusional profile.

Darken Method for Multi Component Solid Solutions. The progress in the understanding of the interdiffusion phenomenology has been obtained recently. It allows to analyze open, spatially limited and multicomponent systems. The key concepts that have to be always considered when dealing with transport in multi component system comprise:

i) the postulate that the total mass flow is a sum of diffusion and drift flux[1] [2],

ii) the careful analysis of transport process in order to include/neglect the effects of temperature gradient, stress, electric field (ionic conductors), etc.

iii) selection of an adequate constitutive equation describing the diffusion flux.

iv) the expansion or compression are inherent processes during the diffusion. Thus, the complete description of the transport may not neglect the local momentum conservation. Consequently, the N a v i e r - L a m e equation has to be included in the analysis of the interdiffusion and stress (in R1) and in all processes in the real geometry (R2 and R3).

A general phenomenological treatment of the interdiffusion problem is given below. The models that allow independent (un-coupled) diffusion and "magical transmission of information" (non-local models) will not be presented. I do believe they are temporary models only and can not be avoided in very limited situations.

2. Theory

The models of diffusional mass transport in solids [1–4] use the same physical law(s). Namely, the equation of mass conservation. The key difference is in most cases the

[1] The translation flow, convection flow etc. are the other expressions that describe the same.

postulated flux formula. When any compound (media) acts upon a field (e.g. chemical potential gradient), the different elements respond in different ways. In case of a multicomponent medium, the force arising from any concentration gradient causes the atoms of the particular component to move with a velocity (v_i) which in general may differ from velocity of the atoms of some or all the other components. As the medium is common for all the transported species, all the fluxes are coupled and their local changes can affect the common compound drift velocity (v). The above phenomenon is called interdiffusion. The physical law that governs this process is continuity equation:

$$\frac{\partial \rho_i}{\partial t} = -\text{div } J_i \quad ,$$

$$[\text{accumulation}] = \begin{bmatrix} \text{accumulation due to} \\ \text{mass transport,} \\ \text{local change of flux} \\ \text{in the external} \\ \text{reference frame} \end{bmatrix} \tag{15}$$

The *i*-component conservation in the external reference frame out is expressed by the equation of mass conservation (local continuity equation of an *i*-th component). Note that the reaction term (local sink/source of mass) is neglected in Eq. (15). Formation of the new compounds is not allowed in the course of the analyzed interdiffusion process. The flux can be expressed by combination of different constitutive equations for diffusion and Darken's drift flow:

$$J_i = J_i(diff) + J_i(drift) = \rho_i v_{d,i} + \rho_i v = \rho_i v_i , \tag{16}$$

Namely, by Fickian flow:

$$J_i = - D_i \frac{\partial \rho_i}{\partial x} + \rho_i v , \tag{17}$$

Nernst-Planck flow:

$$J_i = B_i \rho_i \sum_{j=1}^{n} F_j + \rho_i v , \tag{18}$$

where B_i is the mobility of the diffusing element [1] and F_j denotes the forces acting on it, e.g., chemical potential gradient, electrical potential gradient, stress, etc.

$$J_i = \sum_{j=1}^{n} L_{ij} X_j + \rho_i v \tag{19}$$

[1] The mobility and self diffusion coefficient are related through Nernst – Einstein relation: $D_i = B_i kT$.

where L_{ij} and X_j denote the transport coefficients and generalized forces respectively. Thus, upon substituting Eqs.(15) and selected formula for diffusion flux (Eqs. (16-19)), the equation describing the mass conservation of the i-component in the ERF takes the usual form of the continuity equation, where the physical sense of all the terms is given below the equation:

$$\frac{\partial \rho_i}{\partial t} = -\operatorname{div} J_{d,i} - \upsilon \cdot \operatorname{grad} \rho_i - \rho_i \operatorname{div} \upsilon = -\operatorname{div}(\rho_i \upsilon_i),$$

$$\begin{bmatrix} accumulation; \\ IRF \neq ERF \end{bmatrix} = \begin{bmatrix} diffusion; \\ ERF = IRF \end{bmatrix} + \begin{bmatrix} drift\ flow, \\ transalation; \\ ERF \neq IRF \end{bmatrix} + \begin{bmatrix} drift \\ generation; \\ ERF \neq IRF \end{bmatrix} = \begin{bmatrix} massflow; \\ ERF \neq IRF \end{bmatrix} \tag{20}$$

It should be pointed out that the drift generation term can be the result of all local processes. Without external force fields, only the accumulation may affect locally the drift velocity, may generate the drift. The drift production term as well as a local drift velocity are always common for all the transported components.

In the general case of diffusional transport in the r-component mixture, r-continuity equations for all diffusing components must be fulfilled in any elementary volume within an open system. The continuity equation, Eq.(20), in the unidimensional mixture becomes:

$$\frac{\partial \rho_i}{\partial t} = -\frac{\partial}{\partial x}(\rho_i \upsilon_i). \tag{21}$$

The important assumption of the local equilibrium in a mixture should be included in all analysis. This assumption is also a foundation of the majority of phenomenological models of transport (interdiffusion) [1, 2]. Successful applications of these models in describing the mass transport justify the incorporation of this fundamental concept of non-equilibrium thermodynamics into the transport equations. The postulate of local equilibrium is as follows: "For a system in which irreversible processes are taking place, all thermodynamic functions of state exist for each element of the system. These thermodynamic quantities for the nonequilibrium system are the same functions of local state variables as the corresponding equilibrium quantities". [7].

From this assumption it follows that (in the course of the analyzed processes of interdiffusion at constant temperature), the total concentration of the mixture is constant (as in the equilibrium state). In the other words it is assumed, that the transport processes do not affect the local medium properties. Namely it is assumed the transport processes do not affect the constant concentration of the mixture.

Darken method of interdiffusion in the r-component alloy

When we are not interested in the temperature effects (they can be neglected), the interdiffusion may be treated as a diffusional mixing (the process has low free energy of the

reaction). New expanding area is chemical (reactive) interdiffusion a s a process that leads to formation of the new phases.

In the most general case of Darken method the following unknowns are of interest: λ_1 and λ_2 – the positions of the mixture boundaries; density of the all component; drift velocity and the pressure of the mixture (or stress in general).

Physical laws are the same as in original Darken model. The local mass conservation law for the i-th component is given by Eq. (21), where v_i is the i-th component velocity, i.e.

$$\rho_i v_i = -\Theta_i(\rho_i, ..., \rho_r)\frac{\partial \rho_i}{\partial x} + \rho_i v$$

$$\begin{bmatrix}\text{total flux}\\ \text{of the i-th}\\ \text{component}\end{bmatrix} = \begin{bmatrix}\text{diffusional flux of the}\\ \text{i-th component, where}\\ \text{diffusivieties may depend}\\ \text{on mixture composition}\end{bmatrix} + \begin{bmatrix}\text{drift flux}\\ \text{of the i-th}\\ \text{component}\end{bmatrix} \qquad (22)$$

and the postulate of constant concentration of the mixture;

$$\frac{1}{M_1}\rho_1 + ... + \frac{1}{M_r}\rho_r = c. \qquad (23)$$

All the important differences are in the formulation of the initial conditions which must be known:

1^0 $\lambda_1(0) = -\Lambda$, $\lambda_2(0) = \Lambda$ – initial position of the mixture boundaries;

2^0 $\rho_i(0, x) = \mathring{\rho}_i(x)\,(i = 1, ..., r)$ – initial, arbitrary distribution of the mixture components;

3^0 $\dfrac{d}{dt}\displaystyle\int_{\lambda_1(t)}^{\lambda_2(t)} \rho(t, x)\, x\, dx \Big|_{t=0} = P$ – initial momentum of the mixture

and in boundary conditions:

1^0 $\dot{\lambda}_j(t) = u(t, \lambda_j(t))$ $(j = 1,2)$ – the velocities of the mixture boundaries;

2^0 $[\rho_i(v_i - v)](t, \lambda_j(t)) = 0$ $(1 \le i \le r, 1 \le j \le 2)$ – total flux of the i-th component in the internal reference frame (i.e. mass flow through the mixture boundaries does not occur, the mixture is in a closed system);

3^0 $p(t, \lambda_1(t)) - p(t, \lambda_2(t)) = D(t)$ – the resultant (the net) thrust force acting on the boundary of the mixture.

Such generalization allows for numerous modifications, allows to analyze big class of problems, e.g.,

A) The r-component alloy couple (mixture segment) may be placed vertically on a rigid immovable surface, one can put $\lambda_1 \equiv -\Lambda = const.$.

B) If the movement (evolution) of the couple is known, then one can bypass the determining of the pressure p, and eliminate: the Navier-Stokes equation and some data and initial condition.

Unlimited number of problems can be analyzed, some are presented in this volume (R. Filipek).

The analysis of the model [10] allowed:

1. proving uniqueness and existence of the solution. Namely, theorem that if certain regularity assumptions concerning the initial data and the quantitative condition concerning the diffusion coefficients are fulfilled, then there exists the unique solution of the problem;
2. chosing method of numerical solution of the above problem (Faedo – Galerkin method)
3. finding an effective algebraic criterion for parabolicity (concerning the components diffusivities, i.e. D_1 ..., D_r)
4. finding condition for formation of „the diffusional structers" (i.e., ternary „up-hill diffusion").
5. showing the new directions to more general problems, e.g., case of variable viscosity coefficient.

Acknowledgments

This work has been supported by the Polish State Committee for Scientific Research under Grant No. 4 TOBC03024 (financed during the period 2003 – 2005).

REFERENCES

[1] C. Wagner, Diffusion and High Temperature Oxidation of Metals, in „Atom Movements" (American Society for Metals, Cleveland, Ohio 1951).
[2] L.S. Darken, Trans. AIME, **174**, 184 (1948).
[3] R.W. Balluffi, Acta Metallurgica, **8**, 871 (1960).
[4] S.J. Prager, Chem. Phys., **21**, 1344 (1953).
[5] M. Danielewski, Netsu Sokutei, **20**, 7 (1993).
[6] M. Danielewski, Defect and Diffusion Forum, **95-98**, 125 (1993).
[7] D.D. Fitts, Nonequilibrium thermodynamics (McGraw-Hill, New York 1962), pp. 21, 44, 88.
[8] A.J. Chorin, J.E. Marsden, A Mathematical Introduction to Fluid Mechanics (Springer Verlag, New York 1990), p. 10.
[9] A.D. Romig, J. Appl. Phys., **21**, 3172 (1983).
[10] K. Holly, M. Danielewski, Phys. Rev. B, **50**, 1336 (1994).
[11] M. Danielewski, R. Filipek, A. Milewska, Solid State Phenomena, **72**, 23 (2000).
[12] M. Danielewski, W. Krzyżański, R. Bachorczyk, Solid State Phenomena, **72**, 141(2000).
[13] R. Bachorczyk, M. Danielewski, W. Krzyżański, Defect and Diffusion Forum, **194-199**, 217 (2001).
[14] M. Danielewski, R. Bachorczyk, A. Milewska, Y. Ugaste, Defect and Diffusion Forum, **194-199**, 223 (2001).

Received: 1 March 2004.

ARCHIVES OF METALLURGY AND MATERIALS
Volume 49 2004 Issue 2

R. FILIPEK *

IN TERDIFFUSION IN NON-IDEAL SYSTEMS

DYFUZJA WZAJEMNA W UKŁADACH NIEIDEALNYCH

Darken's method of interdiffusion for multi-component systems is presented. A postulate that the total mass flow is a sum of the diffusion and the drift flows, is applied for the description of interdiffusion in the bounded open system. Nernst-Planck's flux formula assuming chemical potential gradient as a driving force for the mass transport is used for computation of the diffusion flux in non-ideal multi-component systems. An idea of the generalized solution was applied for obtaining the solution to the problem. Numerical solution using finite element method (Galerkin's approximation) is shown. Applications of the model describing interdiffusion in the Cu-Fe-Ni non-ideal alloys including diffusion mixing in the closed systems and the evolution of an alloy composition due to selective oxidation (open system) are presented.

W pracy przedstawiono model dyfuzji wzajemnej Darkena dla układów wieloskładnikowych. Model ten zakłada, iż strumień masy każdego ze składników jest sumą strumienia dyfuzyjnego i strumienia unoszenia. Zastosowanie wyrażenia Nernsta-Planck'a, w którym gradient potencjału chemicznego składników jest siłą napędową dyfuzji, pozwoliło na obliczenie strumieni dyfuzyjnych składników w układach nieidealnych. Zdefiniowano pojęcie rozwiązania słabego zagadnienia dyfuzji wzajemnej w wieloskładnikowych nieidealnych układach otwartych oraz opracowano metodę rozwiązania problemu. Przedstawiono efektywne wzory na rozwiązanie numeryczne problemu przy użyciu metody elementów skończonych (metoda Galernika). Model zastosowano następnie dla opisu procesu dyfuzji wzajemnej w układzie nieidealnym Cu-Fe-Ni. Modelowano proces dyfuzyjnego mieszania się składników w trójskładnikowych parach dyfuzyjnych (układ zamknięty) oraz selektywne utlenianie niklu (układ otwarty). Wyniki obliczeń porównano z wynikami eksperymentalnymi.

1. Introduction

Modelling of interdiffusion in multi-component systems has broad applicability in the materials science and engineering. Most of the modern materials used in advanced

* FACULTY OF MATERIALS SCIENCE AND CERAMICS, DEPARTMENT OF SOLID STATE CHEMISTRY, AGH UNIVERSITY OF SCIENCE AND TECHNOLOGY, 30-059 CRACOW, AL. MICKIEWICZA 30, POLAND

technologies are multi-component and multi-phase. The diffusion processes in multi-component alloys influence the thermal stability and lifetime of electrical contacts, brazed joints and the durability of high temperature coatings. The understanding of the mechanisms of the mass transport in such complex materials is critical for achieving theirs optimal mechanical and physico-chemical properties for special applications. A theoretical approach for the description of interdiffusion in multi-component and non-ideal alloys is presented below.

For the phenomenological description of interdiffusion problem let us consider isothermal and isobaric multi-component single-phase region in which diffusion occurs in one direction only (Figure 1). The two alloys of different composition and/or components are joined together to form a diffusion couple (Figure 1a). From now on the components start to diffuse from the region where theirs concentration is higher to the lower one (Figure. 1b). When any compound interacts with a field, resulting in a gradient of chemical potential, the different elements respond in different ways. In case of multi-component solutions the force being a result of chemical potential gradient causes the atoms of the particular component to move with a velocity v_i, which may differ from the velocity of the atoms of the other elements. Because the system is common for the components all the fluxes are coupled and their local changes may affect the common system drift velocity v. This phenomenon is called interdiffusion [1]. Because of interdiffusion the concentration profiles of all components are affected. At the end of the process in the finite system a homogeneous solution is formed (Figure 1c).

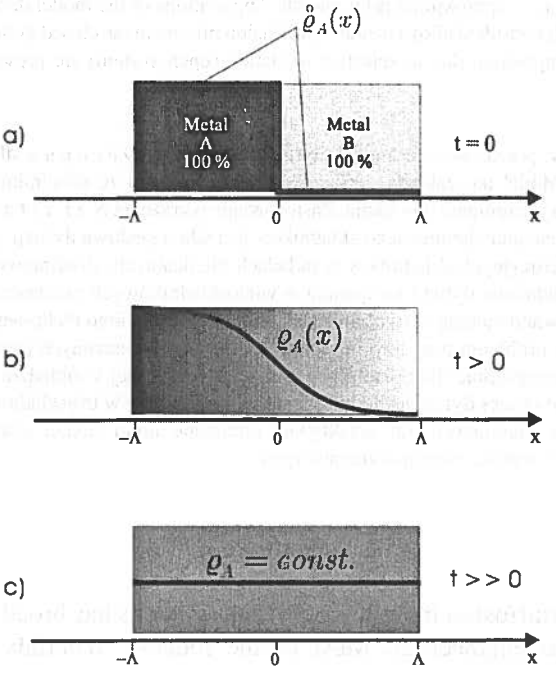

Fig. 1. Schematic graph of interdiffudsion in a binary diffusion couple A/B: (a) initial state – initial density profile of the component A, $\rho_A(x)$ at $t = 0$, (b) density profile $\rho_A(x)$ after some time t > 0 and (c) for long time $t \gg 0$.

The phenomenological description of diffusion process proposed by Onsager [2] and developed by Kirkaldy [3,4], Dayananda [5,6], van Loo [7,8], Morral [9,10] and others [11,12] dominates interdiffusion studies. Investigations of multi-component diffusion based on the Onsager concept are usually restricted to the determination of interdiffusion coefficients and fluxes in ternary systems [4]. One can find only few applications for quaternary systems [6,13,14]. The use of Onsager phenomenology for more than four-component systems is unattainable due to the serious theoretical and experimental obstacles [13,15]. The Onsager phenomenological scheme is useful in describing the diffusion in the closed system. In the open system the translation velocity usually does not vanish [16] and consequently interdiffusion in the multi-component open system can not be described by a simple extension of the methods currently used.

A different method to describe interdiffusion was proposed by Darken [1]. In his model he assumed that the total mass flux is a sum of the diffusion flux and the drift flux. The drift velocity is a physical (real) velocity of an "ideal" marker placed in the diffusion zone. This velocity gives rise to so called Kirkendall effect [17]. In this paper Darken's method for multi-component non-ideal open systems is presented. The equations of mass conservation, the postulate of constant molar volume of the system and the appropriate initial and boundary conditions allow computing the concentration profiles of the components and the drift velocity in the interdiffusion zone. The main advantages of this method are the generalized initial and boundary conditions, which allow the quantitative analysis of the interdiffusion process for the arbitrary initial concentration profiles of the components in the open as well as in the closed systems.

Formulation of the model describing interdiffusion in the ideal closed [18,19] and ideal open systems [20] as well as for non-ideal closed systems [21] have been already published. In this paper the mathematical model of interdiffusion in multi-component non-ideal open system is formulated and method of its solution is presented. A possible answer to such problem is based on the more general diffusion flux formula. It is postulated that the diffusion flux is more adequately described by Nernst-Planck equation [22].

2. Formulation of the model

In this section formulation of the model, i.e., the initial boundary-value problem for the interdiffusion in multi-component non-ideal open systems is presented in a classical way, i.e., presenting data, physical laws, initial and boundary conditions and finally the unknowns to be calculated.

Data

1. $M_1 > 0,...,M_r > 0$ – molar masses of the elements, where r – is the number of components in the system;
2. $\Lambda > 0$ – a position of the right end of the system (its right border – see Figure 1);

3. $\overset{0}{\rho}_1 = \overset{0}{\rho}_1(x),...,\overset{0}{\rho}_r = \overset{0}{\rho}_r(x)$ – the initial distributions of the components $\overset{0}{\rho}_i : [-\Lambda, \Lambda] \to \mathbb{R}_+$, $i = 1,...,r$, such that:

$$c = \sum_{i=1}^{r} \frac{1}{M_i} \overset{0}{\rho}_i = const.$$

where $c > 0$ is the molar concentration of the system;
4. $D_1^* = D_1^*(\rho),..., D_r^* = D_r^*(\rho)$ – self diffusion coefficients of the components, which may depend on components' densities, $\rho = (\rho_1,...\rho_r)$;
5. $a_1 = a_1(\rho),..., a_r = a_r(\rho)$ – the activities of the components as functions of components' densities;
6. $\hat{t}$ – the time of the process duration;
7. $j_{iL}, j_{iR}[0,\hat{t}] \to \mathbb{R}$ $i = 1,...,r$ – evolution of mass flow of the i-th component through the left and right boundary. As a consequence of constant concentration of the system these fluxes satisfy the following relation:

$$\sum_{i=1}^{r} \frac{1}{M_i} j_{iL}(t) = \sum_{i=1}^{r} \frac{1}{M_i} j_{iR}(t) \text{ for } t \in [0,\hat{t}].$$

Therefore only $2r - 1$ fluxes are independent.

Physical Laws

1. Law of the mass conservation of an i-th element. That law tells that a local change of density of an i-th element is a result of its net in- or outflow only:

$$\frac{\partial \rho_i}{\partial t} + \frac{\partial J_i}{\partial x} = 0 \quad i = 1,...,r \tag{1}$$

Following D a r k e n ' s drift flow idea [1], it is postulated that the flux of an i-th element, J_i, is a sum of its diffusion flux, J_i^d, and the drift flux, $(\rho_i v)$:

$$J_i := J_i^d + \rho_i v. \tag{2}$$

In the next sections it will be shown that the effective solution of D a r k e n ' s model for multi-component systems can be obtained when the diffusion flux is expressed by [22]:

$$J_i^d = B_i \rho_i \sum_j F_j, \tag{3}$$

where B_i is the mobility of an i-th element and $\sum_j F_j$ – the sum of the internal or external forces which act on a system.

2. A postulate of the constant molar volume of the system. Consequently the molar concentration of the system being a sum of the concentrations of all elements at any position for every time is constant:

$$\frac{1}{M_1}\rho_1 + \ldots + \frac{1}{M_r}\rho_r = c = const. \tag{4}$$

Initial and boundary conditions

1. The initial density distributions of the components in the system:

$$\overset{0}{\rho}_i(x) = \rho_i(0,x) \quad for\ x \in [-\Lambda, \Lambda],\ i = 1,\ldots,r.$$

2. The following boundary conditions are postulated:

$$J_i(t,-\Lambda) = j_{iL}(t), \quad J_i(t,+\Lambda) = j_{iR}(t), \quad for\ t \in [0,\hat{t}],\ i = 1,\ldots,r. \tag{5}$$

In the open system the functions, $j_{iL}(t)$ and $j_{iR}(t)$, have to be known. They can be calculated e.g., from the known rate of reactions at the boundary or from the experimental data. In the closed system the gradients of all the components at both boundaries vanish, i.e., the flux of an i-th component at the boundary equals zero:

$$J_i(t,\pm\Lambda) = 0 \quad for\ t \in [0,\hat{t}],\ i = 1,\ldots,r.$$

The unknowns

1. Densities of the components as functions of time and position, $\rho_i(t,x)$, $i = 1,\ldots,r$.
2. A drift velocity as a function of time and position, $v(t,x)$.

3. The diffusion flux formula

In this section the Eq. (3) describing the diffusion flux will be rearranged into the form, which allows obtaining an effective numerical solution. It is generally accepted, that the diffusion force in the Eq. (3) can be described as the spatial gradient of the chemical potential, μ_i, and the corresponding flux can be expressed by the following expression

$$J_i^d = -B_i\rho_i\frac{\partial\mu_i}{\partial x}. \tag{6}$$

The thermodynamic definition of the chemical potential is

$$\mu_i(\rho_1,...,\rho_r) = \mu_i^o + kT \ln a_i(\rho_1,...,\rho_r), \tag{7}$$

where k – the Boltzmann's constant, T — an absolute temperature and μ_i^o is the standard-state chemical potential usually referred to unit thermodynamic activity ($a_i = 1$). The gradient of the chemical potential can be calculated as follows

$$\frac{\partial \mu_i}{\partial x}(\rho) = \sum_{j=1}^{r} \frac{\partial \mu_i}{\partial \rho_j}(\rho) \frac{\partial \rho_j}{\partial x}. \tag{8}$$

Using Eqs. (6),(7) and (8) the diffusion flux can be expressed in the from

$$J_i^d = - B_i kT \rho_i \sum_{j=1}^{r} \frac{\partial \ln a_i}{\partial \rho_j} \frac{\partial \rho_j}{\partial x}. \tag{9}$$

Substituting the Nernst-Einstein relation ($D_i^* = B_i kT$) into Eq. (9), we get

$$J_i^d = - D_i^* \rho_i \sum_{j=1}^{r} \frac{\partial \ln a_i}{\partial \rho_j} \frac{\partial \rho_j}{\partial x}. \tag{10}$$

Above diffusion flux formula can be rearranged to the final form

$$J_i^d = - \sum_{j=1}^{r} D_{ij} \frac{\partial \rho_j}{\partial x}, \tag{11}$$

where the partial instrinsic diffusivities, D^i_j, are defined as follows

$$D_{ij}(\rho) := D_i^*(\rho) \rho_i \frac{\partial \ln a_i}{\partial \rho_j}(\rho). \tag{12}$$

One can notice that in the ideal system, when activity coefficients equal one, the diffusion fluxes become

$$J_i^d = - D_i^* \frac{\partial \rho_i}{\partial x}. \tag{13}$$

4. The solution to the model

Some mathematical aspects critical for understanding the solution to the model are presented bellow. Obtaining this solution involves several steps:
(1) mathematical reformulation of the problem,

(2) formulation of the generalized solution,
(3) numerical solution using G a l e r k i n-like method, which reduce an infinite dimension problem to finite one,
(4) solving the resulting system of ordinary differential equations.

Basic concepts on the generalized solution of interdiffusion model in a simple binary system have been already published [23]. In this section the solution of interdiffusion in multi-component non-ideal open system is presented.

Mathematical Reformulation of the Problem
Let us multiply and add equations (1) of local mass conservation

$$\sum_{i=1}^{r} \frac{1}{M_i} \frac{\partial \rho_i}{\partial t} + \frac{1}{M_i} \frac{\partial J_i}{\partial x} = 0.$$

Taking into account Eq. (4) we get

$$\frac{\partial}{\partial t} c + \frac{\partial}{\partial x} \sum_{i=1}^{r} \frac{1}{M_i} J_i = 0.$$

Because $c = const$ (see Eq.(4)) one can notice that $\sum_{i=1}^{r} \frac{1}{M_i} J_i$ does not depend on a position in the system, consequently

$$exists\ K(t) \in \mathbb{R}\ \ such\ that \sum_{i=1}^{r} \frac{1}{cM_i} J_i(t,x) = K(t) \quad for\ t \geq 0,\ x \in [-\Lambda, +\Lambda].$$

After inserting the expression for the flux $J_i(t,x)$ we have

$$\sum_{i=1}^{r} \frac{1}{M_i} \left(-\sum_{k=1}^{r} D_{ik}(\rho) \frac{\partial \rho_k}{\partial x} + \rho_i v \right) = cK(t),$$

and finally after rearrangements

$$v = K(t) + \sum_{k=1}^{r} \sum_{i=1}^{r} \frac{1}{cM_i} D_{ik}(\rho) \frac{\partial \rho_k}{\partial x}. \tag{14}$$

For further transformations let us introduce the following notations

$$\begin{aligned} m_i(t) &= \frac{1}{2\Lambda c M_i} \int_{-\Lambda}^{\Lambda} \rho_i(t,x)\, dx, \\ w_i(t,x) &= \frac{1}{cM_i} \rho_i(t,x) - m_i(t), \end{aligned} \tag{15}$$

where

$$m_i(t) = \frac{1}{2\Lambda c M_i} \int_{-\Lambda}^{0} \rho_i(x)\,dx + \frac{1}{2\Lambda c M_i} \int_{0}^{t} (j_{i,L} - j_{i,R})(\tau)\,d\tau, \tag{16}$$

which means that $m_i(t)$ is known function of time.
One can notice that the following relations are fulfilled

$$\sum_{i=1}^{r} m_i(t) = 1, \quad \sum_{i=1}^{r} w_i(t,x) = 0, \quad \int_{-\Lambda}^{\Lambda} w_i(t,x)\,dx = 0 \;\; i = 1,\ldots,r. \tag{17}$$

Using defined variables (15) we obtain the following expressions

$$\begin{aligned} \frac{\partial}{\partial t}(w_i + m_i) &= -\frac{\partial}{\partial x} \sum_{k=1}^{r} \hat{D}_{ik}(w) \frac{\partial w_k}{\partial x} + (w_i + m_i)\upsilon, \\ \upsilon &= K(t) + \sum_{k=1}^{r} d_k(w) \frac{\partial w_k}{\partial x}, \end{aligned} \tag{18}$$

where $d_k = \sum_{i=1}^{r} \hat{D}_{ik}$ *and* $\hat{D}_{ik} = \frac{M_k}{M_i} D_{ik}$.
According to the standards in modern theory of partial differential equations let us define the solution to the problem (18) in generalized (weak) sense using an integral formula in the special function space V [24]. From the mathematical point of view we can look at $w_i = w_i(t,x)$ (which is function of two variables) as a function of the time only, t

$$w(t)(x) := (w_1(t,x),\ldots,w_r(t,x)) \quad x \in [-\Lambda, \Lambda],$$

so

$$w(t) \in V \quad w : [0,\hat{t}] \to V.$$

This function takes values in the function space V.

Generalized Solution
After some mathematical calculations the problem of interdiffusion in multi-component non-ideal open systems can be formulated as follows:

We look for a function: $w : [0,\hat{t}] \to V$ *which satisfies the condition:*

$$\int_{-\Lambda}^{\Lambda} w(t) \circ \phi dx - \int_{-\Lambda}^{\Lambda} w_0 \circ \phi dx =$$
$$= \int_0^t (\Gamma(\tau) \circ \phi)|_{-\Lambda}^{\Lambda} d\tau - \int_0^t \int_{-\Lambda}^{\Lambda} \mathscr{A}\left(w(\tau) + m(\tau), \frac{\partial w}{\partial x}\right) \circ \frac{\partial \phi}{\partial x} dx d\tau + \int_0^t K(\tau) \int_{-\Lambda}^{\Lambda} w(\tau) \circ \frac{\partial \phi}{\partial x} dx d\tau \tag{19}$$

for all $t \in [0,\hat{t}]$ *and* $\phi \in V$, *where* $u \circ v = \sum_{i=1}^{r} u_i v_i$ *is the standard scalar product in* $\mathbb{R}^r$ *and* $w_0 = w(0)$.

In the above equation $\mathscr{A}$ and Γ are known functions defined as follows

$$A(\kappa,\xi) = A(\kappa)\xi + \kappa \sum_{j=1}^{r} a_j(\kappa)|\xi_j, \quad \text{for } \kappa,\xi \in \mathbb{R}^r,$$

where $A(\kappa)$ is a matrix whose exact form depends on the partial intrinsic diffusivities

$$a_j(\kappa) = \sum_{i=1}^{r} D_{ij}(\kappa), \quad A(\kappa) = [D_{ij}(\kappa)],$$

and $\Gamma = (\Gamma_1,...,\Gamma_r)$ where

$$\Gamma_i(t,\pm\Lambda) = K(t) m_i(t) - \frac{1}{cM_i} j_i(t,\pm\Lambda) \quad \text{for } i = 1,...,r.$$

Numerical Solution Using Galerkin Method

The solution to the problem (19) can be approximated numerically using the standard Faedo-Galerkin method. In this approach equation (19) is projected onto some finite subspace $V_N \subset V$. The approximated solution shall satisfy the equation:

$$\forall t \in [0,\hat{t}], \forall\ \phi \in V_N$$
$$\int_{-\Lambda}^{\Lambda} {}^{N}_{w}(t) \circ \phi dx - \int_{-\Lambda}^{\Lambda} {}^{N}_{w_0} \circ \phi dx = \tag{20}$$
$$= \int_0^t (\Gamma(\tau) \circ \phi)|_{-\Lambda}^{\Lambda} d\tau - \int_0^t \int_{-\Lambda}^{\Lambda} A\left({}^{N}_{w}(\tau) + m(\tau), \frac{\partial {}^{N}_{w}}{\partial x}\right) \circ \frac{\partial \phi}{\partial x} dx d\tau + \int_0^t K(\tau) \int_{-\Lambda}^{\Lambda} {}^{N}_{w}(\tau) \circ \frac{\partial \phi}{\partial x} dx d\tau.$$

It can be proved that such approximation $({}^{N}_{w})_{N=1}^{\infty}$ converges to the exact solution if we take suitable spaces V_N. Without going into mathematical details, we will present briefly the method to obtain the approximation of the exact solution in the form of finite sum ${}^{N}_{w}(t) = \sum_{i=1}^{N} \lambda_i(t)\phi_i$, where $\{\phi_i\}$ are the base functions. The details of this method exceed the scope of this paper and can be found [25].

There are many possible choices for the base $\{\phi_i\}$. In our numerical calculations we have been using the standard polynomial functions in one variable which proved to be very efficient:

$$\phi_i(x) = \varphi_l(x)\tilde{e}_{si}$$

where φ_l has the graph of the form – shown in Figure 2 and $\tilde{e}_s$ is some ortogonal base [25].

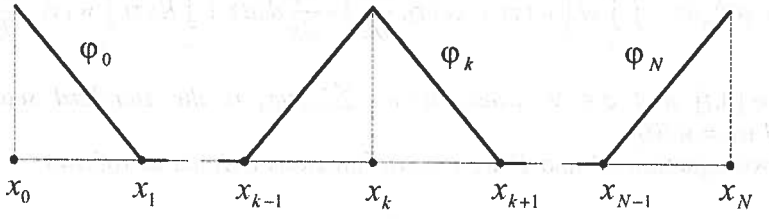

Fig. 2. Graphical representation of the base functions $\varphi_k(x)$. The interval $[-\Lambda,\Lambda]$ was divided into N equal subintervals $[x_k,x_{k+1}]$ where $k = 0,...,N-1$. Nodes $x_k = -\Lambda + k(2\Lambda/N)$ define triangular-like functions $\varphi_k(x)$

After inserting $\overset{N}{w} = \sum_{i=1}^{N}\lambda_i(t)\phi_i(t)$, with the above defined functions φ_i, into the equation (20), after some calculations we finally arrive at the system of nonlinear ordinary differential equations (ODE) for the unknown functions $\lambda(t) = (\lambda_1(t),...,\lambda_N(t))$ of the form

$$\dot{\lambda}(t) = \frac{3N}{\Lambda}B^{-1}R(t,\lambda(t)) \quad with \quad \lambda(t) = (\lambda_{ns}(t))_{0\le n\le N,1\le s\le r-1},$$

where B is a tridiagonal matrix of the form

$$B = \begin{bmatrix} 2 & 1 & 0 & \dots & 0 \\ 1 & 4 & 1 & & \vdots \\ 0 & 1 & \ddots & \ddots & 0 \\ \vdots & & \ddots & 4 & 1 \\ 0 & \dots & 0 & 1 & 2 \end{bmatrix}$$

and $R(t,\lambda) = [R_{ls}(t,\lambda)]_{0\le l\le N,0\le s\le r-1}$. The explicit form of the entry $R_{ls}(t,\lambda)$ is given as follows

$$R_{ls}(t,\lambda) = z_0 - z_1 + K(t)z_2 + z_3 + m(t)\circ\tilde{e}_s z_4, \tag{21}$$

where

$$z_0 = \delta_{0l}\Gamma_R(t) - \delta_{Nl}\Gamma_L(t) - \frac{\Lambda}{2N}(\bar{\delta}_{0l} + \bar{\delta}_{Nl})\dot{m}(t)\circ\tilde{e}_s,$$

$$z_1 = \frac{N}{2\Lambda}\sum_{p=1}^{r-1}\bar{\delta}_{0l}D(l-1)(\tilde{e}_p)\circ\tilde{e}_s(\lambda_{lp} - \lambda_{l-1p}) + \bar{\delta}_{Nl}D(l)(\tilde{e}_p)\circ\tilde{e}_s(\lambda_{lp} - \lambda_{l+1p}),$$

$$z_2 = \frac{1}{2}(\bar{\delta}_{0l}\lambda_{l-1s} + (\delta_{Nl} + \delta_{0l})\lambda_{ls} - \bar{\delta}_{Nl}\lambda_{l+1s}),$$

$$z_3 = \frac{N}{4\Lambda}\sum_{p=1}^{r-1}(\bar{\delta}_{0l}d(l-1)\circ\tilde{e}_p(-\lambda_{l-1p}\lambda_{l-1s}+\lambda_{lp}\lambda_{l-1s}-\lambda_{l-1p}\lambda_{ls})+$$

$$+(\bar{\delta}_{0l}d(l-1)\circ\tilde{e}_p+\bar{\delta}_{Nl}d(l)\circ\tilde{e}_p)\lambda_{lp}\lambda_{ls}+\bar{\delta}_{Nl}d(l)\circ\tilde{e}_p(-\lambda_{l+1p}\lambda_{ls}+\lambda_{lp}\lambda_{l+1s}-\lambda_{l+1p}\lambda_{l+1s})),$$

$$z_4 = \frac{N}{2\Lambda}\sum_{p=1}^{r-1}\bar{\delta}_{0l}d(l-1)\circ\tilde{e}_p(\lambda_{lp}-\lambda_{l-1p})+\bar{\delta}_{Nl}d(l)\circ\tilde{e}_p(\lambda_{lp}-\lambda_{l+1p}), \tag{22}$$

where δ_{ij} and $\bar{\delta}_{ij}$ have the following meaning

$$\delta_{ij}=\begin{cases}1 & if\ i=j\\ 0 & if\ i\neq j\end{cases},\quad \bar{\delta}_{ij}=1-\delta_{ij}=\begin{cases}0 & if\ i=j\\ 1 & if\ i\neq j\end{cases}.$$

Together with the initial condition $\overset{o}{\lambda}$ (which can be found from $\overset{0}{\rho}$), this is a standard Cauchy initial problem for ODE:

$$\begin{cases}\dot{\lambda}\mathrm{p}(t)=\dfrac{3N}{\Lambda}B^{-1}R(t,\lambda(t))\\ \lambda(0)=\overset{o}{\lambda}.\end{cases} \tag{23}$$

After having solved the above system of ODEs we can compute the approximation of the profiles $\overset{N}{W}$

$$\overset{N}{W}(t,x)=\sum_{n=0}^{N}\sum_{p=1}^{r-1}\lambda_{np}(t)\varphi_n(x)\tilde{e}_p. \tag{24}$$

and subsequently using eqs. (15) and (16) compute density profiles of the components $\rho_i=\rho_i(t,x)$.

5. Solving the resulting system of ordinary differential equations

Any numerical method can be applied to solve the system (23) and obtain the values of $\lambda(t)$. For this particular system the standard Runge-Kutta of fourth-order with adaptive step size was chosen. The reason was that the Runge-Kutta method requires relatively small number of right-hand side evaluations, what was especially important in the above system because right-hand side of the ODE is complex and its evaluation is time consuming. The Runge-Kutta Fehelberg [26] method using special pair Runge-Kutta forth and fifth order method was implemented in our procedure. It needs only 5 evaluation in one step and allows to control the level of accuracy of the solution.

6. Modelling interdiffusion in Cu-Fe-Ni Alloy

Formulated above model will be applied for demonstrating the possibility of interdiffusion modelling in non-ideal system. Two different boundary conditions will be analysed:

- interdiffusion in the closed system and
- interdiffusion due to selective oxidation – open system.

For demonstration Cu-Fe-Ni system has been chosen. Cu-Fe-Ni system at 1273 K have a miscibility gap and a wide single phase region (Figure 3). Thermodynamic data for this system has been assessed by J a n s s o n [27] and re-evaluated by R ö n k a et al [8]. In the Figure 4 some isoactivity curves of copper, iron and nickel at 1273 K are presented. Isoactivity data illustrated in Figure 4 were applied to calculate partial intrinsic diffusivities – Eq. (12) and intrinsic fluxes – Eq. (11).

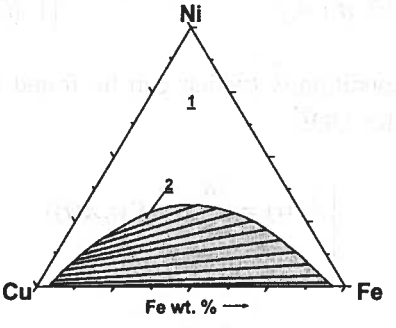

Fig. 3. Ternary phase diagram Cu-Fe-Ni at 1273 K: 1 – single phase alloy, 2 – two phase alloy. The miscibility gap based on experimental results and thermodynamic reassessment [8]

Modelling Interdiffusion in the Cu-Fe-Ni Closed System

Interdiffusion modelling in the Cu-Fe-Ni closed system has been done using DifSim software [28] and compared with the experimental results [21]. For the calculations the following data have been used:

(1) Initial concentration profiles – step functions defined by the terminal composition of the diffusion couple, see Figure 5.

$$Cu = \begin{cases} 42\ wt.\% & x \in [-\Lambda, 0] \\ 0\ wt.\% & x \in [0, \Lambda] \end{cases}, \quad Fe = \begin{cases} 0\ wt.\% & x \in [-\Lambda, 0] \\ 24\ wt.\% & x \in [0, \Lambda] \end{cases}, \quad Ni = \begin{cases} 58\ wt.\% & x \in [-\Lambda, 0] \\ 76\ wt.\% & x \in [0, \Lambda] \end{cases}$$

(2) Average molar concentration of the Cu-Fe-Ni alloy, $c = 0.144\ mol\ cm^{-3}$.

(3) Thickness of the diffusion couple, $2\Lambda = 0.07\ cm$.

(4) Calculated average self-diffusion coefficients of copper, iron and nickel in Cu-Fe-Ni diffusion couple [21] at 1273 K

$$C_{Cu} = 2.89 \cdot 10^{-11}\ cm^2 s^{-1}$$
$$D_{Fe} = 1.52 \cdot 10^{-11}\ cm^2 s^{-1}$$
$$D_{Ni} = 2.09 \cdot 10^{-11}\ cm^2 s^{-1}$$

(5) Thermodynamic activity data – Figure 4.

(6) Time of the process duration, $\hat{t} = 612\ ks$.

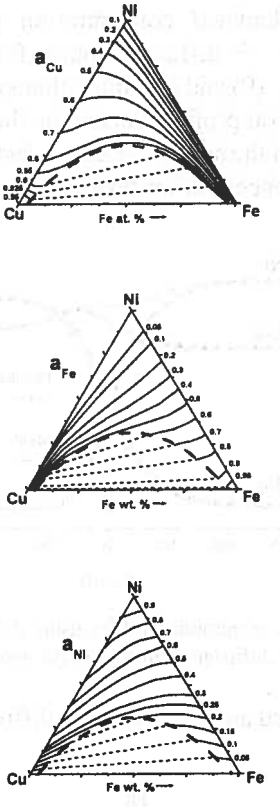

Fig. 4. Calculated isoactivity curves for Cu, Fe and Ni at 1273 K based on pure element reference state at 1273 K (1 atm) [8]

In the Figure 5 the calculated concentration profiles of Cu, Fe and Ni are compared with the experimental results and show satisfactory agreement.

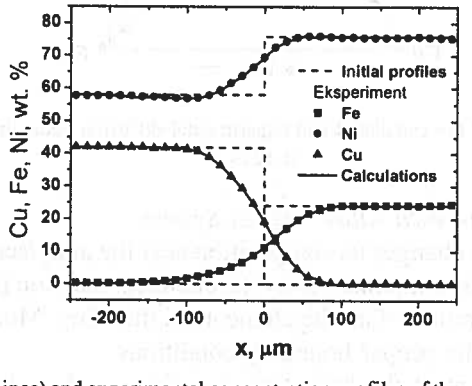

Fig. 5. The calculated (solid lines) and experimental concentration profiles of the components (points) in Cu-Fe-Ni alloy after 612 ks of diffusion annealing at 1273 K in argon

The next figure shows calculated concentration profiles of Cu, Fe and Ni in 48MNi-52Cu/19.7Ni-80.3Fe (wt. %) diffusion couple for a chemical potential gradien as a driving force for diffusion – Eq. (9) and assuming that system is ideal – Eq. (13). One can notice that calculated concentration profiles depend on the used flux formula. Consequently, the assumption of „ideality" of the system – i.e., neglecting of thermodynamic data – can strongly affect the calculated concentration profiles.

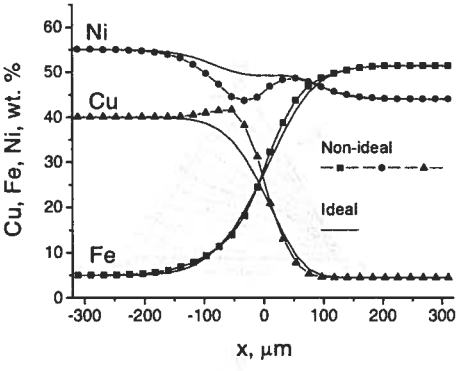

Fig. 6. The comparison of calculated concentration profiles using different flux formulae: (a) for a chemical potential gradien as a driving force for diffusion (points) and (b) assuming the system is ideal (dashed lines)

In the Figure 7 some calculated and experimental diffusion paths for Cu-Fe-Ni system at 1273 K are assembled.

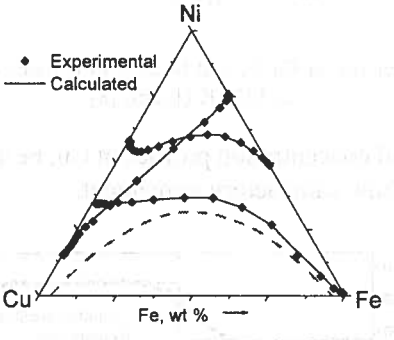

Fig. 7. The comparison of the calculated and experimental diffusion paths in the Cu-Fe-Ni systems at 1273 K

Selective oxidation of Cu-Fe-Ni Alloy – Open System

Initially uniform alloy changes its composition near the alloy/scale boundary due to the oxidation process. In multi-component alloy the chemical reaction (oxide formation) at the boundary effects concentration of all the elements in the alloy. Modelling of such process involves formulation of the proper boundary conditions.

The flux of component at the boundary, (i.e. for $x = \Lambda$), which is oxidised (forms a scale) can be expressed as follows

$$J_i(t,\Lambda) = J_i^{diff}(t,\Lambda) + c_i(t,\Lambda)\frac{d\Delta X}{dt}(t), \tag{25}$$

where $d\Delta X/dt$ is the rate of the alloy consumption due to oxidation.
If some element in the alloy does not form a scale then its flux through the boundary equals zero

$$J_i(t,\Lambda) = 0 \tag{26}$$

and consequently

$$J_i^{diff}(t,\Lambda) = -\,c_i(t,\Lambda)\frac{d\Delta X}{dt}(t). \tag{27}$$

If the scale (oxide) is compact and adheres to the alloy, the rate of the alloy consumption is inversely proportional to instantaneous thickness of the oxide layer, which in turn is proportional to the displacement of the alloy surface ΔX. Thus the rate of the alloy consumption is

$$\frac{d\Delta X}{dt} = \frac{k_c}{\Delta X} \tag{28}$$

where k_c is a parabolic rate constant of an alloy consumption. The displacement of the alloy surface due to oxidation can be obtained solving the equation (28)

$$\Delta X = \sqrt{2k_C t} \tag{29}$$

and consequently

$$\frac{d\Delta X}{dt} = \sqrt{\frac{k_c}{2t}}. \tag{30}$$

Expressions (25), (26) and (30) introduced into equations (5) describe boundary conditions for the selective oxidation.

In this section modeling of interdiffusion in a selectively oxidised Cu-50Fe-40Ni (wt.%) alloy at 1273 K is demonstrated. For the calculations the following data have been used:

(1) Initial concentration profiles – uniform concentration profiles:

$$c_{Cu}(0,x) = 10\ wt.\%$$
$$c_{Fe}(0,x) = 50\ wt.\%$$
$$c_{Ni}(0,x) = 40\ wt.\%$$
$$for\ x \in [-\Lambda, \Lambda]$$

(2) Average molar concentration of the Cu-Fe-Ni alloy, $c = 0.144\ mol\ cm^{-3}$.
(3) Thickness of the diffusion couple, $2\Lambda = 0.06\ \mu m$.

(4) Average self-diffusion coefficients of copper, iron and nickel in Cu-Fe-Ni at 1273 K (see above)
(5) Thermodynamic activity data – Figure 4.
(6) Parabolic rate constant of an alloy consumption [29], $k_c = 3.5 \cdot 10^{-7}\ cm^2 s^{-1}$.

In the Figure 8 the calculated concentration profiles of copper, iron and nickel due to iron selective oxidation of Cu-Fe-Ni are presented. After initial enrichment of the alloy in nickel its concentration decreases for longer times.

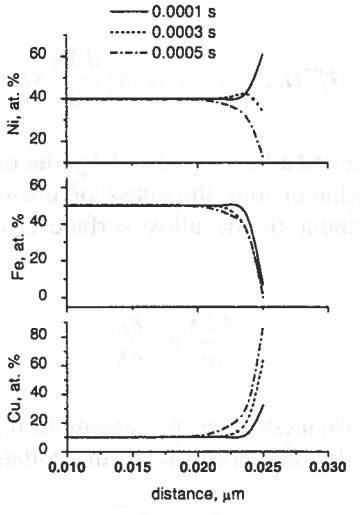

Fig. 8. The calculated Cu, Fe and Ni concentration profiles in selectively (iron) oxidised Cu-50Fe-40Ni-alloy at 1273 K

In the Figure 9 the diffusion paths of the selectively oxidised Cu-Fe-Ni alloy are shown. This figure illustrates the fact that due to oxidation process initially single-phase alloy can change to multi-phase when the diffusion path crosses miscibility gap and cross over to a two phase region.

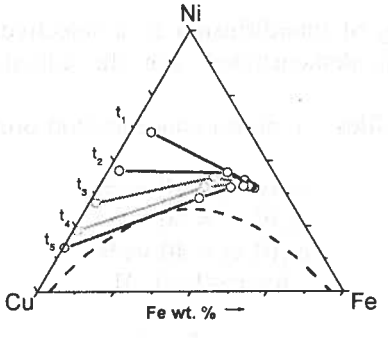

Fig. 9. The diffusion paths in profiles in selectively (iron) oxidised Cu-50Fe-40Ni alloy at 1273 K

7. Summary and conclusions

1. Mathematical model of interdiffusion in multi-component, non-ideal open systems has been formulated. For the known thermodynamic data (components' activities), kinetic data (self diffusivities) and reaction rate at the boundary (fluxes of the components) the evolution of the concentration profiles and drift velocity can be found.
2. Using idea of generalized solution and Galerkin approximation, the numerical solution to the model has been obtained. Complicated system of non-linear partial differential equations (PDE) describing interdiffusion process has been transformed to the system of ordinary differential equations (ODE), which is much simpler to solve.
3. Effective formulae enable to calculate the concentration profiles of the elements and the drift velocity as a function of time and position have been presented.
4. The model can be used both for a quantitative description of interdiffusion in the open and closed systems.
5. Application of the model for modelling interdiffusion in the Cu-Fe-Ni diffusion couple (closed system) was demonstrated. The calculated concentration profiles were consistent with experimental results
6. Iron selective oxidation of Cu-50Fe-40Ni alloy was chosen to demonstrate modelling interdiffusion in the open system. It was demonstrated that initially single-phase alloy can change to multi-phase due to oxidation process when the diffusion path crosses miscibility gap and cross over to a two phase region.
7. These examples show the potential of the model in describing interdiffusion in a wide range of diffusion limited process. An effective application of the model involves knowledge of the thermodynamic and kinetic data. Kinetic data – self diffusivities – can be obtained using e.g. radiotracer technique [30] or using inverse methods [31]. Significant progress is observed in the software. Programs like Thermo-Calc [32], FactSage [33] etc. can be used as an effective tool for obtaining thermodynamic activities even in a multi-component systems.
8. So far results and analysis of general flux formulae – Eq. (3) – show prospect of the extension of this model in modelling stresses affected diffusion, electromigration, diffusion in electrolytes, etc.

Acknowledgments

This work was supported by the Polish State Committee for Scientific Research Grants No. 4T08A 001 25 during the period (2003-2005) and No. 10.10.160. 975. The author is indebt to Professor M. Danielewski (AGH University of Science and Technology) for stimulating discussions and K. Szyszkiewicz (WSB-NLU Nowy Sącz) for mathematical assistance.

REFERENCES

[1] L.S. Darken, Trans. AIME 175, 184 (1948).
[2] L. Onsager, Phys. Rev. **38**, 2265 (1931).

[3] J.S. Kirkaldy, series of articles in Can. J. Phys (1957-1969).
[4] J.S. Kirkaldy, D.J. Young, Diffusion in The Condensed State, The Institure of Metals, London (1987).
[5] M.A. Dayananda, in Diffusion in Solid Metals and Alloys, Landolt-Börnstein, Numerical Data and Functional Relationships in Science and Technology, New Series III/26, Ed., H. Mehrer, Springer-Verlag, Berlin (1991).
[6] M.A. Dayananda, in Proc. Symp. Diffusion in Solids. Recent Developments, Metall. Soc. of AIME 195-, Warrendale, PA, 1984, Eds., M.A. Dayannada and G.E. Murch (eds), Detroit, USA (1985).
[7] F.J.J. van Loo, Proc. Solid St. Chem. **20**, 1251 (1990).
[8] K.J. Ronka, A.A. Kodentsov, P.J.J. Van Loon, J.K. Kivilahti, F.J.J. Van Loo, Metall. and Materials Transactions A **27A**, 2229 (1996).
[9] M.S. Thomson, J.E. Morral, Acta metall. **34**, 2, 339 (1986).
[10] J.E. Morral, H. Chen, Scripta Mater. **43**, 699 (2000).
[11] C.E. Campbel, W.J. Boettinger, U.R. Kattner, Acta Materialia, **50**, 775 (2002).
[12] T. Helander, J. Agren, Acta Mater. **47**, 11, 3291 (1999).
[13] M.A. Dayananda, Deffect and Diffusion Forum **83**, 73 (1992).
[14] M.A. Dayannda, Mater. Sci. Eng. **A121**, 351 (1989).
[15] C. Cserhati, U. Ugaste, M.J.H. van Dal, N.J.H.G.M. Lousberg, A.A. Kodentsov, F.J.J. van Loo, Deffect and Diffusion Forum. **194-199**, 189 (2001).
[16] S.R. de Groot, P. Mazur, Non-Equilibrium Thermodynamics, Dover Publications, Inc., New York (1984).
[17] A.C. Smigelskas, E.O. Kirkendall, Trans. AIME **171**, 2071 (1947).
[18] K. Holly, M. Danielewski, Phys. Review B, **50**, 13336 (1994).
[19] M. Danielewski, K. Holly, W. Krzyzanski, Polish J. Chem. **68**, 2031 (1994).
[20] M. Danielewski, R. Filipek, K. Holly, B. Bozek, phys. stat. sol (a) **145**, 339 (1994).
[21] R. Bachorczyk, M. Danielewski, R. Filipek, Defect and Diffusion Forum **216-217**, 141 (2003).
[22] M. Planck, Ann. Phys. Chem. (Wiedemann) **39**, 161 (1890).
[23] M. Danielewski, R. Filipek, J. Comp. Chem. **17**, 13, 1497 (1996).
[24] J. L. Lions, E. Magenes, Non-homogeneous boundary value problems and applications, Springer-Verlag, Berlin (1972).
[25] R. Filipek, K. Szyszkiewicz, Numerical solution to the Interdiffusion Problem in Multi-component Non-ideal Open Systems, in Proc. of International Conference DIMAT 2004, Trans. Tech, Defect and Diffusion Forum, to be published (2005).
[26] E. Fehlberg, Computing **4**, 93 (1969).
[27] A. Jansson, TRITA-MAC-0340, The Royal Institute of Technology Stockholm, 1-14 (1987).
[28] Demonstration version of the software is available at the web site http://ceramrtr.ceramika.agh.edu.pl/~rof/demo.html.
[29] Z. Grzesik, PhD Thesis, Krakow (1992).
[30] St. Frank, U. Södervall, Chr. Herzig, Phys. Stat. Sol (b), **191** 45 (1995).
[31] S. Datta, R. Filipek, M. Danielewski, Defect and Diffusion Forum **203-205**, 47 (2002).
[32] *Thermo-Calc* is a registered trade mark of Thermo-Calc Software.
[33] *FactSage* is a registered trade mark of ESM Software, Inc.

Received: 1 March 2004.

ARCHIVES OF METALLURGY AND MATERIALS
Volume 49 2004 Issue 2

D.L. BEKE *, Z. ERDÉLYI*, I.A. SZABÓ*, G.A. LANGER*, G. KATONA*, C. CSERHÁTI*

DIFFUSION IN NANOSCALE

DYFUZJA W NANOSKALI

Mass transport on nanoscale has specific features because of the presence of high number of grain- and interphase boundaries, as well as because of the fundamental problems related to the very short diffusion distances. In the first part examples on the changes (as the micro-metre scale is reduced to nanometre dimensions) of the overall mass transport due to the boundary effects are exposed. Then examples of processes, in which the diffusion coefficient depends strongly on the concentration (non-linearity) and the diffusion distance is typically few nanometres, will be discussed.

Opis transportu masy rozpatrywanego w skali nano posiada swoja specyfikę ze względu na znaczną ilość granic tak międzyziarnowych jak i międzyfazowych oraz na istotne problemy związane z bardzo niewielką drogą dyfuzji. W pierwszej części opracowania przedstawiono przykłady zmian transportu masy związanych z efektami granicznymi (przy przejściu od skali mikro do nano). Następnie dyskutowane są przykłady procesów, w których współczynnik dyfuzji silnie zależy od stężenia i gdy typowa droga dyfuzji wynosi kilka nanometrów.

1. Introduction

Grain boundaries (GB) are, generally, diffusion short circuits. Consequently, the major part of material transport will occur by GB diffusion in nanomaterials where a large amount of atoms can lie on grain or interphase boundaries (50% as well as 20% for grain size equal to 5 nm and 10 nm, respectively). As we will see one of the interesting questions is related to the classical classification [1,2] into the well-known type *A*, *B* and *C* regimes of *GB* diffusion. This classification fails in nanomaterials, even if it contains only one type of short circuits with one diffusion coefficient only [3], because the B regime can not be realized and

* DEPARTAMENT OF SOLID STATE PHYSICS, UNIVERSITY OF DEBRECEN, 4010 DEBRECEN, P.O.Box.2, HUNGARY

a variety of the possible sub-regimes can be treated ((C-C, B-B, AB-B, A-B sub-regimes as compared to the classical division for *A*, *B* and *C* regimes) and investigated experimentally [4,5]. Similarly segregation effects can also be different form the well-known microcrystalline case [3,6].

Diffusion in nanostructures presents challenging features even if the role of structural defects (dislocations, phase- or grain-boundaries) can be neglected. This can be the case for diffusion in amorphous materials or in epitaxial, highly ideal thin films or multilayers where diffusion along short circuits can be ignored and "only" fundamental difficulties, related to nanoscale effects, raise. For example the continuum approach can not be automatically applied [3,6].

In this paper, based on the research experience of our group, most of the above challenging phenomena will be exposed and/or discussed in more details.

2. Role of structural defects (grain- and interphase-boundary effects)

If the *role of structural defects* (dislocations, phase- or grain-boundaries) is important, a set of interesting phenomena can be observed even if the nanomaterial contains only one type of short circuits with one diffusion coefficient only [3]. It is well known from the classical treatments (e.g. [1,2]) that there are three different GB diffusion regimes: type *A*, *B* and *C*. *For grain sizes, d, in the order of 10 nm the A or C regimes will be more important and the B regime* – in contrast to micro-crystalline samples where it is the most frequently realized case – *can not be observed.* It can be seen from the condition for type B regime [1,2] ($100\delta < L = (Dt)^{1/2} < d/20$, where δ ($\equiv$0.5nm) is the *GB* thickness and t is the time of diffusion), that if $d \equiv 10$ nm this condition can not be fulfilled. Thus, according to the conditions for the type *A* and *B* regimes ($L \gg d$ for *A* and $20\,L < \delta$ for *C*) – depending on t -, either *A* or *C* regimes will be observed. In type *A* regime – according to classical handbooks on diffusion [7] – a significant enhancement of intermixing or solid state reactions is observed, with an effective interdiffusion coefficient given by the Hart's equation [1,7]:

$$D_{eff} = gDg + (1-g)D \qquad (1)$$

where g is the grain-boundary volume fraction ($g \approx \delta/d$; the factor of proportionality depends on the grain shape, but is in the order of unity). If $d \equiv 10$ nm, then only the first term will be dominant, since usually $Dg/D > 10^4$. Very recently Belova and Murch [8] have shown that that for the estimation of this effective diffusivity the generally accepted Hart equation should be replaced by the Maxwell equation (known from the random resistor network problem) on nanoscale (in order to avoid an overestimation by about 50%):

$$D_{eff} = D_g[(3-2g)D + 2gD_g]/\{gD + (3-g)D_g)\}. \qquad (2)$$

It was also found from Monte Carlo simulations that the usual condition for type *A* regime is too stringent and the transition occurs already at $L \equiv 0.2d$.

Accordingly, in *A* regime a high effective diffusion coefficient will characterize the rate in any technically important interdiffusion or solid state reaction process (e.g. in surface alloying). On the other hand in many cases the process will take part dominantly along grain- or phase boundaries (type *C* regime) leading to phenomena such as degradation of multilayers by grain-boundary grooving, pinhole formation and coarsening [9,10], or solid state phase transformations in thin films.

Additionally, if there is a multi- level organization in the structure (at least two different types of boundaries are present: e.g. closed free surfaces and GBs in vacuum condensed nanomaterials), then the above clear classification falls even in microcrystalline materials (see. e.g.[1,4,5]). For example the measurements in type *B* regimes can not be simply interpreted by one straight line on the *lgI* (I is the specific activity) versus $y^{6/5}$ plots, but – because of the presence of different type of GBs with different diffusion coefficients – a non-linear penetration plot is usually observed [11,12]. The most recent and more precise treatment of the problem can be found in [4,5] where *intermediate regimes between the A, B and C type diffusion regimes* were defined due to the presence of grain- and interagglomerate boundaries in nanocrystalline γ-FeNi [4,13].

It is also an interesting question: Whether *the GB diffusion coefficients* measured in these alloys *are identical to those obtained in microcrystalline state* (e.g. from diffusion experiments made in type *B* regime) *or not*? There is an increasing number of experimental evidences that the above diffusion coefficients agree very well with each other, i.e. in most of the cases the structure of GBs in nanocrystalline and polycrystalline samples is very similar, provided that the grain-boundary structure is already relaxed [3].

In hetero-diffusion experiments *segregation effects* describing the matching conditions between the diffusion source and the GB (as well as between the GB and the free surface, if there is a terminal free surface present in the experiment) should also be taken into account [5,8,14,15,16]. Usually the segregation kinetics is also a process during which the redistribution takes place along distances of few nanometers. Besides of these kinetic effects, there is also a size effect manifested in changes of the character of the segregation isotherm itself. This is the consequence of the finite size of the sample: either the surface perturbed regions can overlap and thus an increase in the solubility limit can be observed [6], and/or the number of sites at interface can be higher than the number of solutes in the sample and a change form the Fowler-Guggenheim- to a McLean-type [6] (or even to the Henry-type) isotherm [17,18] can be observed.

At short diffusion distances in interdiffusion, leading to formation of reaction products, the usual *parabolic law of diffusion can be violated,* if the role of reactions at the interface is taken into account. At short diffusion times the growth of the reaction layer will be controlled not by a parabolic, but by a linear law according to the formula [7]:

$$x^2 + Ax = Bt, \tag{3}$$

where x is the thickness of the reaction layer, A and B are proportional to the reaction rate and interdiffusion coefficients, respectively. The same effect can be observed in many bulk or surface coarsening processes (Ostwald ripening of ensembles of nano-clusters or beaded

films on a surface, if their characteristic distance is large enough to produce a diffusion interacting ensemble but shorter than the characteristic length, defined above).

It is also well-know, that *the nucleation of a new phase* always needs a certain critical size, d_c, which is typically in the nanometer range. If, for example, in a solid state diffusion reaction the width of the diffusion zone, L, is less than d_c the given phase cannot form [19]. In case of more than one diffusion product this can lead to different interesting observations in the first stages of the heat-treatments.

Sometimes – e.g. in diffusion in MBE (Molecular Beam Epitaxy) grown thin films or multilayers – the diffusion distances can be shorter than the typical distance between the sources and sinks of diffusion vehicles. While in "normal" diffusion *the equilibrium concentration* of such *defects* are set by the sources or sinks (and the characteristic distance, l, between them is much shorter than the macroscopic diffusion length, L), if $L<l$ the mechanism of diffusion can change, similarly as it was already observed, on more macroscopic scale, for diffusion in dislocation free Si single crystals [20].

Bokstein and his co-workers [5,21,22] illustrated that *the mechanical stress field* (both the stress gradient and its hydrostatic component) *can have a considerable influence on the GB diffusion in thin films.* The effect of the stress gradient and the effect of the hydrostatic component can be separated as "gradient effect' and "mobility effect". In [21] the authors argue that the mechanical stress can reach as high values as 1 GPa and the small film thickness can lead to large gradients as well. Furthermore at low temperatures the stress relaxation can be hindered and the hydrostatic component of the stress field can also enhance or supress the grain boundary diffusion (across the exponential dependence of the mobility on the pressure). At the moment there is lack of equivocal evidences for explanations of the existing order of magnitude differences of the grain boundary diffusion coefficients measured e.g. in thin films on different substrates (and thus being in different stress states), although the above explanation offers a plausible solution.

3. Fundamental difficulties

For diffusion in amorphous materials or in ideal bi- or multilayers, where diffusion along short circuits can be ignored, "only" fundamental difficulties, related to nanoscale effects, raise. The most important difference, compared to diffusion along long distances (orders of magnitude longer than the atomic spacing, a), is that the continuum approach can not be automatically applied and there is a gradient energy correction to the driving force for diffusion. This correction becomes important again if large changes in the concentration take place along distances comparable with a, and results in an additional term in the atomic flux, proportional to the third derivative of the concentration. It was shown recently in our group [3,6,9,23-30], that these effects can lead to unusual phenomena especially if there is a strong non-linearity in the problem i.e. if the diffusion coefficient has a strong concentration dependence.

3.1. Basic equations

For exchange mechanism in a binary AB alloy (consisting of a slab of material with N lattice planes, normal to the y axis and each atom in a plane has z_1 nearest neighbours in this plane as well as z^v in planes adjacent to this), with the coordination number $Z = z_1 + 2z_v$ the change in relative concentration of B in plane i is given by (see e.g. [6])

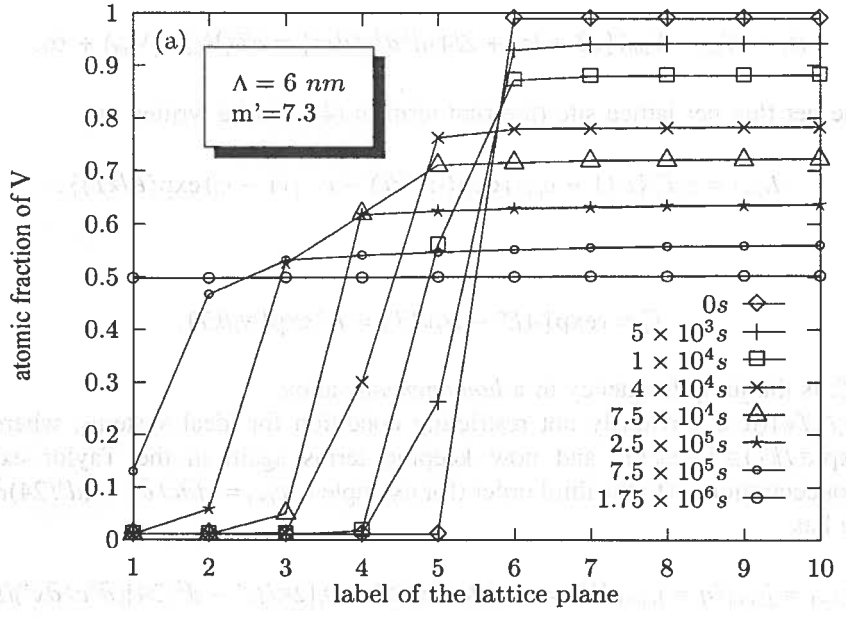

Fig. 1. Concentaration distributions at different times in Mo-V system (m' = 7.3) [23] at T = 1053 K and for Λ = 6 nm

$$dc_i/dt = -z_v[c_i(1-c_{i-1})\Gamma_{i,I-1} - (1-c_i)c_{i-1}\Gamma_{i-1,I} + c_i(1-c_{i+1})\Gamma_{i,i+1} - c_{i+1}(1-c_i)\Gamma_{i+1,i}]. \quad (4)$$

where e.g. $\Gamma_{i,i+1}$ gives the exchange frequency of a B atom in layer i with an A atom in layer $i+1$. Assuming an Arrhenius–type temperature dependence of the jump frequencies ($\Gamma_{i,i+}^{\ 1} = \nu\exp[-E_{i,i+1}/kT$, with the attempt frequency ν), an appropriate choice of the activation energies $E_{i,i+1}$ can be such [3,6,24,31] that

$$E_{i,i+1} = E^v - \alpha_i + \varepsilon_i \quad \text{and} \quad E_{i+1,i} = E^v - \alpha_i - \varepsilon_i, \quad (5)$$

where E^v is the saddle point energy and α_i and ε_i are functions of $c_{i,-1}$, c_i, c_{i+1} and c_{i+2} [3,6]:

$$\alpha_i = [z_v(c_{i-1} + c_{i+1} + c_i + c_{i+2}) + z_l(c_i + c_{i+1})](V_{AA} - V_{BB})/2 \quad (6)$$

and

$$\varepsilon_i = [z_v(c_{i-1} + c_{i+1} - c_i - c_{i+2}) + z_l(c_i - c_{i+1})]V. \quad (7)$$

Here V_{AA}, V_{BB} and V_{AB} are the pair interaction energies and the interaction energy, V, has its usual meaning ($V = V_{AB} - \{V_{AA} + V_{BB}\}/2$).

Furthermore, if the surface concentration, $n = cd/\Omega$ (Ω is the atomic volume and d is the distance between the atomic planes), is expanded in Taylor series (up to the third order) and the relations $(c_{i-1})-(c_{i+1}-c_{i+2}) = (d^2)\partial^2 c/\partial x^2$ and $c_i + c_{i+1} = (d/2)\ \partial^2 c/\partial x^2 + 2c$ are also used [6,30];

$$\alpha_i = (V_{AA} - V_{BB})\{cZ + (z_v + Z/4)d^2\partial^2 c/\partial x^2\} = cZ(V_{AA} - V_{BB}) + \alpha_i. \qquad (8)$$

Thus the net flux per lattice site (the first term in (4)) can be written as

$$J_{i,i+1} = z_v \Gamma_i \{c_i(1 - c_{i+1})\exp(-\varepsilon_i/kT) - c_{i+1}(1 - c_i)\exp(\varepsilon_i/kT)\}. \qquad (9)$$

with

$$\Gamma_i = \nu\exp[-(E^o - \alpha_i)/kT] = \Gamma_i^h \exp[\alpha_i/kT]. \qquad (10)$$

Here Γ_i^h, is the jump frequency in a *homogeneous* alloy.

If $\varepsilon_i/kT \ll 1$(it is obviously not restricting condition for ideal systems, where $\varepsilon_i = 0$) then $\exp(\varepsilon_i/kT) \cong 1 + \varepsilon_i/kT$, and now keeping terms again in the Taylor expansion of the concentration up to the third order (for example $c_i - c_{i+1} = -d\partial c/\partial x - (d^3/24)\partial^3 c/\partial x^3$) [6], one has

$$j_{i,i+1} = j_{i,i+1}/q = j_{i,i+1}d/\Omega = -D_i(\partial c/\partial x)/\Omega + D_i[2\kappa/f_o'' - d^2/24](\partial^3 c/\partial x^3)/\Omega \qquad (11)$$

where q is the area of the specimen perpendicular to the direction of diffusion. In (11) D_i is the intrinsic diffusion coefficient, $D_i = z_v d^2 \Gamma_i \theta$, θ is the so called thermodynamic factor [32] and $\theta = 1 - 2ZVc(1-c)/kT$ i.e. for an ideal system $\theta = 1$. κ and f_o'' are the gradient energy coefficient and the second derivative of the free energy of the homogeneous system [7,32], respectively.

Expression (11) – except for the second term proportional to d^2 in the bracket – is similar to the well-known Cahn-Hilliard expression [6,32]. However, while the classical Cahn-Hilliard expression contains a diffusion coefficient belonging to a *homogeneous* alloy, here in the exponent of D_i the α_i' is proportional to the second derivative of the concentration (see eq. (8)), i.e. inhomogeneity corrections lead not only to the term proportional to the third derivative of concentrations, but also to an additional factor in D_i!

For ideal solutions, where $V = 0$ and thus $\kappa = 0$, the presence of the term proportional to d^2 (because of its negative sign), would lead to composition oscillations (D is positive – and if it is independent of composition – the sign of the second term corresponds to $2\kappa/f_o'' < 0$ "Cahn-Hilliard" term but with $f_o'' > 0$ [32]). This is possibly due to the simplifications made during the transition from the discrete model to the continuous one (see also [6]). Nevertheless, the role of these refinements would need more attention if diffusion takes place on nanoscale and one uses continuum equations. One can expect for example that

from the solutions of equation (11), solutions with wavelength $\Lambda \leq 2d$ should be excluded (the oscillations take place with a concentration wave of $\Lambda = 2d$). For composition dependent D the situation can be even much more complex. These remarks can be important in the description of nanodiffusion in amorphous systems (see also [3]), where no discrete models are available and one can rely only on the "improved" continuum equations.

For concentration independent jump frequencies $\Gamma_{i,i+1} = \Gamma_{i+1,i} = \Gamma$ and the Fick II. law (eq. (4)) has the form:

$$\partial c_i / \partial t = \Gamma (c_{i+1} + c_{i-1} - 2c_i). \tag{12}$$

The term in the bracket, divided by d^2, can be easily rewritten to the second derivative of the relative concentration. Now, it is easy to show [7] that taking a sinusoidal concentration profile ($c \sim \sin\{2\pi x/\Lambda\}$) the solutions of the continuum Fick equation and (12) will be identical only for $\Lambda > 10$d. However, in the case of a strongly composition dependent interdiffusion coefficient the validity limit of the continuum approach – even in an ideal system – can be shifted to larger length by about one order of magnitude [24], i.e. it will be in the order of 10 nm. These results were obtained in [24] by carrying out calculations for diffusion intermixing in multilayers of ideal solid solutions, from the discrete model as well as from the continuum Fick II. equation by finite volume calculations with diffusion coefficients equivalent to that used in the atomic model. The strength of the composition dependence of D in the continuum model is measured by m' defined as

$$\log D(c) = \log D(0) + \text{m'c}. \tag{13}$$

In the discrete model (see also the first term in eqs. (8) as well as eq. (10)) $m = Z(V_{AA} - V_{BB})/kT$ and in the calculations of [24] m' (m' = m lg$e$) was 7.3 (Mo/V system).

3.2. Results of simulations and experiments

3.2.1. Homogenization by the shift of the interface

It was obtained in [23], from finite volume calculation of the solutions of (4) in Mo/V multilayers, that for a strong concentration dependence of $D_{Mo} = D_V = D$ the interface between the *Mo* and *V* remains atomic sharp and shifts as a whole until the component with small D has not been consumed (Fig.1). It can also be seen that the diffusion is very asymmetrical: there is a fast dissolution and diffusion of Mo into *V*, but there is no diffusion in *Mo*. This behaviour, as it is illustrated in Fig. 2, was indeed observed very recently in amorphous Si/Ge system by Auger-depth profiling technique [25] (in both systems is $V \cong 0$.)

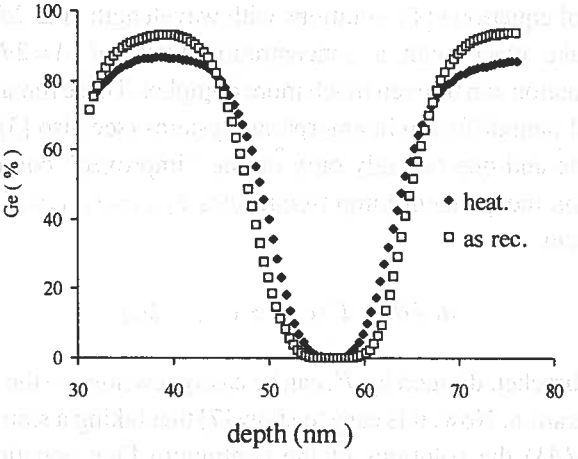

Fig. 2. Auger depth profiles for the as-received and annealed (at 680 K for 100 h) amorphous Si/Ge multiplaxer [25]. The Si content increases in Ge and the Si layer shrinks

3.2.2. Non-parabolic shift of sharp interface in ideal systems

The non-linearity (strong composition dependence of D) can lead to even more interesting results if we have dissolution of a thin film into a substrate [26]. Fig. 3. shows the results of simulations carried out for Ni dissolution into Cu (again the system is ideal, i.e. $V=0$). It can be seen that the dissolution starts at the interfacial layer, and until this is not consumed, the next layer remains complete. Thus the interface shifts step by step. This layer-by-layer dissolution takes place until the moving "interface" reaches the Ni layer just before the last. Then, due to the driving force for surface segregation, the intermixing will be continued by the saturation of Cu in the top layer and the change in the second layer will be retarded according to the segregation isotherm. The layer-by-layer dissolution – if the substrate is semi-infinite and the diffusion coefficient depends strongly on the concentration [26] – results in a periodic behaviour as a function of time: each plane practically dissolves subsequently reproducing the same process. Therefore *the average value of v should be constant, independent of time, and the interface shifts linearly with time, which is in contrast to the parabolic law ($v \propto t^{-1/2}$) would be expected from a continuum model.* Of course, after the dissolution of more and more layers one will have a transition to the parabolic dissolution. Obviously, this transition will depend on the value of m' [26]. Fig. 4a. shows the position of the interface versus time, obtained from simulation for a semi-infinite Cu(111) substrate with 100 atomic layers of Ni. Due to the periodicity, mentioned above, the curve has periodic oscillations around the straight line fitted, but the slope of the straight line is $1 \pm 8 \times 10^{-4}$, i.e. the average shift is indeed linear. It was also shown by simulations that already for 1000 atomic layers and at longer times the dissolution is indeed obeys the parabolic law [6,26].

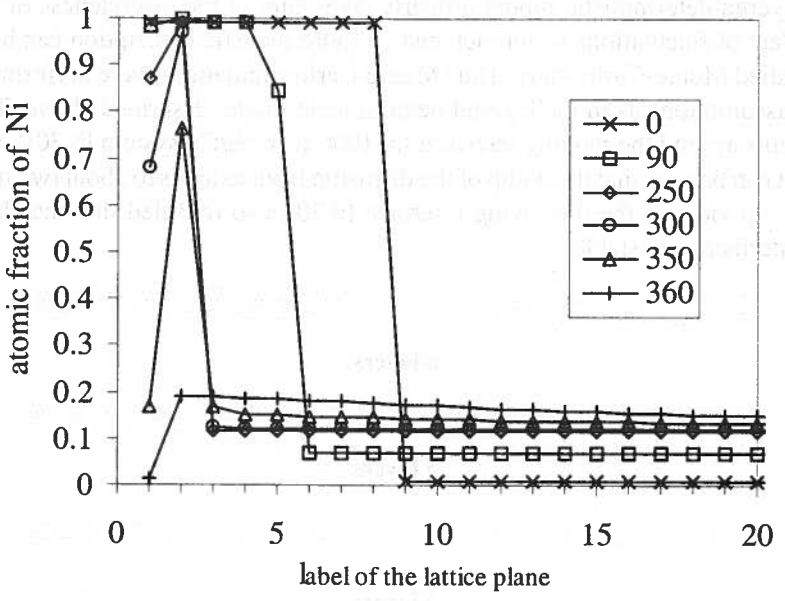

Fig. 3. Concentration profilesfor Ni dissolution into 51 layers of Cu(111) (of which only 12 is shown here) for different times (given in special untis [26])

Although the oscillating character of the dissolution – because of technical difficulties – could not be resolved experimentally in [26], the above simulation result was confirmed by measuring the kinetics of the Auger signals of Ni and Cu from the top of the 8 monolayer Ni. Fig. 4b. shows the final results for the average time evolution of the Ni thickness versus time for 679 K. It can be seen that n is indeed a linear function of time up to the second layer.

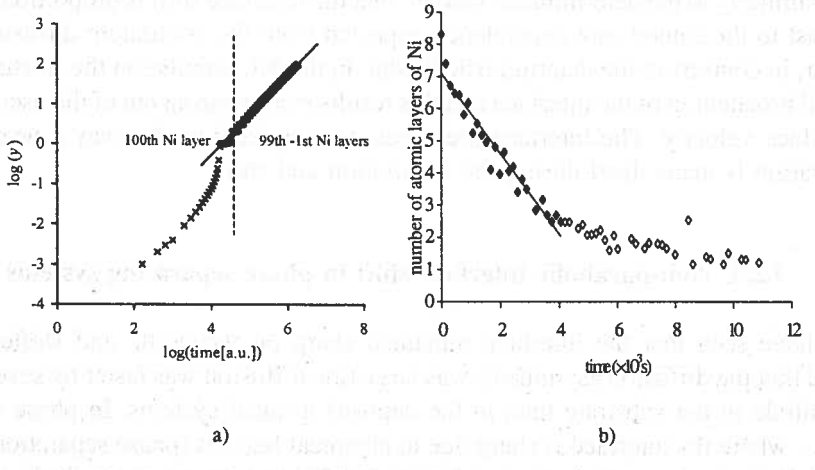

Fig. 4. a): Position of the interface versus time for the dissolution of 100 Ni layer into Cu(111) substrate (see also the text), b): Change of the Ni thickness at 679 K [26]

The layered deterministic model properly takes care of the discreteness of the lattice, but the effect of fluctuations is not included. A more realistic description can be achieved with a detailed Monte-Carlo study. Thus Monte-Carlo simulations were performed [6] with the same assumptions as in the layered deterministic model described above. The atomic arrangements around the moving interface (at 1000 K in Ni/Cu system [6,30]) can be seen on Fig.5. It can be seen that the width of the diffusion front extends to about two monolayers only. The top view of the dissolving interface [6,30] also revealed that the shape of the moving interface was stable.

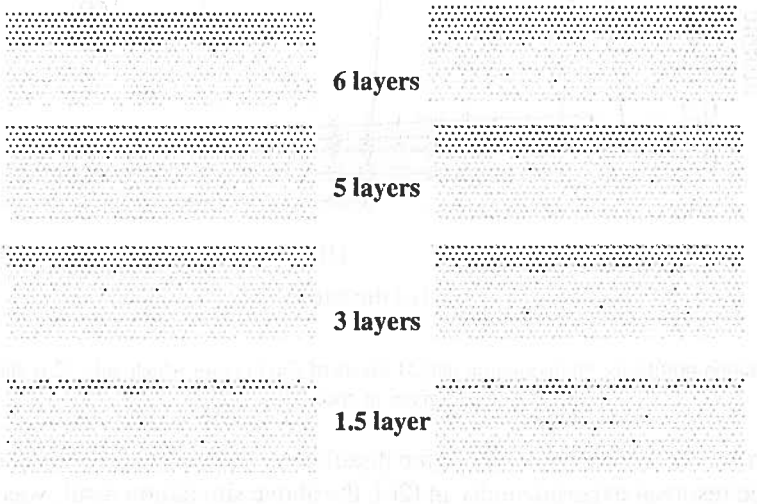

Fig. 5. Cross-section of the sample at different times in two MC simulation runs [6]. The black and gray dots represent different atoms

In conclusion, after taking into account the fluctuations by MC simulation, we have found – similarly to the deterministic model - that the interface shift is proportional to time, in contrast to the square root dependence expected from the continuum diffusion model. However, in contrast to the deterministic model, in the MC simulation the fluctuations led to a small broadening of the interface and this results in a smearing out of the oscillations of the interface velocity. The interface preserves its shape and in this way a nearly steady configuration is maintained during the dissolution and shift.

3.2.3. Non-parabolic interface shift in phase separating systems

We have seen that the interface remained sharp on nanoscale and shifted linearly provided that the diffusion asymmetry was large (the diffusion was faster by several orders of magnitude in the substrate than in the deposit) in ideal systems. In phase separating systems – where the interface is sharp due to chemical reasons (phase separation) – it was obtained from previous computer simulations [33-35] that the interface displacement was proportional to the square root of the time. However, in these simulations the composition

dependence of the diffusivity (diffusion asymmetry) was neglected. Thus it was very plausible to study the interplay of the diffusion asymmetry (composition dependence of diffusion coefficient) and the phase separation tendency (chemical effect) in the kinetics of the interface shift during dissolution in a binary system with restricted solubility. In [29] we have demonstrated by computer simulations (in fcc structure for 111 plane; $z_l = 6$ and $z_v = 3$) how these parameters could influence the kinetics of the interface motion.

The position of the interface was fixed to the plane with the composition 0.5 (it can obviously lie between two atomic planes). After determining this position, logarithm of the shift versus the logarithm of the time was plotted. Fitting a straight line to the data (which implies power law behaviour: $y \propto t^{k_c}$), its slope gave the power of the function describing the shift of the interface (it is called *kinetic exponent* and denoted by k_c). Obviously for parabolic interface shift $k_c = 0.5$. Since we wanted to demonstrate the effects of the composition dependence of diffusion coefficients as well as the phase separation tendency on the kinetics of the interface shift, the parameters m' and V (or V/kT) were changed during the calculations.

Figure 6a shows the initial values of the kinetic exponent, k_c, (obtained by fitting to the interval corresponding to the dissolution of the first five atomic planes) versus V/kT for different m' values. It can be seen that k_c is almost constant and, as it is expected, it is very close to 0.5 for small m' (week composition dependence of the diffusion coefficients). At the same time, the deviation from the square root kinetics increases with increasing m' for a fixed value of V/kT. The deviation from the parabolic law is again a real "nano-effect", because after dissolving a certain number of layers (long time or macroscopic limit), the interface shift returns to the parabolic behaviour independently of the input parameters (see Fig. 6b).

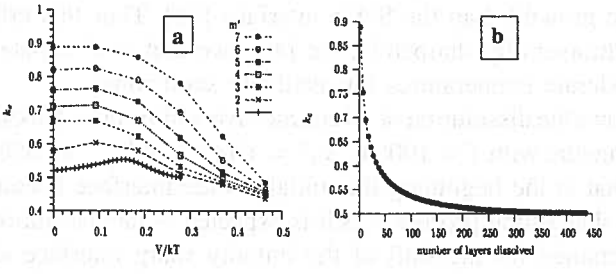

Fig. 6. Initial value of the kinetic exponent versus V/kT for different m' values [29], b): Change of k_c during dissolution ($m' = 7$, $V/kT = 0.09$). The more layers are dissolved the closer the value of k_c to 0.5 is

On the basis of our previous results on the linear shift of a sharp interface in ideal binary systems, obtained by Monte Carlo simulations, it is expected that the above conclusions (drawn from the deterministic model) on the non-linear interface shift in phase separating systems remain valid including the fluctuations as well.

Thus Fig. 6 reflects an interplay of two effects: i) the change of k_c due to the gradient energy effects scaled by V/kT, ii) the change of k_c due to the diffusion asymmetry measured

by m'. This latter nano-effect – similarly to the case of the shift of the interface in an ideal binary system – as it can be seen in Fig.6b, should diminish for long diffusion distances/times.

3.2.4. Sharpening of an initially diffuse interface in ideal binary systems

Another interesting feature obtained again by the same type of model calculations and also by Monte Carlo technique [27], is that an initially wide A/B interface can become sharp on nanoscale even in an ideal system. While such a process is obvious in an alloy with large miscibility gap (the metastable solid solution in the smeared interface region decomposes and a sharp interface is formed), it is surprising at first sight in systems with complete mutual solubility, because according to the macroscopic Fick I law the direction of the atomic flux is always opposite to the direction of the concentration gradient. Indeed, for composition independent D, the concentration profile will gradually decay and only a flattening of the (sharp or broadened) interface, produced experimentally, is generally expected.

The problem is interesting not only from fundamental point of view, but has technological importance as well. The Ni/Cu system for example is a model material for giant magnetoresistance (GMR), and in these systems the abruptness of the interface, and the knowledge of the possibilities for their improvement, is a key point. Furthermore, multilayers made of Mo and V (which is also an ideal binary system) are model materials for X-ray mirrors, or Si/Ge systems are basic semiconductor structures, where again the sharpness of the interfaces can be very important requirement for many applications. It is also well known that in Si-Ge multilayers grown by MBE the Ge/Si interface, produced by the deposition of Si on Ge, is always less sharp (due to the mixing driven by the segregation of Ge during the growth) than the Si/Ge interface [36]. Thus this effect offers a way to improve the multilayers by sharpening the interface and to eliminate the asymmetry by annealing at moderate temperatures for relatively short times.

Figure 7a shows the dissolution of 10 atomic layers of A into a bulk B(111) semi-infinite substrate (fcc structure with T = 1000 K, V_A^A = -074 eV and V_B^B = -058 eV i.e. for m' = 9). It can be seen that at the beginning the initially wide interface becomes more and more sharp. After the sharpening process – as it is expected – the dissolution takes place in the same way as obtained for the shift of the initially sharp interface above: the interface remains atomic sharp and shifts step-by-step. The process clearly reflects the asymmetry of the diffusion: there is practically no diffusion in pure A and the diffusion is a very fast in pure B, leading to a gradual sharpening of the composition profile.

As it was already mentioned an initially abrupt interface can remain sharp during diffusional intermixing in multilayers as well (see Fig. 1). Therefore, it is an interesting question whether an originally wide interface can also become sharper in multilayers. The situation differs from the dissolution of a thin film into semi-infinite substrate: the most important effect is that Ni atoms can saturate the Cu layer, and this leads to the change of the diffusivity there. However, as Fig. 7b shows, the first part of the process is the interface

sharpening in this case as well, after which the interface shifts step-by step and just after consuming of the whole Ni layer complete homogenization takes place.

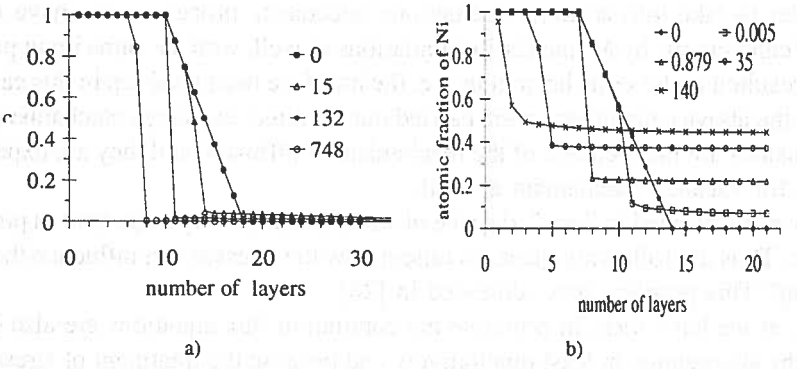

Fig. 7. a): Sharpening of the initially linear concentration profile of Ni during interdiffusion with Cu [27]. b): 16 Interface sharpening in an A/B multilayer system. (Time units shown must be multiplied by 10^6)

The above result gives also a plausible explanation for the apparent contradiction with the continuum Fick I law:

$$\mathbf{j} = -D\,grad\,\rho, \tag{14}$$

where ρ is the density ($\rho = c/\Omega$). Since in ideal binary systems D has a positive value and, for concentration independent diffusion coefficients, this equation should lead to flattening of the interface. If the concentration gradient is constant along the interface it is only D on which the absolute value of the atomic flux depends. Therefore the 'flux distribution' follows the $D = D(c)$ function and thus even the continuum flux equation is capable to describe some sharpening.

Obviously at longer annealing times – as it is expected from general thermodynamics – homogenization should take place. Indeed this is the case for the multilayer sample: although at the beginning the process decreases the gradient by filling up of layer Cu with Ni (and not by flattening of the interface), the final state is the completely intermixed homogeneous alloy. For the case of semi-infinite geometry the first part of the intermixing (the initial sharpening and linear shift of the interface) will be extended to times under which the deposited film consumes. Of course for thick films, before reaching this stage, the kinetics of the dissolution will gradually change from linear to parabolic (as we have seen before), and this transition time will be determined by the "strength" of the concentration dependence of the diffusion coefficient, m'. For m' = 0 the "normal" intermixing with the formation of a symmetrical diffusion profile will take place, while with increasing m' the diffusion profile will be more and more asymmetrical and finally the above discussed effects can be observed on nanoscale.

It is important to note that m' is inversely proportional to the temperature (see the text below eq. (13)), and thus with decreasing temperature it is easy to reach those values for

which the above non-linear effects can be observed. Indeed, as it can be checked from the known pair interaction energies or from the experimental D values, it is very general that at low temperatures m' is large enough that the sharpening of the interface is expected.

In order to take into account fluctuations (stochastic processes) we have performed computer calculations by Monte Carlo simulations as well, with the same input parameters, and they resulted in the same behaviour, i.e. the interface became sharp in this case as well. Although the above calculations were carried out for direct exchange mechanism of atoms, the conclusions are independent of the mechanism of diffusion and they are expected to be valid e.g. for vacancy mechanism as well.

As it was mentioned in Sec. 2, the role of stresses can be very important in processes on nanoscale. Thus the following question raises: how the stresses can influence the interface sharpening? This problem was addressed in [28].

Since, as we have seen, in principle the continuum flux equations are also capable to describe the sharpening, at least qualitatively and because the treatment of stress effects is not well developed for the discrete, atomistic kinetic approach [32], computer simulations were carried out in the framework of Stephenson's continuum model [37] for Mo-V multilayer system. Exponential composition dependent diffusion coefficients were used and it was assumed that $D_v = 2D_{Mo}$. The modulation length of the multilayer was 6 nm, the initial 'wideness' of the interface between the Mo and V layers was 1 nm. Fig. 8 shows the time evolution of the composition profile when all the stress effects are ignored, and beside the 'filling-up' of V by Mo, there is indeed interface sharpening, similarly as observed above in the discrete model. The time scale is normalized; t_r is the stress relaxation time (corresponding to a simple Newtonian flow; $t_r = 6\eta(1-\nu)/E$; η the viscosity, E the Young modulus and ν the Poisson ratio, respectively).

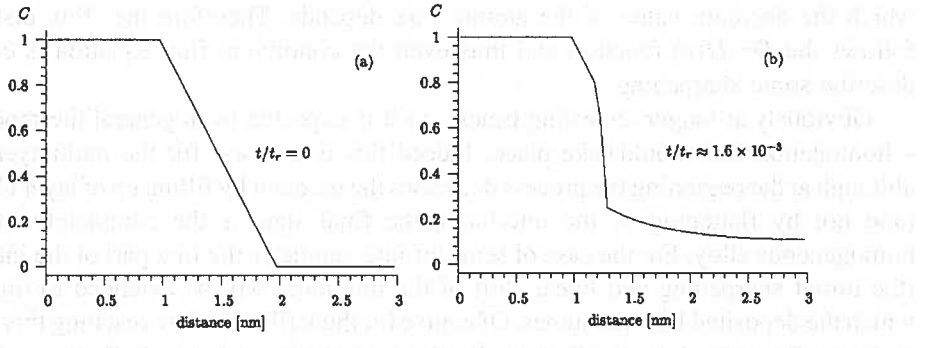

Fig. 8. Time evolution of the composition profile of Mo, at two different normalized times, when all the stress effects are ignored [28]

In Fig. 9 the sample initially is stress free and during mixing a stress peek develops on the Mo side close to the interface and on the V side an almost homogeneous stress field (with opposite sign) appears. This is because the Mo atoms near the interface can easily dissolve into the *V* and diffuse there, whereas the V atoms practically cannot penetrate into the Mo (diffusion asymmetry due to the strong composition dependence of D_i).

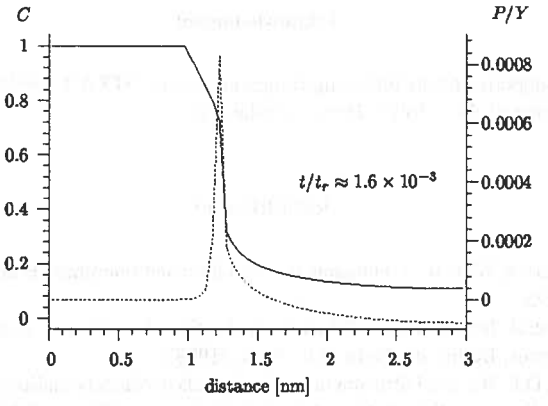

Fig. 9. Time evolution of the composition profile of Mo at $t/t_r = 1.6 \times 10^{-3}$ when only the diffusional stress ($D_V/D_{Mo} = 2$) is taken into account (The initial state is the same as in Fig. 8. The dotted line is the normalized pressure (P/Y)

In order to illustrate stronger stress effects, in Figure 10 the dashed line corresponds to five times larger volume flow (the diffusion induced stress is determined by the net volume flow caused by the differences of D_i). It can be seen that in the second case a slowing down effect is already visible, but the sharpening is still present (obviously with a slower rate). The slowing down effect is due to the presence of the pressure peak in the Mo side just at the sharp interface formed (see e.g. Fig. 9). The pressure peak shifts with the moving interface and there is a steady state during which the height of the pressure peak is almost constant (it decreases only because of the finite size of the V layer). The presence of the stress gradient, due to this peak, practically compensates the difference in the atomic fluxes, as it is expected from the LeChatelier-Braun principle: the diffusion induced stresses compensate the effect generating them. This results in a slowing down of the intermixing and to the slowing down of its first stage (sharpening).

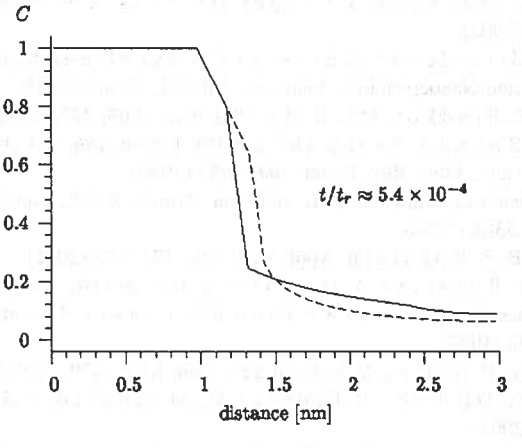

Fig. 10. Demonstration of the influence of the strength of the diffusional stress: $D_V/D_{Mo} = 2$ solid line, $D_V/D_{Mo} = 10$ dashed line

Acknowledgment

This work has been supported by the following Hungarian grants: OTKA T-038125, F-043372 and T-043464. C. Cserháti is a grantee of the "Bolyai János" scholarship.

REFERENCES

[1] I. Kaur, Y. Mishin, W. Gust, Fundamentals of Grain and Interphase Boundary Diffusion, London, J. Wiley & Sons, 1995.
[2] D.L. Beke, General Introduction, Diffusion in Semiconductors and Non-Metallic Solids Landolt-Bornstein, New Series, Berlin; ed. Beke D.L. 33-A, (1998).
[3] J. Bernardini, D.L. Beke, Diffusion in Nanomaterials in Nanocrystalline Metals and Oxides: Selected Properties and Applications; Eds. P. Knauth and J. Schoonman; Kluwer Publ. Boston (2001).
[4] S. Divinski, J.-S. Lee, Chr. Herzig, Nanodiffusion, special issue of Journal of Metastable and Nanocrystalline Materials; Ed. D.L. Beke, (2004).
[5] B. S. Bokstein, Nanodiffusion, special issue of Journal of Metastable and Nanocrystalline Materials; Ed. D.L. Beke, (2004).
[6] D.L. Beke, C. Cserhti, Z. Erdélyi, I.A. Szabó, Segregation in Nanostructures in Advances in Nanophase Materials and Nanotechnology Vol. Nanoclusters and Nanocrystals; Ed. H.S. Nalwa; American Scientific Publ. Califronia USA, (2003) p.211.
[7] J. Philibert, Atom Movements. Diffusion and Mass Transport in Solids, Les Ulms, France, Les Editions des Physique, Paris, (1991).
[8] I.V. Belova, G. E. Murch, Nanodiffusion, special issue of Journal of Metastable and Nanocrystalline Materials; Ed. D.L. Beke, (2004).
[9] D.L. Beke, G.A. Langer, A. Csik, Z. Erdélyi, M. Kis - Varga, I.A. Szabó, Z. Papp, Defect and Diffusion Forum, **194-199**, 1403 (2001).
[10] M. Bobeth, A. Ullrich, W. Pompe, Nanodiffusion, special issue of Journal of Metastable and Nanocrystalline Materials; Ed. D.L. Beke, (2004).
[11] D.L. Beke, Gödény, I., Erdélyi, G. Kedves, F.J. Phil. Mag. **A56**, 659 (1987).
[12] G. Erdélyi, W. Lokowski, D.L. Beke, Phil.Mag. **A56**, 672 (1987).
[13] S.V. Divinski, F. Hisker, Y.-S. Rang, J.-S. Lee, Chr. Herzig, Acta Mater. (2003) in press.
[14] J. C. M., Hwang, J. D. Pan, R. W. Balluffi, J. Appl. Phys., **50**, 1339 (1979).
[15] Z. Erdélyi, Ch. Girardeaux, G.A. Langer, D.L. Beke, A. Rolland, J. Bernardini, J. Appl. Phys. **89**, 3971 (2001).
[16] J. Bernardini C. Girardeaux, Z. Erdélyi, C. Lexcellent, Nanodiffusion, special issue of Journal of Metastable and Nanocrystalline Materials; Ed. D.L. Beke, (2004).
[17] B.S. Bokstein, V.E. Fradkov, D.L. Beke, Phil. Mag. **A65**, 277, (1992).
[18] C. Cserhati, D.L. Beke, I.A. Szabo, Def. and Dif. Forum, **156**, 121,(1998).
[19] P. Desre, A.P. Yavari, Phys. Rev. Letters, **64**, 1553 (1990).
[20] N. Stolwijk, Diffusion in Semiconductors and Non-Metallic Solids, Landolt-Bornstein, New Scries, Berlin; ed. Beke D.L. **33-A** (1998).
[21] A. S. Ostrovsky, B. S. Bokstein, Appl. Surf. Sci., **173**, 312 (2001).
[22] N. Balandina, B.S. Bokstein, A. Ostrovsky, Def. and Dif. Forum, **143-147**, 1499 (1997).
[23] D.L. Beke, P. Nemes, Z. Erdélyi, I.A. Szabó, D.G. Langer, Proc. of MRS Spring Meeting, San Francisco, **527**, 99-110, (1998).
[24] Z. Erdélyi, D.L. Beke, P. Nemes, G.A. Langer, Phil. Mag. **A79**, 1757 (1999).
[25] A. Csik, G. Langer, D.L. Beke, Z. Erdélyi, M., Menyhárd, A. Sulyok, Journal of Appl. Phys. **89**/1, 804-806 (2001).
[26] Z. Erdélyi, C. Girardeaux, Zs. Tökei, D.L. Beke, C. Cserháti, A., Rolland, Surf. Sci **496**, 129 (2002).

[27] Z. Erdélyi, D.L. Beke, I.A. Szabó, Phys, Rev. Letters **89**, 165901 (2002).
[28] Z. Erdélyi, D.L. Beke, Phys. Rev. **B.68**, 092102 (2003).
[29] Z. Erdélyi, G. Katona, D.L. Beke, submitted to Phys. Rev. B.
[30] D.L. Beke, Z. Erdélyi, I.A. Szabó, C. Cserháti, Nanodiffusion, special issue of Journal of Metastable and Nanocrystalline Materials; Ed. D.L. Beke, (2004).
[31] G. Martin, Diffusion in Materials (eds. A.L. Laskar J. C. Bocquet, G. Brebec, C. Monty) Nato ASI Series Series E Applied Sciences, ,Kluwer Academic Press, Dordrecht **179** 129 (1990).
[32] A.L. Greer, F. Speapen, *Synthetic Modulated Structures* (Eds. Chang, L.L. and Giessen, B.C.), Academic Press, New York, p. 419 (1985).
[33] A. Saúl, B. Legrand, G. Tréglia, Surf. Sci. **331-333**, 805 (1995).
[34] S. Delage, B. Legrand, F. Soisson, A. Saúl, Phys. Rev **B58**, 15810 (1998).
[35] J. M. Roussel, A. Saúl, G. Tréglia, B. Legrand, Phys. Rev. **B60**, 13890 (1999).
[36] D.E. Jesson, *Handbook of Thin Film Process Technology,* Eds. D.A. Glocker, S.I. Shah; IOP Publishing Ltd. Bristol and Philadelphia, (1997) p. F1:1.
[37] G.B. Stephenson, Acta Metall. **36**, 2663 (1988).

Received: 1 March 2004.

A R C H I V E S O F M E T A L L U R G Y A N D M A T E R I A L S
Volume 49 2004 Issue 2

CHR. HERZIG *, S.V. DIVINSKI*

DIFFUSIONAL PROPERTIES IN TECHNOLOGICALLY ADVANCED INTERMETALLICS

WŁAŚCIWOŚCI DYFUZYJNE ZWIĄZKÓW MIĘDZYMETALICZNYCH

We have extensively investigated bulk and grain boundary diffusion in technologically important Ni- and Ti-aluminides. These compounds exhibit different lattice structures and different types and concentrations of lattice defects on their sublattices (vacancies, anti-structure atoms of constitutional and/or thermal origin). This study therefore provides fundamental insight into the interdependence of diffusion behavior and diffusion mechanisms on structure and ordering. An overview is presented, including the direct tracer diffusion measurements of the transition metal component and the determination of the Al diffusivity through interdiffusion data and by using Al-substituting solutes, like Ga. The interpretation of the experiments is strongly supported by EAM-potential calculations of defect properties and Monte-Carlo simulations of possible diffusion mechanism. Among other features, the experimentally established curvature in the Arrhenius plot of Ti self-diffusion in TiAl, the surprising effect of the missing diffusion enhancement from structural Ni-vacancies in Al-rich NiAl, the paradoxically appearing deep minimum of the chemical diffusion coefficient in stoichiometric NiAl, and interphase diffusion along oriented Ti_3Al/TiAl interfaces are successfully explained.

Autorzy przeprowadzili systematyczne badania dyfuzji, zarówno objętościowej jak i na granicy ziaren w związkach międzymetalicznych Ni- i Ti-Al, ważnych z technologicznego punktu widzenia. Związki te różnią się zarówno strukturą sieci jak i rodzajem oraz koncentracją defektów w podsieciach. Praca dostarcza podstawowych informacji na temat zależności pomiędzy mechanizmami dyfuzji, a strukturą i uporządkowaniem. Między innymi przedstawiono wyniki badań dyfuzji metodą atomów znaczonych dla metali przejściowych oraz określenie dyfuzyjności Al, tak z badań dyfuzji wzajemnej, jak i przy użyciu zamienników Al, takich jak np. Ga. Przy interpretacji wyników zastosowano obliczenia potencjału EAM defektów oraz symulację Monte-Carlo dla różnych mechanizmów dyfuzji. Autorom udało się również wytłumaczyć między innymi takie wyniki jak otrzymany kształt krzywej wykresu Arrheniusa dla samodyfuzji Ti w stopie TiAl, dość zaskakujący brak przyspieszenia dyfuzji przez strukturalne wakancje Ni w bogatych w Al stopach NiAl, obserwowane minimum wartości współczynnika dyfuzji chemicznej w stechiometrycznym NiAl, i wreszcie dyfuzję międzyfazową wzdłuż zorientowanej granicy fazowej Ti_3Al/TiAl.

* INSTITUT FÜR MATERIALPHYSIK, UNIVERSITÄT MÜNSTER, WILHELM-KLEMM-STR. 10, D-48149 MÜNSTER, GERMANY

1. Introduction

The development of intermetallic compounds to application as structural materials inevitably requires the knowledge of relevant bulk- and grain boundary (GB) self- and solute diffusion data [1]. During the last decade defect- and diffusion phenomena in binary nickel- and titanium aluminides have attracted much attention and self-diffusion was thoroughly investigated in numerous research papers, see e.g. overviews [2, 3, 3, 5]. Combination of the ample experimental information and extended atomistic simulation allowed to elaborate detailed presentations on the diffusional behavior of the binary aluminium in question.

In this overview some essential results in diffusion behavior of ordered binary nickel- and titanium aluminides are highlighted. Since these aluminides form different structures, such as e.g. *B2* (NiAl), $L1_2$ (Ni_3Al), $D0_{19}$ (α_2-Ti_3Al), and $L1_0$ (γ-TiAl), the impact of order, thermal and structural defects, and composition will be discussed. We will confine ourselves to the most prominent (from author's point of view) features of diffusion behavior is these aluminides, such as the non-Arrhenius temperature dependence of Ti diffusion in γ-TiAl, the absence of Ni diffusion enhancement in Al-rich NiAl alloys with structural vacancies, and the regularities of Ti diffusion along interphase boundaries in two-phase TiAl alloys.

2. Lattice Structures and Diffusion Mechanisms in Ni- and Ti-Aluminides

A simple comparison of phase diagrams shows that the single-phase fields of the ordered Ni- and Ti-aluminides differ already qualitatively. Whereas the TiAl phase field extends predominantly on the Al-rich side of the stoichiometric composition [6], NiAl can accommodate a remarkable excess of both Al and Ni atoms [7]. The Ni_3Al phase field also exists on both sides of the stoichiometric composition, but in a limited temperature interval [8]. From a fundamental point of view, therefore, the NiAl phase is most interesting, because the compositional dependence of diffusion can be extensively studied as function of the type and the concentration of the constitutional defects. On the other hand, two-phase α_2-Ti_3Al/γ-TiAl alloys are most attractive as a basis of technological applications [9].

In Figure 1 the ideally ordered crystalline structures of Ni- and Ti-aluminides at zero temperature and at perfect stoichiometric compositions are schematic ally presented. As the temperature increases and/or the composition deviates from stoichiometry, point defects are inevitably generated and they have to be taken into account to describe diffusion behavior.

It is known that both the Ti aluminides [4] and Ni_3Al [10] belong to the anti-structure-defect type of intermetallic compounds, since anti-structure atoms are predominantly generated to accommodate the deviation from the stoichiometry. In contrast, NiAl reveals a triple-defect-type of point defect disorder and constitutional Ni vacancies exist in NiAl on the Al-rich side [11]. Moreover, the Ni vacancy concentration is fairly large also on the Ni-rich side, *e.g.* $C_{V_{Ni}} \sim 10^{-4}$ at $T = 0.75T_m$ [12] (T_m is the corresponding melting point). In

all aluminides under investigation, the vacancy concentration on the Al sublattice is generally much smaller, up to several orders of magnitude, than on the transition metal sublattice [4, 5].

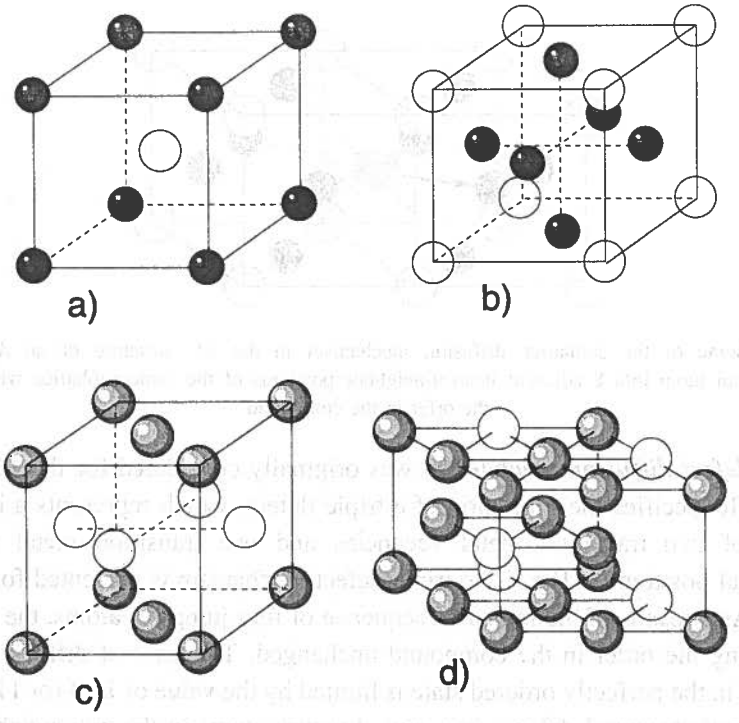

Fig. 1. Schemes of the lattice structures of the phases $B2$-NiAl (a), $L1_2$-Ni_3Al (b), $L1_0$-TiAl (c), and $D0_{19}$-Ti_3Al (d). Ni, Ti, and Al atoms are represented by black, grey, and white spheres, respectively

It is known that diffusion in pure metals is mostly mediated by the random motion of vacancies. Due to the ordered structure of intermetallic compounds and the different probabilities to find a vacancy on a particular sublattice more sophisticated jump sequences involving several atoms were suggested for ordered intermetallics: *e.g.* the 6-jump cycle [13], the triple defect mechanism [14], the anti-structure bridge (ASB) mechanism [15] and others. Below we briefly describe the diffusion mechanisms which were found to be most important in ordered aluminides.

Sublattice diffusion mechanism. When one of the components (usually the transition metal component in the systems under considerstion) forms a lattice structure which permits nearest-neighbor jumps through the respective sublattice, random jumps of the vacancy on this sublattice will not affect the order in the compound and will provide long-range diffusion. As an example, this mechanism is schematically presented in Fig. 2 for the $L1_2$ structure of Ni_3Al. It is important that this mechanism can dominate diffusion not only of the majority component, but also of the this mechanism can dominate diffusion not only of the majority component, but also of the minority component. In such a case, a minority atom jumps into the "wrong" sublattice and continues its migration through this sublattice. The

sublattice diffusion mechanism was extensively analyzed in [16, 17]. We emphasize that the sublattice diffusion mechanism does not couple the diffusivities of different components in binary intermetallics.

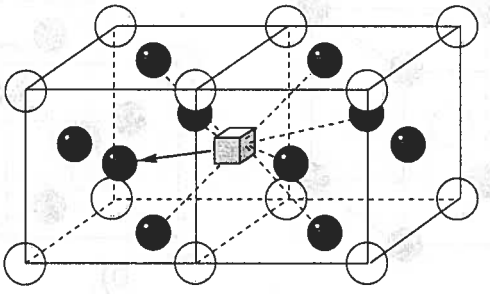

Fig. 2. A scheme of the sublattice diffusion mechanism in the $L1_2$ structure of an A_3B compound. The vacancy can jump into 8 adjacent nearest-neighbor positions of the same sublattice without changing the orfer in the compound

The triple defect diffusion mechanism was originally considered for the $B2$ compound CoGa [14]. It specifies the migration of a triple defect, which represents a bound entity composed of two transition metal vacancies and one transition metal atom in an anti-structural position. In Fig. 3 the triple defect mechanism is presented for the case of NiAl [18]. As a results of the indicated sequence of four jumps of atoms, the triple defect moves leaving the order in the compound unchanged. The ratio of diffusivities of both components in the perfectly ordered state is limited by the value of 13.3 (or 113.3) [14]. In the presence of structural defects (e.g. anti-structure atoms in the non-stoichiometric $B2$ structure) the value of this factor will be larger.

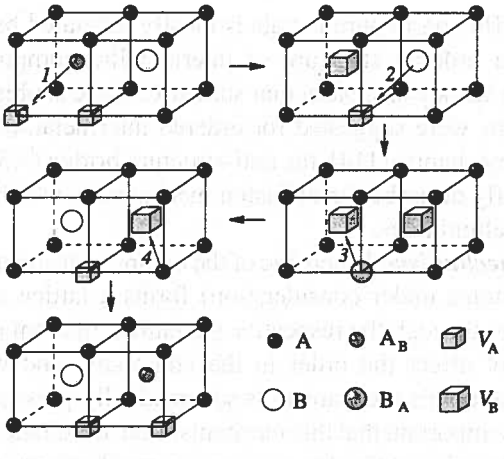

Fig. 3. A scheme of the triple defect diffusion mechanism in a $B2$ structure AB. The modification of this mechanism which is specific for NiAl [18] is shown. As a result both, the Al and the Ni atoms have equally migrated on the distance of one lattice parameter from the right to the left

The anti-structure bridge mechanism was first considered for the $B2$ structure [15] and only later extended to other structures (e.g. $L1_2$) [19]. The anti-structure bridge (ASB) mechanism is schematically presented in Fig. 4a. As a result of the two indicated jumps, the vacancy and the anti-structure atom exchange their positions. Since the vacancy can in fact jump up to the 4th or 5th coordination shell from its initial position (depending on the lattice structure [19]), the resulting large geometrical factor of the ASB mechanism increases its contribution to the diffusivity.

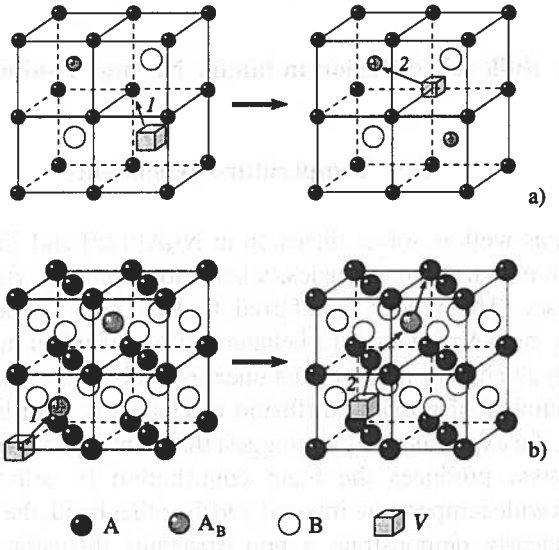

Fig. 4. A scheme of the anti-structure bridge (*ASB*) mechanism in a $B2$ structure (a) and a variant of the *ASB* mechanism in a $L1_0$ structure (b). As a results, the vacancy V and the anti-structure atom A_B exchange their initial positions. In the $B2$ structure the anti-structure atom A_B can be situated at any B-atom position from 26 unit cells which neighbor the unit cell with the vacancy. In (b) the vacancy moves along the 'bridges' formed by the anti-structure atoms A_B

It is important that the contribution of this mechanism has a percolation nature in the sense that long-range diffusion by the ASB mechanism will ocur only if the concentration of the anti-structure atoms is sufficiently large. Although a relatively high critical concentration for a $B2$ structure was initially estimated by purely geometrical arguments [15], the Monte-Carlo simulation yields the percolation threshold of ~ 5% [19].

In the $L1_0$ structure of the phase TiAl other types of the ASB mechanism are of prime importance [20, 4]. One of such variants is presented in Fig. 4b. After the indicated two jumps ($1+2$) the A vacancy has moved between A atom layers using an anti-structure A atom as a 'bridge'. This mechanism is important when considering the diffusional anisotropy in TiAl (see Chapter 3.3). If a further anti-structure atom in a suitable nearest-neighbor position is available for the vacancy after its second jump, the next ASB sequence may start, as it is indicated in Fig. 4b. In this case, the Monte-Carlo calculation of the percolation threshold for the long-range diffusion yields about 11 % of the anti-structure atoms as the critical concentration.

Since during the ASB sequence of jumps only one type of atoms moves, the diffusivities of the two components are not coupled.

In a strict sense, the genuine ASB mechanism operates only after the percolation threshold is reached. However, in combination with another mechanism (usually the sublattice diffusion mechanism) the ASB mechanism (*e.g.* jump sequence $1 \rightarrow 2$ in Fig. 4b) can substantially contribute to long-range diffusion without any percolation threshold [20, 4, 21].

3. Bulk self-diffusion in binary Ni- and Ti-aluminides

3.1. Temperature dependence

Self-diffusion as well as solute diffusion in Ni_3Al [22] and Ti_3Al [23] follow almost ideal linear Arrhenius dependencies, a behavior which is typical for the majority of intermetallic phase. (The reader is referred to Ref. [22] for a critical discussion of Arrhenius vs. non-Arrhenius behavior of Ni diffusion in Ni_3Al). From a simple point of view such a behevior is somewhat unexpected heving in mind the variety of point defects and the number of possible diffusion mechanisms in ordered intermetallics (see above). However, the experimental data suggest that in many intermetallic phases only one diffusion mechanism produces the main contribution to self-diffusion and operates dominantly over a wide temperature interval. On the other hand, the equiatomic compounds NiAl and TiAl clearly demonstrate a non-Arrhenius diffusion behavior, however in different temperature regions and most likely for different reasons.

3.1.1. Arrhenius vs. non-Arrhenius temperature dependence of self- and solute diffusion in γ-*TiAl*

One of the phases where a remarkable non-Arrhenius temperature dependence of self-diffusion was measured is γ-TiAl [20], see Fig. 5a. The diffusivity follows a linear Arrhenius line up to about $T = 1470$ K with a subsequent upward deviation to larger D^*_{Ti} values at higher temperatures. This pronounced curvature of Ti self-diffusion is explained by two operating diffusion mechanisms in TiAl. At lower temperatures, the Ti-sublattice mechanism dominates Ti self-diffusion in TiAl [20]. As the temperature increases, the ASB mechanism (Fig. 4b) profits from the increasing high concentration of Ti anti-structure atoms and enhances Ti self-diffusion. It is an important feature of the not perfectly ordered $L1_0$ lattice of TiAl that both diffusion mechanisms act in parallel and thus there is no percolation threshold for the relevant ASB mechanism in this lattice structure.

Opposite to Ti self-diffusion, Al diffusion reveals an almost linear Arrhenius temperature dependence as it was established by analysis of the interdiffusion experiments

[20, 24]. The magnitude of the Al diffusivity is similar to that of Ti at medium and higher temperatures (Fig. 5b), whereas Ti diffuses faster than Al at lower temperatures ($T < 1250$ K). This behavior allows us to conclude about the specific diffusion mechanism of Al. Since the vacancy concentration in the Ti sublattice is much larger than in the Al sublattice, Al atoms jump to the Ti sublattice, diffuse over the Ti sublattice, and then jump back to the Al sublattice, with the intersublattice jumps determining the diffusion rate of Al atoms. The difference between the activation enthalpies Q_{Al} and Q_{Ti} in the low-temperature interval, where the Ti-sublattice diffusion mechanism dominates the Ti atom diffusivity, therefore is mainly attributed to the formation enthalpy of anti-structure Al atoms on the Ti sublattice.

Some systematic diffusion behavior was established for solute diffusion in TiAl [21]. The solutes which predominantly substitute Al (e.g. Ga) demonstrate almost perfect linear Arrhenius dependence [25] (Fig. 5b). This fact results from the diffusion process of Ga atoms which consists in jumps from the Al to the Ti sublattice, migration through the Ti sublattice, and reverse jumps on the Al sublattice, a behavior which is similar to that of the Al component [25]. Again, the difference between Q_{Ga} and Q_{Ti} in the low-temperature interval ($T < 1400$ K) is related to the formation enthalpy of Ga atoms as anti-structure atoms on the Ti sublattice.

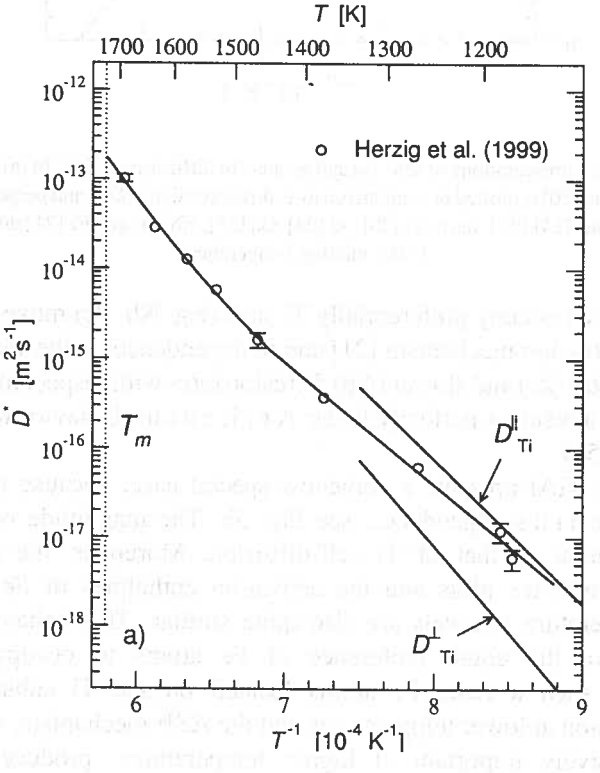

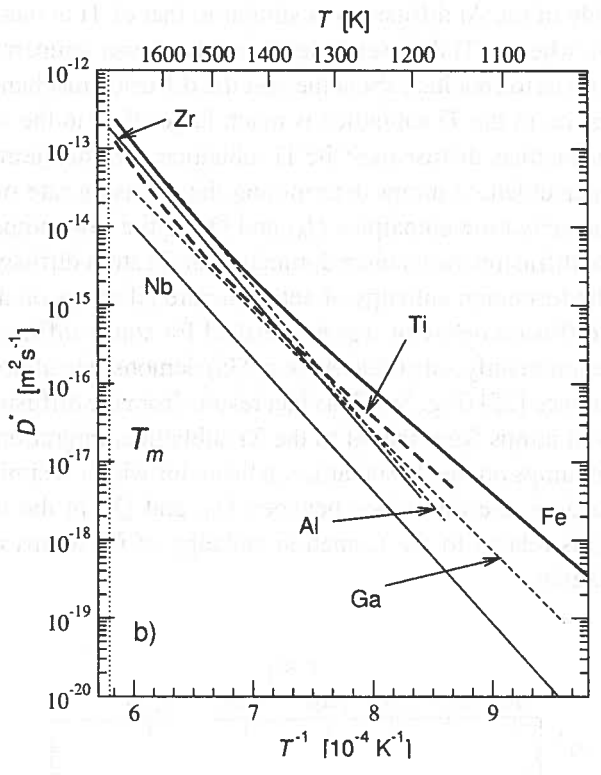

Fig. 5. The Arrhenius presentations of self- (a) and solute- (b) diffusion in TiAl. In (a) Ti self-diffusion in the polycrystalline TiAl alloy [20] is plotted in comparison to Ti diffusion along (D^{II}_{Ti}) and perpendicular (D^{II}_{Ti}) to the Ti layers in single crystalline TiAl [41]. In (b) Ti [20], Al [24], Ga [25], Nb, Zr, and Fe [21] diffusion is presented. T_m is the melting temperature

The solutes which occupy preferentially Ti sites (e.g. Nb, Zr) move predominantly by the Ti sublattice diffusion mechanism [21] and in dependence on the vacancy-solute atom interaction both faster (Zr) and slower (Nb) diffusion rates with respect to Ti self-diffusivity were observed. As a result, a perfectly linear Arrhenius behavior was determined for such solutes (Fig. 5b).

Fe diffusion in TiAl presents a somehow special case, because it reveals a strong non-linear Arrhenius dependence, see Fig. 5b. The magnitude of the Fe diffusion coefficients is similar to that of Ti self-diffusion. Moreover, the curvatures of the Ti and Fe Arrhenius plots and the activation enthalpies of Fe and Ti diffusion in the lower-temperature intervals are also quite similar. This behavior was explained [21] in relation to the equal preference of Fe atoms to occupy Ti or Al sites in TiAl [26]. In such a case, Fe atoms located on the Ti sublattice most likely dominate Fe diffusion at lower temperatures and the ASB mechanism, which additionally becomes progressively important at higher temperatures, produces a curvature of the Arrhenius dependence [21].

3.1.2. The ordered *B*2 NiAl phase

A non-A r r h e n i u s temperature dependence was also observed for Ni diffusion in *B*2 NiAl. The upward deviation of D^*_{Ni} from the otherwise linear A r r h e n i u s dependence begins systematically at $T > 1500$ K and does not appreciably depend on the particular composition of the NiAl alloys (Fig. 6) [18]. This behavior qualitatively correlates with recent results of differential dilatometry measurements performed in the group of Th. Hehenkamp in the NiAl phase [27], where a non-linearity in the A r r h e n i u s plot of the vacancy concentration was established in the similar temperature interval. The results of additionally performed positron annihilation experiments in these alloys indicate that bound triple defects (entities consisting of two Ni vacancies and one Ni anti-structure atom in nearest-neighbor positions) are the dominant thermal defects at $T \leq 1400$ K, whereas formation of divacancies should be taken into account at higher temperatures [27]. The exact physical reason of the observed non-A r r h e n i u s temperature dependencies in self-diffusion and vacancy formation behavior in NiAl is still to be elucidated.

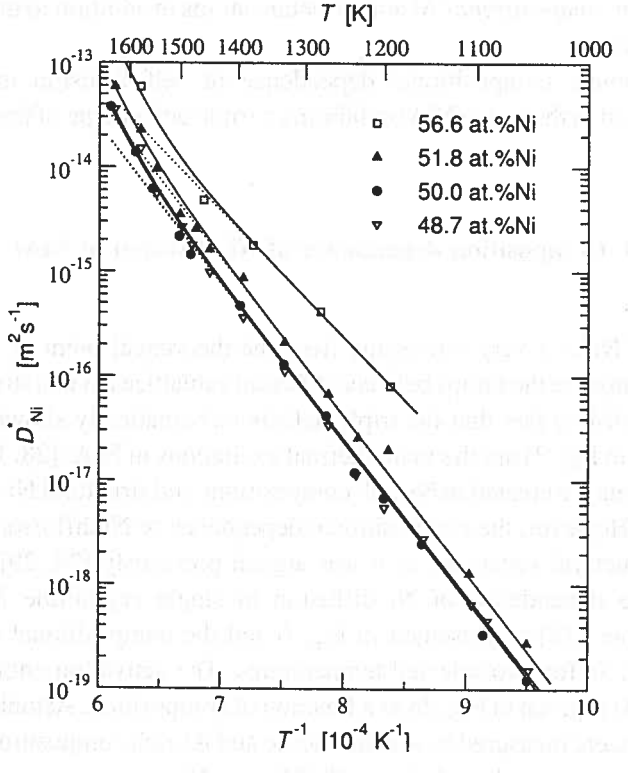

Fig. 6. The Arrhenius diagram of Ni diffusion in different NiAl alloys (the composition is indicated in at.%Ni). The dotted lines present the high – temperature extrapolation of the A r r h e n i u s fits obtained in the low-temperature interval, $T < 1500$ K

3.2. Composition dependence

The systematic investigations demonstrate that the anti-structure atom compounds, *i.e.* compounds with the anti-structure-defect type of disorder (Ni_3Al [22], Ti_3Al [23], and TiAl [20]), reveal only a weak compositional dependence of self-diffusivity. This behavior originates from a number of reasons: (*i*) the transition-metal sublattice forms a connected network for intrasublattice nearest-neighbor jumps of atoms which preserve the given state of the order in the compound, Fig. 1b–d; (*ii*) the vacancy concentration on the transition-metal sublattice is by several orders of magnitude larger than that on the Al sublattice, and (*iii*) the sublattice diffusion mechanism is the dominant contribution to atomic motion in these compounds. Note that in TiAl the latter argument is relevant only at temperatures below about 1470 K, where a linear A r r h e n i u s dependence is observed, Fig. 5a.

Al diffusion in Ni_3Al and Ti_3Al, calculated from the interdiffusion data, reveals a slight, but clear increase of D_{Al} with increasing Al content on the Al-rich side of the compositions. This feature is related to the transition metal sublattice diffusion mechanism for Al atoms and the appearance of *compositional* Al anti-structure atoms in addition to the thermal ones in these compositions.

The most prominent compositional dependence of self-diffusion in Ni- and Ti-aluminides is observed in the phase NiAl exhibiting a triple defect type of thermal disorder.

3.2.1 Composition dependence of Ni diffusion in NiAl

The *B*2 structure of NiAl is very interesting from the theoretical point of view, since all nearest-neighbor jumps are the jumps between different sublattices in this structure, see Fig. 1a. It is a well-established fact that the triple defects (schematically shown as initial and final configurations in Fig. 3) are the main thermal excitations in NiAl [28, 11]. In addition Ni anti-structure atoms are created in Ni-rich compositions and structural Ni vacancies exist on the Al-rich side. However, the compositional dependence of Ni diffusion in NiAl is not produced by the structural vacancies as it was argued previously [28, 29].

The temperature dependence of Ni diffusion in single crystalline NiAl alloys of different compositions [18] is presented in Fig. 6 and the compositional dependence of D^*_{Ni} is shown in Fig. 7a for two selected temperatures. The activation enthalpy Q_{Ni} of Ni self-diffusion in NiAl is given in Fig. 7b as a function of composition. Astonishingly, nearly the same D^*_{Ni} values were measured in stoichiometric and Al-rich compositions [18] and Q_{Ni} results in the nearly constant value of about 290 kJ/mol at Ni concentrations smaller than 53 at . % . Q_{Ni} substantially decreases in alloys with larger Ni concentrations adopting the value of 230 kJ/mol in $Ni_{56.6}Al_{43.4}$.

Possible diffusion mechanisms in NiAl were analyzed [30, 18] in dependence on the composition. The calculated and experimental results suggest that the triple defect mechanism (Fig. 3), for which a constant activation enthalpy of about 300 kJ/mol independent of the composition was calculated, most likely dominates Ni diffusion in NiAl [18]. Although the formation energy of solely Ni vacancies or Ni anti-structure atoms strongly depends on composition [11, 31], the triple defect (the entity consisting of two Ni vacancies and a Ni anti-structure atom) has a composition independent formatiom energy in *B*2 NiAl [18]. Therefore, if Ni diffusion proceeds through migration of triple defects, its activation enthalpy should not depend on composition in NiAl. This conclusion agrees with the interpretation of recent differential dilatometry measurements [27].

The observed increase of D^*_{Ni} and the decrease of Q_{Ni} at compositions with larger Ni content correspond to the activation of the ASB mechanism after reaching the percolation threshold at about 55.5 at. % Ni [18]. These results do not exclude an expected [31] additional and strong contribution of next-nearest-neighbor (*nnn*) jumps of Ni atoms at lower temperatures in Al–rich compositions. The calculated relatively small activation enthalpy (about 200 kJ/mol) would favor such a diffusion process [31], but the rather small involved migration entropy prohibits a stronger contribution of *nnn* jumps already at moderate temperatures [18].

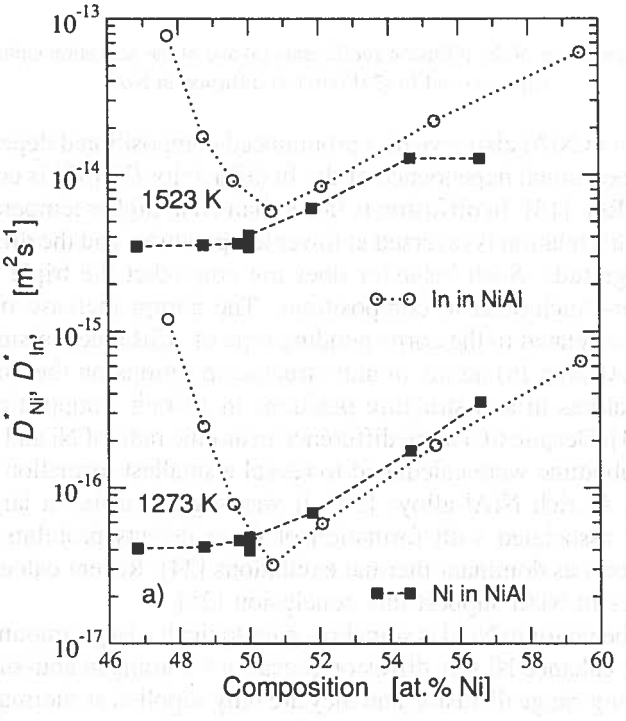

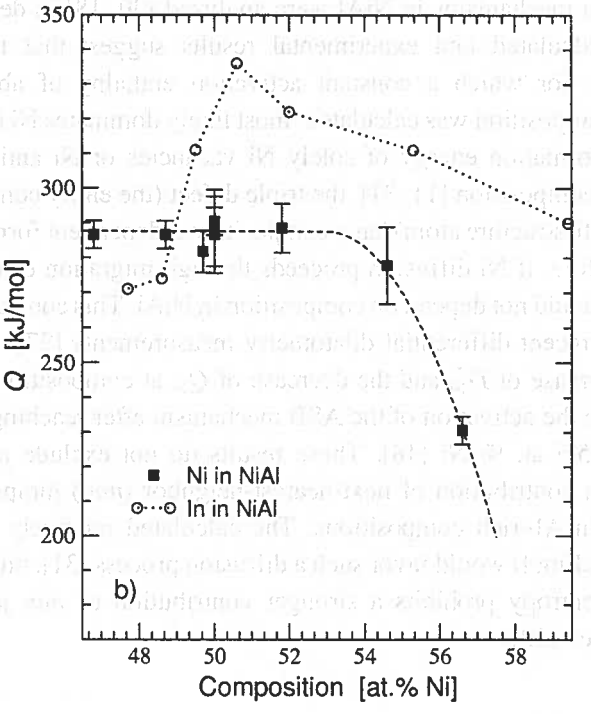

Fig. 7. Composition dependence of the diffusion coefficients (a) and of the activation enthalpies (b) of Ni [18] (squares) and In [32] (circles) diffusion in NiAl

Solute diffusion in NiAl also reveals a pronounced compositional dependence [32, 33]. In Fig. 7a the compositional dependence of the In diffusivity D^*_{In} [32] is compared with Ni tracer diffusion of Ref. [18]. In diffusion is faster than Ni at higher temperatures in Ni-rich compositions and this telation is reversed at lower temperatures and the difference amounts to an order of magnitude. Such behavior does not contradict the triple defect diffusion mechanism in near-stoichiometric compositions. The abrupt increase of D^*_{In} in Al-rich compositions can be related to the corresponding type of ASB mechanism which involves Ni vacancies and Al (and In) atoms in anti-structure positions on the Ni sublattice. The appearance of Al atoms in anti-structure positions in Al-rich compositions of NiAl was indicated in [11, 34]. Despite of a large difference in atomic radii of Ni and Al atoms, the Al atoms on the Ni sublattice were calculated to reveal a smallest formation energy between thermal defects in Al-rich NiAl alloys [34]. It was suggested that a large and negative formation entropy associated with formation of these defects prohibits their formation favoring triple defects as dominant thermal excitations [34]. Recent calculations of defect formation entropies in NiAl support this conclusion [35].

This diffusion behavior in NiAl is somehow paradoxical: a large amount of structural Ni vacancies does not enhance Ni self-diffusion (because Ni atoms in anti-structure positions are necessary for long-range diffusion and they are only supplied as thermally created triple defects), whereas they facilitate diffusion of the Al component. Analyzing In tracer

diffusion data and interdiffusion experiments in NiAl (see below) one can predict a moderate increase of Al diffusivity on the Ni-rich side and a pronounced increase of D^*_{Al} in Al-rich NiAl alloys, with a minimum of D^*_{Al} being reached in the stoichiometric NiAl alloy. Triple defect mechanism most likely governs both Ni and Al diffusion in near-stoichiometric NiAl resulting in similar magnitudes of D^*_{Ni} and D^*_{Al}, while in Al-rich compositions the ASB mechanism produce additional contribution to Al diffusivity and Ni and Al atoms diffuse more independently one from another.

3.2.2. Ternary *B*2 NiFeAl alloy

Recently we initiated a systematic study of Ni and Fe diffusion in ternary NiFeAl alloys within the *B*2 phase region [36, 37]. The activation enthalpy Q_{Ni} of Ni diffusion is presented in Fig. 8 as a function of Fe amount in $Ni_{50-x}Fe_xAl_{50}$ alloys. For completeness, Q_{Ni} in binary NiAl [18] and FeAl [38] alloys are also indicated (the sym bols in parenthesis). A non-monotonous change in Q_{Ni} is observed with a minimum at the Fe concentration of about 5 to 10 at.%. These results appear somehow controversial to the data on the Fe creep resistance in NiFeAl ternary alloys. Particularly, the $Ni_{40}Fe_{10}Al_{50}$ alloy was found to reveal the highest creep resistance [1]. Moreover, interdiffusion measurements also yield a minimum in the ternary interdiffusion coefficients $\tilde{D}^{Fe}_{NiNi}$ and $\tilde{D}^{Fe}_{AlAl}$ at about 10 at.% Fe addition to NiAl [39]. Careful measurements of thermodynamic activities of all components should be carried out to resolve this contradiction.

Recently site occupation and point defect concentrations were determined in the *B*2 NiFeAl phase and the triple defect structure was observed over the entire phase field [40]. In the $Ni_{50-x}Fe_xAl_{50}$ alloys, Fe atoms were found to occupy both Ni as well as Al sites creating additional Ni structural vacancies, with the Fe anti-structure atoms, Fe_{Al}, being the main defects in the ternary compositions near the binary terminal composition NiAl [40]. Furthermore, the concentration of the Ni anti-structure atoms, Ni_{Al}, is decreased with respect to binary NiAl on the expense of these Fe_{Al} anti-sites [40]. Thus, two types of triple defects can generally be introduced in the ternary NiFeAl alloys – with a Ni (Ni-TD) or with a Fe (Fe-TD) atom in an anti-structure position as neighbors of two Ni vacancies. It is important that the triple defect during the migration through the NiFeAl crystal occasionally changes its configuration from Ni-TD to Fe-TD and vice versa. Since the Fe anti-sites were concluded to be more stable than Ni anti-sites [40], an increase in the amount x of Fe in the $Ni_{50-x}Fe_xAl_{50}$ alloys near the binary terminal alloy NiAl will increase the probability that Fe-TD are created. Then, the observed decrease of the effective activation enthalpy of Ni diffusion with small Fe additions to stoichiometric NiAl, Fig. 8, suggests an easier formation and/or easier migration of a Fe-TD with respect to Ni-TDs. The measured similar values of the activation enthalpies of Ni and Fe diffusion in the ternary $Ni_{40}Fe_{10}Al_{50}$ alloy (270 and 279 kJ/mol, respectively [36]) also favor the triple defects as dominant diffusion vehicles in this material.

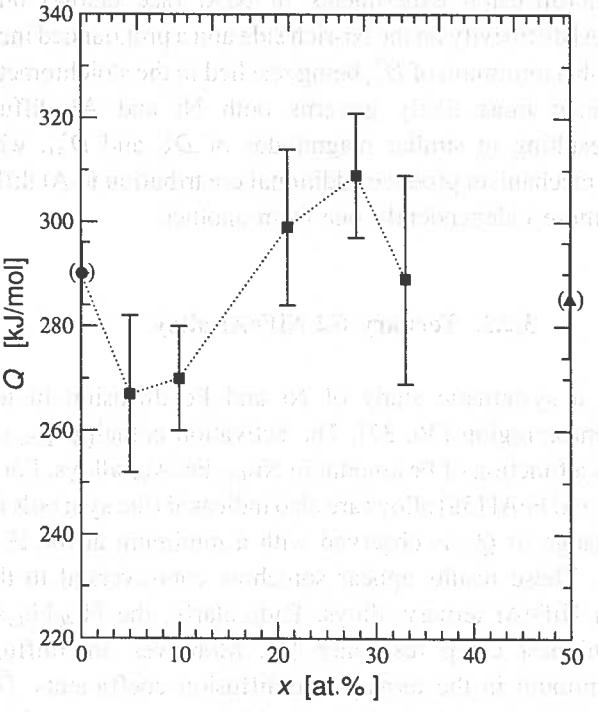

Fig. 8. Activation enthalpy Q_{Ni} of Ni diffusion in ternary $Ni_{50-x}Fe_xAl_{50}$ alloys as a function of Fe concentration x (in at.%). Q_{Ni} for binary $Ni_{50}Al_{50}$ [18] (circle) and $Fe_{50}Al_{50}$ [38] (triangle) are also presented (the symbols in parenthesis)

3.3. Anisotropy of diffusion

Diffusion in cubic $B2$ and $L1_2$ lattices is isotropic. On the other hand, TiAl crystallizes in the slightly tetragonally distorted $L1_0$ structure and diffusion in this layered structure is anisotropic [41] (Fig. 5a). Ti diffusion along Ti layers in the $L1_0$ structure (Fig. 1c) is faster than perpendicular to this direction. The geometrical consideration of the $L1_0$ structure suggests that the Ti-sublattice diffusion mechanism should result in a strong anisotropic contribution, whereas the ASB mechanism, which occurs by intersublattice jumps of the Ti atoms, corresponds to an almost isotropic mass-transport. As the temperaturw increases, the contribution of the ASB mechanism increases and the anisotropy of Ti diffusion should decrease, as it was observed in Ref. [41]. This increase in the diffusional contributions of the ASB mechanism with increasing temperature was already manifested in the non-linear Arrhenius dependence of Ti self-diffusion in polycrystalline TiAl [20].

3.4. Validity of the darken-manning equation in aluminides

In the case of random alloys, the interdiffusion- and tracer diffusion data ($\tilde{D}$ and D^*) are related by the well-known Darken-Manning equation [42, 43]. Applying this relation to aluminides we have (neglecting by volume effects):

$$\tilde{D} = (N_{Al} D^*_{TM} + N_{TM} D^*_{Al}) \cdot \Phi \cdot S. \quad (1)$$

Here N_{TM} and N_{Al} are the mole fractions of the transition metal element and Al in the compound, respectively; Φ is the thermodynamic factor; and S is the vacancy wind factor. For the random alloy model Manning has shown that

$$1 \leq S \leq \frac{1}{f_0}, \quad (2)$$

where f_0 is the geometrical correlation factor for the given lattice [43] and thus S is of the order of unity.

Equation (1) was experimentally verified for several ordered compounds where it was possible to measure tracer diffusivities of both components [44, 45]. Since there exist no reliable and directly measured data on Al tracer diffusion in aluminides, Eq. (1) cannot be verified in such systems at present. However, one can use Eq. (1) to extract D^*_{Al} implying that the Darken-Manning relation is valid in that case, too. Application of Eq. (1) to the Ni_3Al, Ti_3Al, and TiAl phases results in convincing data for the Al tracer diffusivity, which generally turns out to be similar to the diffusivities of Al-substituting solutes (e.g. Ga), as it is expected [5].

Although the condition $S \simeq 1$ is usually applied, the correlated diffusion mechanisms, which are considered in well-ordered intermetallic compounds, result in values of S which do not necessarily fall into the limits imposed by Eq. (2). For example, S can be as low as 0.42 for the $B2$ compounds when only the six-jump cycle mechanism operates [46]. Likewise the upper value of S is not bound to f_0^{-1} in the $L1_2$ structures [47]. Therefore, each factor in Eq. (1) has to be thoroughly analyzed when applying this equation to a given intermetallic compound.

NiAl. Interdiffusion in NiAl was investigated in several papers [48, 49]. A substantial compositional dependence of the interdiffusion coefficient $\tilde{D}$ was determined [49] characterized by a deep minimum around the stoichiometric composition. Using the thermodynamic data [50] for calculating Φ the contribution of Ni tracer diffusion to the interdiffusion coefficient can be estimated as $\tilde{D}_{calc} \cong N_{Al} \cdot D^*_{Ni} \cdot \Phi \cdot S$. By neglecting for the moment a non-zero Al tracer diffusion contribution $\tilde{D}_{calc}$ is certainly *underestimated.*

Assuming now $S = 1$, $\tilde{D}_{calc}$ is compared in Fig. 9a with the experimental data from Ref. [49]. The purpose of this comparison is to elucidate the paradoxical difference between the measured interdiffusion coefficient $\tilde{D}_{exp}$ and $\tilde{D}_{calc}$, especially around stoichiometric NiAl. $\tilde{D}_{exp}$ is by about two orders of magnitude smaller than $\tilde{D}_{calc}$ in $Ni_{50}Al_{50}$ (Fig. 9a).

Supposing that $S \neq 1$ one can estimate a hypothetical value of S, which would satisfy the Darken-Manning relation as $S = \tilde{D}_{exp}/\tilde{D}_{calc}$. In Fig. 9b this value is compared with the results of recent Monte-Carlo calculations of the vacancy wind factor according to the

triple defect diffusion model [51]. The qualitative agreement supports the conclusion that the triple defect mechanism is the dominant mechanism of diffusion in NiAl, especially around the stoichiometric composition and is responsible for the difference between $\tilde{D}_{exp}$ and $\tilde{D}_{calc}$. In the perfectly ordered $B2$ structure of NiAl the triple defect mechanism would result in $S = 0$ at stoichiometry, because the triple defect mechanism results in *exactly* the same macroscopic displacements of Ni and Al atoms in the $Ni_{50}Al_{50}$ compound. For example, in Fig. 3 the *total* displacements of both Al and Ni atoms are just one lattice parameter from the right to the left. The equality of Al and Ni atom fluxes can be established for any possible jump sequences corresponding to the triple defect mechanism. Since these fluxes are equal, motion of the triple defects does not contribute to interdiffusion in $Ni_{50}Al_{50}$.

Here it is the existence of thermal defects that gives rise to $S \neq 0$ in the stoichiometric $Ni_{50}Al_{50}$ alloy [51], since an encounter of a triple defect and e.g. a Ni anti-structure atom would disturb the above mentioned equality of the Al and Ni diffusion fluxes and would contribute to intermixing of Al and Ni atoms (i.e. to interdiffusion). Correspondingly, S is temperature dependent in $Ni_{50}Al_{50}$ and contributes additionally to the activation enthalpy of the interdiffusion process by about 70 kJ/mol [51]. Indeed, the activation enthalpy of interdiffusion in $Ni_{50}Al_{50}$, $Q(\tilde{D}) \cong 365$ kJ/mol [49], is larger than the activation enthalpy of Ni tracer diffusion in $Ni_{50}Al_{50}$, $Q(D^*_{Ni}) \cong 290$ kJ/mol [18], by about 75 kJ/mol. In the non-stoichiometric alloys the triple defect mechanism gives rise to "normal" values of the vacancy wind factor $S \approx 1$ due to the existence of a large amount of structural defects, e.g. Ni anti-structure atoms in Ni-rich compounds.

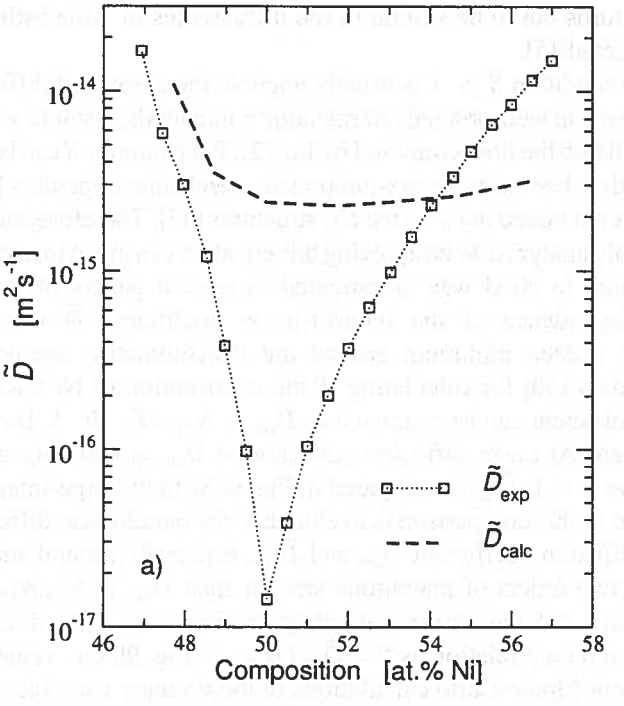

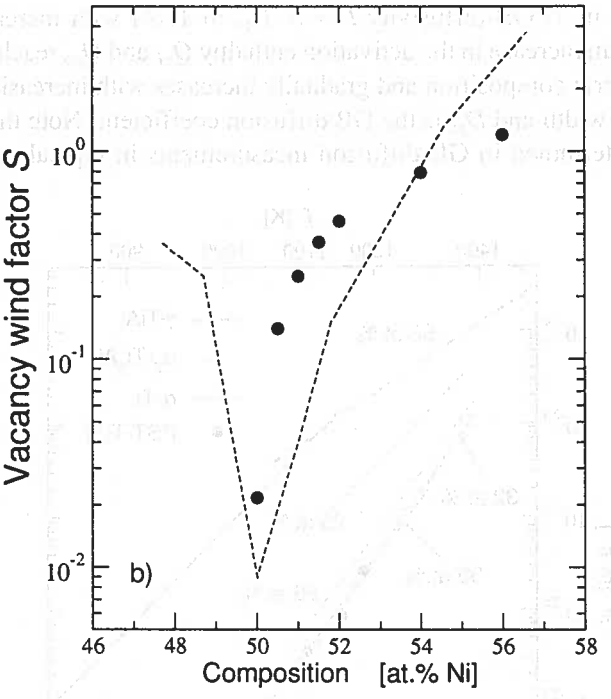

Fig. 9. Comparison of experimentally measured $\tilde{D}_{exp}$ [49] and estimated (see text) $\tilde{D}_{calc}$ interdiffusion coefficients in NiAl (a). In (b) the vacancy wind factor S estimated as $S = \tilde{D}_{exp}/\tilde{D}_{calc}$ (dashed line) is compared with the values of S calculated by Monte-Carlo simulation for the triple defect diffusion mechanism [51] (full circles)

4. Grain and interphase boundary diffusion in two-phase lamellar TiAl

Nowadays, two-phase TiAl alloys consisting of alternating layers of α_2-Ti_3Al and twined γ-TiAl phases present a promising material for high-temperature structural applications, since especially their lamellar structure offers good toughness and high-temperature strength [9]. In single crystalline form (i.e. in the absence of high-angle grain boundaries) these materials are often called polysynthetically twined (PST) crystals. Knowledge of self-diffusion in the existing α_2/γ interphase boundaries is important to receive direct information on the diffusivity of the titanium atoms for estimating *e.g.* the creep behavior. Specially designed experiments on such two-phase materials are attractive since both bulk [20, 23] and grain boundary (GB) diffusion [52] in the constituting phases were already studied in detail.

In Fig. 10, Ti GB self-diffusion in pure α-Ti is plotted in comparison with Ti GB self-diffusion in α_2-Ti_3Al and γ-TiAl [52]. While Ti bulk self-diffusion in Ti_3Al was found to be almost independent of the alloy composition [23], Ti GB diffusion in Ti_3Al changes significantly with the composition. An increase in the Al content from 25 to 35 at. % reduces Ti GB self-diffusion up to an order of magnitude. For comparison, Ti GB self-diffusion in γ-TiAl is practically independent of the composition [52].

The decrease in Ti GB diffusivity $P = \delta \cdot D_{gb}$ in Ti_3Al with increasing Al content is accompanied by an increase in the activation enthalpy Q_{gb} and Q_{gb} reaches the lowest value at the stoichiometric composition and gradually increases with increasing Al content [52]. Here δ is the GB width and D_{gb} is the GB diffusion coefficient. Note that only the product $\delta \cdot D_{gb}$ can be determined in GB diffusion measurements in typical conditions.

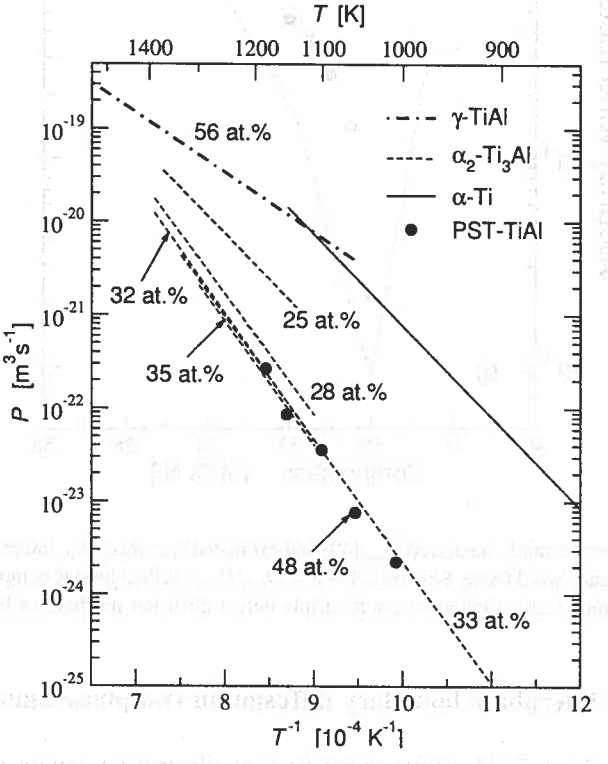

Fig. 10. Coparison of Ti GB diffusion in pure α-Ti (solid line), α-Ti_3Al (dashed lines), γ-TiAl (dotted-dashed line) [52], and α_2/γ TiAl interphase boundaries (circles) [53, 54]. The Al content of the corresponding alloys is indicated in at.%

In the investigated PST TiAl crystal (48 at.% Al) two different types of boundaries existed, namely γ/γ and α_2/γ interfaces [54]. However, the γ/γ interfaces are only twin and/or pseudo-twin boundaries and such boundaries do not significantly contribute to the total interfacial diffusion flux [54, 55]. There is a strict crystallographic relationship between the α_2 and γ lamellae in the applied PST crystal: $\{111\}_\gamma \parallel (0001)_{\alpha_2}$ and $\langle 1\bar{1}0]_\gamma \parallel \langle 11\bar{2}0\rangle_{\alpha_2}$, and the diffusion direction was parallel to the α_2/γ interfaces and corresponded to the $[11\bar{2}]$ direction in the (111) plane of the γ-TiAl phase [54]. In Fig. 10, the results on interphase boundary diffusion of Ti in two-phase PST TiAl are presented. Diffusion in α_2/γ interphase boundaries is fairly slow and is close to the GB diffusion data in the Al-richest α_2-Ti_3Al phase. These low values of the diffusivity in the interphase boundaries reflect their specific compact structure and were explained within the vacancy-mediated mechanism of

GB diffusion [53]. While on the α_2 side of an α_2/γ interface a Ti atom can migrate along the diffusion direction within its own Ti sublattice, it would continuously jump between the Ti and Al sublattices in order to migrate on the γ side of the interface that would involve larger activation barriers with respect to diffusion within solely the Ti sublattice [54].

The activation enthalpy of Ti GB diffusion in Al-rich α_2-Ti_3Al, $Q_{gb}^{(\alpha_2)}$, turned out to be fairly large and is similar to the activation enthalpy $Q_{bulk}^{(\alpha_2)}$ of Ti bulk diffusion in Ti_3Al, $Q_{gb}^{(\alpha_2)} \approx 0.9 \cdot Q_{bulk}^{(\alpha_2)}$ [52]. Similarly, the activation enthalpy Q_{IPB} of Ti interphase boundary diffusion along α_2/γ interfaces is close to the activation enthalpies of Ti bulk diffusion in both α_2-Ti_3Al and γ-TiAl, $Q_{IPB} \approx 0.9 \cdot Q_{bulk}^{(\alpha_2)} \approx 1.0 \cdot Q_{bulk}^{(\gamma_2)}$.

5. Conclusions

1. Self-diffusion of the transition metal component in Ni_3Al, Ti_3Al, and TiAl mainly occurs by nearest-neighbor jumps via vacancies in the transition metal sublattice (sublattice diffusion mechanism), while this mechanism does not dominate in NiAl because next–nearest–neighbor jumps of Ni atoms would be involved. The triple defect diffusion mechanism produces the main contribution in the near-stoichiometric NiAl alloys. Under specific conditions (high temperatures in TiAl, $T > 1450$K, or large Ni content in NiAl, $c_{Ni} \geq 55$at.%) the anti-structure bridge (ASB) mechanism additionally becomes important in these intermetallics.
2. Diffusion in the transition metal sublattice superimposed by the ASB mechanism governs Al diffusion in Ni_3Al, Ti_3Al, and TiAl. Ga, which dissolves exclusively on the Al sublattice in Ni- and Ti-aluminides, represents a suitable solute to 'simulate' Al diffusion in these compounds because it diffuses by the same mechanisms as Al. Al diffusion in near-stoichiometric NiAl alloys mainly occurs by the triple defect mechanism and the ASB mechanism dominates Al diffusion in Al-rich compositions.
3. Bulk self-diffusion in the anti-structure-defect type Ni- and Ti-aluminides (Ni_3Al, Ti_3Al, and TiAl) reveals only a marginal compositional dependence, whereas a pronounced compositional dependence of D_{Ni} is observed in the triple-defect-type NiAl phase. This behavior is related to the fact that mainly the sublattice diffusion mechanism operates in Ni_3Al, Ti_3Al, and TiAl.
4. The Darken-Manning relationship most likely is valid in ordered aluminides, too. Large deviations of the vacancy wind factor S from unity to very low values occur in the stoichiometric NiAl alloys due to the dominance of the triple defect mechanism. The experimentally observed deep minimum in $\tilde{D}$ qualitatively reflects the calculated variation of S and strongly supports the triple defect mechanism.
5. Addition of Fe to stoichiometric NiAl alloy results in non-monotonous composition dependence of D_{Ni}^{*} in ternary $Ni_{50-x}Fe_xAl_{50}$ alloys. A minimum in the activation enthalpy Q_{Ni} is observed at $x \simeq 10$ at.%.

Acknowledgments

The present investigation was supported by funds of the Deutsche Forschungsgemeinschaft (Projects He898/25-1 and 25-3).

REFERENCES

[1] G. Sauthoff, Intermetallics (Wertheim, VCH 1995).
[2] H. Mehrer, Mater. Trans. Japan Inst. Metals **37**, 1259 (1996).
[3] M. Koiwa, Mater. Trans. Japan Inst. Metals **39**, 1169 (1998).
[4] Y. Mishin, Chr. Herzig, Acta mater. **48**, 589 (2000).
[5] Ch. Herzig, S.V. Divinski, St. Frank, T. Przeorski, Defect and Diffusion Forum **194-199**, 389 (2001).
[6] C. McCullough, J.J. Valencia, C.G. Levi, R. Mehrrabian, Acta Metall. **37**, 1321 (1989).
[7] H. Okamoto, J. Phase Equilibria **14**, 257 (1993).
[8] R. Kainuma, M. Palm, G. Inden, Intermetallics **2**, 321 (1994).
[9] M. Yamaguchi, H. Inui, in Structural Intermetallics, ed. R. Darolia, J.J. Lewandovski, C.T. Liu, *et al.*, p. 127, Metallurgigcal Society of AIME, Warrendale, PA (1993).
[10] H.E. Schaefer, K. Badura-Gergen, Defect Diffusion Forum **143-147**, 285 (1997).
[11] P.A. Korzhavy, A.V. Ruban, A.Y. Lozovoi, Y.K. Vekilov, I.A. Abrikosov, B. Johansson, Phys. Rev. B **61**, 6003 (2000).
[12] M. Kogachi, Y. Takeda, T. Tanahashi, Intermetallics **3**, 129 (1995).
[13] E.W. Elcock, C.W. McCombie, Phys. Rev. B, **109**, 605 (1958).
[14] N.A. Stolwijk, M. van Gend, H. Bakker, Phil. Mag. A **42**, 783 (1980).
[15] C.R. Kao, Y.A. Chang, Intermetallics **1**, 237 (1993).
[16] H. Wever, Defect Diffusion Forum **83**, 55 (1992).
[17] H. Numakura, T. Ikeda, M. Koiwa, A. Almazouzi, Phil. Mag. A, **77**, 887 (1998).
[18] St. Frank, S.V. Divinski, U. Södervall, Chr. Herzig, Acta Mater. **49**, 1399 (2001).
[19] S.V. Divinski, L.N. Larikov, J. Phys.: Condens. Matter. **9**, 7873 (1997).
[20] Chr. Herzig, T. Przeorski, Y. Mishin, Intermetalics **7**, 389 (1999).
[21] Chr. Herzig, T. Przeorski, M. Friesel, F. Hisker, S.V. Divinski, Intermetallics **9**, 461 (2001).
[22] St. Frank, U. Södervall, Chr. Herzig, Phys. Stat. Sol. B **191**, 45 (1995).
[23] J. Rüsing, Chr. Herzig, Intermetallics **4**, 647 (1996).
[24] W. Sprengel, N. Oikawa, H. Nakajima, Intermetallics **4**, 185 (1996).
[25] Chr. Herzig, M. Friesel, D. Derdau, S.V. Divinski, Intermetallics **7**, 1141 (1999).
[26] Y.L. Hao, D.S. Xu, Y.Y. Cui, R. Yang, D. Li, Acta Mater. **47**, 1129 (1999).
[27] P. Scholz, PhD Thesis, University Göttingen (2002).
[28] Y.A. Chang, J.P. Neumann, Progr. Solid State Chem. **14**, 221 (1982).
[29] G.F. Hancock, B.R. McDonnell, Phys. Stat. Sol. **A4**, 143 (1971).
[30] S.V. Divinski, St. Frank, Chr. Herzig, U. Södervall, Solid State Phenomena **72**, 203 (2000).
[31] Yu. Mishin, D. Farkas, Phil. Mag. A, **75**, 177 (1997); *ibid*, 187.
[32] Y. Minamino, Y. Koizumi, Y. Inui, Defect Diffusion Forum **194-199**, 517 (2001).
[33] Y. Minamino, Y. Koizumi, N. Tsuji, T. Yamada, J. Jap. Inst. Metals **66**, 67 (2002).
[34] B. Meyer, M. Fähnle, Phys. Rev. B **59**, 6072 (1999).
[35] S.V. Divinski, Chr. Herzig, Intermetallics **8**, 1357 (2000).
[36] S. Divinski, Y.-S. Kang, W. Löser, Chr. Herzig, Intermetallics **12**, 511 (2004).
[37] S. Divinski, F. Hisker, Y.-S. Kang, W. Löser, U. Södervall, Chr. Herzig, Verhandlungen der Deutschen Physikalischen Gesellschaft, Ser. VI, **38**, Dresden, (2003).

[38] S. Peteline, S. Divinski, B. Sepiol, H. Mehrer, Verhandlungen der Deutschen Physikalischen Gesellschaft, Ser. VI, **38**, Dresden, (2003).
[39] T.D. Moyer, M.A. Dayananda, Metal. Trans. A **7**, 1035 (1976).
[40] L.M. Pike, I.M. Anderson, C.T. Liu, Y.A. Chang, Acta Mater. **50**, 3859 (2002).
[41] T. Ikeda, H. Kadowaki, H. Nakajima, Acta Mater. **49**, 3475 (2001).
[42] L.S. Darken, Trans. AIME **175**, 184 (1948).
[43] J.R. Manning, Acta Metall. **15**, 817 (1967).
[44] T. Shimozaki, Y. Goda, Y. Wakamatzu, M. Onishi, Defect Diffusion Forum **95-98**, 629 (1993).
[45] H. Numakura, T. Ikeda, H. Nakajima, M. Koiwa, Defect Diffusion Forum **194-199**, 337 (2001).
[46] G.E. Murch, I.V. Belova, Defect Diffusion Forum **194-199**, 533 (2001).
[47] G.E. Murch, I.V. Belova, Defect Diffusion Forum *194-199*, 541 (2001).
[48] S. Shankar, Metal. Trans. A **9**, 1467 (1978).
[49] S. Kim, Y.A. Chang, Metall. Mater. Trans. A **31**, 1519 (2000).
[50] A. Steiner, K.L. Komarek, Trans. TMS-AIME **230**, 786 (1964).
[51] S.V. Divinski, Chr. Herzig, Defect Diffusion Forum **203**, 177 (2002).
[52] Chr. Herzig, T. Wilger, T. Przeorski, F. Hisker, S.V. Divinski, Intermetallics **9**, 431 (2001).
[53] Chr. Herzig, Y. Mishin, S.V. Divinski, Metal. Mater. Trans. A **33**, 765 (2002).
[54] S.V. Divinski, F. Hisker, A. Bartels, Chr, Herzig, Scr. Mater. **45**, 161 (2001).
[55] M. Nomura, V. Vitek, Interface Science. **11**, 99 (2003).

Received: 1 March 2004.

ARCHIVES OF METALLURGY AND MATERIALS
Volume 49 2004 Issue 2

A. PAUL *, M.J.H. VAN DAL*, A.A. KODENTSOV*, F.J.J. VAN LOO*

ON THE BEHAVIOUR OF KIRKENDALL MARKERS IN SOLID-STATE INTERDIFFUSION

O ZACHOWANIU SIĘ MARKERÓW W PROCESIE DYFUZJI WZAJEMNEJ W CIELE STAŁYM

The migration of inert markers as a result of unequal mobilities of the components during solid-state interdiffusion in a binary system can be rationalized using a Kirkendall velocity construction. It is demonstrated that in a diffusion-controlled interaction the Kirkendall plane, identified by inert particles (markers) placed at the original contact surface of a reaction couple, need not be unique. Multiple planes can develop, but, on the other hand, markers at the original interface sometimes can get dispersed into a diffuse zone on both sides of the contact surface and no unique location of the Kirkendall planes can be defined. It is also shown that the location of the Kirkendall plane(s) inside the diffusion zone can be identified by grain morphology changes within the microstructure of the reaction products. A physico-chemical approach is developed which elucidates the role of the Kirkendall effect in the morphogenesis of interdiffusion systems. The occurrence of one or more Kirkendall planes, characterized by morphology changes in the reaction layers, turns out to be related to different nucleation sites of the product grains.
Keywords: Diffusion; Kirkendall effect; Intermetallics; Microstructure

Opis ruchu markerów w procesie dyfuzji wzajemnej w ciele stałym, będący wynikiem różnych ruchliwości poszczególnych składników, można zracjonalizować używając graficznej konstrukcji prędkości Kirkendalla. Zostanie pokazane, że położenie płaszczyzny Kirkendalla, identyfikowanej przez obojętne cząstki (markery) umieszczone w miejscu początkowej płaszczyzny kontaktu w parze dyfuzyjnej, nie musi być jednoznaczne. Oprócz tego, że możliwych jest kilka płaszczyzn Kirkendalla, to z drugiej strony, markery położone w chwili początkowej w miejscu początkowej płaszczyzny kontaktu mogą ulegać rozproszeniu po jej obu stronach i w tej sytuacji nie można jednoznacznie zdefiniować jej położenia.. Zostanie także pokazane, że położenie płaszczyzny (płaszczyzn) Kirkendalla w strefie dyfuzji wzajemnej można określić na podstawie zmian morfologii ziaren i mikrostruktury produktu reakcji. Przedstawiono próbę wyjaśnienia wpływu efektu Kirkendalla na morfogenezę dyfuzji wzajemnej. Pokazano, że występowanie jednej lub kilku płaszczyzn Kirkendalla związane ze zmianą morfologii w warstwach reakcji może wynikać z różnych miejsc zarodkowania ziaren produktu reakcji.

* LABORATORY OF SOLID STATE AND MATERIALS CHEMISTRY, EINDHOVEN UNIVERSITY OF TECHNOLOGY, P.O. BOX 513, 5600 MB EINDHOVEN, THE NETHERLANDS

1. Introduction

Since the discovery, as far back as 1947 [1], and the following analysis by D a r k e n [2], the K i r k e n d a l l effect assumed a prominent role in the diffusion theory, as it is seen as the most explicit evidence for the occurrence of a vacancy mediated mechanism in diffusion processes in solids.

It is to be remarked right away that although this subject is treated in all textbooks on solid-state diffusion and is taught in many university curricula, the rationalization and description of the K i r k e n d a l l effect is by no means trivial as it looks at first sight. Scientists dealing with the diffusion phenomena thought that they had a reasonable notion of the K i r k e n d a l l effect induced migration of inert inclusions (markers) inside the diffusion zone and the uniqueness of the K i r k e n d a l l plane (as marked by inert particles positioned at the initial contact surface between the couple halves) has not been questioned for quite a long time.

This all changed when in 1972, C o r n e t and C a l a i s [3] published a paper in which they described hypothetical diffusion couples, in which more than one "K i r k e n d a l l marker plane" can emerge. Though this demonstration was a really remarkable one, only within the past four years, several systematic studies into the microstructural stability of the K i r k e n d a l l plane have been undertaken [4 - 6]. A clear-cut experimental verification of the ideas of C o r n e t and C a l a i s was found and a number of fundamental concepts related to the K i r k e n d a l l effect have been reconsidered.

The present paper focuses on the identification of some outstanding issues of the K i r k e n d a l l effect and attempts to elucidate its role in the morphological evolution of interdiffusion system. Much of the discussion is a product of the authors' own research in this field conducted over the last decade. Throughout the text, reference has been made to our original publications, in which the questions considered have already been raised. By reading these original articles one gains a broader understanding and clearer insights into the finer nuances of the K i r k e n d a l l effect manifestations mentioned.

In order to develop a coherent and logical presentation as brief as possible, we will explain most of the basic ideas by examples of interdiffusion in well-defined material systems. Each of the examples is chosen for its clarity of illustration and its relation to the particular point in discussion.

2. General considerations: concept of the Kirkendall velocity construction in a binary diffusion couple

The diffusion process in a binary *A-B* system can best be visualized by the consideration of the intrinsic fluxes, J_i, of the components with respect to an array of inert ("fiducial") markers, prior to annealing positioned along the anticipated zone of interdiffusion, the so-called K i r k e n d a l l frame of reference:

$$J_i = - D_i \frac{\partial C_i}{\partial x}, \tag{1}$$

where D_i [m^2/s] is the intrinsic diffusion coefficient, C_i [$mole/m^3$] is the concentration of component i (A or B) and x [m] is the position parameter.

The sum of the oppositely directed intrinsic volume fluxes of the components is equal to the velocity, v [m/s] of the inert markers with respect to the laboratory-fixed frame of reference, i.e.

$$v = - (V_B J_B + V_A J_A) = V_A (D_A - D_B) \frac{\partial C_A}{\partial x}, \tag{2}$$

where V_i [m^3/mole] is the partial molar volume of component i, and use is made of the relation $V_B dC_B = - V_A dC_A$.

It is important to keep in mind that in a diffusion-controlled interaction, the inert markers positioned at the location of the original interface between the end-members of the semi-infinite couple ("K i r k e n d a l l p l a n e") are the only markers that (from the beginning) stay at a constant composition and move parabolically in time with a velocity

$$v_K = \frac{dx}{dt} = \frac{x_K - x_o}{2t} = \frac{x_K}{2t}. \tag{3}$$

Here, x_K and x_o (= 0) are the positions of the K i r k e n d a l l plane at times t and *zero*, respectively.

The location of the K i r k e n d a l l plane in the diffusion zone can, therefore, be found graphically as the intersection between the marker velocity plot $2tv$ vs. x (from Eq. (2)) and the straight line $2tv_K = x_K$ given by Eq. (3). Obviously, in order to draw the line $2tv_K = x_K$, one needs to know the position of the plane in the diffusion zone where the "K i r k e n d a l l markers" were located at time $t = 0$ (i.e. $x_o = 0$). If the total volume of the reaction couple does not change upon interdiffusion, this can readily be determined through the usual M a t a n o - B o l t z m a n n analysis [7]. If, on the other hand, the partial molar volumes of the components are composition dependent, the S a u e r - F r e i s e method should be used [8].

3. Experimental procedure

Throughout the investigation the diffusion couple technique has been used. Plane slices of the "as-supplied" or arc-melted homogeneous and equilibrated materials were clamped together and heat-treated in vacuum (~ 10^{-6} mbar) for varying times and at various temperatures.

Prior to annealing, particles of thorium dioxide (ThO_2) were introduced as fiducial (inert) markers at the contact interface between the initial end-members. The oxide powder

with particle size of ~ 0.5 – 1 μm was dispersed in acetone and then applied to the bonding faces of the couple halves. By means of this technique agglomerates (up to 5 μm) of ThO_2 plate-like crystals can more or less evenly be spreaded at the contact surface of the couple.

After standard metallographic preparation, cross-sections of the annealed diffusion couples were examined by optical microscopy and scanning electron microscopy. Concentration profiles across the interaction zones were measured using electron-probe microanalysis and the behaviour of the inert ThO_2-markers during interdiffusion was monitored.

4. Appearance of a stable and unstable Kirkendall marker plane in an interdiffusion system

Let us now take two examples of interdiffusion in the Ni-Pd and Fe-Pd systems at 1100 °C. Both systems exhibit a minimum in the solidus curve and a strong dependence of the inter-, intrinsic and tracer diffusion coefficients on the alloy composition, which is reflected by the presence of a distinct maximum on their plot vs. composition [9]. However, the behaviour of the "K i r k e n d a l l markers" in the Ni/Pd and Fe/Pd diffusion couples was found to be remarkably different. This can be appreciated by comparing Figs. 1a and 1b, which show back-scattered electron images of the diffusion zones in these couples after annealing. In these experiments small particles (0.5 – 1 μm) of thorium dioxide (ThO_2) were used as markers between the end-members of the couples. One can clearly see that after interaction, the ThO_2-particles, used as the K i r k e n d a l l markers appeared in the Ni/Pd diffusion couple as a straight row of plate-like inclusions, whereas the initial planar array of the fiducial markers at the contact surface of the Fe/Pd couple has been transformed into an array of ThO_2-particles spatially distributed in the diffusion direction, and the shape of the markers are more round-like. In the last case, it looks as if the system has "missed" the original contact interface and no unique location of the K i r k e n d a l l plane can be defined. This is an important observation which has invoked a re-examination of some basic concepts involved in the analysis of the K i r k e n d a l l marker behaviour.

From a purely phenomenological standpoint, the appearance of a distinct K i r k e n - d a l l marker plane at a specific position in a diffusion zone suggests that this plane of fixed (constant in time) composition acts as "attractor" for markers. During interdiffusion, such attractor plane accumulates the markers in its vicinity resulting in a microstructurally (spatially) *stable* K i r k e n d a l l plane. In mathematical terms, it means that corresponding marker velocity near the location of the Kirkendall plane must have a negative gradient with respect to the position parameter. Indeed, in such a case, if markers (for whatever perturbations) appear slightly ahead of the K i r k e n d a l l plane position, they would slow down (lower velocity) and, if markers were slightly behind this position, they would move more rapidly (higher velocity).

a)

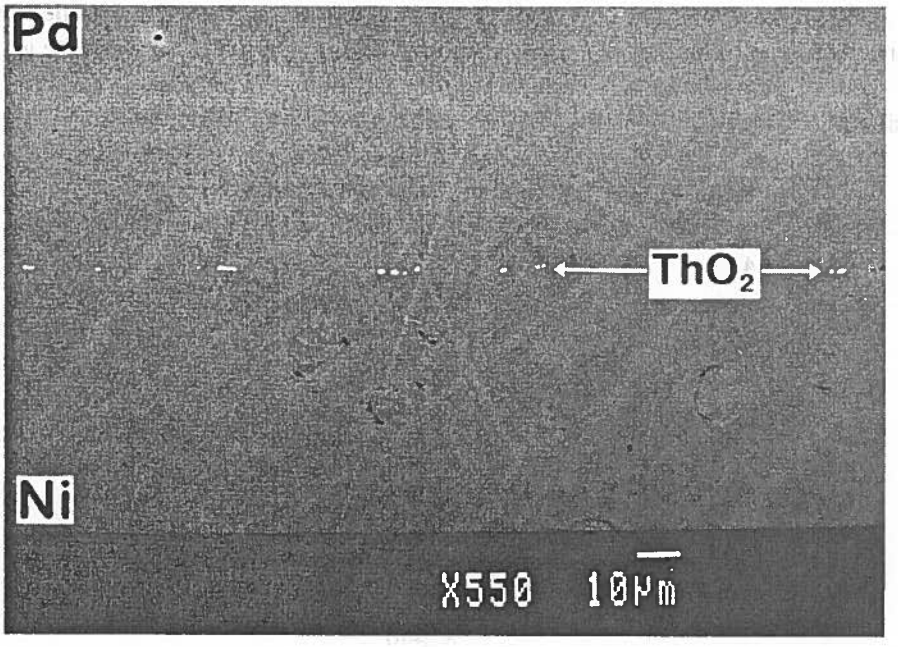

b)

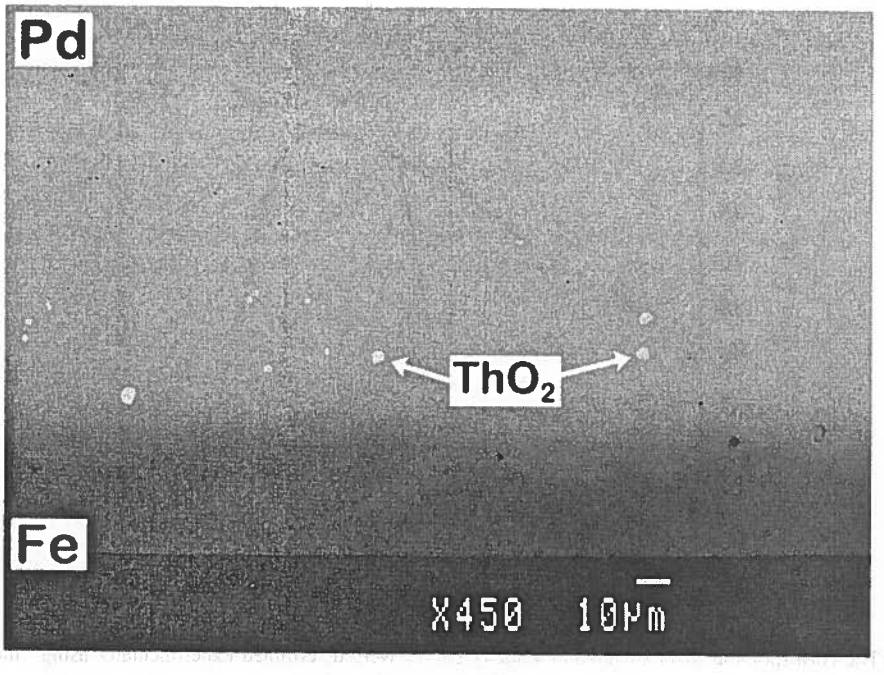

Fig. 1. Back-scattered Electron Images (BEI) of:
a) Ni/Pd diffusion couple annealed at 1100° C in vacuum for 121 hrs;
b) an Fe/Pd couple after interdiffusion at 1100° C in vacuum for 144 hrs.
(The ThO_2 – markers exhibit a white contrast.)

Following a similar line of argument, it is clear that a K i r k e n d a l l plane is *unstable* (in respect to perturbations in marker positions) during interdiffusion when the gradient at the point of intersection between the K i r k e n d a l l velocity and the line $2tv_K = x_K$ is positive.

a)

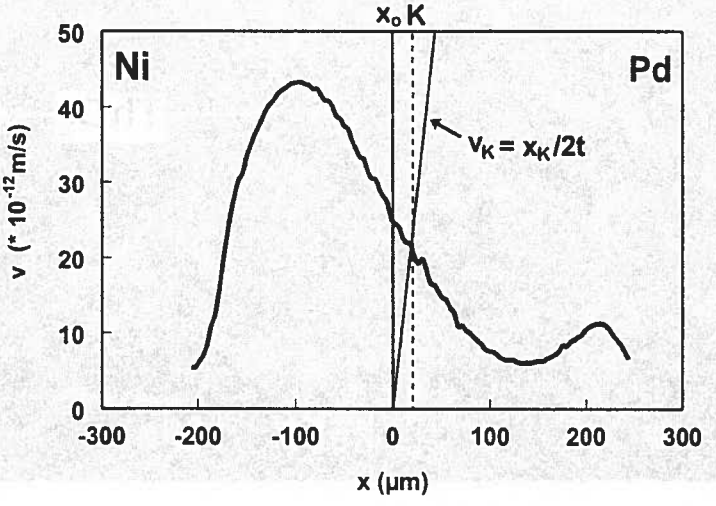

b)

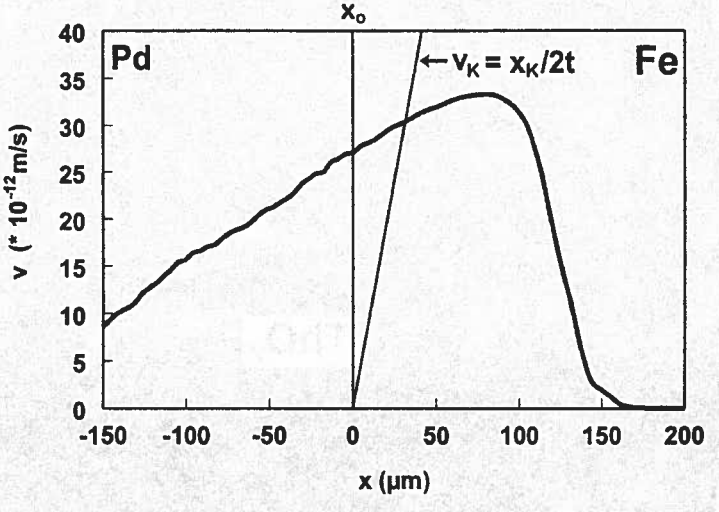

Fig. 2. K i r k e n d a l l velocity constructions pertaining to:
a) the Ni/Pd couple annealed at 1100° C in vacuum for 121 hrs;
b) the Fe/Pd couple after annealing at 1100° C in vacuum for 144 hrs.
(The corresponding K i r k e n d a l l velocity curves were determined experimentally using "multi-foil" diffusion couples [9].)

Figs. 2a and 2b show K i r k e n d a l l velocity constructions for the annealed Ni/Pd and Fe/Pd diffusion couples obtained using experimental techniques explained in Ref. [9]. It can

be seen that in the Ni/Pd couple the Kirkendall plane position is fixed by the intersection between the velocity curve and the straight line $2tv_K = x_K$ at the location in the diffusion zone where the gradient of the Kirkendall velocity is negative. In other words, this interdiffusion system has a moving attractor for markers. On the contrary, in the Fe/Pd system, the velocity curve at the point of intersection has a positive slope. Obviously, there is no "attractor" (i.e. no stable Kirkendall plane) present inside the interaction zone which leads to the observed marker behaviour.

In our recent publications [5, 6], we described marker behaviour in a hypothetical *A/B* couple, in which on the *A*-rich side, *A* is the faster diffusing species and on the *B*-rich side, *B* diffuses faster. In such a case, the Kirkendall velocity will be positive on the *A*-rich side and negative on the *B*-rich side of the diffusion zone (Eq. (2)). In this situation, there is no theoretical restriction for the straight line $2tv_K = x_K$ to intersect the velocity curve more than once. This could, in principle, lead to the formation of multiple Kirkendall plane(s) in the interdiffusion zone. However, it should be stressed that such behaviour of the Kirkendall markers has not been observed yet in "pure" solid solution systems. On the other hand, it was demonstrated that a Kirkendall marker plane can, under certain (predictable) circumstances, bifurcate during interdiffusion in a single-phased reaction product layer [6].

5. Bifurcation of the Kirkendall plane in a diffusion-grown phase layer

For the sake of explanation, let us consider behaviour of Kirkendall markers inside a reaction layer of phase β growing in a binary diffusion couple from its adjacent phases α and γ. Suppose that the β-phase exists over a fairly wide concentration range. It is then conceivable that difference in intrinsic diffusivities of the components and, hence, the corresponding Kirkendall velocity (Eq. (2)) may have a "different sign" in different domains of the product layer. In this case, the plot of the Kirkendall velocity versus the distance parameter pertaining to the product phase β may be of type schematically shown in Fig. 3, and it is possible for the line $2tv_K = x_K$ to intersect the velocity curve up to three times as is indicated in this figure. The latter implies that in such a diffusion couple three Kirkendall planes (K_1, K_2, K_3) might exist, which move parabolically in time. However, one should realize that only two of the three predicted marker planes can be found experimentally within the reaction zone. It follows from the preceding section that if an unstable Kirkendall plane (K_2 in Fig. 3) is situated between two stable ones, the stable planes will accumulate all markers during the initial stage of interdiffusion. Therefore, only two Kirkendall marker planes (at the position K_1 and K_3) are expected to appear in this couple.

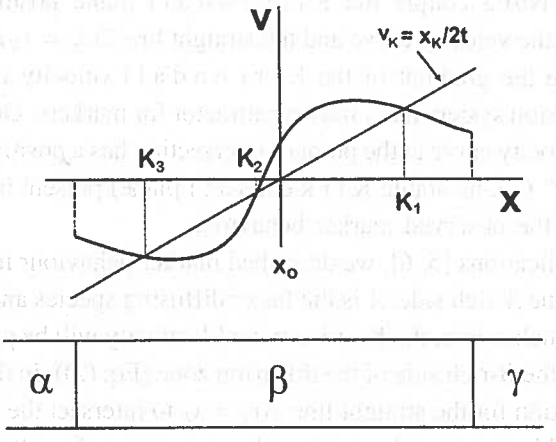

Fig. 3. The K i r k e n d a l l velocity diagram (schematically), pertaining to a hypothetical binary couple, in which a layer of a non-stoichiometric phase β is growing between its adjacent phases, and the difference in intrinsic diffusivities of the components has a "different sign" in different domains of the product layer. Three intersections between the velocity curve and the line $2tv_K = x_K$ (K_1, K_2 and K_3) are found, of which only two correspond to stable Kirkendall planes (at K_1 and K_3).

Very telling examples of a multiple K i r k e n d a l l plane is provided by experiments on diffusional growth of *AB*-intermetallic with *B*2 (CsCl-type) structure in incremental reaction couples. We recall that most of the *B*2 phases have a wide range of homogeneity around the stoichiometric (1:1) composition [10] and are broadly classified into two different groups in terms of defect structure, which compensates the off-stoichiometry composition. In one group, on both sides of the stoichiometry antisite defects are present like in AuZn, AuCd, AgMg, CuZn. In the other group, on one side of equiatomic composition antisites are created whereas on the other side of the stoichiometry, constitutional (structural) vacancies are present like in NiAl, CoAl, NiGa and CoGa on the Al and Ga-sublattices.

Such a peculiar defect structure has great influence on the diffusion behaviour of the intermetallic compounds, which can change drastically with deviation from the stoichiometric composition [11]. Changes in magnitude and sign of the difference $(D_A - D_B)$ within the homogeneity range lead to a velocity curve that makes bifurcation of the Kirkendall marker plane possible.

It is, however, important to emphasize that the location of the K i r k e n d a l l plane(s) emerging inside the product layer during interdiffusion is determined not only by shape of the velocity curve, but also depends on the position of the plane, x_o, in the diffusion zone where the K i r k e n d a l l markers were situated before the interaction. To put it differently, the question whether bifurcation of the K i r k e n d a l l marker plane inside a diffusion-grown layer of B2 intermetallic phase will occur or not, is highly sensitive to the initial compositions of the end- members of the reaction couple since these define the position $x_o = 0$, through which the line $2tv_K = x_K$ runs. For this reason, the simultaneous

appearance of two K i r k e n d a l l marker planes moving with different velocities inside a diffusion-grown layer of B2 intermetallic has been, up to now, observed only in well-chosen cases as presented in Fig. 4 [6, 12].

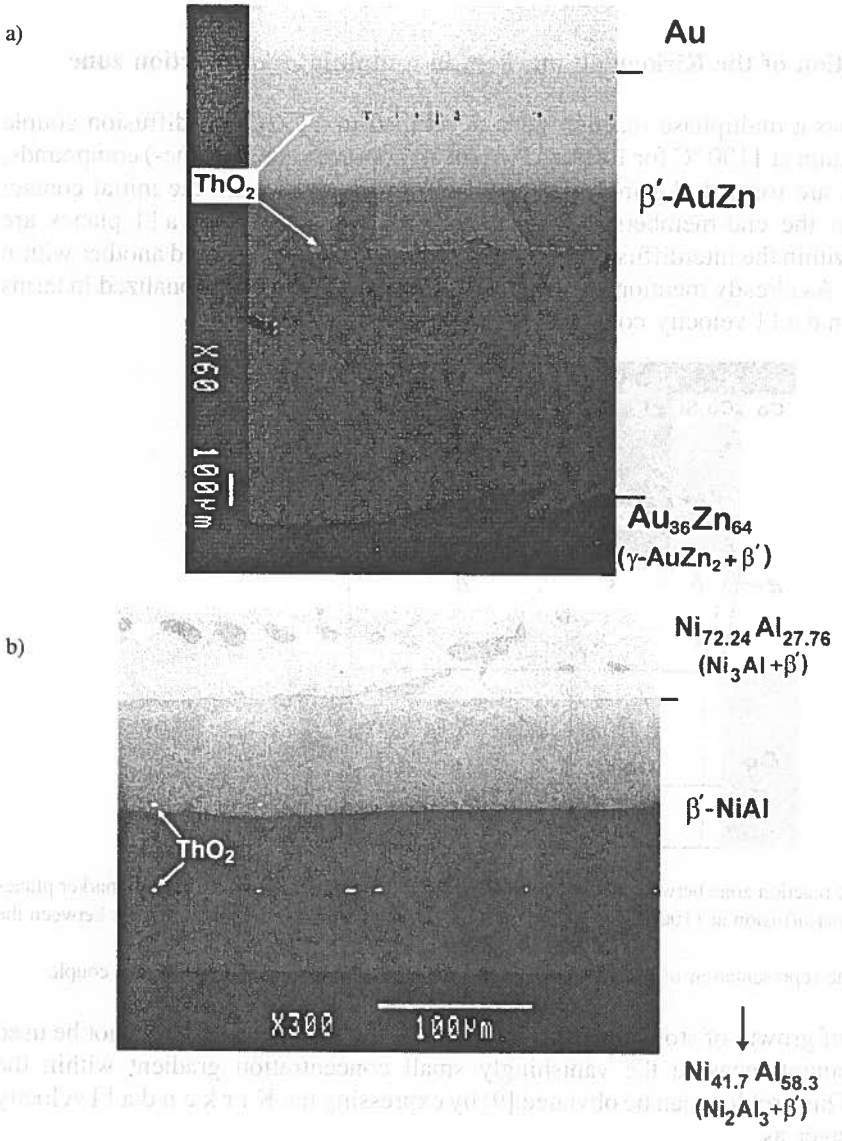

Fig. 4. Simultaneous appearance of two K i r k e n d a l l marker planes inside a layer of B2 intermetallic compound during diffusion-controlled growth of:
a) β'-AuZn phase between pure Au and a $Au_{36}Zn_{64}$ (γ- $AuZn_2$ + β') two-phase alloy (500° C; 17.25 hrs; argon);
b) β'- NiAl phase in a reaction couple between two-phase alloys with nominal compositions $Ni_{41.7}Al_{58.3}$ and $Ni_{72.24}Al_{27.76}$ (1000° C; 24 hrs; vacuum). The original $Ni_{41.7}Al_{58.3}$ – alloy is much further away from the marker plane.
ThO_2 – particles were used as the K i r k e n d a l l markers. (Back-scattered Electron Images.)

The appearance of more than one K i r k e n d a l l plane is by no means restricted to diffusion zones composed of a single-phased reaction product nor need two-phase alloys be the end-members. This phenomenon turns out to be quite general.

6. Migration of the Kirkendall markers in a multilayered reaction zone

Fig. 5a shows a multiphase reaction zone developed in a $Co/CoSi_2$ diffusion couple annealed in vacuum at 1100 °C for 100 hrs. Two (nearly) stoichiometric (line-) compounds, Co_2Si and CoSi are formed. Again, ThO_2-particles were used to mark the initial contact surface between the end-members. After interaction, two K i r k e n d a l l planes are clearly visible within the interdiffusion zone: one inside the Co_2Si-layer and another within the CoSi-phase. As already mentioned, such marker behaviour can be rationalized in terms of the K i r k e n d a l l velocity construction.

a)

b)

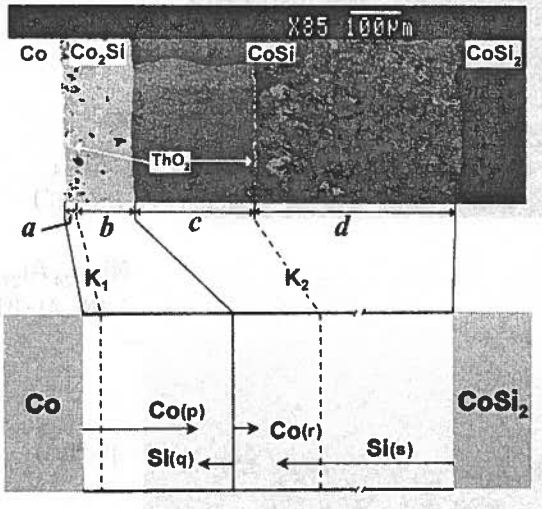

Fig. 5. a) BEI of the reaction zone between Co and $CoSi_2$ showing the formation of two Kirkendall marker planes (K_1 and K_2) after interdiffusion at 1100° C for 100 hrs (ThO_2 – particles were used as inert markers between the couple halves);
b) a schematic representation of the diffusion process in the reaction zone of the $Co/CoSi_2$ couple

In the case of growth of stoichiometric compounds, the Eqs. (1) and (2) cannot be used because one cannot measure the vanishingly small concentration gradient within the product layer. This problem can be obviated [9] by expressing the K i r k e n d a l l velocity inside such a layer as

$$v = \frac{V_B\left(\frac{D_A}{D_B}\right) - 1}{V_m\left[\frac{V_B}{V_A}\frac{D_A}{D_B}\right]N_B + N_A}\left(\frac{\tilde{D}_{int}}{d}\right) \tag{4}$$

with N_i being the mole fraction of the component i in the product phase, V_m its molar volume and d is the thickness of the reaction layer in question. $\tilde{D}_{int}$ is the integrated diffusion coefficient in this phase which is defined for a line-compound as the interdiffusion coefficient in the phase integrated over its (unknown) homogeneity limits. This parameter can be determined experimentally from a concentration profile measured across the multiphase diffusion zone as explained in Ref. [13].

Since the integrated diffusion coefficient is a material constant, its value does not depend on the starting materials of the reaction couple. From the cited work it also follows that thickness of the product layers can be predicted for any type of semi-infinite diffusion couple if the values of $\tilde{D}_{int}$ are known for all compounds formed during reaction.

The ratio of the intrinsic diffusivities of components in the Co-silicides can be determined using the diffusion couple technique. It was shown that when the Kirkendall plane is found inside the layer of a stoichiometric compound growing between its saturated adjacent phases, this ratio can readily be obtained by graphical method [14]. These data are summarized in Table [14]. Molar volumes of the phases were calculated with the lattice parameter values given in Ref. [15].

TABLE

The integrated diffusion coefficients, $\tilde{D}_{int}$, molar volumens V_m of the Co_2Si and CoSi and ratio's of intrinsic fluxes of Si and Co, $V_{Co}D_{Si}/V_{Si}D_{Co}$ in these phases at 1100 °C

	Phase	
	Co_2Si	CoSi
$\tilde{D}_{int}$ [m^2s^{-1}]*	$(1.5\pm0.5)\times10^{-14}$	$(4.6\pm0.3)\times10^{-14}$
$\frac{V_{Co}D_{Si}}{V_{Si}D_{Co}}$	0.06 ± 0.025	35 ± 15
V_m [m^3.$mole^{-1}$]	6.56×10^{-6}	6.60×10^{-6}

*) *average values obtained from different diffusion couples* [14]

According to Eq. (4), each fiducial marker present within the product layer of line-compound will move during interdiffusion process with the same Kirkendall velocity. This leads to a "stepwise" plot $2tv$ vs. x.

The Kirkendall velocity diagram experimentally constructed for the annealed $Co/CoSi_2$ diffusion couple is given in Fig. 6. The position x_o (= 0) was found by subjecting the concentration profile measured across the reaction zone of this couple to the Sauer-Freise treatment. One can see that the straight line $2tv_K = x_K$ intersects the velocity plot twice in the domains of the reaction zone corresponding to the single-phased product layers of Co_2Si and CoSi, i.e. two Kirkendall planes should be expected. Returning to Fig. 5a one sees that, indeed, the theoretical predictions are consistent with the experimental observations.

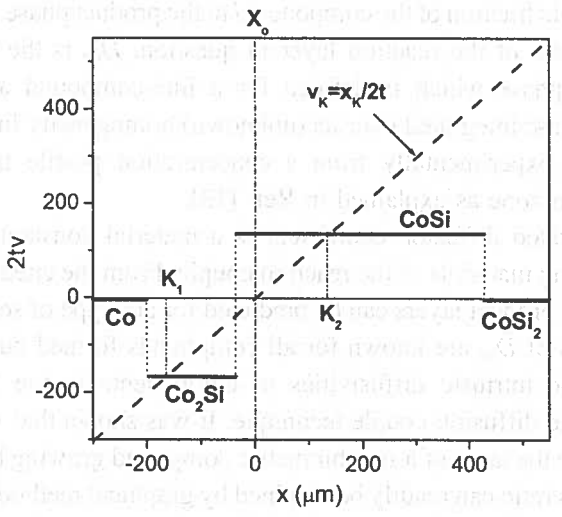

Fig. 6. The Kirkendall velocity diagram experimentally constructed for the annealed $Co/CoSi_2$ couple (1100° C; 100 hrs). The positions of the Kirkendall planes are found as intersections of the line $2tv_K = x_K$ and the velocity plot. In each product layer a Kirkendall plane exists (K_1, K_2)

Recently, another important conclusion emerged from our experimental studies on the Kirkendall effect manifestations. It was shown that the velocity of markers in a product layer, the appearance of the multiple Kirkendall plane(s), their locations and the morphological features of the reaction products can be explained (and predicted) from a purely chemical point of view considering the diffusion-controlled interactions at the interphase interfaces.

7. A physico-chemical treatment of a multiphase diffusion growth

From a phenomenological viewpoint it is conceivable that at the reaction interfaces a product Co-silicide nucleates and grows by the loss of Co- or Si-atoms from or by adding Co- or Si-atoms to the adjoining phase layer. In terms of chemical reaction equations it can be re-stated as (Fig. 5):

At the interface Co/Co_2Si on the Co_2Si-side:

$$2qCo + q[Si]_d \rightarrow 3qCo_{\frac{2}{3}}Si_{\frac{1}{3}}$$

At the interface $Co_2Si/CoSi$ on the Co_2Si - side:

$$4qCo_{\frac{1}{2}}Si_{\frac{1}{2}} \rightarrow q[Si]_d + 3qCo_{\frac{2}{3}}Si_{\frac{1}{3}}$$

$$2pCo_{\frac{1}{2}}Si_{\frac{1}{2}} + p[Co]_d \rightarrow 3pCo_{\frac{2}{3}}Si_{\frac{1}{2}}$$

At the interface $Co_2Si/CoSi$ on the CoSi - side:

$$3rCo_{\frac{2}{3}}Si_{\frac{1}{3}} \rightarrow r[Co]_d + 2rCo_{\frac{1}{2}}Si_{\frac{1}{2}}$$
$$3sCo_{\frac{2}{3}}Si_{\frac{1}{3}} + s[Si]_d \rightarrow 4sCo_{\frac{1}{2}}Si_{\frac{1}{2}}$$

At the interface $CoSi/CoSi_2$ on the CoSi - side

$$3rCo_{\frac{1}{3}}Si_{\frac{2}{3}} + r[Co]_d \rightarrow 4rCo_{\frac{1}{2}}Si_{\frac{1}{2}}$$
$$3sCo_{\frac{1}{3}}Si_{\frac{2}{3}} \rightarrow s[Si]_d + 2sCo_{\frac{1}{2}}Si_{\frac{1}{2}}$$

Here, the symbols $[Co]_d$ and $[Si]_d$ denote the diffusing atom species in the product layer; they do not represent the phases Co and Si.

The parameters p and q are the total amount of moles of Co- and Si-atoms, respectively, transported per unit area of the product layer of Co_2Si during the total diffusion time, t. Analogously, r and s are the number of moles of Co- and Si-atoms transported during interaction across unit area of the CoSi-phase layer.

Apparently, the resultant thickness of the product layer depends on the growth from, and at the same time, consumption by the neighbouring layers. The total thickness of each reaction product, however, always increases with time.

For a diffusion-controlled growth of the product layer, one can write

$$p = \int_0^t |J_{Co}|dt = \int_0^t \frac{const}{\sqrt{t}}\,dt = 2t|J_{Co}|, \qquad (5)$$

since the intrinsic flux, J_i is inversely proportional to $t^{\frac{1}{2}}$ if only one (volume) diffusion mechanism is operative during the whole diffusion process. Similarly, $q = 2t|J_{Si}|$, and therefore, the ratio $\frac{q}{p} = 0.06$ equals the ratio of the instantaneous intrinsic fluxes J_{Si} and J_{Co} in the Co_2Si-product layer, that is value of $\frac{V_{Co}D_{Si}}{V_{Si}D_{Co}}$ in Table. In the same way, we found for the product layer of CoSi, $\frac{s}{r} = 35$.

The reaction zone developed in this couple can be considered as if it were composed of four regions separated by the K i r k e n d a l l planes and the interphase boundaries. The thickness of the parts of the phase layer growing on either side of the K i r k e n d a l l planes (a, b and c, d in Fig. 5) can be expressed by:

$$
\begin{aligned}
&V_m^{Co_2Si}\tfrac{1}{3}\tfrac{1}{3} \times 3q = a \\
&V_m^{Co_2Si}\tfrac{1}{3}\tfrac{1}{3} \times (3q + 3p - 3r - 3s) = b \\
&V_m^{Co_1Si}\tfrac{1}{2}\tfrac{1}{2} \times (2r + 4s - 4q - 2p) = c \\
&V_m^{Co_1Si}\tfrac{1}{2}\tfrac{1}{2} \times (4r + 2s) = d .
\end{aligned}
\tag{6}
$$

Comparing Eqs. (2) and (5), we conclude that for any product layer formed in the reaction zone

$$2tv_K = -\,2t(V_{Si}J_{Si} + V_{Co}J_{Co}). \tag{7}$$

It is important to realise that data on partial molar volumes of the components in the Co-silicides ('line-compounds") are not available, and there are no simple experimental methods to determine them. In the present discussion, we assumed, for the sake of explanation, that $V_{Si} = V_{Co} = V_m$ for the line-compounds involved in the interaction. On the other hand, we may also assume that the partial molar volumes of the components in the phase are equal to the molar volumes of the pure elements. However, the difference in the calculated values of the K i r k e n d a l l velocity using these two different assumptions appeared to be within the limit of the experimental error connected to the diffusion couple techniques used.

The marker velocity and the location of the K i r k e n d a l l plane, x_K in each product layer of the Co/$CoSi_2$ couple can be found as follows:

$$
\begin{aligned}
&\textit{for the } Co_2Si \textit{ layer:} \quad && V_m^{Co_2Si}(q - p) = 2tv_K^{Co_2Si} = x_K^{Co_2Si} \\
&\textit{for the } CoSi \textit{ layer:} \quad && V_m^{CoSi}(s - r) = 2tv_K^{CoSi} = x_K^{CoSi} \quad .
\end{aligned}
\tag{8}
$$

This shows the equivalence of the "diffusion-based" and the "physico-chemical" approaches in evaluating the growth of a product phase layer. In fact, the results could not be otherwise, since both models describe the same phenomenological process in terms of purely phenomenological quantities.

To simplify further calculations, we ignored the presence of the solid solution of Si in the cobalt next to the intermetallic layer. This means that the value of a will be slightly overestimated because a small amount of that part of the Co_2Si-layer will actually dissolve in the cobalt end-member. With these assumptions, the parameters a, b, c and d in Eq. (6) were computed using values of integrated diffusion coefficients and ratio's of intrinsic diffusion fluxes in the product phases as listed in Table. It was found that $a = 32\ \mu m$, $b = 133\ \mu m$, $c = 168\ \mu m$ and $d = 294\ \mu m$. Accordingly, the coefficients p, q, r and s in the equations of the interfacial reactions were determined using Eq. (6) as 0.6, 21.0, 1.6 and 26.8 mole/m^2, respectively.

This leads, through Eq. (7), to the same values of the K i r k e n d a l l velocity in the product layers (-2.3×10^{-10} and 1.9×10^{-10} m/s for Co_2Si and CoSi, respectively) as deduced from the diffusion model. These results as well as the co-ordinates of the K i r k e n d a l l planes (-165 and 135 μm for Co_2Si and CoSi, respectively), predicted in this manner, agree with those determined by means of the K i r k e n d a l l velocity construction (Fig. 6) and with those found experimentally (Fig. 5a).

Before terminating this part of the discussion, it should be mentioned that using the chemical reaction equations as a starting point, it is also possible to elucidate the significance of the K i r k e n d a l l effect for the morphogenesis of the interdiffusion system. In the past, it was noticed that a "duplex" grain morphology may sometimes develop inside diffusion-grown compound layers [16, 17]. The terms "duplex" is used in this context to underline that a layer of the same chemical compound looks in the examined reaction zone as if it consists of two sub-layers demarcated by a distinct boundary and differing by shape, size and orientation of the grains. This microstructural feature was found in the product layers of the reaction zone in the Co/$CoSi_2$ couple as well. In Fig. 5a one can see two different grain morphologies developed in each silicide layer on either side of the K i r k e n d a l l plane(s), and the "demarcation" line separating the sub-layers coincides with the marker plane(s). The appearance of such "boundaries" inside the single-phase layers can be considered as a manifestation of the K i r k e n d a l l effect, and the location of the stable K i r k e n d a l l plane(s) can be identified by the boundary between the different grain morphologies within the microstructure of the reaction products. This phenomenon is independent of the presence of any inert (fiducial) markers, and it can be (qualitatively) understood by considering the different nucleation sites of the grains in the growing phase layers [18]. In the present case, each Co-silicide is growing from two sides with a different type of nucleation, and these differently nucleated grains meet at the K i r k e n d a l l plane resulting in this conspicuous change in crystal morphology.

These conclusions are confirmed by our recent experiments on the Zn/Ag system. A microstructure of a Zn/Ag diffusion couple annealed at 370° C for 5 hrs in argon is shown in Fig. 7, which is a montage of a series of back-scattered electron images taken under different conditions (i.e. with different brightness and contrast). As expected from the binary Ag-Zn phase diagram [19], three layers of intermetallics, ε-"$AgZn_3$", γ-"Ag_5Zn_8" and β- "AgZn" were formed. Here, the Ag-Zn phases are denoted by their binary formulae. However, it is to be pointed out that the intermediate phases in this system exist over wide concentration ranges around the stoichiometric compositions.

One sees that ThO_2- markers, introduced at the original interface between the Zn- and Ag- couple halves, emerged after interaction as row of particles inside the ε – as well as in the γ – phase, i.e. two well-defined K i r k e n d a l l planes are present in the multiphase diffusion zone. It was demonstrated that the observed bifurcation of the marker plane in this reaction couple can be rationalized using the same concept of the K i r k e n d a l l velocity construction [20].

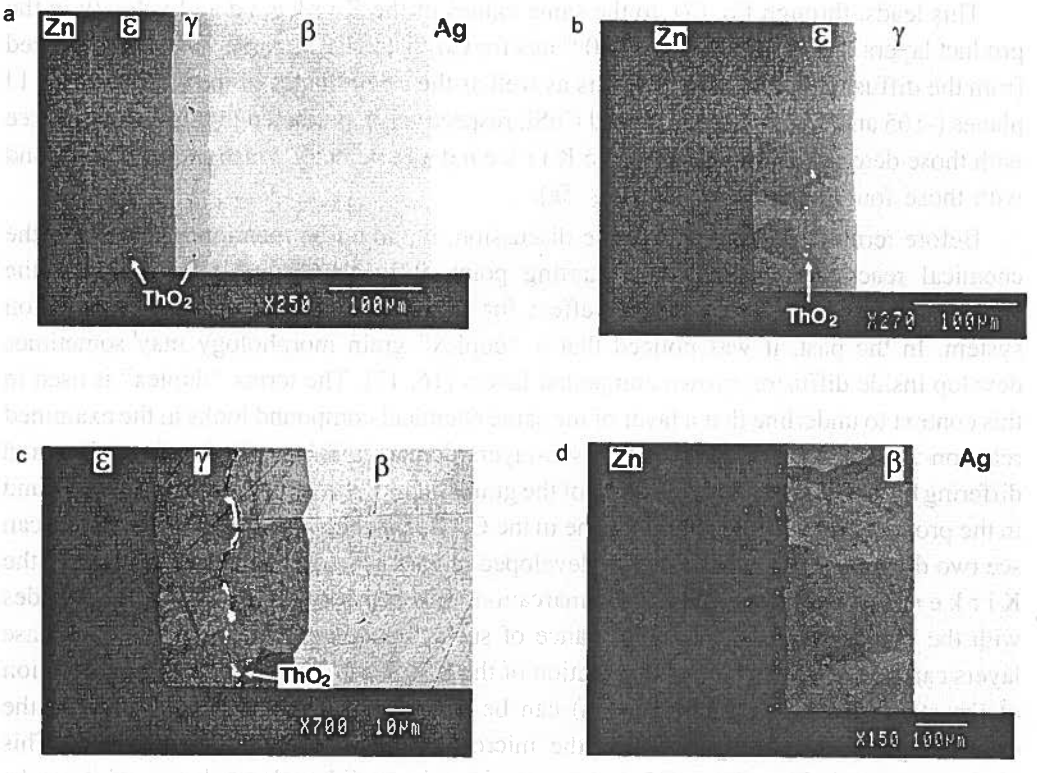

Fig. 7. A series of back-scattered electron images of a multiphase diffusion zone in a Zn/Ag reaction couple annealed at 370° C in argon for 5 hrs:

a) After interdiffusion two K i r k e n d a l l planes marked by ThO_2 – particles are found, one inside the ε- and one inside the γ- phase layer, and no marker plane is present in β- phase;

b), c) Different crystal morphology in the reaction product layer on either side of the K i r k e n d a l l plane is clearly visible;

d) The 'uniform" grain morphology within the product layer of β- phase is indicative for the absence of a K i r k e n d a l l plane

Following the progression of the micrographs given in the last figure, the role of the K i r k e n d a l l plane in developing of a duplex grain morphology inside the ε – and γ– phase layers is apparent. The changes in grain structure are seen to be associated with the presence of the (stable) marker plane(s) inside the reaction products. On the other hand, no duplex structure has been formed in the β– phase, and no marker plane is present inside this intermetallic layer (Fig. 7d). The "uniform" crystal morphology within the product layer is indicative for the absence of a K i r k e n d a l l plane.

In fact, the location of a stable K i r k e n d a l l plane in a diffusion zone can be identified by the grain morphology changes within the microstructure of the reaction products. In other words, in this case, there is no need for any fiducial markers at all to find the position of the K i r k e n d a l l plane(s)!

8. Concluding remarks

The examples we discussed above, show that a Kirkendall effect-mediated behaviour of fiducial markers originally situated at the contact surface between the end-members of the diffusion couple can be complex in both temporal and spatial domains. It also clear that an understanding of the Kirkendall effect manifestations has a great potential for providing insights into the finer nuances of solid-state interdiffusion.

The available models can be used not only to predict the microstructural stability and location of the Kirkendall plane(s), but also to elucidate the role of the Kirkendall effect in the morphogenesis of interdiffusion systems associated with the nucleation and growth of product phase layers.

The message in the present paper is highly important for a broad scientific community, because the conclusions made here will influence the way, in which multiphase diffusion in the solid state is treated. This also will have strong technological implications, e.g. in the field of composite materials, thin-film electronic devices, etc.

Acknowledgements

We like to express our indebtedness to Prof. A.M. Gusak (Cherkasy State University, Ukraine) and Dr. C. Cserháti (University of Debrecen, Hungary) for their contribution especially at the early stage of this study. The lessons learned from Prof. Gusak concerning the general criterion of Kirkendall plane instability were particularly valuable.

The constant help and the expert assistance provided by H.A.M. van der Palen is also greatly appreciated.

REFERENCES

[1] A. Smigelskas, E. Kirkendall, Trans. AIME **171**, 130-141 (1947).
[2] L. Darken, Trans. AIME **175**, 184-201 (1948).
[3] J.-F. Cornet, D. Calais, J. Phys. Chem. Solids **33**, 1675-1684 (1972).
[4] M. van Dal, A. Kodentsov, F. van Loo, Intermetallics **9**, 451-456 (2001).
[5] M. van Dal, A. Gusak, C. Cserhati, A. Kodentsov, F. van Loo, Phys. Rev. Lett. **86**, 15, 3352-3355 (2001).
[6] M. van Dal, A. Gusak, C. Cserháti, A. Kodentsov, F. van Loo, Phil. Mag A, **82**, 5, 943-954 (2002).
[7] C. Matano, Japan J. Physics **8**, 109-113 (1933).
[8] F. Sauer, V. Freise, Z. Elektrochem. **66**, 353-363 (1962).
[9] M. van Dal, M. Pleumeekers, A. Kodentsov, F. van Loo, Acta mater 48, 385-396 (2000).
[10] Y. Chang, I. Gyuk, J. Franks, Acta Met **19**, 939-953 (1971).
[11] C. Kao, Y. Chang, Intermetallics **1**, 237-250 (1993).
[12] A. Paul, A. Kodentsov, F. van Loo, Acta mater. Accepted for publication.
[13] C. Wagner, Acta Met. **17**, 99-107 (1969).
[14] M. van Dal, D. Huibers, A. Kodentsov, F. van Loo, Intermetallics **9**, 409-421 (2001).
[15] P. Villars, L. Calvert, Pearson's Handbook of Crystallographic Data for Intermetallic Phases, American Society for Metals, Ohio (1985).
[16] K. Przybylski, W. Smeltzer, J. Electrochem. Soc. **128**, 897-902 (1981).

[17] J. van Beek, S. Stolk, F. van Loo, Z. Metallkd. **73**, 439-444 (1982).
[18] A. Paul, M. van Dal, A. Kodentsov, F. van Loo, Acta mater. **52**, 623 (2004).
[19] Th. B. Massalski, Binary Alloy Phase Diagrams, American Society for Metals (1986).
[20] A. Kodentsov, A. Paul, F. van Loo, Z. Metallkd. **95**, 258 (2004).

Received: 1 March 2004.

ARCHIVES OF METALLURGY AND MATERIALS
Volume 49 2004 Issue 2

J. WOJEWODA *, G.A. LÓPEZ **, P. ZIĘBA*, E.J. MITTEMEIJER**

DIFFUSION PROCESSES IN DIFFUSION-SOLDERED INTERCONNECTIONS

PROCESY DYFUZYJNE W SPOINACH UZYSKANYCH W WYNIKU LUTOWANIA DYFUZYJNEGO NISKOTEMPERATUROWEGO

The paper presents fundamentals of the diffusion processes occurring in interconnections produced by means of diffusion soldering. The stages involved in the formation of the interconnection are described for the Al–Ni system as an example. The growth of the formed intermetallic phases is the most important step from the kinetic point of view because it determines the rate of the whole process. If the growth-controlling factor is bulk diffusion, then the solution of the diffusion problem leads to Wagner's integral interdiffusion coefficient. To solve Wagner's equation it is necessary to determine the growth constant k_p. The procedure leading to a proper determination of k_p from a plot of the intermetallic layer thickness as function of time is described in details. Finally, examples of kinetic calculations for the intermetallic phase growth in the Al–Ni, Cu–Sn, Cu–In and Cu-In-Sn systems are presented.

W pracy przedstawiono opis procesów dyfuzyjnych zachodzących w spoinie (lutowinie) utworzonej w wyniku niskotemperaturowego lutowania dyfuzyjnego. Na przykładzie złącza Ni/Al/Ni zostały opisane poszczególne etapy tworzenia lutowiny. Najważniejszym etapem, determinującym kinetykę całego procesu jest okres wzrostu faz międzymetalicznych. W przypadku, gdy czynnikiem kontrolującym wzrost jest dyfuzja objętościowa, wtedy rozwiązanie zagadnienia dyfuzji sprowadza się do wyznaczenia uśrednionego współczynnika dyfuzji wzajemnej z równania Wagnera. Zastosowanie równania Wagnera wymaga wyznaczenia stałej wzrostu parabolicznego k_p. Pokazana została procedura pozwalająca na poprawne wyznaczenie k_p z wykresu zależności pomiędzy grubością warstwy fazy metalicznej, a czasem trwania lutowania dyfuzyjnego. Przedstawiono również przykłady obliczeń kinetyki wzrostu faz międzymetalicznych w układach Al-Ni, Cu-Sn, Cu-In oraz Cu-In-Sn.

* POLISH ACADEMY OF SCIENCES, INSTITUTE OF METALLURGY AND MATERIALS SCIENCE, 30-059 CRACOW, 25 REYMONTA ST., POLAND
** MAX PLANCK INSTITUTE FOR METALS RESEARCH AND INSTITUTE OF PHYSICAL METALLURGY, UNIVERSITY OF STUTTGART, 3 HEISENBERG ST 70569 STUTTGART, GERMANY

1. Introduction

Lead-free interconnection technologies attract growing interest mainly because of a strong concern to protect the environment, particularly due to the harmful effect of lead and the use of toxic fluxes like chlorofluorocarbon (CFC) for conventional soldering. This trend was initiated in the U.S. in the early 1990s and advanced later, even more rapidly, in Europe and Japan [1, 2]. Therefore, new solder materials that could replace the commonly used Pb–Sn solders are searched, especially in electronics production. Moreover, the performance of modern devices for electronic and electrical applications depends critically on the reliability of the interconnections for mechanical support and electrical connection between the components. Progressive miniaturization of components and contact areas increases the specific load of contacts due to heat dissipation. Heat dissipating power components such as chip resistors and resistant heating elements cannot be connected to leads, using a conventional soldering process. This results from the limitations of soft-soldered joints like:

- working temperature, which is 60–100 °C below the soldering temperature (usually 220–260 °C for Pb–Sn solders),
- amount of the solder alloy and the joint size which may be large in comparison with the size of the area which has to be joined,
- the use of flux and need for cleaning of the component with solvents like CFC after soldering.

2. Diffusion soldering

One of the promising techniques, which has a large potential to be applied to the fabrication of thermally and mechanically stable bonds, is diffusion soldering. It is based on the principle of isothermal solidification [3–7]. This is schematically presented in Fig. 1 for a hypothetical binary phase diagram containing two intermetallic phases (Fig. 2).

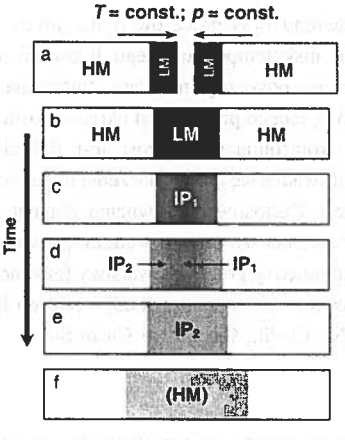

Fig. 1. Schematic diagram ilustrating the diffusion soldering process. LM and HM are the low- and high-melting components, respectively. IP_1 and IP_2 are successively formed intermetallic phases and (HM) is the high-melting solid solution finally formed after very long reaction times

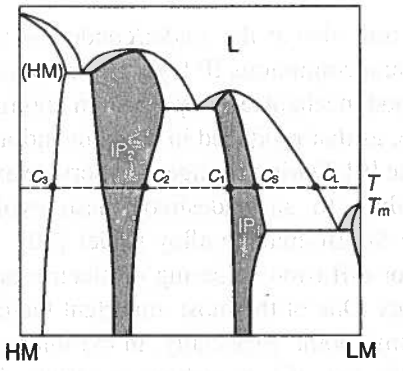

Fig. 2. Hypothetical binary phase diagram containing two intermetallic phases IP_1 and IP_2; L = liquid

A low-melting material (LM) is sandwiched between two pieces of high-melting material (HM). The sandwich can be accomplished by coating of the HM components with a thin LM layer (Fig. 1a) or using a thin-foil interlayer of LM. The assembly is clamped and then heated up from room temperature to the melting temperature of the LM (T_m), *heating stage*. Upon heating, interdiffusion may occur between the LM and HM at the LM/HM interface. However, this is not so significant because usually the heating rate is very high.

Upon further heating up to the temperature of joining, T, the interlayer of LM is melt and part of the HM is dissolved into the liquid, *dissolution stage* (Fig. 1b). The width of the liquid zone increases and reaches its maximum at the end of the dissolution stage. After a certain time the composition of the liquid reaches C_L (Fig. 2). Subsequent holding of the assembly at T, for a specified time and under a certain pressure p, leads to saturation of the liquid. At this moment a precipitation reaction takes place, most probably at the interfaces between the liquid and the substrates. The so-called *isothermal solidification* stage begins. The process can be controlled by diffusion of LM atoms into the solid HM. As local equilibrium at the precipitate/liquid interface is assumed, the concentrations at these interfaces are C_L and C_S, respectively (Fig. 2). The width of the liquid zone shrinks gradually, until the whole liquid is solidified. The joint formed consists of an intermetallic phase IP_1 (Fig. 1c).

As soon as the whole liquid is consumed, upon further annealing at T, solid-state interdiffusion takes place and the interconnection zone is enriched with HM atoms. After a certain time the change in composition promotes the formation and growth of another intermetallic phase IP_2 (Fig. 1d). The compositions at the interfaces between both IPs are C_1 and C_2 (Fig. 2). This is the final stage, called *growth of intermetallic phases*. Successively IPs with increasing concentration of HM are formed depending on the specific alloy system. In some circumstances two IPs can also coexist with unconsumed liquid [8].

The intermetallic phases are characterized by melting temperatures much higher than the temperature used for the fabrication of the joint. In this way, the joint features advantageous intrinsic properties of the IPs, in particular high thermal and mechanical stability. The joint is also extremely thin, usually less than several microns, which adds to the mechanical properties and it facilitates the use in electronics.

It is known that IPs form also at the solder/conductor interface in the conventional soldering process. A thin and continuous IP layer is the consequence of good wetting and leads to a bonding with good mechanical properties. In contrast, a too thick IP layer at the solder/conductor interface, as that produced in the conventional process, may degrade the reliability of the solder joint [9]. During storage or in service existing IPs will grow and also new IPs may form, leading to an undesired phase evolution as the formation of a Sn-depleted zone in the Sn–Bi eutectic alloy solder [10].

Potential candidates for diffusion soldering of electric and electronic devices should satisfy several requirements. One of the most important factors in designing of the solder (filler) material is its melting point. Especially, in the microelectronic industry, the Si/Si interconnection requires the use of low-melting materials. Quite recently, several alloy systems have been designed and successfully used for diffusion soldering. These are Ag–In, Ag–Sn, Ni–Sn, Cu–Sn, Au–In, Au–Sn, Cu–In, Sn–In and Ni–Al, used especially for electric purposes; for details see [7]. The last one will be shortly described in the next chapter to illustrate the changes in structure and chemistry, and the sequence of the intermetallic phases appearing in the joint.

3. Formation of diffusion-soldered Ni/Al/Ni interconnections

In this section details on the production of Ni/Al/Ni joints by means of diffusion soldering will be given. The Ni–Al equilibrium phase diagram is presented in Fig. 3. At a temperature slightly above the melting point of Al (660 °C), several intermetallic phases are formed, namely Al_3Ni, Al_3Ni_2, AlNi and $AlNi_3$. They are thermally stable up to 854, 1133, 1638 and 1360 °C, respectively.

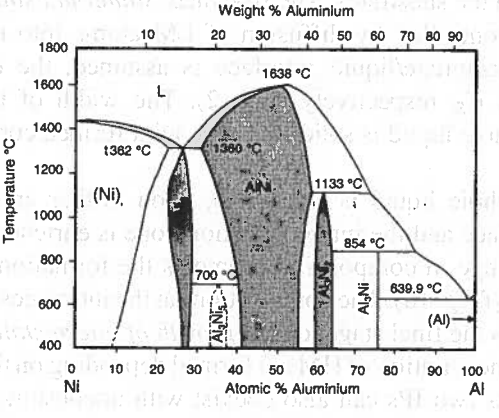

Fig. 3. The simplified version of the Ni–Al equilibrium phase diagram based on data of O k a m o t o [11]

Ni/Al/Ni bonds were accomplished by means of isothermal solidification and subsequent interdiffusion of Ni and Al in samples held at 720 °C [8, 12]. The formation of the Ni/Al/Ni joint started from the reaction of liquid Al with solid Ni to form Al_3Ni (Fig. 4).

The reaction is very fast so that after 2 min of annealing Al_3Ni_2 is also present in the joint in spite of the fact that liquid Al has not been completely consumed. Further annealing at 720 °C resulted in the formation of two variants of the NiAl phase, namely a Ni-rich zone (60 at.% Ni) and stoichiometric AlNi. The AlNi phase is gradually consumed by the growth of AlNi (Ni-rich) compound, and after 10 h of annealing only $AlNi_3$ and AlNi (Ni-rich) exist in the joint. The joining process is completed after 30 h of reaction with solely $AlNi_3$ to be present in the Ni/Al/Ni interconnection zone. Figure 5 is a schematic presentation of the sequence of phase appearance in Ni/Al/Ni interconnections. It can be summarized in the followin way:

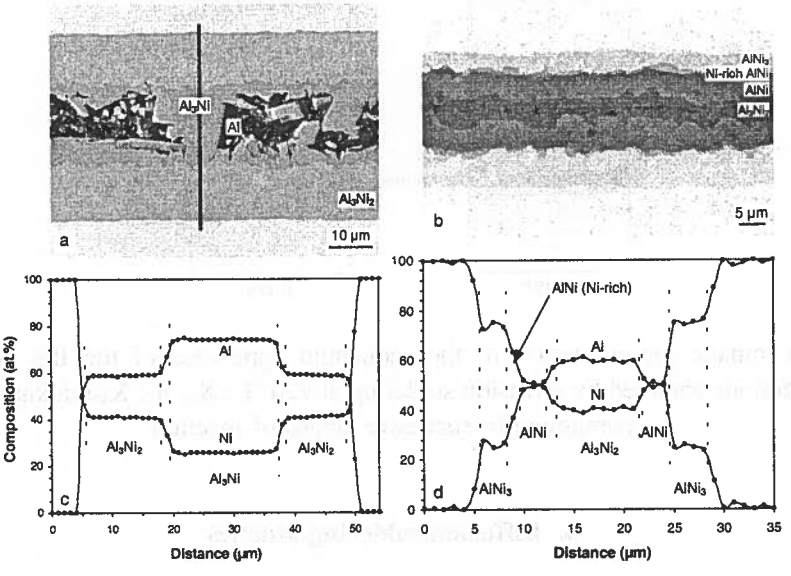

Fig. 4. SEM images of a cross-sectional view of a Ni/Al/Ni interconnection after 2 min (a) and 20 min (b) of reaction time at 720 °C. (c) Corresponding electron probe line-scans made along solid line in Fig. 4a and (d) energy-dispersive *X*-ray line-scans for Ni and Al [8]

liquid Al → Al_3Ni → Al_3Ni_2 → AlNi (stoichiometric) → AlNi (Ni-rich) → $AlNi_3$.

In the intermediate stages even four intermetallic phases can coexist simultaneously (see Figs. 5c and d).

The quality of the resultant bond and the high melting point of the $AlNi_3$ phase (1360 °C) indicate a great potential of the diffusion soldering process for the joining of heat dissipating elements used in electronics and electro-techniques. This makes the Ni/Al/Ni diffusion soldering process very attractive for joining of heating elements and thick-film hot plates. The manufacturing can be stopped in an intermediate stage because all the intermetallic phases have a high stability temperature. In this way, the manufacturing time could be reduced without losing the mechanical advantages. An optimisation of the process should lead to a selection of the most efficient time to reach a relatively suitable mechanical behaviour without going until solely Ni_3Al in the interconnection zone.

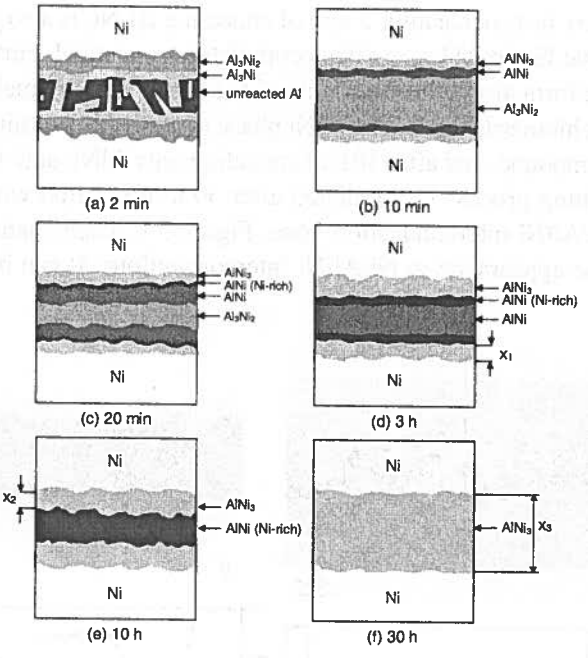

Fig. 5. Schematic representation of the sequential apperance of the IPs in Ni/Al/Ni interconnections obtained by diffusion soldering at 720 °C. X_1, X_2, X_3-thickness of $AlNi_3$ compound in succesive stages of reaction

4. Diffusion soldering kinetics

4.1. Integral diffusion coefficient

The example presented in the previous chapter clearly shows that diffusion soldering results in a number of intermediate phases, for which the ranges of composition have been observed to be very narrow. A general form of the expression to calculate position-dependent chemical interdiffusion coefficients for any phase of composition N*, assuming that the molar volume is constant and does not depend on the composition, was derived by Wagner [13] in the following form:

$$\tilde{D}_{(N^*)} = \frac{1}{2t(\partial N/\partial x)_{x=x^*}}\left[\frac{N^+ - N^*}{N^+ - N^-}\times\int_{-\infty}^{x^*}(N - N^-)\,d\partial x + \frac{N^* - N^-}{N^+ - N^-}\times\int_{x^*}^{\infty}(N^+ - N)\,dx\right], \quad (1)$$

where x^* and N^* mean particular values of the distance and composition for which $\tilde{D}_{(N)}$ is calculated, N^- and N^+ are the initial mole fractions of the diffusion couple on the left-hand

and the right-hand side of the origin of the co-ordinate system, x is the distance co-ordinate. The values of N in the brackets change from N^- to N^* for the first integral and from N^* to N^+ for the second one.

The composition across the intermetallic phase within the diffusion zone is generally assumed to vary linearly, which makes that δ_N/δ_X) remains constant and equal to $\Delta N^i/\Delta x^i$. Therefore, only an average value of $\tilde{D}_{(N^*)}$ can be determined from Eq. (2):

$$\tilde{D}^i_{(N),\mathrm{av}} = \frac{\Delta x_i}{2t\Delta N_i}\left[\frac{N^+ - N^i}{N^+ - N^-}\int_{-\infty}^{x^{(i-1,i)}}(N - N^-)\,dx + \frac{(N^i - N^-)(N^+ - N^i)}{N^+ - N^-}\Delta x^i + \right.$$
$$\left. + \frac{N^i - N^-}{N^+ - N^-}\int_{X^{(i,i+1)}}^{\infty}(N^+ - N)\,dx\right], \tag{2}$$

where i is a serial number of the particular phase corresponding to the average interdiffusion coefficient, $x^{(i-1,i)}$ is the distance to the interface between the phases i and (i-1), $x^{(i,i+1)}$ is the distance to the interface between the phases i and ($i+1$), and $\Delta x^i = x^{(i,i+1)} - x^{(i-1,i)}$ is the width of phase i.

The very narrow homogeneity range of the intermetallic phase i means a constant composition across it, and then $N \cong N^{(i)'} \cong N^{(i)''} \cong N^{(i)}$. This makes serious difficulties when calculating the diffusion coefficient from the concentration profile because the concentration gradient approaches zero (the diffusion coefficient approaches infinity). Therefore, W a g n e r [13] introduced a so-called integral diffusion coefficient having the following form:

$$\tilde{D}^i_{\mathrm{int}} = \int_{N^{i'}}^{N^{i''}} \tilde{D}dN = \tilde{D}^i_{(N),\mathrm{av}} \cdot \Delta N^i. \tag{3}$$

$N^{i'}$ and $N^{i''}$ are limiting mole fractions of the component B in phase i at the distances $x^{(i-1,i)}$ and $x^{(i,i+1)}$, and ΔN^i is the concentration difference of phase i at the interfaces between the phases (i-1) and i and between the phases i and ($i+1$): ($\Delta N^i = N^{i''} - N^{i'}$). $\tilde{D}^i_{(N),\mathrm{av}}$ is the average interdiffusion coefficient of phase i.

One may consider formation of phase i from phases (i-1) and ($i+1$) co-existing with phase i. That implies $N_2^- = N_2^{(i-1)''}$ and $N_2^+ = N_2^{(i+1)'}$ and then the respective contributions to the integrals in Eq. (2) vanish, what results in the following expression:

$$\tilde{D}^i_{\mathrm{int}} = \frac{(N^i - N^{(i-1)''})(N^{(i+1)'} - N^i)}{N^{(i+1)'} - N^{(i-1)''}}\,k_p^{(i)} \quad \text{and} \quad k_p^{(i)} = \frac{(\Delta x^{(i)})^2}{2t}, \tag{4, 5}$$

where N^i is the average mole fraction of component B in phase i, $N_B^{(i-1)''}$ and $N_B^{(i+1)'}$ are the mole fractions of component B in the phases i-1 and $i+1$ in local equilibrium with phase i, and $\Delta N_B = N_B^{(i)'} - N_B^{(i)''}$ is the difference in concentration of B in phase i at the interfaces between the phases i-1 and i and between the phases i and $i+1$. k_p^i is the parabolic rate constant for the formation of phase i.

Equation (4) holds true under the following conditions:
- the interface concentrations do not change with time,
- the diffusion coefficient does not depend on concentration,
- the differences in molar volumes amongst the various phases are negligible.

4.2. Growth rate of the intermetallics in the diffusion-soldered interconnections

To calculate W a g n e r ' s diffusion coefficient it is necessary to know the growth rate constant of the particular phases in the diffusion couple (joint). The value of the exponent equal to 2 in Eq. (5) indicates that the growth rate of the phase is controlled by volume diffusion. For further consideration Eq. (5) will be rewritten as:

$$x_p^2 = 2k_p t, \tag{6}$$

where the subscript p was introduced in order to emphasize the parabolic character of Eq. (6), t is the reaction time.

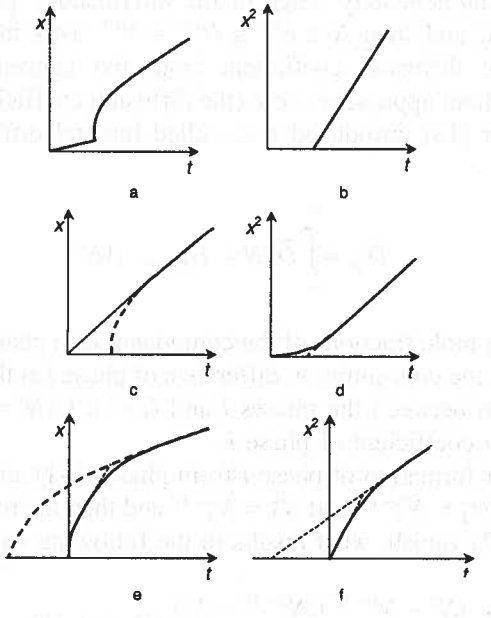

Fig. 6. $x = f(t)$ and $x^2 = f(t)$ dependencies of the thickness of the intermetallic phase on annealing time of a mutiphase diffusion bond

One can distinguish several different forms of the $x - t$ behaviour (Fig. 6). The first one is connected with the situation when the initial surface of the substrates is covered by a thin oxide layer or segregating element. It acts as a diffusion barrier and results in a relatively slow growth period (Fig. 6a) or an incubation period (Fig. 6b) before the stationary case is

reached. Another situation is when the reaction between the elements at the interface is the growth rate-controlling factor, which leads to the formation of an intermetallic phase. In that case the dependence $x(t)$ shows a linear character (the exponent in Eq. 6 equal to 1 instead of 2). After some time of annealing the diffusion process begins to dominate which makes the relation $x(t)$ rather parabolic (Figs. 6c, d). On the other hand, the presence of a fine-grained microstructure in the interconnection (joint) can cause a much more quicker growth of the layer in the beginning of the process due to grain boundary diffusion. After a certain time of annealing the curve takes a parabolic shape, which indicates that the volume diffusion is dominant (Figs. 6e, f).

It is very important to choose the proper formula $x = f(t^{0.5})$ or $x^2 = f(t)$ – to select the appropriate values of the steady-state parabolic growth rate constant. The analysis performed by P i e r a g g i [14] showed that $x = f(t^{0.5})$ better describes the situation when the intermetallic phase formed in the beginning of the growth process (transition period of faster kinetics) does not influence the course of the next parabolic growth of this phase. In this case the following formula is valid:

$$x_p^2 = (x - x_i)^2 = 2k_p(t - t_i), \tag{7}$$

where x is the total thickness of the intermetallic layer after time t, x_i is the thickness of the layer after a preliminary period finished after time t_i (after which the stabilized growth has begun), x_p is the width of the layer formed as a result of the parabolic growth started after time t_i and corresponding to time t-t_i.

In this case the parabolic rate constants k_p and k_p' calculated from Eqs. (8) and (9) – resulting from the transformation of Eq. (7) – are nearly the same and correct values.

$$x_p = \{2k_p(t - t_i)\}^{0.5}, \tag{8}$$

$$x = x_i + \{2k_p'(t - t_i)\}^{0.5}. \tag{9}$$

Here, k_p and k_p' are related through:

$$k_p' = \frac{k_p t}{(t - t_i)}. \tag{10}$$

A second case may occur when the layer of thickness x_i after a preliminary period has a significant influence on the stabilized parabolic growth period. In such a case the starting equation takes the following form:

$$x^2 - x_i^2 = 2k_p(t - t_i) \tag{11}$$

and the dependence $x^2 = f(t)$ gives the correct values of k_p. A similar situation holds when stationary growth appears after an incubation period and there is no substantial transient period. In such a case $x_i = 0$ and the dependence $x^2 = f(t)$ gives the correct solution.

4.3. Kinetics of Ni/Al/Ni joint formation

The kinetics of three intermetallics formed by the diffusion soldering process in Ni/Al/Ni interconnections was studied by Lopez et al. [12]. The layer growth of stoichiometric AlNi, AlNi (Ni-rich) and $AlNi_3$ was measured. The example below shows how to use Eq. (4) in order to calculate the integral interdiffusion coefficient of $AlNi_3$ from the rate constant extracted from the growth of this layer:

$$\tilde{D}_{\text{int}} = \Delta N_{\text{Ni}} \tilde{D}^{\text{AlNi}_3}_{(N),\text{av}} = \frac{(N^{\text{AlNi}_3}_{\text{Ni}} - N^{(\text{AlNi (Ni-rich)})''}_{\text{Ni}})(N^{(\text{Ni})'}_{\text{Ni}} - N^{\text{AlNi}_3}_{\text{Ni}})}{N^{(\text{Ni})'}_{\text{Ni}} - N^{(\text{AlNi (Ni-rich)})''}_{\text{Ni}}} k_p^{AlNi_3}, \qquad (12)$$

where ΔN_{Ni} is the difference in Ni concentration of $AlNi_3$ at the interfaces between AlNi (Ni-rich) and $AlNi_3$ and between $AlNi_3$ and (Ni) solid solution ($N^{(AlNi_3)'}_{Ni} - N^{(AlNi_3)''}_{Ni}$); $N^{(AlNi_3)'}_{Ni}$ and $N^{(AlNi_3)''}_{Ni}$ are the Ni concentrations of $AlNi_3$ at the interfaces between AlNi Ni-rich and $AlNi_3$ and between $AlNi_3$ and (Ni) solution, respectively. Data for $(N^{(AlNi(Ni-rich))''}_{Ni}$, the Ni concentration of Ni-rich AlNi at the interface between AlNi (Ni-rich) and $AlNi_3$, and for $N^{(Ni)'}_{Ni}$, the Ni concentration of (Ni) solid solution at the interface between $AlNi_3$ and (Ni), are taken from the published phase diagram. The value for $N^{AlNi_3}_{Ni}$ is taken to be equal to the average composition for this phase as determined by electron probe microanalysis or energy-dispersive X-ray microanalysis.

The growth of the intermetallic phases is presented in Fig. 7. The appearance of stoichiometric AlNi requires a certain incubation time as it clearly follows from a plot of Δx^2 versus t (Fig. 7a). The rate constant k_p can straightforwardly be determined from the slope of the straight line fitted to the data points in the plot. Similarly, it is concluded that the growth of Ni-rich AlNi requires no incubation time (Fig. 7b). For the growth of the $AlNi_3$ phase a Δx vs. $t^{1/2}$ plot was applied because such a plot exhibits more clearly than a Δx^2 vs. t plot that a transition period preceding the parabolic growth stage occurs (Fig. 7c). Eliminating the data points corresponding to the transition period, Fig. 7d shows a Δx^2 vs. t plot for the remaining data and the rate constant for the parabolic growth of the $AlNi_3$ phase has been derived from the slope of the straight line fitted through the data points in this plot. The calculated growth rate constants for the intermetallic phases present in the Ni/Al/Ni interconnections (Table 1) clearly indicate the fastest growth for stoichiometric AlNi and the slowest growth for AlNi Ni-rich. Moreover, the integral interdiffusion coefficients for the three intermetallic phases indicate the faster growth of the stoichiometric AlNi phase, in which the concentration gradient is not large, is attributed to a relatively high value of the diffusion coefficient. Both types of AlNi phase were considered separately because of the former growth of stoichiometric AlNi.

The integral diffusion coefficients obtained in this study and volume diffusion coefficients from other studies [15–18] determined for the same temperature have been given in Table 1. In Refs. [15, 18], where values for AlNi were reported for the "AlNi" phase, no distinction between stoichiometric AlNi and Ni-rich AlNi was made, which makes a direct comparison with the present data difficult. In fact, all data from the cited literature can only be taken as an indication of the order of magnitude for the diffusion coefficients because they were obtained using various approaches.

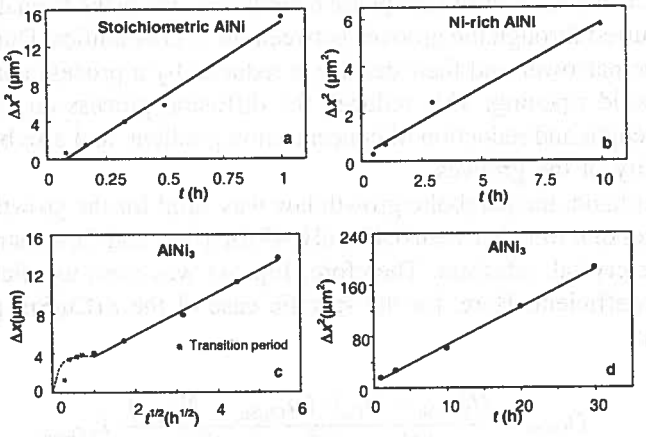

Fig. 7. Time dependence of the layer width for stoichiometric NiAl, Ni-rich NiAl and $AlNi_3$ in Ni/Al/Ni interconnections upon reaction at 720 °C

TABLE

Growth rate constants and integral interdiffusion coefficients for the intermetallic phases present in Ni/Al/Ni interconnections

Phase	This paper (Equation 12)		Ref. [15]	Ref. [16]	Ref. [17]	Ref. [18]
	k_p [$\mu m^2 h^{-1}$]	$\tilde{D}_{int}$ [$m^2 s^{-1}$]				
AlNi (stoichiometric)	8.00	1.1×10^{-16}	8.0×10^{-16}	2.4×10^{-14}	1.1×10^{-18}	2.2×10^{-17}
AlNi (Ni-rich)	0.28	3.2×10^{-18}		3.2×10^{-21}	4.2×10^{-16}	
$AlNi_3$	2.94	5.4×10^{-17}	4.0×10^{-16}	1.0×10^{-15}	–	4.9×10^{-18}

In any case it can be concluded that the results presented in this work are in good agreement with the tendency that the diffusion in stoichiometric AlNi is the fastest and in AlNi (Ni-rich) is the slowest (e.g. compare with the results in Ref. [15]). It should be noted that differences as large as three orders of magnitude occur between the $\tilde{D}_m$ values obtained by different authors. The value determined here for $AlNi_3$ falls between the extreme values reported in [15, 18].

4.4. Kinetics of Cu/Sn/Cu joint formation

The growth of the intermetallic compounds in Cu/Sn/Cu diffusion-soldered joints was studied by B a d e r, G u s t and H i e b e r [19]. At the beginning of annealing in the temperature range 513–573 K two intermetallics grew simultaneously: $\eta(Cu_6Sn_5)$ and $\varepsilon(Cu_3Sn)$. However, the growth velocity of the η phase was much faster compared to the ε phase. The corresponding n parameter in the $x(t^{0.5})$ dependence was found to be 0.21 and 0.25 at 513 and 573 K, respectively. This means that the parabolic growth was not fulfilled. The reason for such a large deviation from $n = 0.5$ was attributed to the fact that a large part

of transport of Cu and Sn atoms to the phase boundaries, where the formation of the η phase took place, occurred through the grooves between the η crystallities. During annealing the grooves become narrower and their density is reduced by a process comparable to grain growth or Ostwald ripening. This reduced the diffusion process due to the increase in diffusion path length and reduction of concentration gradient, and also by the reduction of transport capacity of the grooves.

On the other hand, the parabolic growth law was valid for the growth of the $\varepsilon(Cu_3Sn)$ phase. The values of n were between 0.45 and 0.49 for a thin-foil Cu substrate and 0.48–0.49 for a Cu single crystal substrate. Therefore, Eq. (4) was used to calculate the integral interdiffusion coefficient. Here, for the specific case of the $\varepsilon(Cu_3Sn)$ phase it takes the following form:

$$D_{Cu_3Sn} = \frac{(N_{Cu_3Sn} - N''_{Cu}) \cdot (N'_{Cu_6Sn_5} - N_{Cu_3Sn})}{\Delta N_{Cu_3Sn} \cdot (N'_{Cu_6Sn_5} - N''_{Cu})} \cdot k_{pCu_3Sn}, \tag{13}$$

where N_{Cu_3Sn} is the average composition of the ε phase, N''_{Cu} is the saturation concentration of Sn in Cu ($N''_{Cu} = 0$), $N'_{Cu_6Sn_5}$ is the Sn concentration of the η phase in equilibrium with the ε phase and ΔN_{Cu_3Sn} is the homogeneity range of the ε phase.

Figure 8 shows the Arrhenius plot of the obtained integral interdiffusion coefficients. One can see that D_{int} of the thin-film specimens are approximately twice as large as those of the single-crystal specimens. The difference decreases with increasing temperature. The following explanation for such a behaviour was given by B a d e r, G u s t and H i e b e r [19]. Because of the small grain size in the thin-foil Cu substrate, the effective interdiffusion coefficient is the weighted average of the volume diffusion coefficient, D_v, and the grain boundary diffusion coefficient, D_b, according to Eq. (14):

$$D_{ef} = D_v + a(2\delta/d)D_b, \tag{14}$$

where d is the average grain size, δ is the thickness of the grain boundary and a is a shape constant ($a \approx 1$).

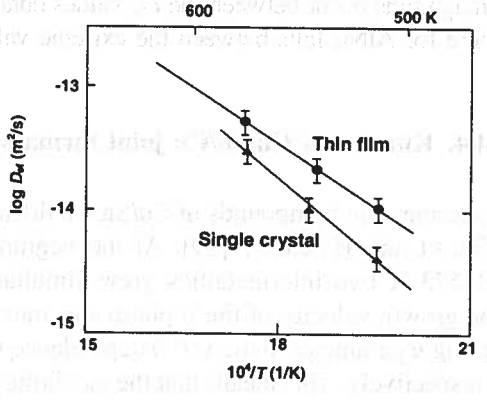

Fig. 8. Arrhenius plot of D_{ef} from thin-film and single-crystal experiments on Cu/Sn/Cu interconnections [19]

One can see that with decreasing grain size, D_{ef} increases considerably because $D_b >> D_v$. The activation energy, Q_{ef}, determined from the slope of the straight lines in Fig. 8 was found to be 66.1 and 81.6 kJ/mol for thin-film and single-crystal Cu substrate, respectively. The lower value Q_{ef} for the thin-film Cu substrate is associated with a reciprocal dependence of the effective diffusion coefficient on the grain size.

4.5. Kinetics of Cu/In/Cu joint formation

The growth kinetics of the intermetallics formed in the interconnection zone of Cu/In/Cu diffusion solders in the temperature range 180–430 °C was examined by Sommadossi, Gust and Mittemeijer [20]. The experimental results showed that the average n values were rather close to 0.5 in the $x(t^{0.5})$ relationship which confirmed that volume diffusion was the rate-controlling factor. In a consequence, it was possible to apply Eq. (4) for the calculation of the integral interdiffusion coefficients for the $\delta(Cu_7In_3)$ and $\eta(Cu_2In)$ phases:

$$\tilde{D}^{\delta}_{\text{int}} = \frac{(N_\delta - N_{Cu'})(N_{\eta''} - N_\delta)}{(N_{\eta''} - N_{Cu'})} k_{p\delta}, \tag{16}$$

$$\tilde{D}^{\eta}_{\text{int}} = \frac{(N_\eta - N_\delta)(N_{Cu_{11}In_9''} - N_\eta)}{(N_{\delta''} - N_{Cu_{11}In_9''})} k_{p\eta}. \tag{17}$$

The equilibrium concentration values were taken from the phase diagram. The $N_{Cu'}$ value was considered to be zero since the composition profiles showed no presence of In atoms in Cu at the Cu/IP interface.

The activation energies for $\eta(Cu_2In)$ and $\delta(Cu_7In_3)$ were found to be 100–110 kJ/mol (Fig. 9). Such low values may be ascribed to the presence of fast diffusion paths. It has also been suggested that a growing intermetallic phase may contain a relatively large amount of vacancies, which enhances substitutional diffusion. It is noted that the growth mechanism for the Cu_7In_3 phase was found to be independent of the reaction temperature being above or below 310 °C, which means independent of the presence or absence of $Cu_{11}In_9$.

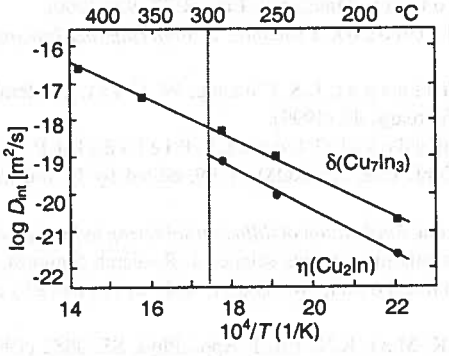

Fig. 9. Arrhenius plot of the integral interdiffusion coefficients for the Cu_2In and Cu_7In_3 phases existing in the Cu/In/Cu interconnection [20]

4.6. Kinetics of Cu/In–Sn eutectic alloy /Cu joint formation

The kinetics of the $\zeta(Cu_{10}(Sn,In)_3$ phase was investigated by S o m a d o s s i, G u s t and M i t t e m e i j e r [21]. The samples were annealed in the temperature range 220–400 °C. For all interconnections the n value was close to 1. This means the growth has a linear character and the growth-controlling process is the reaction at the phase boundary. Evidence of linear growth was also noticed for the Cu_6Sn_5 phase in Cu/Sn couples annealed at low temperatures ($T < 100$ °C) [22, 23]. On the other hand, the parabolic growth was observed at higher temperatures. There are two important advantages of linear growth from the diffusion soldering process point of view – faster formation of the intermetallic phase and shorter time needed to create a joint.

5. Concluding remarks

1. Diffusion soldering has a great potential for the fabrication of mechanically and thermally stable joints.
2. A detailed description of the successive formation and growth of the intermetallic phases within the interconnection zone of a Ni/Al/Ni joints is given.
3. The way of determining diffusion parameters is different from the procedure in conventional diffusion couples. An appropriate treatment is summarized here.
4. A comprehensive procedure leading to a suitable selection of the growth rate constant for the determination of the diffusion coefficients is presented.
5. Examples of kinetic calculations for the growth of intermetallic phases in the Al–Ni, Cu–Sn, Cu–In and Cu–In–Sn systems are presented.

REFERENCES

[1] N. Ch. L e e, Adv. Microelectr., September/October, 29 (1999).
[2] M. A b t e w, G. S e l v a d u r a y, Mater. Sci. Eng. R **27**, 95 (2000).
[3] G. H u m p s t e n, D.M. J a c o b s o n, *Principles of soldering and brazing*, ASM International, Materials Park, OH (1993).
[4] P.K. K h a n n a, S.K. B h a t n a g a r, L.S. C h a n g, W. G u s t, Z. Metallkd. **90**, 470 (1999).
[5] W.F. G a l e, J. Metals, February, 49 (1999).
[6] P.K. K h a n n a, S. S o m m a d o s s i, G. L o p e z, E. B i e l a ń s k a, P. Z i ę b a, L.S. C h a n g, W. G u s t, E.J. M i t t e m e i j e r, Conf. Proc., EUROMAT 99, edited by B. Jouffrey, J. Svejcar, **4**, Willey-VCH, Weinheim, 219 (2000).
[7] P. Z i ę b a, J. W o j e w o d a, *Application of diffusion soldering in lead-free interconnection technology*. In: Recent research developments in materials science 4, Research Signpost, Kerala, 261 (2003).
[8] G.A. L o p e z, S. S o m m a d o s s i, W. G u s t, E.J. M i t t e m e i j e r, P. Z i ę b a, Interface Sci. **10**, 13 (2002).
[9] C.Y. L i u, C. C h e n, A.K. M a i, K.N. T u, J. Appl. Phys. **85**, 3882 (1999).
[10] K.J. R ö n k ä, F.J.J. v a n L o o, J.K. K i v i l a h t i, Scripta Mater. **37**, 1575 (1997).
[11] H. O k a m o t o, J. Phase Equilibria **14**, 257 (1993).

[12] G. Lopez, P. Zięba, S. Sommadossi, W. Gust, E.J. Mittemeijer, Mater. Chem. Phys. **78**, 459 (2003).
[13] C. Wagner, Acta Metall. **17**, 99 (1969).
[14] B. Pieraggi, Oxid. Met. **27**, 177 (1987).
[15] M.M.P. Janssen, G.D. Rieck, Trans. AIME **239**, 1372 (1967).
[16] S. Shankar, L.L. Seigle, Metall. Trans. A **9**, 1467 (1978).
[17] S. Kim, Y.A. Chang, Metall. Mater. Trans. A **31**, 1519 (2000).
[18] S.P. Garg, G.B. Kale, R.V. Patil, T. Kundu, Intermetallics **7**, 901(1999).
[19] S. Bader, W. Gust, H. Hieber, Acta Metall. Mater. **43**, 329 (1995).
[20] S. Sommadossi, W. Gust, E.J. Mittemeijer, Mater. Sci. Techol. **19**, 528 (2003).
[21] S. Sommadossi, W. Gust, E.J. Mittemeijer, Mater. Chem. Phys. **77**, 924 (2002).
[22] N.K. Tu, R.D. Thompson, Acta Metall. **30**, 947 (1982).
[23] R.N. Chopra, M.N. Ohring, R.S. Oswald, Thin Solids Films **94**, 279 (1982).

Received: 1 March 2004.

A R C H I V E S O F M E T A L L U R G Y A N D M A T E R I A L S
Volume 49 2004 Issue 2

G.A. LÓPEZ *

FUNDAMENTALS OF DIFFUSION ALONG MOVING GRAIN BOUNDARIES

CHARAKTERYSTYKA PROCESÓW DYFUZJI NA MIGRUJĄCYCH GRANICACH ZIAREN

Diffusion along moving grain boundaries often controls the evolution of microstructure and the properties of engineering materials at elevated temperatures. The knowledge of the diffusion characteristics of moving grain boundaries and a deep fundamental understanding of this phenomenon are critical to many materials applications. Moving grain boundaries are involved in many solid-state phase transformations such as discontinuous precipitation, discontinuous coarsening, and discontinuous dissolution. All these reactions are characterized by a discontinuous (i.e. abrupt) change in the orientation and composition between the matrix phase in the reactant and the product aggregate across the migrating boundary (i.e. reaction front) that provides a short-circuit path of diffusion. The present review provides a comprehensive description of the above-mentioned reactions. A particular emphasis has been placed on the recent findings in case of the local approach in treating the growth kinetics of these reactions.

Dyfuzja na migrujących granicach ziaren jest często czynnikiem kontrolującym rozwój mikrostruktury a także własności materiałów konstrukcyjnych w podwyższonych temperaturach. Znajomość parametrów dyfuzji na migrujących granicach ziaren i dokładne zrozumienie tego zjawiska jest sprawą pierwszorzędnej wagi dla wielu zastosowań materiałowych. Migrujące granice ziaren biorą udział w wielu przemianach fazowych w stanie stałym takich jak: nieciągłe wydzielanie, nieciągłe pogrubianie, a także nieciągłe rozpuszczanie. Reakcje te charakteryzują się nieciągłą (skokową) zmianą orientacji i składu pomiędzy osnową fazy wyjściowej oraz osnową produktów reakcji w kierunku prostopadłym do frontu reakcji będącym kierunkiem dyfuzji. W pracy przedstawiono obszerny opis wspomnianych powyżej reakcji. Szczególny nacisk położono na wyniki ostatnich badań wykorzystujących lokalną koncepcję procesów dyfuzji do określenia kinetyki wzrostu.

1. Introduction

Diffusion along moving grain boundaries (GBs) can occur during a number of solid-state transformations, for example, in case of discontinuous precipitation, discon-

* INSTITUT FÜR METALLKUNDE DER UNIVERSITÄT STUTTGART, HEISENBERG – STR. 3, D-70569 STUTTGART, GERMANY

tinuous coarsening, and discontinuous dissolution. These phase transformations change the microstructure and properties of engineering materials at elevated temperature. The knowledge of the diffusion characteristics of moving GBs and a deep fundamental understanding of this phenomenon are critical to many materials applications.

The determination of the grain boundary diffusivity from studies on the growth kinetics of these reactions offers an alternative route of diffusion measurements, especially in systems and/or at temperatures where radiotracer data are not available.

2. Discontinuous precipitation (DP)

Discontinuous precipitation is a solid-state reaction in which a supersaturated solid solution α_0 of composition x_0 is decomposed in a typically lamellar two-phase microstructure $\alpha + \beta$ behind a moving reaction front (RF):

$$\alpha_0 \quad \alpha + \beta, \tag{1}$$

where α is the depleted solid solution and β is the precipitate phase. β can be an intermetallic compound or a solid solution, depending on the phase diagram of the alloy under investigation. In this reaction, the crystal structure of the solute-depleted phase remains the same as the parent phase. A discontinuous change in both the crystal orientation and the solute concentration of the parent phase across the moving RF characterizes this kind of reaction. The supersaturation of the starting solid solution is achieved when a sample is quenched from the homogenisation temperature T_H to the reaction temperature T_R (Fig. 1).

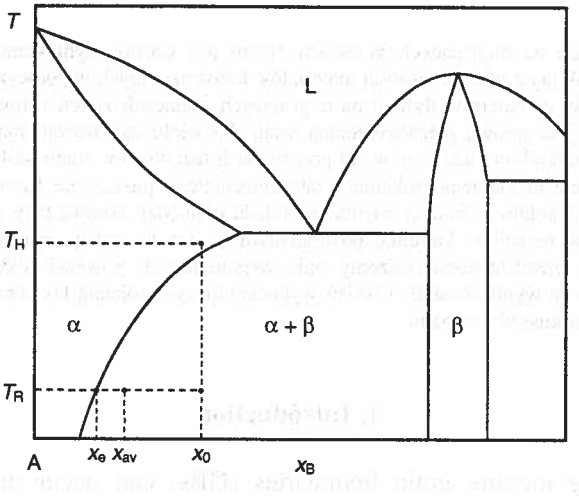

Fig. 1. Schematic illustration of the *A*-rich side of the phase diagram of a binary system *A* – *B*. x_0, x_{av}, x_e – concentration of the homogeneous initial solid solution, α-lamella formed by DP, and α-phase in case of equilibrium, respectively; L – liquid

The DP reaction starts at a high-angle GB and is occurring along the RF, transporting the excess solute atoms from the centre of the α-lamella to the neighbouring β-lamellae. Upon annealing at certain temperature in the two-phase region of the equilibrium phase diagram, after nucleation at the original grain boundary (Fig. 2) and a non-regular period of growth, a steady-state stage of growth takes place with a constant reaction front velocity v_{av}. The growth kinetics can be described by the P e t e r m a n n – H o r n b o g e n equation [1, 2]:

$$s\delta\tilde{D}_b = \frac{RT}{-8\Delta G} v_{av}\lambda^2_{\alpha,av} \cong \frac{RT}{-8\Delta G} v_{av}\lambda^2_{av}, \tag{2}$$

where s is the segregation factor, δ is the GB width, $\tilde{D}_b$ is the chemical GB diffusion coefficient, v_{av} is the (globally averaged) velocity of the RF, $\lambda_{\alpha,av}$ is the (averaged) width of the α-lamellae, λ_{av} is the (averaged) interlamellar spacing, ΔG is the change in G i b b s energy (driving force) upon DP, T is the absolute temperature, and R is the gas constant.

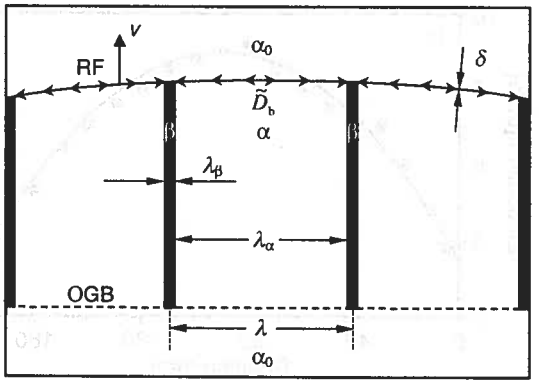

Fig. 2. Schematic diagram illustrating the DP reaction. v – migration velocity; δ – GB width; $\tilde{D}_b$ chemical GB diffusion coefficient; λ – interlamellar spacing; λ_α, λ_β – width of the α- and β- lamellae, respectively; OGB – original grain boundary [1]

A transmission electron microscopy (TEM) image of the DP reaction can be seen in Fig. 3a. Figure 3b shows the solute concentration profile just behind the RF. The experimental data points were fitted to the solution of C a h n ' s [4] diffusion equation using a non-linear regression least-square method:

$$x(y) = (x_e - x_0)\frac{\cosh(\sqrt{C}(y - 0.5))}{\cosh(\sqrt{C}/2)} + x_0. \tag{3}$$

x_0 is the solute content in the homogeneous alloy, x_e is the solute content in an α-lamella in contact with the β-lamella (i.e., there is local equilibrium at the α/β interface), y is a normalized

co-ordinate measured from the edge of the β-lamella and running perpendicular to the α-lamella. In this model a more rigorous treatment of the diffusion process along the moving RF was applied in comparison with the P e t e r m a n n – H o r n b o g e n model.

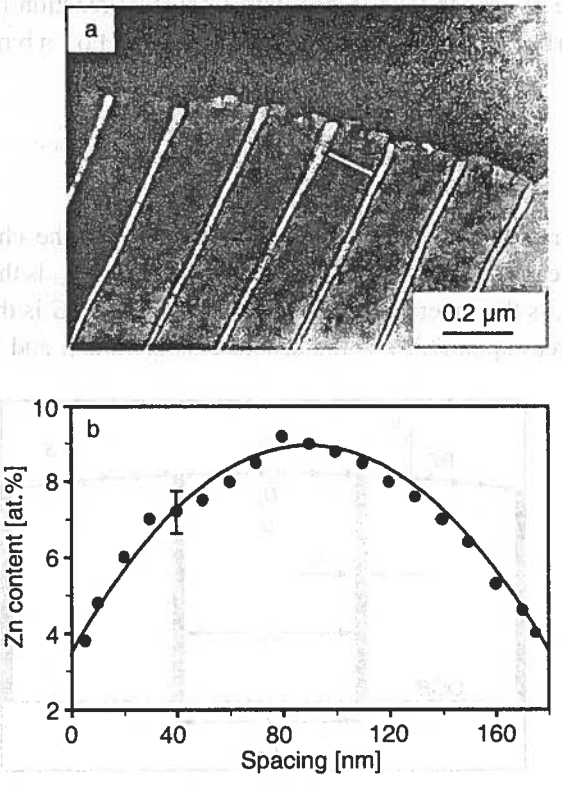

Fig. 3. TEM image showing DP in an Al – 22 at.% Zn alloy aged at 450 K for 10 min (a) and an example of the Zn concentration profile taken across an α-lamella just behind the RF as indicated on the image (b). The error of energy-dispersive X-ray spectral analysis is indicated by an error bar [3]

The dimensionless C a h n parameter C is expressed by:

$$C = \frac{v\lambda_\alpha^2}{s\delta\tilde{D}_b} \quad \text{or} \quad s\delta\tilde{D}_b = \frac{v\lambda_\alpha^2}{C}. \tag{4}$$

The solid line in Fig. 3b represents the best fit of Eq. (3) to the experimental data, and provides values of the parameters C and x_e. Then it is possible to determine the diffusivity at the moving RF via Eq. (4). The $s\delta\tilde{D}_b$ values are shown in Fig. 4 in form of an Arrhenius diagram. These data were calculated on the basis of the *local approach* to the growth kinetics of the DP reaction (for details, see Ref. [6]). Here, an individual concentration

profile – as shown in Fig. 3b – and the corresponding individual values of v and λ_α for the particular lamella are used for the calculation of the $s\delta\tilde{D}_b$ values.

Figure 4 contains also data obtained by applying the *global approach*, which is relevant not for a single cell, but for the whole population of the DP colonies in a sample. In this approach, average values for the growth velocity v and the interlamellar spacing λ are employed. The data reported by A b d o u et al. [5] were obtained applying Eq. (2) and using the *global approach*, while the data by Z i ę b a et al. [3] were calculated by using Eq. (4) and *the local approach*. In addition, values for the radiotracer diffusivity ($s\delta D_b^*$) of stationary GBs for various Al – Zn solid solutions provided by H ä s s n e r [7] are given for comparison. It can be seen that the diffusivity data for moving and stationary GBs are of the same order of magnitude. It should be emphasized that the data points (•) for the *local approach* – five or three values at each temperature – belong to five and three individual GBs, respectively. Therefore, the "scatter" of the data reflects the real differences in the diffusion behaviour of the individual GBs used for the determination of the data.

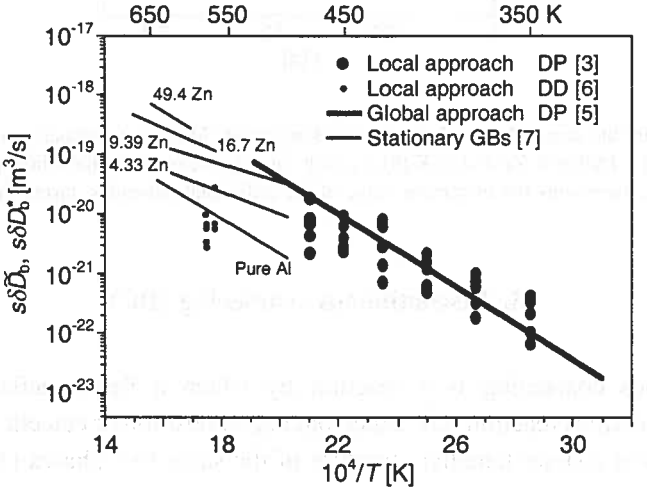

Fig. 4. A r r h e n i u s diagram for the chemical diffusivity ($s\delta\tilde{D}_b$) of the moving RF of the DP [3, 5] and DD [6] reactions in an Al – 22 at.% Zn alloy. The Zn radiotracer diffusivities ($s\delta D_b^*$) for stationary GBs of several Al – Zn alloys [7] are shown for comparison. After Z i ę b a et al. [3, 6]

Finally, in case of DP in Al – 15.0 at.% Zn it has been clearly demonstrated by *in-situ* observations in a high-voltage transmission electron microscope that the RF migration occurs in a stop-and-go fashion (Fig. 5). Consequently, there is a drastic difference between the average velocity and the instantaneous velocity. The only quantity, which can be determined in traditional experiments, is the average velocity to which the P e t e r m a n n – H o r n b o g e n equation [Eq. (2)] is adequate. It is the advantage of the *local approach* to the growth kinetics of the DP reaction that the instantaneous velocity and the relevant individual interlamellar spacing are used for the determination of consistent $s\delta\tilde{D}_b$ data applying the more rigorous C a h n model.

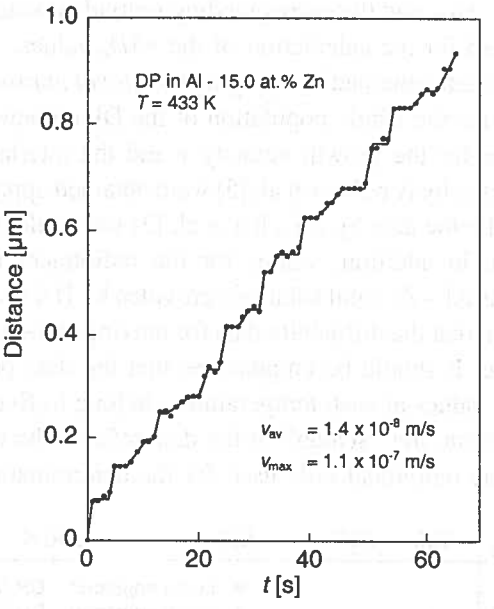

Fig. 5. An example for the stop-and-go fashion of the GB migration: Migration distance as a function of the aging time, t, for DP in Al – 15.0 at.% Zn at 433 K [8]. v_{av} is the average velocity for the whole period of time (66 s), whereas v_{max} represents the maximum value of the individual velocities during the go-periods

3. Discontinuous coarsening (DC)

Discontinuous coarsening is a reaction by which a fine-lamellar microstructure produced by a previous reaction (DP, eutectoid decomposition or eutectic solidification) is transformed into a coarser lamellar structure of the same two phases [1]:

$$(\alpha + \beta)_{\text{fine}} \quad (\alpha + \beta)_{\text{coarse}}. \tag{5}$$

A schematic diagram and an optical micrograph presented in Figs. 6 and 7 illustrate this reaction. Morphologically, this reaction too is characterized by a sharp migrating RF, which separates the coarse-lamellar reaction product from the fine-lamellar initial state. There is a discontinuous change in both the interlamellar spacing and the orientation of the α-phase across the RF. The DC reaction proceeds at a much lower rate (v_2) and has a much larger interlamellar spacing (λ_2) than the preceding reaction.

$$v_2 \approx 10^{-1} \ldots 10^{-2}\, v_1, \tag{6a}$$

$$\lambda \approx 3 \ldots 8\lambda_1. \tag{6b}$$

Further, the mean composition of the α-lamella is closer to the equilibrium value than in the first reaction. In absence of any competing reactions (spheroidization of the fine-lamellar structure or depletion of the lamellae of excess solute by volume diffusion) the growth rate and interlamellar spacing of the DC reaction remain constant during isothermal growth.

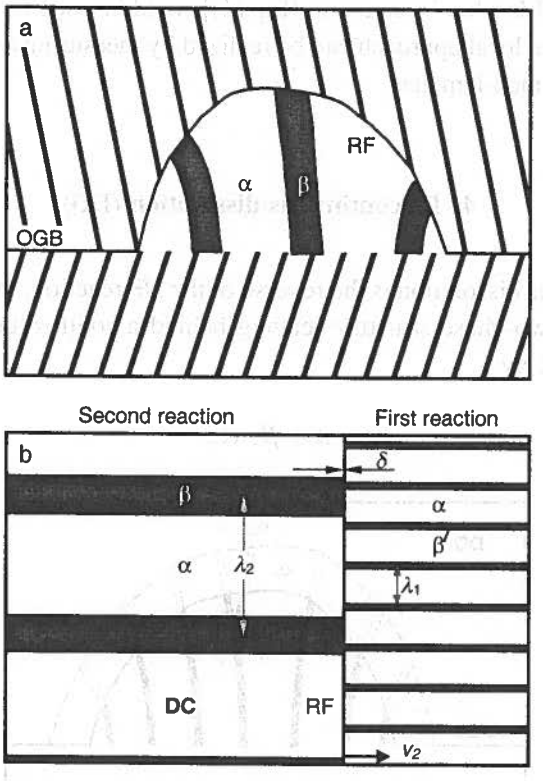

Fig. 6. Schematic diagram illustrating the DC reaction. (a) DC cell and (b) situation at the RF

Fig. 7. Light microscopy (LM) image of DC cells in Ni – 8 at.% Sn aged at 1023 for 806 h [9]

The GB diffusivity at the RF of a DC cell can be described analogous to Eq. (2) by

$$s\delta\tilde{D}_b = \frac{RT}{-8\Delta G_2} v_{2,av}\lambda_{2,av}^2, \quad (7)$$

where the change in G i b b s energy, ΔG_2, driving this reaction is given by the sum of two contributions, namely, a chemical contribution and an interfacial contribution. Also a modified version of C a h n ' s equation [Eq. (4)] could be used for the determination of the $s\delta\tilde{D}_b$ values, if the local approach can be realized by measuring a concentration profile across the newly formed lamellae.

4. Discontinuous dissolution (DD)

The discontinuous dissolution is the reverse of the DP reaction, in that the RF migrates backward into the two-phase structure leaving behind a solid solution α_- (Fig. 8). The reaction is described by

$$\alpha + \beta \quad \alpha_- \quad (8)$$

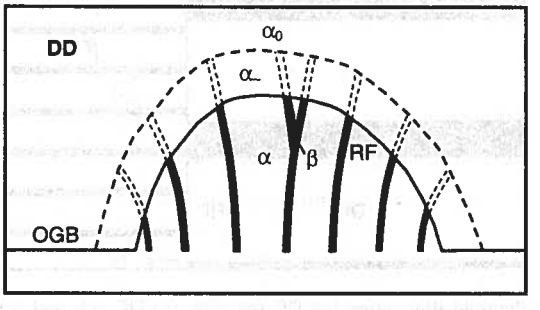

Fig. 8. Schematic diagram illustrating the DD reaction

The resulting solid solution α_- is not homogeneous, but shows remaining concentration fluctuations which are visible through the original lamellar structure as "ghost" images formed by very strong etching (Fig. 9). Thus, a lamellar structure formed by DP would – upon heating in the vicinity of the solvus temperature – start exhibiting DD.

The kinetics of the DD reaction can be described by the P e t e r m a n n – H o r n - b o g e n equation [Eq. (2)] or by a modified form of C a h n ' s equation [Eq. (4)]. $s\delta\tilde{D}_b$ values for moving GBs from DD studies for Al – 22 at.% Zn are included in Fig. 4. Again it should be emphasized that the "scatter" of the $s\delta\tilde{D}_b$ data is reflecting the differences in GB diffusivity of the individual GBs used in the *local approach*. These results support the view that diffusion along migrating GBs is not much faster, but of the same order of magnitude as along stationary GBs. This is so in spite of the fact that the migration velocities during DD

(v_{DD}) are much larger (due to higher temperature at which it occurs) than in the case of DP reaction (v_{DP}):

$$v_{DD} \approx 10^2 \, v_{DP} . \tag{9}$$

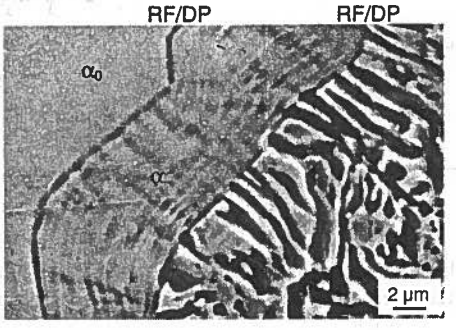

Fig. 9. Scanning electron microscopy (SEM) image of the DD reaction in Fe – 13.5 at.% Zn after aging: first DP at 723 K for 44 h, then DD at 886 K for 28 min [10]. The "ghost lines" at the former positions of the dissolved α-lamellae can clearly be seen. Also the stop-and-go fashion of the RF movement during DD can be seen by a second set of "ghost lines" parallel to the RF

5. Practical significance

5.1. Discontinuous precipitation

In general, negative property changes result from the occurrence of the DP reaction in commercial alloys. However, this reaction can also be utilized positively for commercial needs in the case of grain refinement.

A Pb – 0.11 Sr – 0.80 Sn – 0.023 Al (wt.%) alloy is used for the manufacture of auto batteries. As Pb has only a very slight solubility for Sr at room temperature (0.01 wt.% Sr), the Sr content of 0.11 wt.% causes a large agehardening effect by continuous precipitation (CP), i.e., formation of very small coherent particles in a volume diffusion-controlled process. The as-cast alloy has a macrohardness of 9.0 kp/mm^2 (Fig. 10). After casting the alloy age-hardens rapidly at 298 K to a peak hardness of 19.5 kp/mm^2 after about 2 days. Then the structure and the hardness of the alloy remain constant at room temperature for a period of several days. But after about 5 days, small colonies of DP are observed to have nucleated at several of the GBs. After a period of about 3 months, these cells replace the entire as-cast grain structure and soften the alloy to 12 kp/mm^2. This is bad for the automotive production of car batteries, which requires a minimum hardness of about 15 kp/mm^2 because otherwise the component parts distort under their own weight and block or clog up the automotive assembly machines.

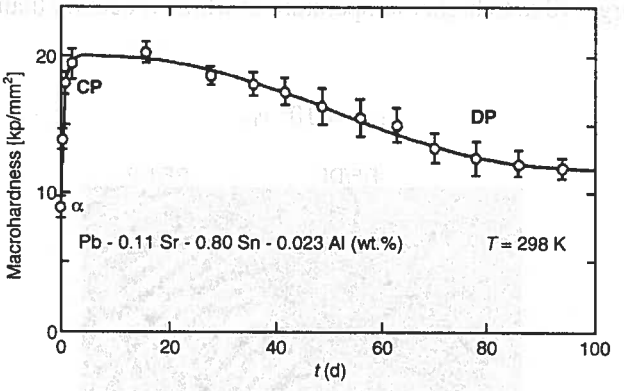

Fig. 10. Macrohardness of car battery material as a function of the aging time at 298 K [11]. α – microstructure of the as-cast material; CP – continuous precipitation

A Pt – 10 wt.% Au alloy is used for spinning jets in the reyon industry. Corresponding to the miscibility gap of the Pt – Au system, the homogenized alloy (α_0) decomposes during annealing at 873 K into an Au-rich solid solution with 20 wt.% Pt and a Pt-rich solid solution with 5 wt.% Au. The decomposition process occurs by CP. It drastically increases the hardness from 150 kp/mm^2 to over 300 kp/mm^2 (Fig. 11). However, this material has the disadvantage that after a long time at operating temperature DP occurs, which decreases the hardness with increasing time. The final value of 130 kp/mm^2 is even lower than the hardness of the initial solid solution α_0. This happens faster in a H_2 atmosphere than in air at 873 K.

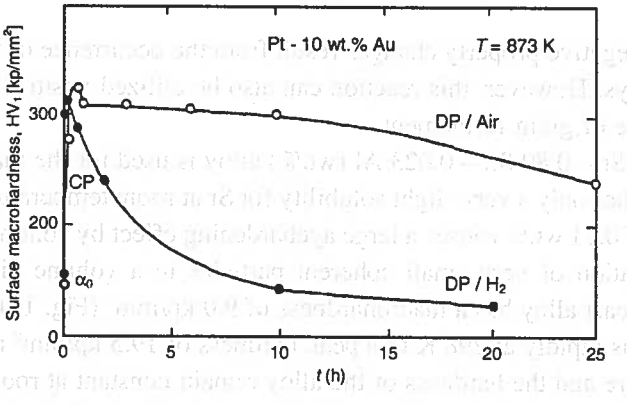

Fig. 11. Surface macrohardness determined with a Vickers instrument (1kg load) as a function of the aging time at 873 K. α_0 – homogeneous solid solution; CP – continuous precipitation; DP – discontinuous precipitation [11]

Mg – Al alloys, for example, also exhibit positive changes in mechanical properties. DP in a Mg – 11 at.% Al alloy increases the hardness by more than 70% over the original hardness of the homogeneous solid solution [12].

Positive changes can also be attained by DP in the case of grain refinement in Ni – Sn alloys, resulting from thermal cycling. A homogenized Ni – 8 at.% Sn alloy has an average grain size of 1 – 2 mm. After a special thermal cycling (first DP: 20 h at 874 K, then continuous dissolution: 2 min at 1143), the grain size is reduced to 10 – 20 μm. Thus, by this simple heat treatment cycle the average grain diameter is reduced by a factor of about 100. By the use of several heat treatment cycles an ultrafine grain size (1 μm !) can be established [11].

5.2. Discontinuous coarsening and dissolution

Discontinuous coarsening can degrade the properties of alloys such as aligned composites, which rely on the stability of their fine-lamellar structures for their application. The aligned composites may be formed by eutectoid decomposition, eutectic solidification or DP, which may find applications as high-temperature creep-resistant materials. Discontinuous coarsening could destroy the creep resistance of this type of material at the operating temperatures.

After discontinuous dissolution the material is indeed single phase, however, strong concentration fluctuations presumably exist, which become visible only through strong etching and are, therefore, easy to overlook. They can only be eliminated by long-time annealing because the homogenization process is controlled by volume diffusion.

6. Summary and concluding remarks

A general overview of discontinuous reactions was presented. All these reactions are controlled by grain boundary diffusion. A careful study of the reaction kinetics offers an alternative route of grain boundary diffusivity determination, especially in systems and/or at temperatures where radiotracer data are not available. The diffusivity values of moving grain boundaries are of the same order of magnitude as those of stationary grain boundaries. The use of the *local approach* to analyse the growth kinetics has the advantage to get $s\delta\tilde{D}_b$ values for individual GBs.

This group of reactions can have a critical influence on the properties of practical materials. Mostly the effects are deleterious, but in some cases this kind of reactions can be usefully employed. In general, it can be said that a good understanding of these reactions help in solving several practical problems.

REFERENCES

[1] I. Kaur, Y. Mishin, W. Gust, *Fundamentals of Grain and Interphase Boundary Diffusion*, 303, John Wiley & Sons, Chichester, 1995.

[2] J. Petermann, E. Hornbogen, Z. Metallkd. **59**, 814 (1968).

[3] P. Zięba, A. Pawlowski, W. Gust, Defect Diff. Forum **194-199**, 1759 (2001).
[4] J. W. Cahn, Acta Metall. **7**, 18 (1959).
[5] S. Abdou, M. El-Boragy, W. Gust, B. Predel, in: *Phase Transformations*, edited by G. W. Lorimer (The Institute of Metals, London, 1988), p. 231.
[6] P. Zięba, W. Gust, Scripta Mater. **39**, 13 (1998).
[7] A. Hässner, Kristall und Technik **9**, 1371 (1974).
[8] S. Abdou, G. Solorzano, M. El-Boragy, W. Gust, B. Predel, Scripta Mater. **34**, 1431 (1996).
[9] U. Klisa, Ph. D. Thesis, University of Münster (1980).
[10] T. –H. Chuang, R. A. Fournelle, W. Gust, B. Predel, Z. Metallkd. **80**, 318 (1989).
[11] T. –H. Chuang, W. Gust, A. Fournelle, in: *Engineering and Science Materials*, edited by A. Blass, **7**, Floreanópolis, Santa Catarina 1986.
[12] M. Frebel, K. Behler, B. Predel, Z. Metallkd. **67**, 228 (1976).

Received: 1 March 2004.

ARCHIVES OF METALLURGY AND MATERIALS
Volume 49 2004 Issue 2

S.V. DIVINSKI *, CHR. HERZIG*

SOLUTE SEGREGATION STUDIED BY GRAIN BOUNDARY DIFFUSION

DYFUZJA GRANIC ZIAREN-BADANIA SEGREGACJI DODATKÓW STOPOWYCH

Radiotracer grain boundary (GB) diffusion measurements have established themselves as an impressive and powerful tool for studying GB segregation. The key point here is the combination of GB diffusion experiments in so-called *B* and *C* kinetic regimes, in which the triple product $P = s \cdot \delta \cdot D_{gb}$ and the GB diffusivity D_{gb} respectively are accessible. Here s is the segregation coefficient and δ the GB width. Using the value of δ established from GB self-diffusion measurements, the segregation factor s is determined as: $s = P/\delta D_{gb}$. Appyling a solute-radiosotope with a well-defined specific activity the absolute amount of the solute in a GB can be estimated as a function of the penetration depth. Typical radiotracer experiments on a polycrystalline material were shown to correspond to the truly dilute limit of solute segregation. This approach has successfully been applied for several solutes in Ag and Cu matrixes and the systematics of GB diffusion and segregation in the these systems is reported. The amount of solute atoms in a GB can be increased by performing diffusion experiment on bicrystals and alloyed polycrystals. This allows us the quantitative study of non-linear solute segregation. In suitable cases, even a segregation isotherm can be derived, as it is demonstrated e.g. for Ag GB segregation in Cu.

Pomiary dyfuzji granic ziaren (GB) metodą atomów znaczonych stały się doskonałym narzędziem w badaniach segregacji na granicy ziaren. Kluczowym elementem jest połączenie eksperymentów dyfuzji GB w tzw. reżimie kinetycznym *B* i *C*, w których można wyznaczyć zarówno iloczyn $P = s\delta D_{gb}$ jak i dyfuzyjność granic ziaren, D_{gb}, gdzie s jest współczynnikiem segregacji, a δ jest szerokością granicy. Wykorzystując wartość δ wyznaczoną w pomiarach samodyfuzji granic ziaren, współczynnik segregacji s jest wyznaczany z zależności: $s = P/\delta D_{gb}$. Stosując izotop dodatku stopowego o ściśle określonej aktywności, można wyznaczyć bezwzględną zawartość tego dodatku rozpuszczonego w granicy, jako funkcję głębokości penetracji. Metodę tę z powodzeniem zastosowano dla szeregu dodatków stopowych rozpuszczonych w osnowach Ag i Cu i wyniki przedstawione w pracy dotyczą zarówno systematycznych badań dyfuzji GB jak i segregacji w tych układach. Liczba atomów dodatku stopowego w GB wzrasta, gdy dyfuzja zachodzi w bikryształach i polikryształach stopowych. Wtedy też możliwe jest ilościowe badanie nieliniowej segregacji dodatku stopowego. W sprzyjających warunkach nawet można wyznaczyć izotermę segregacji, jak to przedstawiono przykładowo dla segregacji srebra w granicy ziaren w miedzi.

* INSTITUT FÜR MATERIALPHYSIK. UNIVERSITÄT MÜNSTER. WILHELM-KLEMM-STR. 10, D-48149 MÜNSTER, GERMANY

1. Introduction

Segregation of impurities to internal interfaces plays an important role in material behavior. Impurity enrichment at grain boundaries (GB) often results in detrimental effects on the material properties: liquid and temper embrittlement, Cobble creep, GB decohesion, etc. [1]. The quantitative characteristics of GB segregation are typically determined by Auger electron spectroscopy [2, 3, 4, 5]. In this case a polycrystalline sample usually has to be fractured *in situ* along a GB and the solute enrichment on the fractured surface is studied. This procedure limits the application of the method to brittle materials, as e.g. to Fe or Fe alloys (see e.g. [2, 6, 7]) or to such solutes which induce embrittlement of the matrix [8]. This technique unfortunately cannot be applied to ductile materials *e.g.* Cu. Furthermore, the sensitivity of the Auger techniques is limited and a considerable fraction of a monolayer of segregated solute is required for detection.

As an indirect method GB diffusion experiments elaborated themselves to a sensitive and unique tool for studying GB segregation [1, 9]. Solute segregation changes the interfacial energy. Applying Borisov's relation [10] one can estimate solute segregation by specially designed self- and solute GB diffusion study [1, 11].

However, GB segregation can be determined in a straightforward manner by combining solute GB diffusion experiments in Harrison's *B* and *C* regimes [12]. One of the authors (C.H.) has followed this approach in a series of systematic experiments in Ag and Cu during the last decade. We present in this paper the cumulative results with emphasis on some perspectives. The segregation behavior and especially the appearance of non-linear segregation of solutes, which can be derived and quantified by GB diffusion experiments, will be highlighted.

2. Fundamentals of GB diffusion

2.1. *B* kinetic regime of GB diffusion

Typical GB diffusion experiments are usually performed in Harrison's *B* regime [13, 14]. This regime corresponds to relatively high temperatures of diffusion anneal, when the bulk diffusion length, $\sqrt{D_v t}$, is much larger than the GB width δ: $s \cdot \delta / 2\sqrt{D_v t} \ll 1$ [12]. Here s is the solute segregation factor, D_v the bulk diffusivity, and t the diffusion time. Then the so-called triple product P can only be determined from the experimental solute penetration profiles, $P = s \cdot \delta \cdot D_{gb}$, with D_{gb} being the GB diffusivity.

The segregation factor s, which enters into the GB diffusion problem in this kinetic regime by the outdiffusion process of the solute from the GB into the adjacent bulk, is defined as the ratio of the solute concentration in the GB, c_{gb}, and in the bulk $c_v(0)$ just near the GB:

$$s = \frac{c_{gb}}{c_v(0)}. \tag{1}$$

One can immediately recognize that this definition is formally different from the definition of the solute enrichment factor b, which can be derived from e.g. the Auger spectroscopy study. The latter value is determined as a ratio of solute GB excess (per meter squared) to the bulk solute concentration [2]. These differences in definition introduce apparent quantitative differences in the results. This delicate problem has recently been treated in detail [15]. Both factors are linked by the relation $s = b \cdot c_{gb}^0$ where c_{gb}^0 is the solute concentration per monolayer of a GB at the saturation level of segregation. Only if c_{gb}^0 equals unity, s and b are numerically equal.

The determination of the triple product P from GB diffusion penetration profiles assumes that the segregation factor s, introduced by Eq. (1), does not change along the corresponding (deepest) part of the penetration profile. This means that the tracer concentrations c_{gb} and $c_v(0)$ have to be sufficiently small to satisfy the dilute limit conditions when solute GB diffusion is studied in a pure metal. By applying solute-radiotracers with a well-defined specific activity, the absolute concentrations of tracer atoms in GBs of polycrystalline material, c_{gb}, can be calculated from the measured specific radiotracer activity of the layer sections along the GB diffusion profiles. Figure 1 represents examples of such penetration profiles, which were measured for Ag GB diffusion in polycrystalline Cu [15]. The GB solute concentration is orders of magnitude lower than unity at the penetration profile depth where the GB diffusivity P was evaluated. As a result, linear solute segregation is to be expected. In the particular case of Ag GB diffusion in polycrystalline Cu the curvature of the B-regime penetration profiles (see Fig. 1) was unambiguously shown [9, 15, 16] to results from a small migration of some of the Cu GBs during diffusion anneal, despite of a careful preannealing treatment of the samples.

Therefore, the measurements in the B regime yield the products $s \cdot D_{gb}$ (supposing that the GB width δ is known, see below) but not these values separately. Since the segregation factor s varies remarkably with temperature and can be very large (see below), no definite information about the GB diffusivity D_{gb} itself is obtained from the P values measured in the B-regime kinetics.

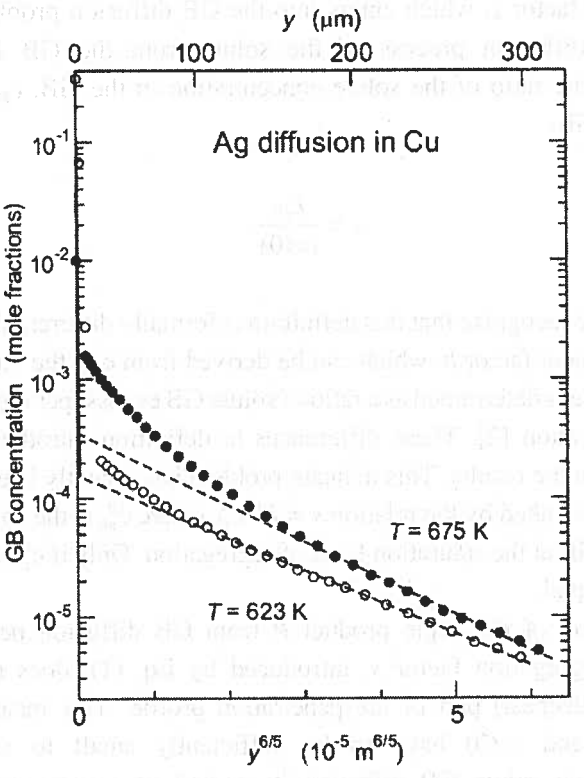

Fig. 1. Penetration profiles of Ag GB diffusion in polycrystalline Cu. The ordinate is recalculated to absolute GB concentrations (in mole fractions, see text). The dashed lines represent corresponding ideal GB diffusion penetration profiles

2.2. *C* regime of GB diffusion

At relatively low temperatures bulk diffusion is suppressed, $s \cdot \delta / 2\sqrt{D_v t} > 1$, and the tracer is exclusively concentrated in the GBs. These conditions correspond to the *C* regime and the GB diffusivity D_{gb} can directly be determined from the corresponding penetration profiles. The type *C* measurements require extremely high sensitivity of the counting facilities and the use of radiotracer with a high specific activity due to the relatively small number of short-circuit diffusion paths (GBs) in well-annealed polycrystalline material.

2.3. Determination of the segregation factor *s*

Investigation of solute GB diffusion presents an elegant way to determine equilibrium segregation characteristics in the dilute (Henry type) limit by GB diffusion measurements in *B* and *C* regimes in the same material. This aproach has already been successfully applied to several Cu- and Ag-based systems, see *e.g.* [15, 17, 18, 19, 20]. Measuring the triple product $P = s \cdot \delta \cdot D_{gb}$ in the *B* regime and determining the GB diffusivity D_{gb} directly under the *C* regime conditions, the segregation factor *s* is evaluated by:

$$s = \frac{P}{\delta \cdot D_{gb}}. \tag{2}$$

Usually the P values are extrapolated to the lower temperatures of the C-type measurements of D_{gb} [18]. Consequently the segregation enthalpy H_s therefore is obtained as the difference of the activation enthalpies of the B and C regime data: $H_s = Q_{gb} - H_{gb}$, where H_{gb} is the activation enthalpy of GB diffusion $D_{gb}(T)$. This method is illustratet in Fig. 2 for the case of Ag GB diffusion in high-purity Cu [15]. The average value of GB width δ is to be known. It can be separately determined by performing the GB *self-diffusion* measurements in types B- and C-regimes, where the relevant segregation factor is unity. Such experiments yielded $\delta \simeq 5 \cdot 10^{-10}$ m in fine-grained NiO [21], pure Ag [22, 23], and very recently in nanocrystalline Fe–Ni alloy for diffusion of both Fe and Ni [24, 25, 26].

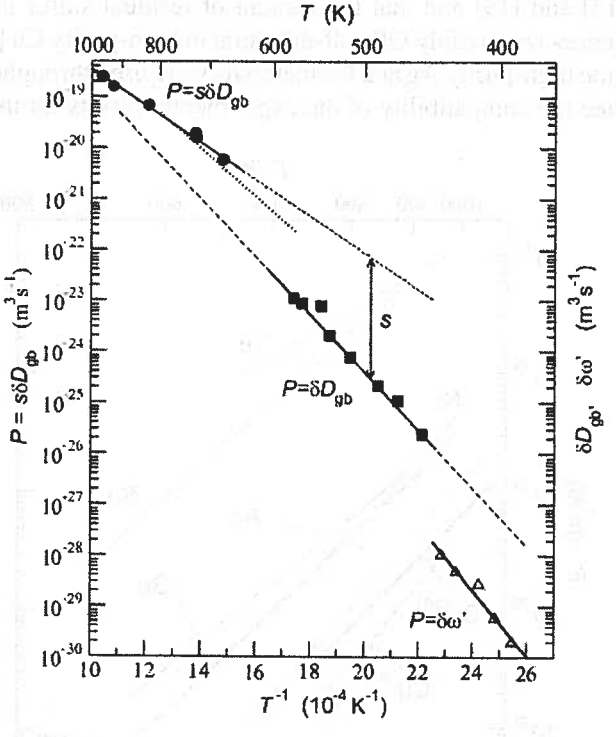

Fig. 2. Arrhenius plot of GB diffusion parameters for Ag in Cu measured in the B ($P = s\delta D_{gb}$ [15] (circles) and [33] (dotted line) and C ($P = \delta D_{gb}$ [15] (squares) and $P = \delta\omega'$ [29] (triangles)) regimes. The determination of the segregation factor s is schematically shown

3. GB diffusion and segregation in pure Cu and Ag

In Fig. 3. the data of P in Cu and Ag matrices are collected for those solutes, for which s and D_{gb} were determined separately (see below). Excluding Te and Se in Ag, the other solutes

(Ge, Ni, Ag, Au) show P values similar to those for self-diffusion in the corresponding matrix. Thus, it is of fundamental importance to determine separately s and D_{gb} in thermodynamical equilibrium conditions. The results of the directly measured GB diffusivities D_{gb} and the resulting solute segregation factors in Cu and Ag matrices are presented in Figs. 4 and 5, respectively. Depending on the solute-matrix combination the measured segregation factors vary from about 2 to 10^5, Fig. 5. Although the triple products P of solute diffusion are generally larger than those of self-diffusion, Fig. 3, smaller D_{gb} values are typically observed in comparison with self – diffusion, Fig. 4. The most pronounced retardation in solute diffusivity was observed for Ni GB diffusion in Ag, which was explained by the segregation of Ni atoms not directly in the GB core, but to the adjacent lattice plane(s) [17, 27]. We note that from all so far investigated solutes only Ni reveals a surface tension superior to that of the matrix element Ag or Cu. When inspecting Figs. 3 and 4 one has to take into account that Cu material of two different purity levels were investigated in [15] and [19] and that the content of residual sulfur impurity already on a ppm-level influences remarkably GB self-diffusion in high-purity Cu [28]. It is important to note that the same high-purity Ag and Cu materials were used throughout our segregation studies to guarantee the compatibility of the experimental results for the different solutes.

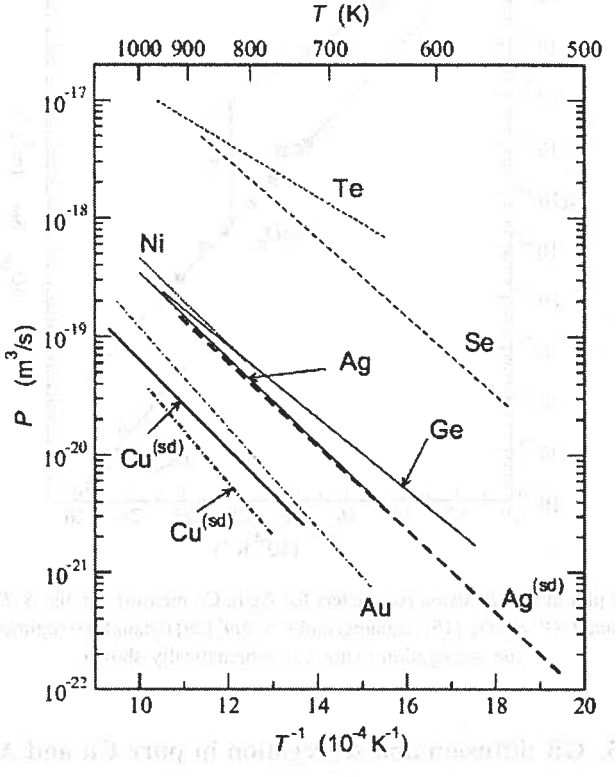

Fig. 3. Arrhenius plot of the product P of self- [23, 28] and solute diffusion in Ag (Ni [17], Te [18], and Se [17], dashed lines) and Cu of two purity levels, 5N (Au [19], dashed-dotted lines) and 5N8 (Ag [15] and Ge [20], solid lines). Self-diffusion data (superindex'sd') are presented by thick lines

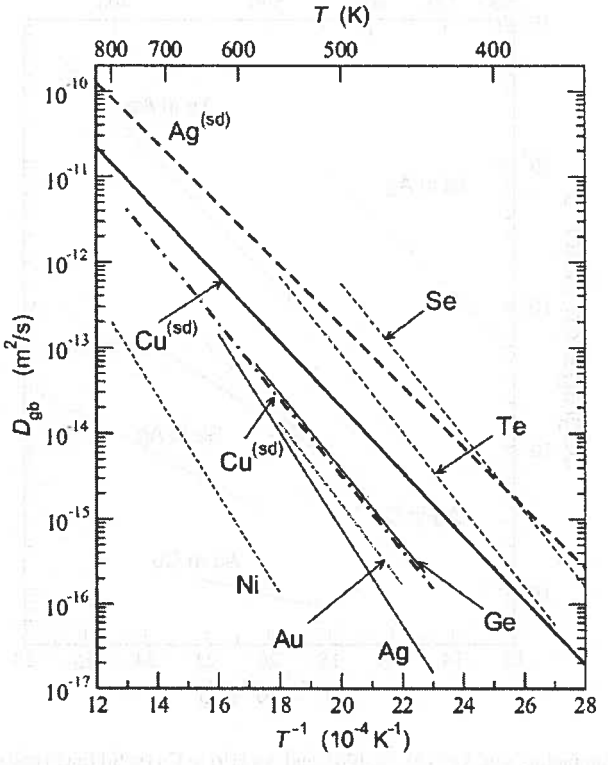

Fig. 4. Arrhenius plot of directly measured GB diffusivities D_{gb} of Ag [15] and Ge [20] in 5N8 Cu (solid lines), Au [19] in 5N Cu (dashed-dotted line) and of Ni [17], Te [18], and Se [17] in Ag (dashed lines). The self-diffusivities of the corresponding matrices (superindex'sd') are also presented by the thick lines

Recently the Hwang - Balluffi method was successfully applied to study Ag GB diffusion in Cu in the *C* regime conditions [29]. This perameation method does not yield the GB diffusivity D_{gb} but the product $\omega' = s \cdot \delta \cdot D_{gb}/s_s \cdot \delta_s$, where δ_s is the width of the segregated layer at the Cu surface and s_s is the relevant surface segregation factor [29]. The comparison with the results of the *B*-type measurements of $P = s \cdot \delta \cdot D_{gb}$ yielded a *surface* segregation enthalpy of about -34 kJ/mol [29]. Unfortunately, one cannot extract the GB segregation factor and the corresponding segregation enthalpy from such measurements.

On the other hand the Ag GB diffusivity D_{gb} in Cu was directly measured by us in Ref. [15]. The activation enthalpy H_s of Ag GB segregation in Cu was determined to be -39.5 kJ/mol. The results of the two investigations are compared in Fig. 2. The values of $\delta\omega'$ are systematically smaller than δD_{gb} by about two orders of magnitude, although the corresponding activation enthalpies are fairly similar. Assuming $\delta_s \simeq \delta$, the ratio of GB and surface segregation factors, s/s_s, can be estimated from Fig. 2 to be $s/s_s \approx 0.01$.

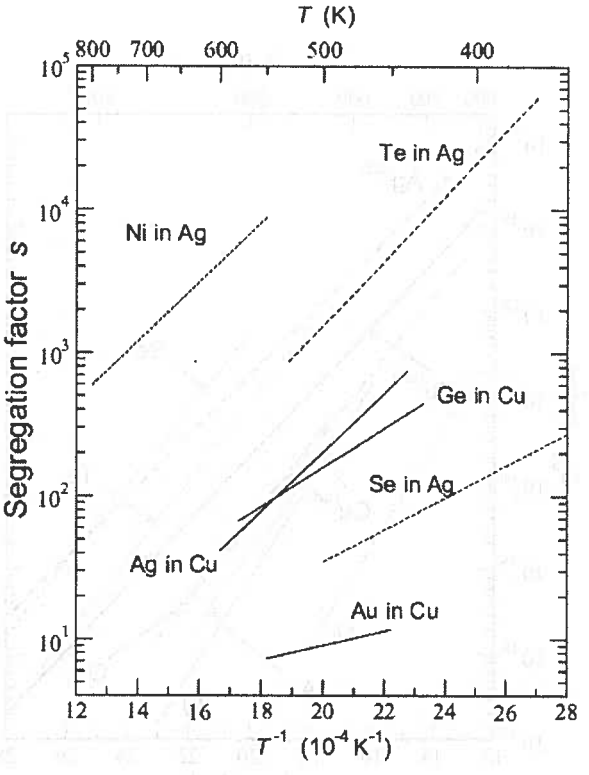

Fig. 5. Solute segregation factors s of Ag [15], Ge [20], and Au [19] in Cu (solid lines) and of Ni [17], Te [18], and Se [17] in Ag (dashed lines) determined by the radiotracer GB diffusion measurements

4. Non-linear segregation

The GB measurements in the *B*- and *C*-kinetic regimes in pure Cu and Ag allowed us to extract the data on linear solute segregation in these metals, since the solute tracer amount satisfied the dilute limit conditions in both, the GBs and the bulk. In order to study the effects of non-linear segregation the amount of a solute has to be increased, at least in the GBs.

4.1. GB diffusion in alloys (Ag in Cu)

One of the experimental possibilities to provoke non-linear segregation effects is alloying of the matrix by the inactive solute element. Subsequent solute radiotracer GB diffusion experiments will proceed under the boundary condition that the segregation factor in the alloy,

$$s^{alloy} = \frac{c_{gb}^{alloy}}{c_v^{alloy}}, \tag{3}$$

does not change along the GB penetration profile. It follows that $s^{alloy} = const$ for the given conditions and depends on the total concentration of the solute in the matrix [30, 31]. Equation (3) can be applied, since the *isotope equilibrium* with respect to radiotracer and inactive solute atoms is maintained between the GB and the adjacent lattice at any depth for typical diffusion times [31].

Generally, when changing the volume concentration of a solute, a non-linear dependence of c_{gb} on c_v is expected [32] and s^{alloy} will differ from the corresponding segregation factor s^{pure} measured in pure metal ($s^{alloy} \leq s^{pure}$).

B e r n a r d i n i *et al.* [33] used Eq. (3) to determine the segregation behavior of Ag in a Cu (Ag) alloy. As a result, however, they estimated in their study the enrichment factor b, which appears in the M c L e a n isotherm [32] (for the difference between b and the segregation factor s see above and [15]). Measurements performed in the B kinetic regime were only required in that approach. The segregation enthalpy was found to be -37 kJ/mol [33] in good agreement with the combined type B and C GB diffusion measurement [15]. A closer inspection of the profiles measured for the Cu(Ag) alloy (0.09 at.% Ag) [33] however reveals that they are partly curved (especially at the two highest temperatures). These features were not analyzed so far. Moreover, no direct measurements of D_{gb} in an alloy existed until very recently.

4.1.1. *C* regime GB diffusion measurements in an alloy

GB diffusion measurements in the Cu–0.2at.%Ag aloy in the C regime were carried out for the first time in Ref. [9]. In Fig. 6, the results of Ag GB diffusion in the Cu–0.2at.%Ag alloy are plotted together with the previous data on Ag GB diffusivity D_{gb} [15] in pure Cu. Both data sets are almost identical. The following Arrhenius dependence is established for Ag GB diffusion in the Cu(Ag) alloy:

$$D_{gb}^{alloy} = 2.5 \cdot 10^{-4} \cdot \exp\left(-\frac{108.8\ \text{kJ/mol}}{RT}\right) \text{m}^2/\text{s}. \tag{4}$$

Very similar values of the pre-exponential factor $D_0^{pure} = 1.7 \cdot 10^{-4}$ m^2/s and the activation enthalpy $Q_{gb}^{pure} = 108.6$ kJ/mol were found for Ag GB diffusion in pure Cu [15]. Thus, *direct* measurements of D_{gb} show that the Ag GB diffusivity in pure Cu and in the Cu–0.2at.%Ag alloy is almost the same within the limits of the experimental errors.

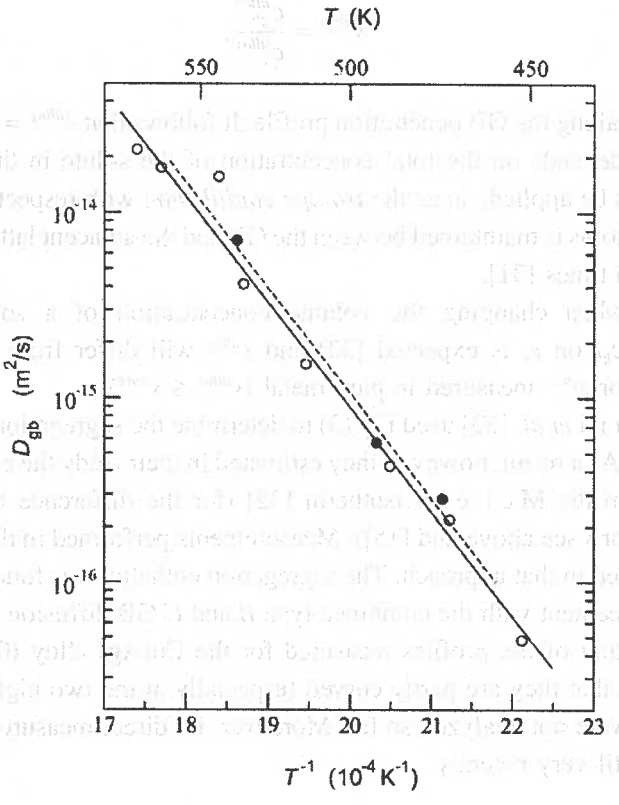

Fig. 6. Temperature dependence of Ag GB diffusion in the Cu–0.2at.%Ag alloy (filled circles, dashed line) in comparison with the Ag GB diffusivity in high-purity Cu [15] (open circles, solid line). All data were measured under *C* regime conditions

4.1.2. *B* regime measurements in an alloy

The penetration profiles measured for Ag GB diffusion in the Cu–0.2at.%Ag alloy turned out to be remarkably curved, Fig. 7, and this curvature does not monotonically depend on the temperature: at low and high temperatures the profiles are almost perfectly linear (*e.g.* at $T = 970$ and 668 K, Fig. 7), whereas the curvature is well pronounced at intermediate temperatures (*e.g.* at $T = 710$, 762, and 892 K, Fig. 7).

This profile curvature cannot be explained by direct bulk diffusion since the volume penetration depths amount to only a few micrometers. Several factors can potentially give rise to the curvature of penetration profiles: *e.g.* (*i*) GB motion [34]; (*ii*) existence of a wide spectrum of GBs with different diffusivities [35, 1]; (*iii*) non-linear segregation of solute atoms [36, 37].

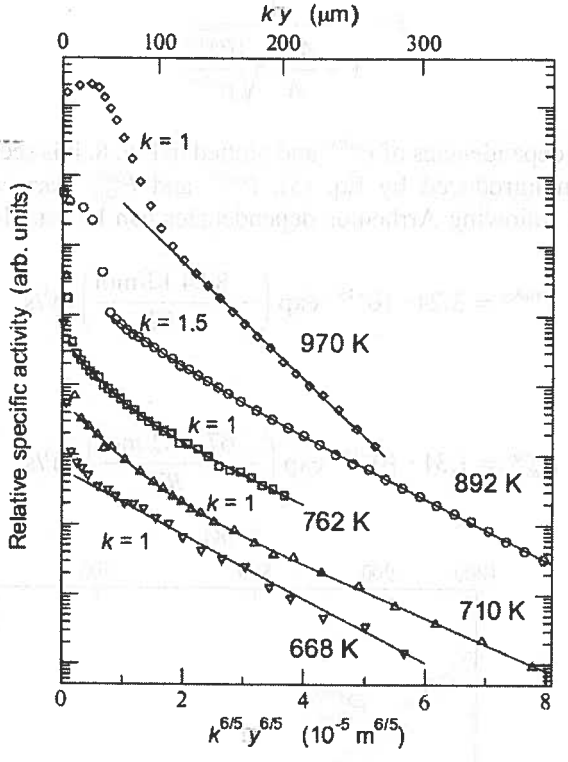

Fig. 7. Penetration profiles of Ag GB diffusion in the Cu–0.2at.%Ag alloy in the *B* regime. k is a scaling factor and y is the penetration depth. The lines present a four-parameter fit according to Eq. (5)

Our careful analysis proved that a hypothetically assumed motion of GBs does not dominate the curvature of penetration profiles in the present case of the Cu–Ag alloy, since the corresponding fractions of moving GBs would *increase* with decreasing temperature, a result which is physically unreasonable.

It was supposed [9] that the curvature of the penetration profiles in Fig. 7 originates from the presence of GBs with very different values of P in the Cu(Ag) alloy. Although the GB diffusivities P may form a continuous spectrum, for simplicity the profiles were fitted by a sum of two Suzuoka solutions [38]:

$$\bar{c}\,(y,t) \cong A \exp\{-q \cdot y^{6/5}\} + A_{fast} \exp\{-q_{fast} \cdot y^{6/5}\}. \tag{5}$$

In this approximation it is assumed that only two classes of GBs with different diffusivities dominate the GB diffusion penetration, with "regular" (A and q) and fast (A_{fast} and q_{fast}) diffusivities. The parameters q and q_{fast} determine the triple products P^{alloy} and P^{alloy}_{fast}, respectively, where the P^{alloy}_{fast} is characterized by the slopes of the linear tails of the GB diffusion profiles in Fig. 7. The fraction f of the GBs with a regular diffusivity can be calculated as

$$f = \frac{1}{1 + \frac{A_{fast}}{A}\sqrt{\frac{P_{fast}^{alloy}}{p^{alloy}}}}. \tag{6}$$

The temperature dependencies of P^{alloy} and plotted in Fig. 8. It is seen that in spite of the crude approximation introduced by Eq. (5), P^{alloy} and P_{fast}^{alloy} vary systematically with temperature and the following Arrhenius dependencies can be established:

$$P^{alloy} = 3.24 \cdot 10^{-15} \cdot \exp\left(-\frac{82.4\ \text{kJ/mol}}{RT}\right) \text{m}^3/\text{s} \tag{7}$$

and

$$P_{fast}^{alloy} = 1.31 \cdot 10^{-15} \cdot \exp\left(-\frac{67.1\ \text{kJ/mol}}{RT}\right) \text{m}^3/\text{s}. \tag{8}$$

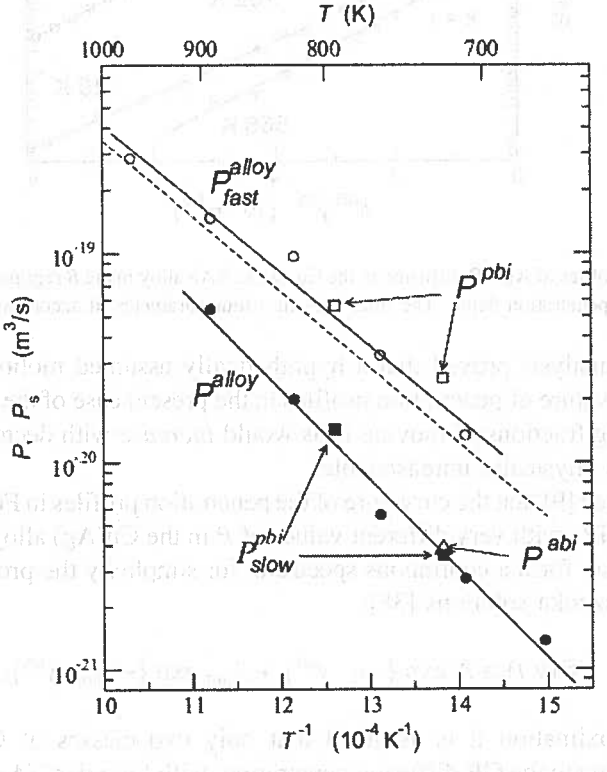

Fig. 8. Temperature dependence of Ag GB diffusivities P_{fast}^{alloy} (open circles) and P^{alloy} (filled circles) in the polycrystalline Cu–0.2at.%Ag alloy and Ag GB diffusivity P in pure Cu (dashed line). The solid lines represent the Arrhenius fits. For comparison, the GB diffusivities P^{pbi} (open squares) and P_{slow}^{pbi} (filled squares) measured in a pure Cu near $\Sigma 5(310)[001]$ bicrystal are shown. The GB diffusivity P^{abi} of a pre-alloyed Cu bicrystal is also presented (triagle)

The difference between P^{alloy} and P^{alloy}_{fast} may result from the difference in the respective s and/or D^{alloy}_{gb} values, since it is reasonable to assume that δ is almost constant.

In Ref. [35] the curvature of the penetration profiles of Zn GB diffusion in Al was explained by the presence of large-angle GBs with remarkably different diffusivities D_{gb}. This effect is not relevant in the present case, since the fraction of GBs showing different diffusivities does not remain independent on temperature but changes regularly with temperature. The key arguments which lead to the conclusion that variations in P are due to variations in s and not in D_{gb}, however, stem from GB diffusion experiments on Cu bicrystals.

4.2. GB diffusion in bicrystals (Ag in Cu)

Anther way to induce the non-linear segregation was established by replacing the polycrystalline samples by bicrystals. Cu bicrystals with orientations close to the $\Sigma = 5(310)[001]$ GB were used [9]. The tilt angle $\theta = 36.0°$ is reasonably far away from the exact $\Sigma 5$ misorientation ($\theta \cong 36.9°$) to result in a GB diffusivity being similar to that of random large-angle grain boundaries in polycrystalline Cu [39].

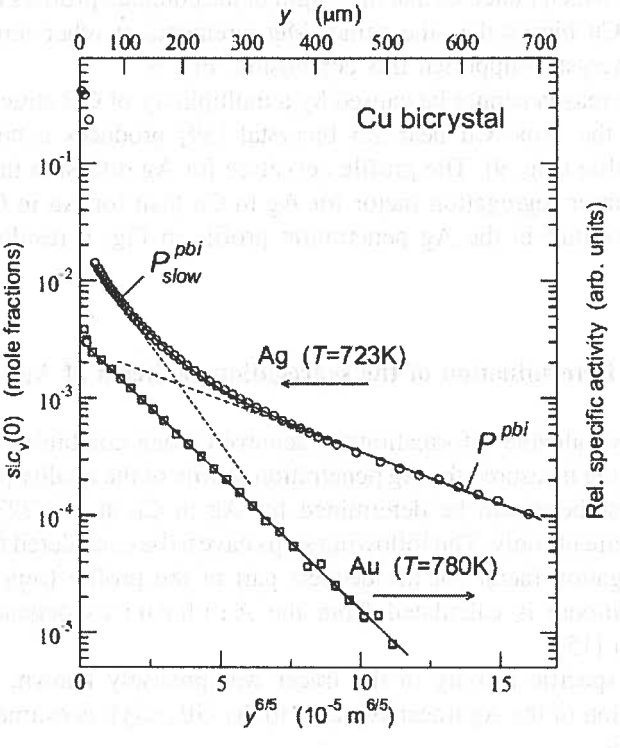

Fig. 9. Penetration profiles of Ag (circles, left ordinate) and Au (squares, right ordinate) GB diffusion in a Cu near $\Sigma = 5(310)[001]$ bicrystal. The Ag concentration is given in mole fractions, s and $c_v(0)$ are the segregation factor and the concentration in the volume adjacent to the GB, respectively. The solid line presents the four-parameter fit according to Eq. (5), from which P^{pbi} and P^{pbi}_{slow} were calculated

An Ag penetration profile measured on the bicrystal at $T = 723$ K is shown in Fig. 9. The absolute Ag concentration in the bulk adjacent to the GB, c_v (0), was deduced from the Ag concentration in a layer section – known from the specific radiotracer activity [9]. Multiplying this value by the known segregation factor s for the dilute limit (determined in [15], see also Fig. 2), an upper estimation of the Ag tracer concentration within the GB was obtained as $s \cdot c_v(0)$, Fig. 9. (The real Ag GB concentration can be smaller than $s \cdot c_v(0)$ in the case of non-linear segregation). The amount of Ag tracer in the single boundary of the bicrystal was found to be orders of magnitude higer than that in high-purity polycrystalline Cu when applying the same initial surface activity. This fact was explained [9] by fast surface diffusion which drives a significant amount of tracer atoms to the single GB in caser of a bicrystal versus a distribution over a larger number of GBs in a polycrystal. As a result, the penetration profile in the bicrystal is substantially curved, a circumstance which becomes especially pronounced due to the large depth of profile detection (up to 700 μm). If the profile in Fig. 9 is processed according to Eq. (5), the values of the GB diffusivity P^{bi}_{slow} and P^{bi} (corresponding to the slow and fast diffusivity parts, respectively) can be determined. These values are shown in Fig. 8 by filled (P^{bi}_{slow}) and open (P^{bi}) squares. Good agreement is observed with the data measured in the polycrystalline Cu–Ag alloy and in the pure Cu bicrystal, which indicates that the origin of the complex profiles in the Cu-Ag alloy and in the pure Cu bicrystal is the same. Measurements at other temperatures and in pre-alloyed Cu bicrystal supported this conclusion, Fig. 8.

This common reason cannot be caused by a multiplicity of GB structures, because Au GB diffusion in the same Cu near $\Sigma 5$ bicrystal [39] produces a nearly perfect type *B* penetration profile (Fig. 9). The profile curvature for Ag diffusion therefore originates from the much larger segregation factor for Ag in Cu than for Au in Cu (Fig. 5).

Thus, the curvature in the Ag penetration profile in Fig. 9 results from non-linear segregation.

4.3. Determination of the segregation isotherm of Ag in Cu

Further extremely valuable informations is achieved when combining the results of the whole study. Having measured the Ag penetration profile of the quality presented in Fig. 9, the segregation isotherm can be determined for Ag in Cu at $T = 723$ K from the GB diffusion measurements only. The following steps have to be considered for this derivation:

1. The segregation factor for the deepest part of the profile (representing Henry type conditions) is calculated from the Arrhenius dependence established in pure Cu [15].
2. Since the specific activity of the tracer was precisely known, the absolute bulk concentration of the Ag tracer adjacent to the GB, $c_v(y)$, is estimated as function of the depth y.
3. Because $D^{alloy}_{gb} \cong D^{pure}_{gb}$ for Ag GB diffusion (Fig. 6) and because there exists no variation of P along the Au penetration profile in the same bicrystal (Fig. 9), it is reasonable to assume that $D_{gb} \cong const$ along the Ag penetration profile.

4. When applying the F i s h e r model [40] and introducing the segregation isotherm $c_{gb} = g(c_v)$, the GB concentration of the Ag tracer follows the equation:

$$\frac{\partial^2 c_{gb}}{\partial y^2} = L^{-2} \cdot c_v = L^{-2} \cdot g^{-1}(c_{gb}). \tag{9}$$

Here L is the reduced depth, $L = \sqrt{\delta D_{gb}} \left(\frac{\pi t}{4 D_v}\right)^{1/4}$.

5. Since the solution of Eq. (9) is known at large depths in terms of the F i s h e r model, $c_v(y) = c_v^0 \cdot \exp(-y/Ls^{1/2})$ and $c_{gb}(y) = s \cdot c_v(y)$, one can integrate Eq. (9) and the relation

$$c_{gb}(y) = L^{-2} \int_{\infty}^{y} dv \int_{\infty}^{v} c_v(u)\, du \tag{10}$$

yields the segregation isotherm (with v and u being the integration variables). The result, *i.e.* c_{gb} as function of c_v, is presented in Fig. 10. We note that one can determine the segregation isotherm already starting from very small GB concentrations by using the very sensitive radiotracer GB diffusion measurements with a suitable tracer on bicrystals. This is an important progress in understanding the segregation behavior at solute concentration levels which were hardly accessible so far in other experiments. Furthermore, it has to be emphasized that all relevant results stem from "in situ" experiments at the corresponding temperatures.

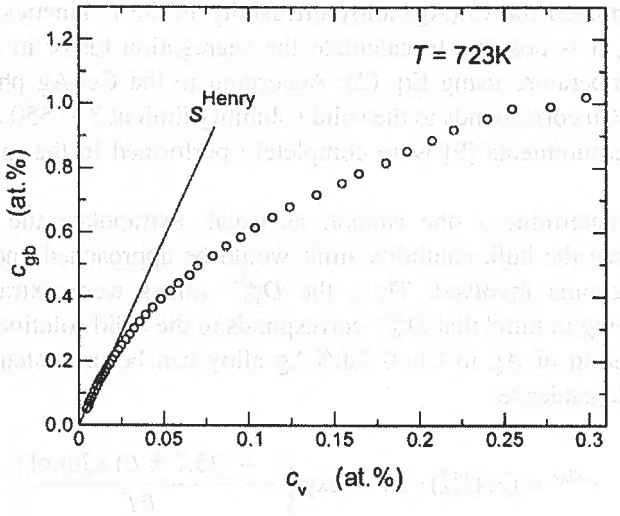

Fig. 10. Segregation isotherm of Ag in Cu GBs at $T = 723$ K [9]

4.4. GB segregation of Ag in pure and alloyed Cu

In Fig. 8 the data on Ag GB diffusion in Cu–0.2at.%Ag alloy are compared with the results on Ag GB diffusion in high-purity Cu [15]. The diffusivity $P_{fast}^{alloy} = s_{fast}^{alloy} \cdot \delta^{alloy} \cdot D_{gb}^{alloy}$ of the "fastest" GBs in the Cu–0.2at.%Ag alloy practically coincides with the data on $P^{pure} = s^{pure} \cdot \delta^{pure} \cdot D_{gb}^{pure}$ in high-purity Cu [15]. Since the direct (*C* regime) measurements of the GB diffusion coefficients in pure Cu and in the Cu–0.2at.%Ag alloy gave the same results, $D_{gb}^{alloy} \cong D_{gb}^{pure}$ (cf. Fig. 6), it is concluded that the segregation factors of Ag in pure Cu, s^{pure}, and in the fastest GBs of the Cu–0.2at.%Ag alloy, s_{fast}^{alloy}, are also similar (it is reasonable to assume that $\delta^{alloy} \cong \delta^{pure}$). The fact that $s_{fast}^{alloy} \cong s^{pure}$ indicates that in the studied temperature interval and for the given alloy composition, the Ag GB concentration in a part of the GBs corresponds to the dilute limit of segregation and diffusivities of such GBs are the same as in pure Cu. Other GBs contain relatively high concentration of Ag atoms, and these are those GBs that reveal the slower diffusivities P^{alloy}.

Since $D_{gb}^{alloy} \cong D_{gb}^{pure}$, the difference between P_{fast}^{alloy} and P^{alloy} is mainly related to the difference in the corresponding segregation factors, meaning that $s^{alloy} < s_{fast}^{alloy}$ and thus $s^{alloy} < s^{pure}$.

It is not unusual observation that segregated atoms do not uniformly cover all GBs in a polycrystalline sample. Using high-resolution transmission electron microscopy in Ref. [41] a broad distribution of the amount of Bi atoms segregated at GBs in polycrystalline Cu was reported. While part of the Cu GBs was covered by Bi atoms, it was impossible to detect Bi segregation in other GBs [41]. Furthermore, in an Auger Electron Spectroscopy study a sample has to be fractured *in situ* along GBs to determine the segregation characteristics. The sample more likely brakes along GBs with a higher concentration of segregated atoms (which usually induce GB brittleness), while less segregated GBs cannot be studied.

Having determined the Cu(Ag) alloy diffusivity in the *C* kinetics, D_{gb}^{alloy}, and in the *B* kinetics, P^{alloy}, it is possible to calculate the segregation factor in the alloy, s^{alloy}, as a function of temperature using Eq. (2). According to the Cu–Ag phase diagram [42], 0.2at.% of Ag in Cu corresponds to the solid solubility limit at $T \sim 550$ K. This means that the *B* regime measurements [9] were completely performed in the interval of Ag solid solution in Cu.

In order to determine s one cannot, as usual, extrapolate the P values to low temperatures, since the bulk solubility limit would be approached and the precipitation enthalpy may become involved. Thus, the D_{gb}^{alloy} values were extrapolated to higher temperatures having in mind that D_{gb}^{alloy} corresponds to the solid solution of Ag in Cu (Fig. 11). The segregation of Ag in Cu–0.2at.%Ag alloy can be presented by the following Arrhenius dependence:

$$s^{alloy} = (3.4^{+4.5}_{-1.9}) \cdot 10^{-2} \cdot \exp\left(-\frac{(-25.7 \pm 6)\ \text{kJ/mol}}{RT}\right). \qquad (11)$$

These values correspond to the GBs significantly covered with segregated Ag atoms.

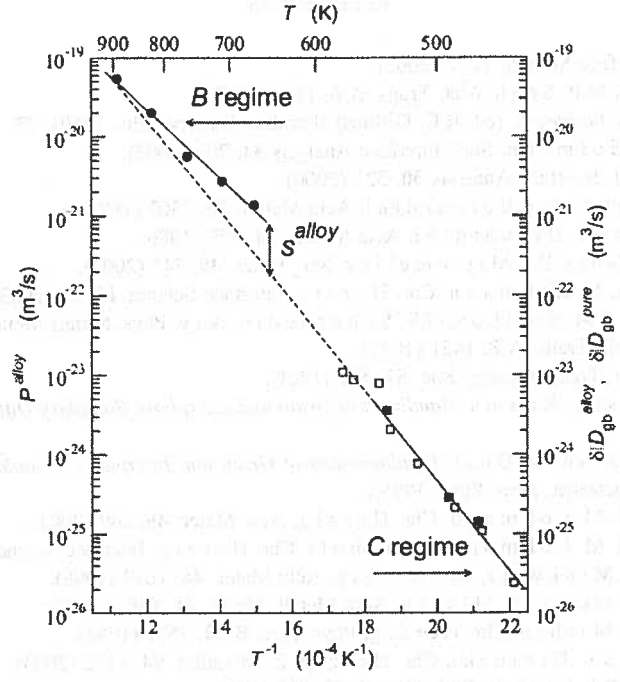

Fig. 11. Determination of Ag segregation factor s^{alloy} in the Cu(Ag) alloy by combined GB diffusion measurements in the B (P^{alloy}, circles) and C (D_{gb}^{alloy}, squares) kinetics. The filled squares represent the product $\delta \cdot D_{gb}^{alloy}$ calculated by using the directly measured D_{gb}^{alloy} values and the open squres correspond to the results evaluated by using D_{gb}^{pure}

5. Conclusions

GB diffusion measurements are shown to represent a powerful tool for studying GB equilibrium segregation in the true dilute (Henry) limit. At present there exist already ample information on equilibrium segregation of different solutes in Cu and Ag.

GB diffusion measurements on bicrystals yield specific and unique information on linear and non-linear segregation behavior. Compiling a large body of experimental data concerning Ag GB diffusion in high-purity polycrystalline Cu, Cu–Ag polycrystalline alloys, and in Cu bicrystals allowed us to extract the corresponding segregation isotherm from GB diffusion data.

Combination of GB diffusion measurements in pure and alloyed metals and in pure and pre-alloyed bicrystals allowed to draw justified conclusions and to distinguish between the effects of moving boundaries, non-linear segregation, and a hypothetical variation of the GB diffusivities D_{gb}.

Acknowledgment

The present investigation was supported by funds of the Deutsche Forschungsgemeinschaft (Project He848/24-1).

REFERENCES

[1] D. Gupta, Interface Science **11**, 7 (2003).
[2] E.D. Hondros, M.P. Seah, Met. Trans. A **8**, 1363 (1977).
[3] E.D. Hondros, *Interfaces*, (ed. R.C. Gifkins) (London, Butterworths, 1969), 77.
[4] P. Lejcek, S. Hofmann, Surf. Interface Analysis **33**, 203 (2002).
[5] P. Lejcek, Surf. Interface Analysis **30**, 321 (2000).
[6] P. Gas, M. Guttman, J. Bernardini, Acta Metall. **30**, 1309 (1982).
[7] P. Gas, S. Poize, J. Bernardini, Acta Metall. **34**, 359 (1986).
[8] G. Lopez, W. Gust, E.J. Mittemeijer, Scr. Mater. **49**, 747 (2003).
[9] S.V. Divinski, M. Lohmann, Chr. Herzig, Interface Science **11**, 21 (2003).
[10] V.T. Borisov, V.M. Golikov, G.V. Scherbedinskiy, Phys. Metals Metallogr. **17**, 80 (1964).
[11] D. Gupta, Metall. Trans. A **8**, 1431 (1977).
[12] L.G. Harrison, Trans. Faraday Soc. **57**, 597 (1961).
[13] I. Kaur, W. Gust, L. Kozma, *Handbook of Grain and Interphase Boundary Diffusion Data* (Ziegler, Stuttgart, 1989).
[14] I. Kaur, Y. Mishin, W. Gust, *Fundamentals of Grain and Interphase Boundary Diffusion* (Wiley & Sons LTD, Chichester, New York, 1995).
[15] S.V. Divinski, M. Lohmann, Chr. Herzig, Acta Mater. **49**, 249 (2001).
[16] S.V. Divinski, M. Lohmann, T. Surholt, Chr. Herzig, Interface Science **9**, 357 (2001).
[17] T. Surholt, C. Minkwitz, Chr. Herzig, Acta Mater. **46**, 1849 (1998).
[18] Chr. Herzig, J. Geise, Y. Mishin, Acta Metall. Mater. **41**, 1683 (1993).
[19] T. Surholt, Y. Mishin, Chr. Herzig, Phys. Rev. B **50**, 3577 (1994).
[20] M. Lohmann, S.V. Divinski, Chr. Herzig, Z. Metallkd. **94**, 1172 (2003).
[21] A. Atkinson, R.I. Taylor, Phil. Mag. A **43**, 979 (1981).
[22] P. Gas, D.L. Beke, J. Bernardini, Phil. Mag. Lett. **65**, 133 (1992).
[23] J. Sommer, Chr. Herzig, J. Appl. Phys. **72**, 2758 (1992).
[24] S.V. Divinski, F. Hisker, Y.S. Kang, J.-S. Lee, Chr. Herzig, Z. Metallkd. **93**, 256 (2002).
[25] S.V. Divinski, F. Hisker, Y.S. Kang, J.-S. Lee, Chr. Herzig, Z. Metallkd. **93**, 265 (2002).
[26] S.V. Divinski, F. Hisker, Y.S. Kang, J.-S. Lee, Chr. Herzig, Interface Science, 11, 67 (2003).
[27] P. Gas, S. Poize, J. Bernardini, F. Cabane, Defect Diffusion Forum, **66-69**, 905 (1989).
[28] T. Surholt, Chr. Herzig, Acta Metall. **45**, 3817 (1997).
[29] Z. Erdélyi, Ch. Girardeaux, G.A. Langer, D.L. Beke, A. Rolland, J. Bernardini, J. Appl. Phys. **89**, 3971 (2001).
[30] J. Bernardini, G. Martin, Scr. Metall. **10**, 833 (1976).
[31] J. Bernardini, P. Gas, Defect Diffusion Forum **95-98**, 393 (1993).
[32] D. Mclean, *Grain Boundaries in Metals*, (Clarendon Press, Oxford, 1957).
[33] J. Bernardini, Zs. Tôkei, D.L. Beke, Phil Mag. A **73**, 237 (1996).
[34] F. Güthoff, Y. Mishin, Chr. Herzig, Z. Metallkd. **84**, 584 (1993).
[35] D.L. Beke, I. Gödény, G. Erdélyi, F.J. Kedves, Phil.Mag. A **56**, 659 (1987).
[36] B.S. Bokstein, V.E. Fradkov, D.L. Beke, Phil. Mag. A **65**, 277 (1992).
[37] Y. Mishin, Chr. Herzig, J. Appl. Phys. **73**, 8206 (1993).
[38] T. Suzuoka, J. Phys. Soc. Japan **19**, 839 (1964).
[39] E. Budke, T. Surholt, S.I. Prokofjev, L.S. Shvindlerman, Chr. Herzig, Acta Mater. **47**, 385 (1999).
[40] J.C. Fisher, J. Appl. Phys. **22**, 74 (1951).
[41] V.J. Keast, D.B. Williams, Acta Mater. **47**, 3999 (1999).
[42] J.L. Murray, Metall. Trans. A **15**, 261 (1984).

Received: 1 March 2003.

A R C H I V E S O F M E T A L L U R G Y A N D M A T E R I A L S
Volume 49 2004 Issue 2

B.B. STRAUMAL *

GRAIN BOUNDARY PHASE TRANSITIONS. INFLUENCE ON DIFFUSION, PLASTICITY AND CHARGE TRANSFER

PRZEJŚCIA FAZOWE NA GRANICACH ZIAREN I ICH WPŁYW NA DYFUZJĘ, PLASTYCZNOŚĆ ORAZ TRANSFER ŁADUNKU

Increased diffusion permeability of polycrystals (especially that of nanograined ones) in many cases can be attributed to the grain boundary (GB) phase transitions. They influence also liquid-phase and activated sintering, soldering, processing of semi-solid materials. The GB wetting phase transition can occur in the two-phase area of the bulk phase diagram where the liquid (L) and solid (S) phases are in equlibrium. The GB wetting tieline appears in the $L+S$ area. Above the temperature of the GB wetting phase transition a GB cannot exist in equlibrium contact with the liquid phase. The liquid phase has to substitute the GB and to separate both grains. The GB wetting tie-line can continue in the one-phase area of the bulk phase diagram as a GB solidus line. This line represents the GB premelting or prewetting phase transitions. The GB properties change drastically when GB solidus line is crossed by a change in the temperature or concentration. In case if two solid phases are in equilibrium, the GB "solid state wetting" (or covering) can occur. In this case the layer of the solid phase *2* has to substitute GBs in the solid phase *1*. Such covering GB phase transition occurs if the energy of two interphase boundaries between phase *1* and *2* is lower than the GB energy in the phase *1*.

Lepsza dyfuzyjność polikryształów (zwłaszcza tych o wielkości ziarna w skali nanometrycznej) często związana jest z tzw. przejściami fazowymi granic ziaren. Przejścia fazowe na granicach ziaren wywierają również istotny wpływ na spiekanie z udziałem fazy ciekłej, spajanie materiałów oraz inne procesy w stanie pół-stałym. Przykładowo zjawisko zwilżania granic ziaren zachodzi w obszarze dwufazowym na wykresie fazowym, gdzie faza ciekła *(L)* i stała *(S)* są w stanie równowagi. Konsekwencją jest istnienie dodatkowych linii zwilżalności w obszarze $L+S$, które określają temperaturę przejścia fazowego zwanego zwilżaniem granic ziaren. Powyżej tej temperatury granica ziarna nie jest w stanie równowagi z fazą ciekłą i przechodzi w stan ciekły, pomimo że ziarna, które rozdziela są w stanie stałym. Linie zwilżania granic ziaren mogą występować także w obszarze jednofazowym wykresu fazowego. Wtedy charakteryzują temperatury innych przejść fazowych granic ziaren definiowanych jako nadtopienie oraz przedzwilżanie. Właściwości granic ziaren ulegają znacznym zmianom w sytuacji, gdy linia solidus dla

* INSTITUTE OF SOLID STATE PHYSICS, CHERNOGOLOVKA, MOSCOW DISTR. 142432 RUSSIA

granicy ziarna krzyżuje się ze zmianą temperatury lub stężenia. Gdy dwie fazy są w stanie równowagi, obserwuje się tzw. zwilżanie w stanie stałym (lub zestalanie). Wtedy warstwa fazy stałej 2 zastępuje granice ziaren w fazie stałej 1.

1. Introduction

The properties of modern materials, especially those of nanocrystalline, superplastic or composite materials, depend critically on the properties of internal interfaces such as grain boundaries (GBs) and interphase boundaries (IBs). All processes which can change the properties of GBs and IBs affect drastically the behaviour of polycrystalline metals and ceramics [1]. GB phase transitions are one of the important examples of such processes [2]. Recently, the lines of GB phase transitions began to appear in the traditional bulk phase diagrams [2–7]. The addition of these equilibrium lines to the bulk phase diagrams ensures an adequate description of polycrystalline materials, particularly their diffusion permeability, deformation behavior and the evolution of the microstructure. In this work the following GB phase transitions are discussed: (a) GB wetting, (b) GB prewetting (or premelting) and (c) GB «wetting» (covering) by second solid phase. The recently obtained experimental data are discussed. Using these data, the new GB lines in the conventional bulk phase diagrams are constructed.

2. Grain boundary wetting phase transitions

In this work GB wetting, prewetting and premelting phase transitions are considered. The GB melting, GB faceting transition and the "special GB – random GB phase transitions" are analyzed elsewhere [8–10]. One of the most important GB phase transitions is the *GB wetting transition*. Since their prediction by Cahn [11] the study of wetting phase transitions has been of great experimental and theoretical interest, primarily for planar solid substrates and fluid mixtures [12–14]. Particularly, it was experimentally shown that the wetting transition is of first order, namely the discontinuity of the surface energy was measured and the hysteresis of the wetting behavior was observed [15, 16]. The important difference is that in case of GB wetting only two phases coexist, namely the liquid (melt) phase and the solid one containing the boundary between the misoriented grains. Therefore, the contact angle θ also depends only on two different surface energies (the GB energy σ_{GB} and the energy of the solid/liquid interphase boundary σ_{SL}) instead of three ones in the usual experiments: $\sigma_{GB} = 2\sigma_{SL} \cos(\theta/2)$. If $\sigma_{GB} < 2\sigma_{SL}$, the GB is incompletely wetted and the contact angle $\theta > 0$ (Fig. 1a). At the temperature T_W of the GB *wetting phase transition* $\sigma_{GB} = 2\sigma_{SL}$ and at $T \geq T_W$ the GB is completely wetted by the liquid phase and $\theta = 0$ (Fig. 1b). If two GBs have different energies the temperatures of their GB wetting transitions will also differ: the lower σ_{GB}, the higher T_W (Figs. 1c and 1d). If the GB wetting phase transition is of first order, there is a discontinuity in the temperature derivative of the GB energy at T_W

which is equal to $[\partial\sigma_{GB}/\partial T - \partial(2\sigma_{SL})/\partial T]$ [11, 16]. If the GB wetting phase transition is of second order, $\partial\sigma_{GB}/\partial T = \partial(2\sigma_{SL})/\partial T$ at T_W. The theory predicts also the shape of the temperature dependence θ (T) at $T \rightarrow T_W$: it must be convex for a first order wetting transition [$\theta \sim \tau^{1/2}$ where $\tau = (T_W - T)/T_W$] and concave for a second order wetting transition: $\theta \sim \tau^{3/2}$ [12]. Our preliminary results demonstrate that the GB phase transitions of the second order may occur in Zn GBs wetted by the Al-rich melt. The $\theta(T)$ dependence is concave in this system and the discontinuity in the temperature derivative of the GB energy at T_W is negligibly small. In polycrystals the whole spectrum of GBs exists with various energies. Therefore, in polycrystals the maximal T_{wmax} and minimal T_{wmin} can be found for high-angle GBs with minimal and maximal energy σ_{GBmin} and σ_{GBmax}, respectively (Fig. 2).

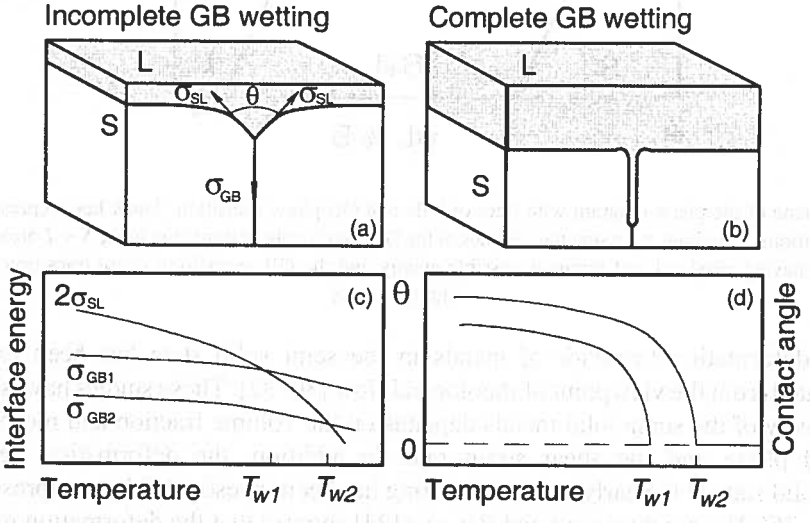

Fig. 1. (a) Scheme of the equilibrium contact between the grain boundary in the aolid phase S and the liquid phase L (incomplete wetting). (b) Complete GB wetting. (c) Sheme of the temperature dependence for the GB energy σ_{GB} (for two different GBs) and the energy of the solid-liquid interface boundary σ_{SL}. (d) Scheme of the temperature dependence of the contact angle θ for two grain boundaries with energies σ_{GB1} and σ_{GB2}. T_{W1} and T_{W2} are the temperatures of the GB wetting phase transition

First indications of the GB wetting phase transitions were found by measuring of the contact angles in polycrystals [17]. Correct measurements were later perfomed using metallic bicrystals with inndividual tilt GBs in the Al–Sn, Cu–In [4], Al–Pb–Sn [3,18,19], Al–Ga, Al–Sn–Ga [20, 21], Cu–Bi [5, 22, 23, 30], Fe–Si–Zn [24–27], Mo–Ni [28], W–Ni [29] and Zn–Sn [7] systems. The tie-lines of the GB wetting phase transition were constructed basing on the experimental data [3, 4, 7, 18–29]. The difference in the GB wetting phase transition temperature was experimentally revealed for GBs with different energies [4, 18]. The indications of presence of the liquid-like phase along the dislocation lines were also found [23].

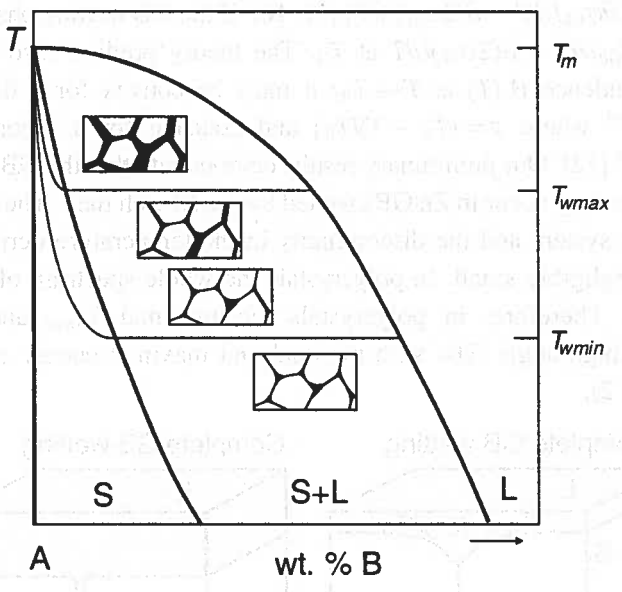

Fig. 2. Scheme of the phase diagram with lines of bulk and GB phase transition. Thick lines represent the bulk phase transitions. Thin lines represent the tie-lines of the GB wetting phase transition in the $S + L$ area for the high angle GBs having maximal and minimal possible energy and the GB premelting phase transition in the solid solution area S

The deformation behavior of metals in the semi solid state has been extensively investigated from the viewpoint of rheological flow [30–32]. These studies have shown that the viscosity of the semi-solid metals depends on the volume fraction and morphology of the solid phase and the shear strain rate. In addition, the deformation behavior in a semi-solid state at the early stages of melting has been investigated by compressive creep tests [33–36]. V a a n d r a g e r and P h a r r [24] showed that the deformation mechanism in a semi-solid state at the early stages of melting is grain boundary sliding accommodated by cavitation in a liquid phase for the copper containing a liquid bismuth. This deformation mechanism in the semi-solid state at the early stages of melting appears to be different from that in the semi-solid state during solidification. The presence of a liquid phase gives rise to complicated effects on the deformation behavior in the semi-solid state. Deformation in the semi-solid state is phenomenologically divided as follows: plastic deformation of solid phases, sliding between solid phases, flow of liquid incorporating solid phases and liquid flow [22]. For compressive deformation, because the liquid phase is squeezed out of boundaries experiencing compressive stresses in a very short time [24], it is difficult to investigate deformation related to the liquid flow by compressive tests. In [37] the shear tests were carried out over a wide temperature range of 480–620°C, including temperatures below and above the solidus temperature, for Al – 5 wt.% Mg alloy to investigate deformation behavior in semi-solid states at early stages of melting. P h a r r et al. [36] showed that the liquid phase significantly affects creep behavior of alloys when a significant portion of the grain boundary area, in excess of 70%, is wet. This revealed that

the volume fraction of the liquid phase is an important factor in the deformation characteristics in the semi-solid state. The same trend has been reported in a semi-solid state at solidification [34]. However, deformation in the semi-solid state is very complicated and cannot be characterized only by the volume fraction of a liquid phase. In [37] the pure shear of Al – 5 wt% Mg alloy was investigated. This method permits to exclude the squeezing of the liquid phase from the sample. The shear strain to failure drops drastically at the solidus temperature (Fig. 3) [37]. In the semi-solid phase it is about 6 times lower than in the solid solution. Using the micrographs of the structure of polycrystals in the semi-solid state from [37] we calculated the fraction of the fully wetted GBs in dependence on the temperature. The continuous increase of the fraction of wetted GBs with increasing temperature influences strongly the mechanism of the deformation. In Fig. 4 the temperature dependence of the shear strain rate is shown recalculated from the data [37]. In the solid solution the shear strain rate increases moderately with increasing temperature, and the activation energy (135 kJ/mol) is very close to the activation energy of Mg diffusion in Al (131 kJ/mol). In the semi-solid state the shear strain rate increases drastically. Close to T_{wmax} the (formally calculated) activation energy is about 1650 kJ/mol, i.e. ten times higher than the activation energy for the viscosity of Al melt. It means that in the semi-solid state no unique thermally activated mechanism is working. Due to the temperature increase of the fraction of wetted GBs, the structure of the solid skeleton changes continuously. It becomes more and more cutted with increasing temperature, therefore, making the shear easier in addition to the pure temperature activation.

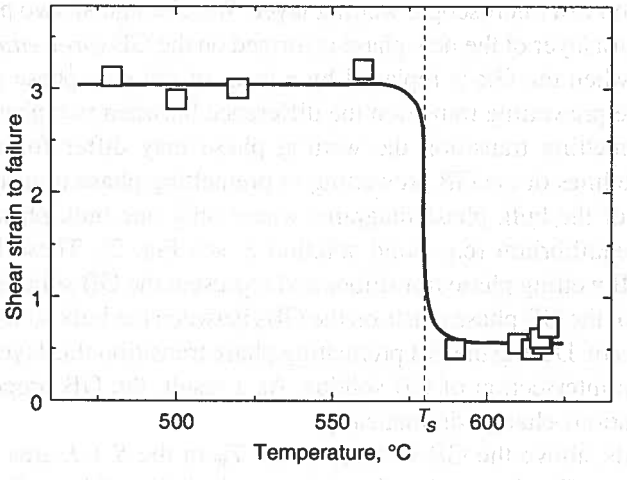

Fig. 3. Temperature dependence of shear strain to failure for Al–5 wt. % Mg alloy in solid and semi-solid state [37]

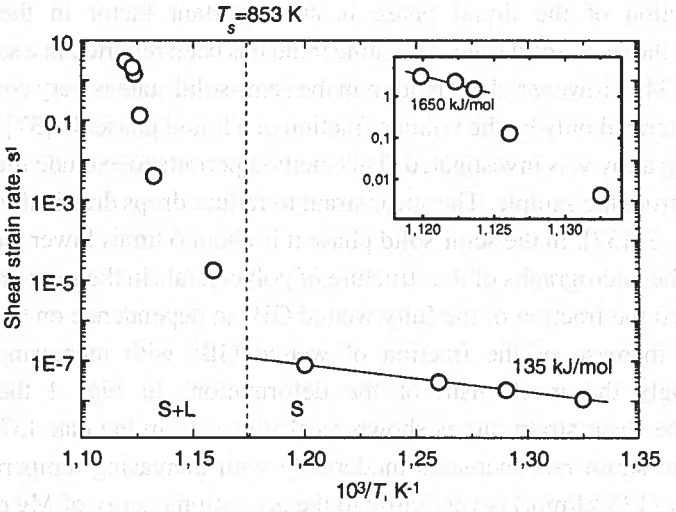

Fig. 4. Temperature dependence of shear strain rate for Al–5 wt. % Mg alloy in solid and semi-solid state [37]

3. Grain boundary prewetting (Premelting) phase transitions

It was pointed out by Cahn [38] that, when the critical consolution point of two phases is approached, GBs of one critical phase should be wetted by a layer of another critical phase, and in the one-phase region of a phase diagram there should be a singularity connected with an abrupt transition to a microscopic wetting layer. We distinguish two possible situations: the first one, when a layer of the new phase is formed on the GB (*prewetting transition*), and the second one, when the GB is replaced by a layer of the new phase (*premelting phase transition*). At the prewetting transition the difference between two phases must be small, while at the premelting transition the wetting phase may differ from that of the bulk dramatically. The lines of the GB prewetting or premelting phase transitions appear in the one-phase areas of the bulk phase diagrams where only one bulk phase can exist in the thermodynamic equilibrium (e.g. solid solution S, see Fig. 2). These lines continue the tie-lines of the GB wetting phase transitions and represent the GB solidus (Fig. 2). The thin liquid-like layer of the GB phase exists on the GBs between the bulk solidus and GB solidus in the phase diagram. During the GB premelting phase transition this layer appears abruptly on the GB by the intersection of GB solidus. As a result, the GB properties (diffusivity, mobility, segregation) change dramatically.

In other words, above the GB wetting tieline T_W in the $S + L$ area of the bulk phase diagram $\sigma_{GB} > 2\sigma_{SL}$. This is true also if we intersect the bulk solidus at $T =$ const and move into the one-phase area S of the bulk phase diagram. The GB energy σ_{GB} in this part of the one-phase region is still higher that the energy $2\sigma_{SL}$ of two solid-liquid interphase boundaries. Therefore, the GB still can be substituted by two solid-liquid interfaces, and the energy gain $\Delta G = \sigma_{GB} - 2\sigma_{SL}$ appears by this substitution. G permits to stabilize the GB

layer of the liquid-like phase. The appearance of the liquid-like phase (otherwise unstable in the bulk) between two *S/L* interfaces instead of GB leads to the energy loss Δg per unit thickness and unit square. Therefore, the GB layer of the liquid-like phase has the thickness l defined by the equation $\sigma_{GB} - 2\sigma_{SL} = \Delta g l$. Thickness l depends on the concentration and temperature and becomes $l = 0$ at the line of GB premelting (or prewetting) phase transition.

The premelting transition has been revealed in the ternary Fe–Si–Zn system by measurements of Zn GB *diffusivity* along tilt GBs in the Fe–Si alloys [24–27]. It was found that the penetration profiles of Zn along GBs consist of two sections, one with a small slope (high GB diffusivity $D_b\delta$) at high Zn concentrations and one with a large slope (low GB diffusivity) at low Zn concentrations (Fig. 5). The transition from one type of behavior to the other was found to occur at a definite Zn concentration c_{bt} at the GB, which is an equilibrium characteristic of a GB and depends on the temperature and pressure. The GB diffusivity increases about two orders of magnitude which is an indication of a quasi-liquid layer present in the GBs at high Zn concentration. The line of GB premelting phase transition in the one-phase area of the bulk phase diagram continues the line of the GB wetting phase transion in the two-phase $L + S$ area: by pressure increase both the GB wetting and the GB enhanced diffusivity disappear together at the same pressure value [27].

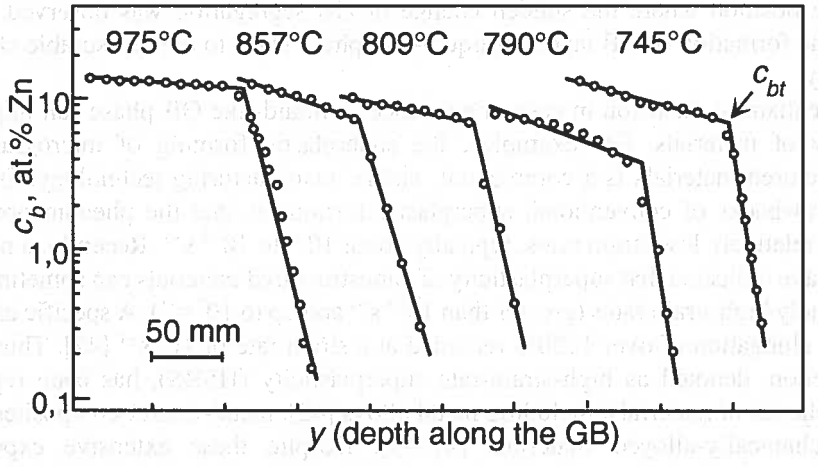

Fig. 5. Dependences of the GB Zn concentration c_b after diffusion into the GBs in Fe–5 at. Si bicrystals on the depth y in Fisher's coordinates $\lg c_b - y$ at various temperatures [24]. All these curves possess the high-$D_b\delta$ part (with low slope) and low- $D_b\delta$ part (with high slope). The $D_b\delta$ changes abruptly at their intersection c_{bt}

The *GB mobility* was studied for two tilt GBs in bicrystals grown of high purity 99.999 wt.% Al and of the same material doped by 50 wt. ppm Ga [21]. The GB mobility increased about 10 times by addition of the Ga content for the both GBs studied. Normally, the addition of a second component can only decrease the GB mobility due to the solution drag [32]. The increase of the GB mobility can only be explained by the formation of the liquid-like Ga-rich layer on the GBs as a result of a premelting phase transition. The *GB segregation* of Bi in Cu was studied in the broad temperature and concentration interval [5,

22, 23, 39, 40]. It was shown that at a fixed Bi concentration the GB segregation Z_Φ changes abruptly at a certain temperature. Below this temperature the GB Bi concentration is constant and corresponds to a thin layer of pure Bi (GB phase). Above this temperature the GB segregation is lower than one monolayer of Bi and decreases gradually with increasing temperature according to the usual laws. These features indicate also the formation of a thin layer of a GB phase in the one-phase area of the bulk Cu–Bi phase diagram. The points of the abrupt change of the GB segregation form the GB solidus line in the bulk Cu–Bi phase diagram [22, 23, 39, 40]. GB segregation was measured with the aid of Auger electron spectroscopy (AES) on the GB fracture surfaces in samples broken *in situ* in the AES instrument. In other words, the multilayer GB segregation in Cu–Bi alloys leads to the increased *GB brittleness*. In [41] the GB energy was measured in Cu–Bi alloys using individual $\Sigma 19$ GB in bicrystals with the aid of the GB thermal grooves. The thermal groove profile was obtained with the aid of atomic force microscopy. The GB Bi segregation was measured simultaneously in the same conditions. The abrupt change of the segregation coincides with the *discontinuity of GB energy*. This fact demonstrates that the GB premelting (or prewetting) phase transition is of first order. The low-temperature measurements of resistivity temperature coefficient $d\rho/dT$ and residual resistivity ρ_0 at 4 K were performed in [40] using the Cu–Bi polycrystals annealed at high temperature and subsequently quenched. Both $d\rho/dT$ and ρ_0 demonstrate well pronounced break exactly at the same position where the sudden change of GB segregation was observed. In other words, the formation of GB layers of liquid-like phase leads to the measurable changes of *resistivity*.

The enhanced diffusion in case of existence of liquid-like GB phase can improve the plasticity of materials. For examplee, the superplastic forming of micrograined and nanostructured materials is a commercial, viable, manufacturing technology. One of the major drawbacks of conventional superplastic forming is that the phenomenon is only found at relatively low strain rates, typically about 10^{-4} to 10^{-3} s^{-1}. Recently, a number of studies have indicated that superplasticity of nanostructured materials can sometimes occur at extremely high strain rates (greater than 10^{-3} s^{-1} and up to 10^{2} s^{-1}). A specific example is a tensile elongation of over 1250% recorded at a strain rate of 10^{2} s^{-1} [42]. Thus far, this phenomenon, denoted as high-strain-rate superplasticity (HSRS), has been reported in several classes of materials, including metal alloys [42], metal-matrix composites [43–46] and mechanically-alloyed materials [47–49]. Despite these extensive experimental observations, the fundamental understanding of the factors leading to HSRS has not yet been arrived at. One very pertinent fact is that all of the materials that exhibit HSRS have a very fine grain size (~ 1 μm and less). Another is that the phenomenon is observed at rather high homologous matrix temperatures and very close to the matrix solidus temperature. In Fig. 7 the example is shown of HSRS for the 7475 Al–Zn–Mg alloy. The data are taken from independent works [50, 51] and reveal the very good reproducibility of the effect. Both temperature dependences have rather narrow maximum few degrees below the solidus temperature T_S. It is important to mention that the soludus temperature was measured by the differential thermal analysis (DTA) in the same works [50, 51]. The maximum elongation to failure reaches 1250 %. Below T_S the maximal elongation is about 500 %, above T_S the maximal elongation drops very quickly down to almost 0%.

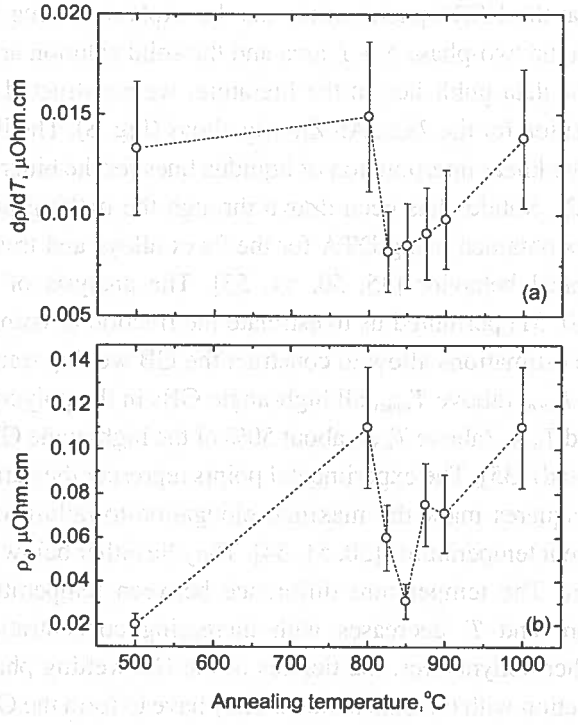

Fig. 6. (a) Dependence of the temperature derivative of the resistivity $d\rho/dT$ and (b) residual resistivity ρ_o of the Cu – 75 at. ppm Bi polycrystals on the annealing temperature

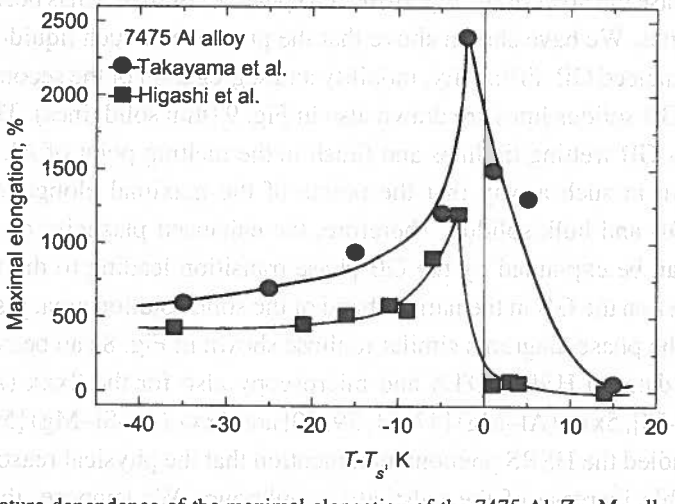

Fig. 7. The temperature dependence of the maximal elongation of the 7475 Al–Zn–Mg alloy samples. T_S is the solidus temperature. Circles represent the data [50] and squares are taken from [51]

We suppose that the HSRS phenomenon can be explained using the ideas on the GB phase transitions in the two-phase $S + L$ area and the solid solution area of the bulk phase diagrams. Using the data published in the literature, we constructed the lines of the GB wetting phase transition for the 7xxx Al–Zn–Mg alloys (Fig. 8). The liquidis line has been constructed using the linear interpolation of liquidus lines for the binary Al–Mg and Al–Zn phase diagrams [52]. Solidus has been drawn through the melting point for Al [52] and experimental points obtained using DTA for the 7xxx alloys and transition from solid to semi-solid mechanical behavior [35, 50, 51, 53]. The analysis of the microstructures published in [35, 50, 51] permitted us to estimate the fraction of completely and partially wetted GBs. These estimations allow to construct the GB wetting transition tie-lines (thin solid lines) for the T_{wmax} (above T_{wmax} all high-angle GBs in the polycrystal are completely wetted) [50, 51] and $T_{w50\%}$ (above $T_{w50\%}$ about 50% of the high-angle GBs in the polycrystal are completely wetted) [35]. The experimental points represent the data of mechanical tests [50, 53–55]. Full squares mark the maximal elongation-to-failure obtained in the tests performed at different temperatures [50, 51, 54]. They lie either below the bulk solidus line or coincide with it. The temperature difference between temperature of the maximal elongation-to-failure and T_s decreases with increasing concentration of Mg and Zn. According to the thermodynamics, the tielines of the GB wetting phase transition cannot finish at the intersection with the bulk solidus. They have to form the GB solidus line which continue in the solid solution area of the bulk phase diagram and finish in the melting point of the pure component. In the limiting case the degenerated GB solidus coincide with the bulk solidus. But in some systems it can extend into the solid solution area like it is shown in Fig. 4. In that case the layer of the liquid-like GB phase exist in the GBs between the GB and bulk solidus lines. We have shown above that the presence of such liquid-like layer in GB leads to the enhanced GB diffusivity, mobility and segregation of the second component [5, 11–17]. Such GB solidus lines are drawn also in Fig. 9 (thin solid lines). They continue the T_{wmax} and $T_{w50\%}$ GB wetting tie lines and finish in the melting point of Al. The GB solidus lines are drawn in such a way that the points of the maximal elongation-to-failure are between the GB and bulk solidus. Therefore, the enhanced plasticity of the nanograined polycrystals can be explained by the GB phase transition leading to the formation of the liquid-like layer on the GB in the narrow band of the solid solution area, just below the bulk solidus line. The phase diagrams similar to those shown in Fig. 8 can be constructed using the published data on HSRS, DTA and microscopy also for the 2xxx (Al–Zn–Mg) [45, 47–59, 51, 56–58], 5xxx (Al–Mg) [47, 51, 59, 60] and 6xxx (Al–Si–Mg) [59, 61–64] alloys. All authors studied the HSRS phenomenon mention that the physical reason of such a huge and reproducible increase of the palsticity is unknown. We suppose, therefore, that the HSRS phenomenon can be explained by the existence of the equilibrium GB liquid-like layer close to the bulk solidus.

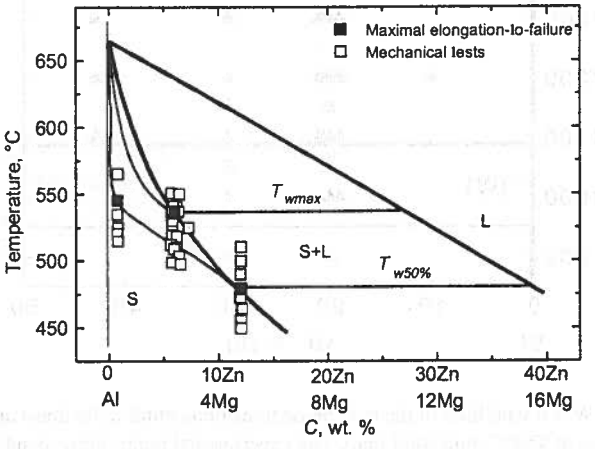

Fig. 8. The phase diagram containing the GB wetting phase transition tie-lines and GB solidus lines constructed for the 7xxx Al–Zn–Mg alloys

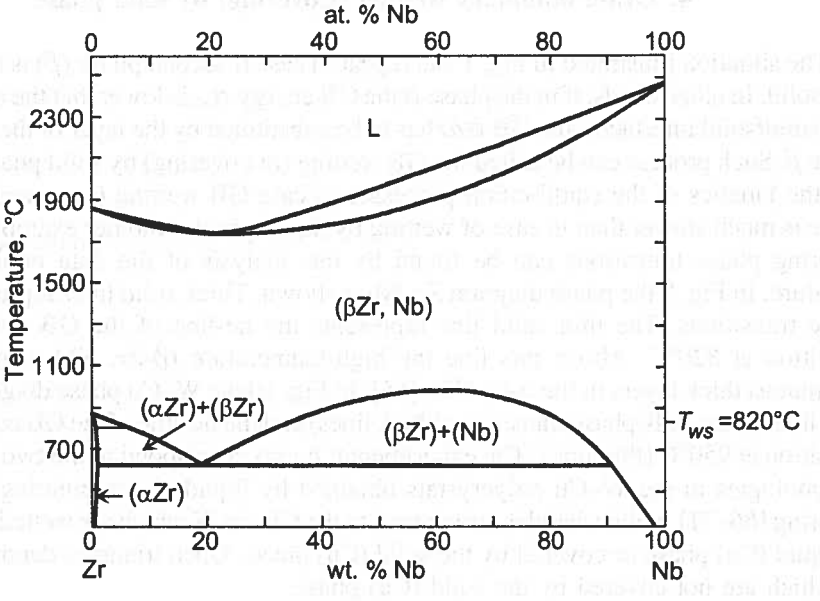

Fig. 9. Phase diagram Zr–Nb with lines of the bulk phase transitions (thick solid lines) and the tie-line of the GB covering phase transition at 820°C (thin solid line)

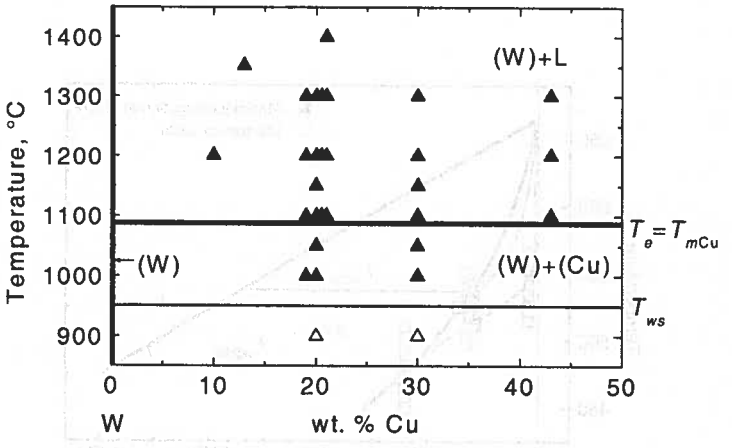

Fig. 10. Phase diagram W–Cu with lines of the bulk phase transitions (thick solid lines) and the tie-line of the GB covering phase transition at 950°C (thin solid line). The experimental points correspond to the two different GB morphologies in the W–Cu polycrystals [66–71]. Solid triangles: GBs in W are wetted by the layers of liquid (Cu) phase or covered by the solid (Cu) phase. Open triangles: GBs in W are not covered by the solid (Cu) phase

4. Grain boundary wetting (Covering) by solid phase

The situation illustrated in Fig. 1 can repeat in case if second phase (β) is not liquid but also solid. In other words, if in the phase α the GB energy $\sigma_{\alpha\alpha}$ is lower that the energy of two α/β solid/solid interfaces, the GB α/α has to be substituted by the layer of the second solid phase β. Such process can be called the GB wetting (or covering) by solid phase. It is clear, that the kinetics of the equlibration processes in case GB wetting (or covering) by solid phase is much slower than in case of wetting by liquid phase. Another examples of the GB covering phase transitions can be found by the analysis of the data published in the literature. In Fig. 9 the phase diagram Zr–Nb is shown. Thick solid lines represent the bulk phase transitions. The thin solid line represents the tie-line of the GB covering phase transition at 820°C. Above this line the high-temperature (β-Zr, Nb) phase forms the continuous thick layers in the α-Zr GBs [65]. In Fig. 10 the W–Cu phase diagram is shown with lines of the bulk phase transitions (thick lines) and the tie-line of the GB covering phase transition at 950°C (thin line). The experimental points correspond to the two different GB morphologies in the W–Cu polycrystals obtained by liquid phase sintering or activated sintering [66–71]. Solid triangles correspond to the GBs in W which are wetted by the layers of liquid (Cu) phase or covered by the solid (Cu) phase. Open triangles denote the GBs in W which are not covered by the solid (Cu) phase.

5. Conclusions

The GB phase transitions can be observed both in two-phase and one-phase areas of the conventional phase diagrams for the bulk phase transitions. In the two-phase $S+L$ area

where solid and liquid phases are in equilibrium the GB wetting phase transition can take place at T_w. Above T_w the GB disappears being substituted by two solid/liquid interfaces and the (macroscopically thick) layer of the liquid phase. The tie-lines of the GB wetting phase transition must have a continuation (GB solidus) in the one-phase S area of the bulk phase diagram. By intersection of GB solidus line the GB prewetting or premelting phase transition proceeds. Between the lines of GB and bulk solidus the grain boundary is substituted by two solid/liquid interfaces and the thin layer of the liquid-like phase. This liquid-like phase is stable in the GB and unstable in the bulk. The liquid-like phase is stabilized in GB due to the energy gain which appears as a result of substitution of GB by two solid/liquid interfaces. The GB wetting and prewetting (premelting) phase transitions observed up-to-date are of first order. If the GB energy is higher than the energy of two solid/solid interfaces, the GB solid state wetting (covering) phase transition can occur in a two-phase $S_1 + S_2$ area of the phase diagram.

Acknowledgements

The financial support of Russian Foundation for Basic Research RFBR Copernicus program of EU (contract ICA2-CT-2001-10008), INTAS grant 03-51-3779 and the German Federal Ministry for Education and Research is acknowledged.

REFERENCES

[1] T.G. Langdon, T. Watanabe, J. Wadsworth, M.J. Mayo, S.R. Nutt, M.E. Kassner, Mater. Sci. Eng. A **166**, 237-242 (1993).
[2] B.B. Straumal, W. Gust, Mater. Sci. Forum, **207-209**, 59-68 (1996).
[3] B. Straumal, D. Molodov, W. Gust, J. Phase Equilibria, **15**, 386-391 (1994).
[4] B. Straumal, T. Muschik, W. Gust, B. Predel, Acta metall. mater. **40**, 939-945 (1992).
[5] L.-S. Chang, E. Rabkin, B.B. Straumal, S. Hofmann, B. Baretzky, W. Gust, Defect Diff. Forum, **156**, 135-146 (1998).
[6] B. Straumal, V. Semenov, V. Glebovsky, W. Gust, Defect Diff. Forum, **143-147**, 1517-1522 (1997).
[7] B.B. Straumal, W. Gust, T. Watanabe, Mater. Sci. Forum, **294-296**, 411-414 (1999).
[8] F. Ernst, M.W. Finnis, A. Koch, C. Schmidt, B. Straumal, W. Gust, Z. Metallk. **87**, 911-922 (1996).
[9] B.B. Straumal, L.S. Shvindlerman, Acta metall. **33**, 1735-1749 (1985).
[10] E.L. Maksimova, L.S. Shvindlerman, B.B. Straumal, Acta metall. **36**, 1573-1583 (1988).
[11] J.W. Cahn, J. Chem. Phys. **66**, 3667-3679 (1977).
[12] S. Dietrich, Wetting transitions in interfaces, in C. Domb and J.H. Lebowitz (eds.), Phase Transitions and Critical Phenomena, **12**, 2-218, Academic Press, London (1988).
[13] D. Jasnov, Rep. Prog. Phys. **47**, 1059-1070 (1984).
[14] G. de Gennes, Rev. Mod. Phys. **57**, 827-863 (1985).
[15] H. Kellay, D. Bonn, J. Meunier, Phys. Rev. Lett. **71**, 2607-2610 (1993).
[16] J.W. Schmidt, M.R. Moldover, J. Chem. Phys. **79**, 379-387 (1983).
[17] N. Eustathopoulos, L. Coudurier, J.C. Joud, P. Desre, J. Crystal Growth **33**, 105-115 (1976).
[18] B. Straumal, W. Gust, D. Molodov, Interface Sci. **3**, 127-132 (1995).

[19] B. Straumal, D. Molodov, W. Gust, Mater. Sci. Forum **207-209**, 437-440 (1996).
[20] B. Straumal, S. Risser, V. Sursaeva, B. Chenal, W. Gust, J. Physique IV 5-C7, 233-241 (1995).
[21] D.A. Molodov, U. Czubayko, G. Gottstein, L.S. Shvindlerman, B.B. Straumal, W. Gust, Phil. Mag. Lett. **72**, 361-368 (1995).
[22] L.-S. Chang, B.B. Straumal, E. Rabkin, W. Gust, F. Sommer, J. Phase Equilibria 18, 128-135 (1997).
[23] L.-S. Chang, E. Rabkin, B. Straumal, P. Lejcek, S. Hofmann, W. Gust, Scripta mater. **37**, 729-735 (1997).
[24] E.I. Rabkin, V.N. Semenov, L.S. Shvindlerman, B.B. Straumal, Acta metall. mater. **39**, 627-639 (1991).
[25] O.I. Noskovich, E.I. Rabkin, V.N. Semenov, L.S. Shvindlerman, B.B. Straumal, Acta metal. mater. **39**, 3091-3098 (1991).
[26] B.B. Straumal, O.I. Noskovich, V.N. Semenov, L.S. Shvindlerman, W. Gust, B. Predel, Acta metall. mater. **40**, 795-801 (1992).
[27] B. Straumal, E. Rabkin, W. Lojkowski, W. Gust, L.S. Shvindlerman, Acta mater. **45**, 1931-1940 (1997).
[28] E. Rabkin, D. Weygand, B. Straumal, V. Semenov, W. Gust, Y. Brechet, Phil. Mag. Lett. **73**, 187-193 (1996).
[29] V.G. Glebovsky, B.B. Straumal, V.N. Semenov, V.G. Sursaeva, W. Gust, High Temp. Mater. Proc. **13**, 67-73 (1994).
[30] M.C. Flemings, Metall. Trans. **A 22**, 957-981 (1991).
[31] P. Kumar, C.L. Martin, S. Brown, Metall. Trans. **A 24**, 1107-1116 (1993).
[32] C.P. Chen, C.-Y.A. Tsao, Acta mater. **45**, 1955-1968 (1997).
[33] M.C. Roth, G.C. Weatherly, W.A. Miller, Acta metall. **28**, 841-853 (1980).
[34] B.L. Vaandrager, G.M. Pharr, Acta metall. **37**, 1057-1066 (1989).
[35] B. Baudelet, M.C. Dang, F. Bordeaux, Scripta Metall. Mater. **32**, 707-712 (1995).
[36] H. Iwasaki, T. Mori, M. Mabuchi, K. Higashi, Acta mater. **46**, 6351-6360 (1998).
[37] G.M. Pharr, P.S. Godavarti, B.L. Vaandrager, J. Mater. Sci. **24**, 784-792 (1989).
[38] J.W. Cahn, J. Phys.Colloq. **43-C6**, 199-213 (1982).
[39] L.-S. Chang, E. Rabkin, B.B. Straumal, B. Baretzky, W. Gust, Acta mater. **47**, 4041-4046 (1999).
[40] B. Straumal, N.E. Sluchanko, W. Gust, Def. Diff. Forum **188-190**, 185-194 (2001).
[41] J. Schölhammer, B. Baretzky, W. Gust, E. Mittemeijer, B. Straumal, Interf. Sci. **9**, 43-53 (2001).
[42] K. Higashi, S. Tanimura, T. Ito, MRS Proc. **196**, 385-390 (1990).
[43] T. Imai, M. Mabuchi, Y. Tozawa, M. Yamada, J. Mater. Sci. Lett. **2**, 255-257 (1990).
[44] M. Mabuchi, T. Imai, J. Mater. Sci. Lett. **9**, 761-762 (1990).
[45] T.G. Nieh, C.A. Henshall, J. Wadsworth, Scripta Metall. **18**, 1405-1408 (1984).
[46] M. Mabuchi, K. Higashi, Y. Okada, S. Tanimura, T. Imai, K. Kubo, Scripta Metall. **25**, 2003-2008 (1991).
[47] T.G. Nieh, P.S. Gilman, J. Wadsworth, Scripta Metall. **19**, 1375-1378 (1985).
[48] T.R. Bieler, T.G. Nieh, J. Wadsworth, A.K. Mukherjee, Scripta Metall. **22**, 81-86 (1988).
[49] K. Higashi, Y. Okada, T. Mukai, S. Tanimura, Scripta Metall. **25**, 2053-2057 (1991).
[50] Y. Takayama, T. Tozawa, H. Kato, Acta mater. **47**, 1263-1270 (1999).
[51] K. Higashi, T.G. Nieh, M. Mabuchi, J. Wadsworth, Scripta metall. mater. **32**, 1079-1084 (1995).
[52] I. Apykhtina, B. Bokstein, A. Khusnutdinova, A. Peteline, S. Rakov, Def. Diff. Forum, **194-199**, 1331-1336 (2001).
[53] T. Imai, M. Mabuchi, Y. Tozawa, Y. Murase, J. Kusul, in R.B. Bhagat. et al. (eds.), Metal & Ceramic Matrix Composites: Processing, Modeling & Mechanical Behavior 235-239, TMS-AIME, Warrendale, Pennsylvania (1990).

[54] M. Mabuchi, K. Higashi, T. Imai, K. Kubo, Scripta Metall. **25**, 1675-1680 (1991).
[55] N. Furushiro, S. Hori, Y. Miyake, in S. Hori et al., (eds.) Proc. Int. Conf. Superplast. Adv. Mats (ICSAM-91) 557-562, Jap. Soc. Res. Superplast., Tokyo (1991).
[56] M. Mabuchi, K. Higashi, T. Langdon, Acta metall. mater. **42**, 1739-1745 (1994).
[57] M. Mabuchi, K. Higashi, S. Wada, S. Tanimura, Scripta Metall. **26**, 1269-1274 (1992).
[58] T.G. Nieh, J. Wadsworth, Scripta Metall. **28**, 1119-1124 (1993).
[59] M. Mabuchi, K. Higashi, K. Inoue, S. Tanimura, Scripta Metall. **26**, 1839-1844 (1992).
[60] J. Koike, M. Mabuchi, K. Higashi, Acta metall. mater. **43**, 199-206 (1995).
[61] M. Mabuchi, K. Higashi, Y. Okada, S. Tanimura, T. Imai, K. Kubo, Scripta Metall. **25**, 2517-2522 (1991).
[62] T. Hikosaka, T. Imai, T.G. Nieh, J. Wadsworth, Scripta Metall. **31**, 118-11186 (1994).
[63] R.B. Grishaber, R.S. Mishra, A.K. Mukherjee, Mat. Sci. & Eng. **A 220**, 78-84 (1996).
[64] T.G. Nieh, D.R. Lesuer, C.K. Syn, Scripta Metall. Mater. **32**, 707-712 (1995).
[65] M.J. Iribarren, O.E. Agüero, F. Dyment, Def. Diff. Forum. **194-199**, 1211-1216 (2001).
[66] Ya.E. Geguzin, Physics of Sintering, 2nd edition. Nauka, Moscow (1984) (in Russian).
[67] V.N. Eremenko, Yu.V. Naidich, I.A. Lavrinenko, Sintering in the Presence of Liquid Phase, Naukova dumka, Kiev (1968) (in Russian).
[68] V.V. Panichkina, M.M. Sirotjuk, V.V. Skorokhod, Poroshk. Metall. **6**, 21-24 (1982) (in Russian).
[69] V.V. Skorokhod, V.V. Panichkina, N.K. Prokushev, Poroshk. Metall. **8**, 14-19 (1986) (in Russian).
[70] V.V. Skorokhod, Yu.M. Solonin, N.I. Filippov, A.N. Poshin, Poroshk. Metall. **9**, 9-14 (1983) (in Russian).
[71] W.J. Huppmann, H. Riegger, Acta metall. **23**, 965-971 (1975).

Received: 1 March 2004.

A R C H I V E S O F M E T A L L U R G Y A N D M A T E R I A L S
Volume 49 2004 Issue 2

W. WOŁCZYŃSKI *, J. KLOCH **

MASS TRANSPORT AT THE SOLID/LIQUID INTERFACE DURING IN SITU GROWTH OF COMPOSITES

TRANSPORT MASY NA FRONCIE KRYSTALIZACJI PODCZAS WZROSTU IN SITU KOMPOZYTÓW

An improved theory for the formation of concentration field ahead the solid/liquid interface of the growing lamellar eutectics is presented. The solution of diffusion equation is given for new formulation of the boundary conditions governing the coupled lamellar growth with a leading phase. The boundary conditions are related to the interplay between the diffusion required for phase separation and the formation of the inter-phase between lamellae. The present analysis of these factors provides a justification for earlier approximate theories. The boundary conditions are formulated in such a way to establish the stability of lamellar structure formation under steady-state. It is assumed that stable growth of the lamellae is ensured by the separation of concentration fields within a boundary layer at the solid/liquid interfaces of α and β phases, respectively. A coordinate system is attached to the s/l interface to be advancing in the z – direction, identically with interface moving at the constant velocity, v. The general mass balance is analysed for the liquid, taking into account the planar s/l interface. The local mass balance is also ensured but it requires to envisage a protrusion of the minor eutectic phase. The existence of lead distance is confirmed experimentally. The difference in undercooling is also considered as a phenomenon associated with the separation of concentration fields and existence of protrusion to relax the assumption of isothermal interface.

W pracy zaprezentowano rozwiązanie problemu formowania się pola stężenia przed frontem krystalizacji eutektyk płytkowych. Zaproponowano stosowne rozwiązanie równania dyfuzji dla nowych warunków brzegowych związanych ze sprzężonym wzrostem eutektyk płytkowych uwzględniającym fazę wiodącą. Warunki brzegowe odniesione są do oddziaływania między dyfuzją wymaganą do separacji faz eutektycznych a formowaniem się granicy między tymi fazami. Prezentowana analiza tych czynników uzasadnia pewne zastosowanie teorii znanych dotąd w tym zakresie. Warunki brzegowe są sformułowane w taki sposób aby zapewnić stabilne formowanie się płytek struktury eutektycznej w warunkach stacjonarnych. Założono że stabilny wzrost płytek jest

* POLISH ACADEMY OF SCIENCES, INSTITUTE OF METALLURGY AND MATERIALS SCIENCE, 30-059 CRACOW, 25 REYMONTA ST. POLAND
** INSTITUTE OF MATHEMATICS, POLISH ACADEMY OF SCIENCES, 31-027 CRACOW, 30 ŚW. TOMASZA STR. POLAND

zapewniony wtedy gdy ma miejsce separacja pól stężenia w strefie dyfuzyjnej przed frontem krystalizacji obydwu faz α i β. Układ współrzędnych jest zaczepiony do frontu krystalizacji i przemieszcza się wraz z nim w kierunku pionowym z ze stałą prędkością v. Analizowany jest ogólny bilans masy dla fazy ciekłej przy założeniu że front krystalizacji jest płaski. Lokalny bilans masy jest również spełniony, ale wymaga uwzględnienia wyprzedzenia fazowego. Istnienie wyprzedzenia fazy zwilżającej przez wiodącą potwierdzono eksperymentalnie. Istnienie różnicy przechłodzenia między frontami faz eutektyki jest również rozważane i traktowane jako zjawisko związane z separacja pól stężenia i istnieniem wyprzedzenia fazowego aby tym samym uwolnić się od założenia o idealnie izotermicznym froncie krystalizacji.

Symbols used in the text

C_E – equilibrium eutectic concentration of solute,
C_S^α – equilibrium solute concentration in α – phase lamella,
C_S^β – equilibrium solute concentration in β – phase lamella,
d – protrusion of the leading minor phase, β, and concentration field parameter,
D – diffusion coefficient in the liquid,
f_α – function used in formulation of boundary condition for α – phase,
f_β – function used in formulation of boundary condition for β – phase,
k_α – partition ratio for the formation of α – phase lamella,
k_β – partition ratio for the formation of β – phase lamella,
S_α – half the width of the α – phase lamella,
S_β – half the width of the β – phase lamella,
T^α – interface temperature resulting from concentration field for α – phase,
T^β – interface temperature resulting from concentration field for β – phase,
T^* – real temperature of the s/l interface,
T_E – equilibrium eutectic temperature,
v – stationary growth rate of the composite *in situ*,
δC^α – concentration field in the liquid ahead the s/l interface of α – phase,
δC^β – concentration field in the liquid ahead the s/l interface of β – phase,
ΔT_α^* – total undercooling of the s/l interface of α – phase,
ΔT_β^* – total undercooling of the s/l interface of β – phase.

1. Introduction

The foundations for theoretical description of mass transport ahead the solid/liquid interface of growing eutectics of lamellar structure has been laid by J a c k s o n - H u n t [1]. The solution of the diffusion equation (known as J-H theory)

$$\nabla^2 C + \frac{v}{D}\frac{\partial C}{\partial z} = 0, \quad \text{with} \quad C = C_E + C_\infty \text{ at } z = \infty \tag{1}$$

was found by J a c k s o n - H u n t [1] under assumption that solid/liquid interface is plane. The J-H theory, that is, steady-state solution of the diffusion equation (1), for a lamellar eutectic growth at constant growth rate, v, with planar s/l interface was given with liquid on or off eutectic composition. So,

$$\frac{\partial C}{\partial x} = 0, \quad \text{at } x = 0 \quad \text{and} \quad x = S_\alpha + S_\beta \tag{2}$$

in the J-H theory. The conservation of mass balance suggested by J-H theory is:

$$\frac{\partial C}{\partial z} = \mp \frac{v C_0^S}{D}; \quad (S = \alpha, \beta) \quad \text{at} \quad z = 0, \quad \text{for} \quad 0 \le x < S_\alpha \quad \text{and} \quad S_\alpha < x \le S_\alpha + S_\beta. \tag{3}$$

t

The solution of equation (1) given by J-H theory is plotted schematically in Fig. 1a. with corresponding undercooling, Fig. 1b and interface curvature, Fig. 1c, [2].

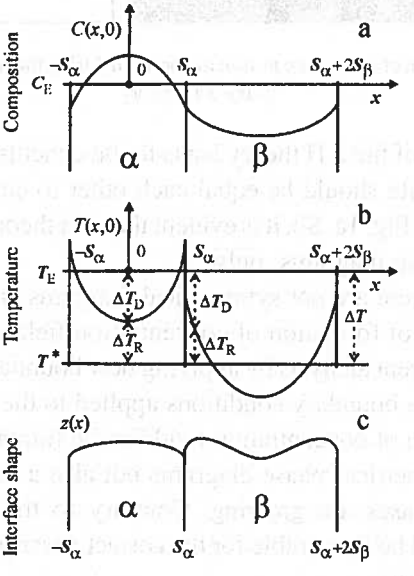

Fig. 1. Scheme of the solid/liquid interface showing a plot of: a/ interface composition, b/ solute undercooling, ΔT_D, curvature undercooling ΔT_R, c/ interface shape, [2]

According to the scheme (Fig. 1a) some parts of α – phase should grow from the liquid of the solute content adequate to the formation of β – phase, rather. It could lead to the changes in inter-lamellar spacing. Some changes of the spacing are possible during the real solidification as described in the model delivered by M a g n i n - T r i v e d i [3]. Adjustments of an inter-lamellar spacing during the composite growth are explained from the viewpoint of the behaviour of a mechanical equilibrium at the triple point of the solid/liquid interface, [3].

An instability of a lamellar structure formation is also the subject of current analysis (Fig. 2a). The observation is compared with some theoretical predictions given in the J-H theory, (Fig. 2b). The J-H stability/instability considerations are developed in some treatments dealing with the s/l interface response on the imposed perturbation (C l i n e [4], H u r l e - J a k e m a n [5], S t r a s s l e r - S c h n e i d e r [6], D a t y e - L a n g e r [7] and K a r m a - S a r k i s s i a n [8]).

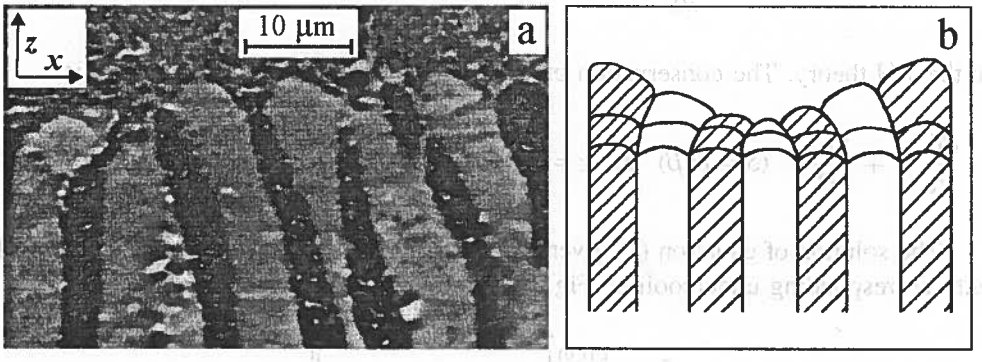

Fig. 2. Instability of the formation of composite *in situ*: a) observed during the real solidification, b) concluded due to the J-H theory

The detailed analysis of the J-H theory leads to the conclusion that the volumes of two solid phases of a composite should be equal each other to ensure the stable growth as it results from the scheme in Fig. 1a. So, it is evident that J-H theory is good approximation for symmetrical eutectic phase diagrams, only.

However, in reality there are not symmetrical diagrams and this restriction should be removed from the theory of formation of concentration field ahead the s/l interface. This attempt is made in the current analysis by applying new boundary conditions to the solution of diffusion equation. The boundary conditions applied to the current analysis ensure not only improved description of concentration field for the formation of eutectic structure of an alloy from real asymmetrical phase diagrams but also a separation of the liquid from which different solid phases are growing. Contrary to the J-H theory, the improved concentration field should be favourable for the correct description of a stable formation of directional eutectic structure.

The assumptions of non separation of concentration fields in the liquid applied in the J-H theory together with concept of ideally coupled growth ($\Delta T^*_\alpha = \Delta T^*_\beta = \Delta T$, Fig. 1b), results in a discontinuity of solute undercooling at the α/β– inter-phase, Fig. 1b. According to the scheme shown in Fig. 1b, some parts of the α– phase lamella should grow outside the assumed regime of the ideally coupled growth: $T^* - T_E$. Analogously, the middle part of the β– phase lamella should also grow outside the mentioned regime: $T^* - T_E$, Fig. 1b.

Moreover, the curvature undercooling compensating a behaviour of solute undercooling within the regime of ideally coupled growth: $T^* - T_E$ produces the non realistic curvature of the s/l interface, Fig.1c.

The detailed analysis of the scheme shown in Fig. 1a, [2], indicates that the concentration profile is not correct. This kind of profile can be observed when α – phase is represented by wider lamella than β – phase, as it results from the solution of equation (1) for which mass balance is satisfied at each z – coordinate. The satisfaction of mass balance is not visible in Fig. 1a. The corrected scheme proper for the solution of equation (1) is shown in Fig. 3a. It corresponds to the phase diagram, Fig. 4b, according which $|C_0^\alpha| < |C_0^\beta|$ and in consequence $S_\alpha > S_\beta$ as it is visible in Fig. 4a. The mentioned condition is not fulfilled in Fig. 1a plotted by Hunt-Jackson [2], next reproduced by Elliott [9], Rutter [10] and Kurz-Fisher [11].

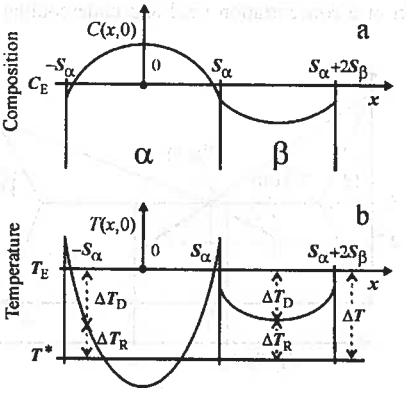

Fig. 3. Corrected schemes of: a) solute profile with satisfaction of mass balance at $z = 0$ and b) adequate solute and curvature undercooling of the solid/liquid interface, due to the J-H theory

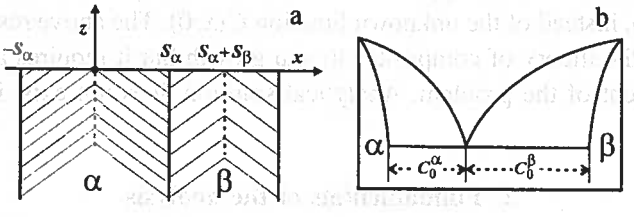

Fig. 4. Schemes of a) planar lamellar composite *in situ* interface showing geometrical definitions of the structure, b) phase diagram giving the definitions of both parameters C_0^α and C_0^β, related to the width of both lamellae, respectively

The solute undercooling corresponding to the concentration profile proper for the J-H theory is shown schematically in Fig. 3b.

A concentration field shown in Fig. 1a as well as undercooling, Fig. 1b could be illustrated on the phase diagram, as it is plotted schematically in Fig. 5.

However, taking into account that the scheme shown in Fig. 1 was corrected in Fig. 3 the adequate interpretation should also be improved. The phase diagram with corrected concentration field and undercooling is given in Fig. 6.

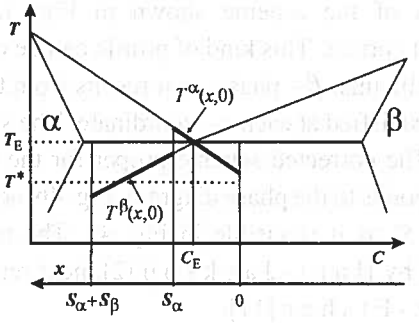

Fig. 5. Interpretation of a concentration field and undercooling both given in Fig. 1

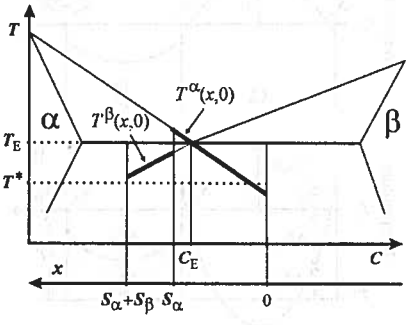

Fig. 6. Interpretation of a corrected concentration field and undercooling from Fig. 3

The boundary condition (3) applied in J-H theory contains the constant C_0^S ($S = \alpha, \beta$), defined in Fig. 4b, instead of the unknown function $C(x, 0)$. The above restriction could be eliminated from the theory of composites in situ growth but it requires an application of numerical treatment of the problem. Analytical solution does not exist in literature.

2. Fundamentals of the analysis

The foundations for the current analysis of a concentration field ahead of the solid/liquid interface of composites *in situ* of lamellar structure are improved in comparison with those of J-H theory. First of all the current model is no more associated with the concept of ideally coupled growth of eutectic structure, that is with
$\Delta T_\alpha^* = \Delta T_\beta^* = \Delta T = \Delta T_D(x, 0) + \Delta T_R(x, 0)$.

The assumed separation of concentration fields ahead of each lamella allows to consider real asymmetrical phase diagrams. Moreover, an improved concentration field is adequate for description of a stable formation of directional eutectic structure. So, α – phase and β – phase lamellae are formed properly to their *liquidus* lines positions within the zone of undercooling, respectively, Fig. 7.

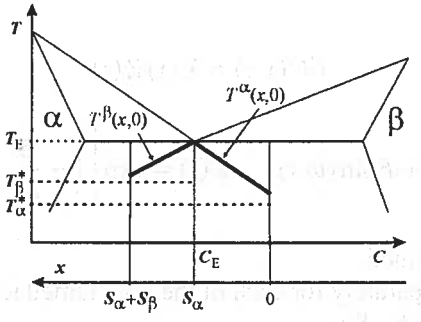

Fig. 7. Interpretation of concentration field and undercooling due to the current model

According to the scheme shown in Fig. 7 the following definitions are assumed in the proposed analysis associated with the concept of coupled growth ($\Delta T^*_\alpha \neq \Delta T^*_\beta$):
a/ for solute undercooling

$$\delta T^\alpha(x,0) = T^\alpha(x,0) - T_E \quad \text{and} \quad \delta T^\beta(x,0) = T^\beta(x,0) - T_E \tag{4}$$

b/ for curvature undercooling

$$\delta T^\alpha_R(x,0) = T^*_\alpha - T^\alpha(x,0) \quad \text{and} \quad \delta T^\beta_R(x,0) = T^*_\beta - T^\beta(x,0) \tag{5}$$

c/ for total undercooling, according to the concept of coupled growth

$$\delta T^\alpha(x,0) + \delta T^\alpha_R(x,0) = \Delta T^*_\alpha \quad \text{and} \quad \delta T^\beta(x,0) + \delta T^\beta_D(x,0) = \Delta T^*_\beta \tag{6}$$

d/ for concentration field

$$\delta C^\alpha(x,0) = C^\alpha(x,0) - C_E \quad \text{and} \quad \delta C^\beta(x,0) = C^\beta(x,0) - C_E. \tag{7}$$

Consequentially,

$$C^\alpha_0(S_\alpha,0) = C^\alpha_S(S_\alpha,0) - C_E < 0 \quad \text{and} \quad C^\beta_0(S_\alpha,0) = C^\beta_S(S_\alpha,0) - C_E > 0. \tag{8}$$

Definitions (8) correspond to parameters C^α_0 and C^β_0 known in J-H theory and shown in Fig. 4b. The boundary condition applied in the model is as follows, (Fig. 7):

$$\delta C(S_\alpha,z) = C(S_\alpha,z) - C_E = 0. \tag{9}$$

The general solution of the diffusion equation

$$\frac{\partial^2 \delta C}{\partial x^2} + \frac{\partial^2 \delta C}{\partial z^2} + \frac{v}{D}\frac{\partial \delta C}{\partial z} = 0 \tag{10}$$

is:

$$\delta C(x,z) = X(x)Z(z) \tag{11}$$

$$X(x) = A\cos(\omega x) + B\sin(\omega x), \qquad Z(z) = \exp\left[\left(-\frac{v}{2D} - \sqrt{\frac{v^2}{4D^2} + \omega^2}\right)z\right] \tag{12}$$

and: A, B, ω are to be defined.
The solutions are given separately for each of the both lamellae under assumption that the s/l interface is plane, Fig. 4a. So,
A/ for the α – phase lamella, that is for $x \in [0, S_\alpha]$, $z \geq 0$
The values of the B and ω parameters yield from conditions:

$$\left.\frac{\partial \delta C(x,z)}{\partial x}\right|_{x=0} = 0 \tag{13}$$

$$\delta C(S_\alpha, z) = 0\,. \tag{14}$$

It is evident from (13) that $-\omega A \sin(\omega \cdot 0) + \omega B \cos(\omega \cdot 0) = 0$, and finally $B = 0$ and from (13) and (14): $A\cos(\omega S_\alpha) = 0$ and $\omega = \omega_{2n-1} = \dfrac{(2n-1)\pi}{2S_\alpha}$, $n = 1,2,....$
Considering (11) and (12) with both above definitions it can be written that general solution of (10) with conditions (13) and (14) is:

$$\delta C(x,z) = \sum_{n=1}^{\infty} A_{2n-1} \cos\left(\frac{(2n-1)\pi x}{2S_\alpha}\right) \exp\left[\left(-\frac{v}{2D} - \sqrt{\frac{v^2}{4D^2} + \left(\frac{(2n-1)\pi}{2S_\alpha}\right)^2}\right)z\right], \tag{15}$$

where A_{2n-1} are constants. Assuming that for slow solidification

$$\frac{(2n-1)\pi}{2S_\alpha} >> \frac{v}{2D}, \tag{16}$$

(15) reduces to:

$$\delta C(x,z) = \sum_{n=1}^{\infty} A_{2n-1} \cos\left(\frac{(2n-1)\pi x}{2S_\alpha}\right) \exp\left(-\frac{(2n-1)\pi}{2S_\alpha} z\right). \tag{15*}$$

The values of A_{2n-1} parameters are calculated from:

$$\left.\frac{\partial \delta C(x,z)}{\partial z}\right|_{z=0} = f_\alpha(x); \quad f_\alpha(x) < 0, \quad x \in [0, S_\alpha]. \tag{17}$$

Applying (16) or (16*), it can be written for rapid and slow solidification, respectively:

$$\left.\frac{\partial \delta C(x,z)}{\partial z}\right|_{z=0} = \sum_{n=1}^{\infty} A_{2n-1}\left(-\frac{v}{2D} - \sqrt{\frac{v^2}{4D^2} + \left(\frac{(2n-1)\pi}{2S_\alpha}\right)^2}\right)\cos\left(\frac{(2n-1)\pi x}{2S_\alpha}\right) \tag{18}$$

$$\left.\frac{\partial \delta C(x,z)}{\partial z}\right|_{z=0} = \sum_{n=1}^{\infty} A_{2n-1}\left(-\frac{(2n-1)\pi}{2S_\alpha}\right)\cos\left(\frac{(2n-1)\pi x}{2S_\alpha}\right). \tag{18*}$$

Additionally, it is to be introduced that

$$f(x), \quad -2S_\alpha \le x \le 2S_\alpha, \quad f(-x) = f(x), \quad f(x + 2S_\alpha) = -f(x). \tag{19}$$

Next the following property of the $f(x)$ – function is to be applied

$$f(x) \approx \frac{a_0}{2} + \sum_{n-1}^{\infty} a_n \cos\left(\frac{n\pi x}{2S_\alpha}\right) \tag{20}$$

$$f(x) \approx \frac{a_0}{2} + \int_0^{2S_\alpha} f(x)\cos\left(\frac{n\pi x}{2S_\alpha}\right)dx. \tag{21}$$

Assuming that $f(x + 2S_\alpha) = -f(x)$ it yields $a_{2k} = 0$, $k = 0, 1, 2,...$ for $n = 2k$ and

$a_{2k-1} = \frac{2}{S_\alpha}\int_0^{S_\alpha} f(x)\cos\left(\frac{(2k-1)\pi x}{2S_\alpha}\right)dx$, $k = 1,2,...$ for $n = 2k - 1$, $k = 1,2,...$.

Finally, the *Fourier* series of the $f(x)$ is:

$$f(x) \approx \sum_{k=1}^{\infty} a_{2k-1}\cos\left(\frac{(2k-1)\pi x}{2S_\alpha}\right). \tag{22}$$

After some rearrangements it can be written:

a/ for rapid solidification

$$A_{2n-1} = \left(-\frac{v}{2D} - \sqrt{\frac{v^2}{4D^2} + \left(\frac{(2n-1)\pi}{2S_\alpha}\right)^2}\right)^{-1} \frac{2}{S_\alpha}\int_0^{S_\alpha} f_\alpha(x)\cos\left(\frac{(2n-1)\pi x}{2S_\alpha}\right)dx, \tag{23}$$

$n = 1,2,...$

b/ for slow solidification

$$A_{2n-1} = -\frac{4}{(2n-1)\pi}\int_0^{S_\alpha} f_\alpha(x)\cos\left(\frac{(2n-1)\pi x}{2S_\alpha}\right)dx, \quad n = 1,2,.... \tag{23*}$$

It can be easily proved that solution of (10) given by (15), (15*) and (23), (23*) satisfies

conditions:

$$\left.\frac{\partial \delta C(x,z)}{\partial x}\right|_{x=0} = \left.\frac{\partial \delta C(x,z)}{\partial x}\right|_{x=2S_\alpha} = 0, \tag{24}$$

$$\left.\frac{\partial \delta C(x,z)}{\partial z}\right|_{z=0} = f_\alpha(x) = f_\alpha(-x) = -f_\alpha(-x+2S_\alpha) = -\left.\frac{\partial \delta C(-x+2S_\alpha,z)}{\partial z}\right|_{z=0} \tag{25}$$

$x \in [0, S_\alpha]$

due to the assumption: $f_\alpha(-x) = f_\alpha, (x), \quad f_\alpha(x+2S_\alpha) = -f_\alpha(x)$.
B/ for the β – phase lamella, that is for $x \in \lfloor S_\alpha,\ S_\alpha + S_\beta \rfloor$, $z \geq 0$

The solution of (10) is given separately for the β – phase lamella, however it is found similarly to that for the α – phase lamella. So,
a/ for rapid solidification

$$\delta C(x,z) = \sum_{n=1}^{\infty} B_{2n-1} \cos\left(\frac{(2n-1)\pi(x - S_\alpha + S_\beta)}{2S_\beta}\right) \exp\left[\left(-\frac{v}{2D^2} - \sqrt{\frac{v^2}{4D^2} + \left(\frac{(2n-1)\pi}{2S_\beta}\right)^2}\right) z\right] \tag{26}$$

$$B_{2n-1} = \left(-\frac{v}{2E} - \sqrt{\frac{v^2}{4D^2} + \left(\frac{(2n+1)\pi}{2S_\beta}\right)^2}\right)^{-1} \frac{2}{S_\beta} \int_{S_\alpha - S_\beta}^{S_\alpha} f_\beta(x) \cos\left(\frac{(2n+1)\pi(x - S_\alpha + S_\beta)}{2S_\beta}\right) dx. \tag{27}$$

b/ for slow solidification

$$\delta C(x,z) = \sum_{n=1}^{\infty} B_{2n-1} \cos\left(\frac{(2n-1)\pi(x - S_\alpha + S_\beta)}{2S_\beta}\right) \exp\left(-\frac{(2n-1)\pi}{2S_\beta} z\right) \tag{26*}$$

$$B_{2n-1} = -\frac{4}{(2n-1)\pi} \int_{S_\alpha - S_\beta}^{S_\alpha} f_\beta(x) \cos\left(\frac{(2n-1)\pi(x - S_\alpha + S_\beta)}{2S_\beta}\right) dx,$$

$$n = 1,2,\ldots, \tag{27*}$$

where

$$\left.\frac{\partial \delta C(x,z)}{\partial z}\right|_{z=0} = f_\beta(x), \quad x \in [0, S_\beta]. \tag{28}$$

Both separately obtained solutions of (10), for slow solidification, for α – phase lamella, (15*) and for β – phase lamella, (26*) are shown schematically in Fig. 8a together with the suggested concept of coupled growth, Fig. 8b.

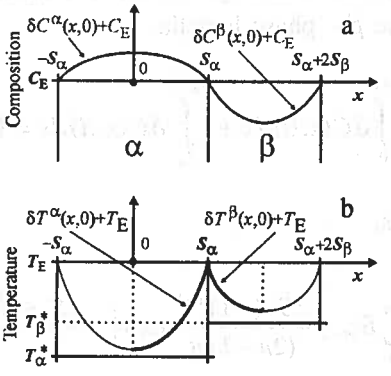

Fig. 8. Schemes of: a) solute profile at $z = 0$ and b) adequate solute and curvature undercooling of the solid/liquid interface due to the current analysis

3. Mass balance within the concentration field

At first the general mass is analysed in order to find the relationship between A_{2n-1} and B_{2n-1} parameters:

A/ general mass balance is:

$$\int_0^\infty \int_0^{S_\alpha} \delta C(x,z)\,dxdz + \int_0^\infty \int_{S_\alpha}^{S_\alpha+S_\beta} \delta C(x,z)\,dxdz + = \sum_{n=1}^{\infty} \frac{4(-1)^{n-1} D}{(2n-1)\pi}$$

$$\left(\frac{A_{2n-1} S_\alpha^2}{\nu S_\alpha + \sqrt{\nu^2 S_\alpha^2 + (2n-1)^2 D^2 \pi^2}} - \frac{B_{2n-1} S_\beta^2}{\nu S_\beta + \sqrt{\nu^2 S_\beta^2 + (2n-1)^2 D^2 \pi^2}} \right) = 0, \tag{29}$$

where

a/ for rapid solidification

$$B_{2n-1} = \frac{A_{2n-1} S_\alpha^2 (\nu S_\beta + \sqrt{\nu^2 S_\beta^2 + (2n-1)^2 D^2 \pi^2})}{S_\beta^2 (\nu S_\alpha + \sqrt{\nu^2 S_\alpha^2 + (2n-1)^2 D^2 \pi^2})}, \quad n = 1,2,\ldots., \tag{30}$$

b/ for slow solidification

$$B_{2n-1} = A_{2n-1}\left(\frac{S_\alpha}{S_\beta}\right)^2, \quad n = 1,2,.... \tag{30*}$$

B/ local mass balance

An analysis of the local mass balance proves that it is satisfied at $z = 0$ for the α – phase lamella and at $z = d$ for the β – phase lamella.

$$\int_0^{S_\alpha} \delta C(x,0)\,dx + \int_{S_\alpha}^{S_\alpha+S_\beta} \delta C(x,d)\,dx = 0\,. \tag{31}$$

After some rearrangements,

$$\sum_{n=1}^{\infty} A_{2n-1}\frac{2S_\alpha(-1)^{n-1}}{(2n-1)\pi} - \sum_{n=1}^{\infty} B_{2n-1}\frac{2S_\beta(-1)^{n-1}}{(2n-1)\pi}\exp\left(-\frac{vS_\beta+\sqrt{v^2S_\beta^2+(2n-1)^2D^2\pi^2}}{2DS_\beta}d\right) = 0 \tag{32}$$

Thus, the definition of the d – phase protrusion is:

a/ for rapid solidification

$$\sum_{n=1}^{\infty} A_{2n-1}\frac{(-1)^{n-1}}{(2n-1)}\times$$

$$\left(1 - \frac{S_\alpha(vS_\beta+\sqrt{v^2S_\beta^2+(2n-1)^2D^2\pi^2})}{S_\beta(vS_\alpha+\sqrt{v^2S_\alpha^2+(2n-1)^2D^2\pi^2})}\exp\left(-\frac{vS_\beta+\sqrt{v^2S_\beta^2+(2n-1)^2D^2\pi^2}}{2DS_\beta}d\right)\right) = 0 \tag{33}$$

b/ for slow solidification

$$\sum_{n=1}^{\infty} A_{2n-1}\frac{(-1)^{n-1}}{(2n-1)}\left(1 - \frac{S_\alpha}{S_\beta}\exp\left(-\frac{(2n-1)\pi}{2S_\beta}d\right)\right) = 0 \tag{33*}$$

C/ α / β – boundary mass balance.

Taking into account that local mass balance is satisfied at $z = 0$ for the wider α – phase lamella and at $z = d$, for the β – phase lamella the boundary mass balance is also considered at the same localization. The existence of the d – protrusion has been confirmed experimentally, Fig. 9a and described theoretically, [12] - [17].

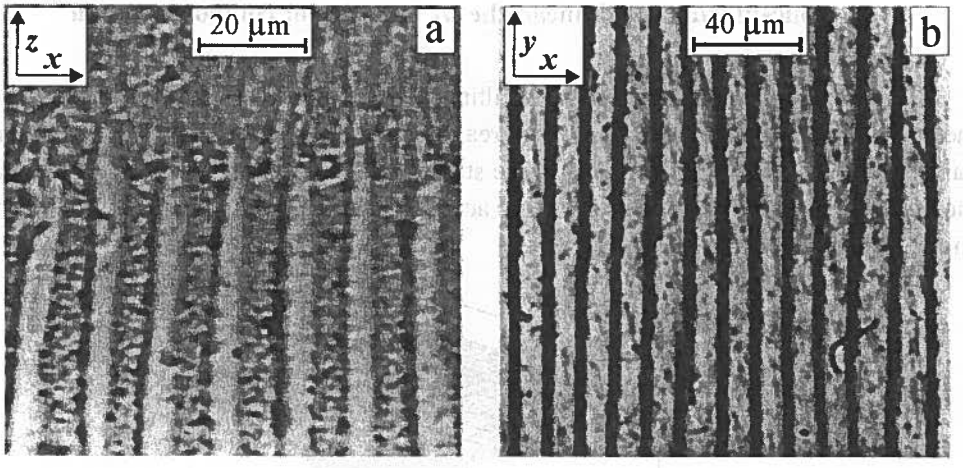

Fig. 9. Morphology of the Pb-Cd composite *in situ*, a) frozen s/l interface revealing the protrusion of lamellae of the (Cd) – phase, b) stationary selection of the lamellae size

It is confirmed experimentally, that usually a minor phase is a leading phase, [13]. It corresponds to the analysis of local mass balance, (31) – (33*) according which the d – protrusion is observable at minor phase interface, only.

The s/l interface mass balance is:

$$S_\alpha \frac{\partial \delta C^\alpha(x,0)}{\partial z} = S_\alpha \frac{v}{D}(1-k_\alpha) C^\alpha(x,0), \quad x \in [0, S_\alpha] \tag{34}$$

$$S_\beta \frac{\partial \delta C^\beta(x,d)}{\partial z} = S_\beta \frac{v}{D}(1-k_\beta) C^\beta(x,d), \quad x \in [S_\alpha, S_\alpha, S_\beta]. \tag{35}$$

The α / β boundary mass balance is:

$$\lim_{x \to S_\alpha^-} S_\alpha \frac{\partial \delta C^\alpha(x,0)}{\partial z} + \lim_{x \to S_\alpha^+} S_\beta \frac{\partial \delta C^\beta(x,d)}{\partial z} =$$
$$S_\alpha \frac{v}{D} C_0^\alpha(S_\alpha,0) + S_\beta \frac{v}{D} C_0^\beta(S_\alpha,d) = \frac{v}{D}(S_\alpha C_0^\alpha(S_\alpha 0) + S_\beta C_0^\beta(S_\alpha,d)) = 0. \tag{36}$$

The satisfaction of the α / β – boundary mass balance means that thermodynamic equilibrium is ensured at the triple point of the s/l interface with protrusion of the leading phase. Additionally, it justifies an application of the boundary condition (14) illustrated in Fig. 7 and Fig. 8.

4. Concentration field ahead the s/l interface of composite *in situ*

A d – protrusion of the minor phase resulting from the local mass balance considerations means that this part of the composite is in reality a transition phase, [15]. Transition phase has properties of the liquid but solid phase structure. So, concentration field exists within the transition phase (S_β, d) and is taken into account in general mass balance, (29). It can be shown schematically as in Fig. 10.

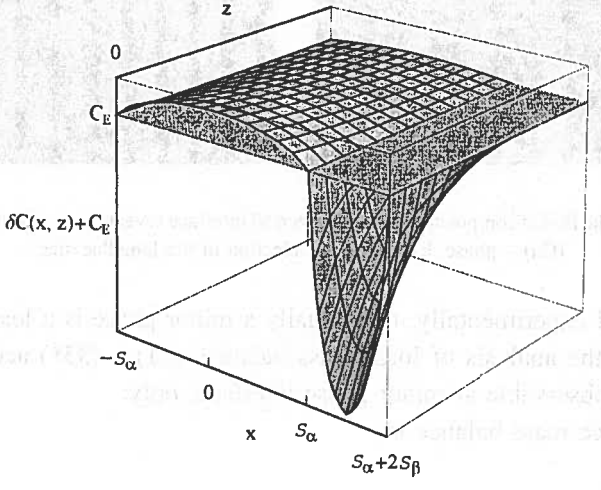

Fig. 10. Concentarion field ahead the solid/liquid interface showing the general mass balance in the liquid; transition phase (S_β, d) is treated as a liquid

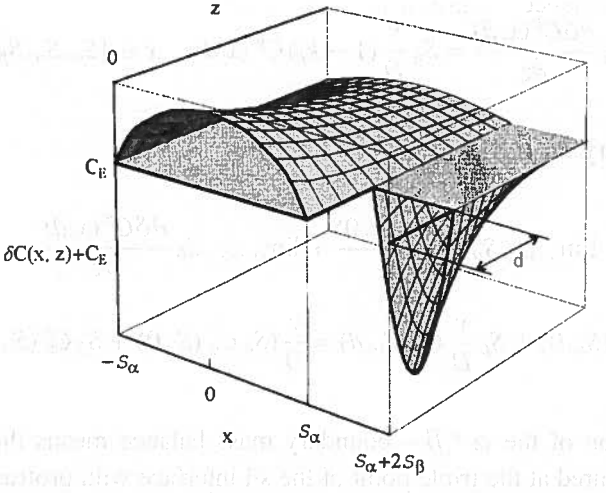

Fig. 11. Concentration field ahead the s/l interface showing the d – protrusion of a leading phase; mass balance is marked with bold line encountering solute profile

However, the transition phase is to be shown while the local mass balance is envisaged, Fig. 11.

The following conditions resulting from the satisfaction of the boundary mass balance are integral parts of both concentration fields shown in Fig. 10 and Fig. 11, respectively.

$$\frac{\partial \delta C(S_\alpha, z)}{\partial z} = const. \quad \text{with} \quad C(S_\alpha, z) = C_E. \tag{37}$$

5. Concluding remarks

The proposed model of coupled growth of both lamellae from the separate liquids, respectively, is favourable for the stable formation of directional eutectic structure of the stationary size. So, some changes in inter-lamellar spacing cannot be observed when solute concentration just ahead the inter-phase boundary is $C|_{x=S_\alpha} = C_E$ for $z \in [0, \infty]$, Fig. 9b. Some perturbations of the separation of both liquids can scarcely lead to unstable growth of the directional structure, Fig. 2a. However, in this case (14) and (37) cannot be satisfied.

The d – protrusion is created during composite growth as proved by (33) or (33*) and confirmed experimentally, Fig. 9a to ensure the mass balance at the solid/liquid interface, Fig. 11. The (S_β, d) – part of the β – phase is the transition phase, which has properties of the liquid, so that the concentration field is created within the transition phase, Fig. 10. The parameter d tends to zero with $z \to \infty$.

Contrary to the concept of ideally coupled growth, [2] the proposed concept of coupled growth is based on a difference in undercooling of the s/l interface of both lamellae. The concept of coupled growth is strictly associated with the separation of concentration fields in the liquid and existence of a protrusion of the leading minor phase to relax the assumption of ideally isothermal s/l interface.

The formula (16) is satisfied for slow solidification which occurs during composite *in situ* formation. Therefore, in this case (30) reduces to (30*) and it can be proved that for slow solidification during composite *in situ* growth not only the equation $B_{2n-1} = A_{2n-1}\left(\frac{S_\alpha}{S_\beta}\right)^2$, $n = 1,2,...$ is satisfied, but $\left|f_\beta\left(x\frac{S_\beta}{S_\alpha}\right)\right| = |f_\alpha(x)|\left(\frac{S_\alpha}{S_\beta}\right)^2$ as well.

It can easily be proved that current description of concentration field (15) or (15*) reduces to the description of concentration field given by the J-H theory. It requires, however to apply some parameters defining the symmetrical phase diagram, that is: $S_\alpha = S_\beta$. Then, $C_0^\alpha = C_0^\beta$ as imposed by the condition $B_0 = 0$, in J-H theory.

In this case the protrusion disappears in the present model, $d = 0$. However, the C_E concentration comes back just at the α/β boundary in J-H theory and local mass balance is satisfied for each z – coordinate, the same for both lamellae. In the consequence, it can be written that $|f_\alpha| = |f_\beta|$ in the present model. Therefore, the condition (14) as well as (37) are also satisfied in the J-H theory.

Thus, it is evident that the J-H theory is good approximation for the so-called symmetrical phase diagrams, only.

The current model shows some relationships not only for composite *in situ* growth (slow solidification) but is developed for rapid solidification as well.

REFERENCES

[1] K.A. Jackson, J.D. Hunt, Trans. AIME, **236** 1129-1142 (1966).
[2] J.D. Hunt, K.A. Jackson, Trans. AIME, **236** 843-852 (1966).
[3] P. Magnin, R. Trivedi, Acta Metall. Mater. **39**, 453-467, (1991).
[4] H.E. Cline, Trans. AIME **242** 1613-1618 (1968).
[5] D.T. Hurle, E. Jakeman, Journal of Crystal Growth **3-4**, 574-582 (1968).
[6] S. Strassler, W.R. Schneider, Phys. Condens. Matter **17**, 153-164 (1974).
[7] V. Datye, J.S. Langer, Phys. Rev. **24B**, 4155-4162 (1981).
[8] A. Karma, A. Sarkissian, Journal of Comp. Phys. **17**, 143-182 (1995).
[9] R. Elliott, Chapter 3 in: Eutectic Solidification Processing, 92-119 1983.
[10] J.W. Rutter, Journal of Crystal Growth **42**, 515-525, (1977).
[11] W. Kurz, D.J. Fisher, Fundamentals of Solidification, 93-115 1992.
[12] V.L. Davies, Journal of the Institute of Metals **93**, 10-14, (1964/5).
[13] W. Wołczyński, Crystal Research and Technology **25**, 1303-1309 (1990).
[14] W. Wołczyński, Crystal Research and Technology **25**, 1433-1437 (1990).
[15] W. Wołczyński, Crystal Research and Technology **26**, 173-178 (1991).
[16] W. Wołczyński, Crystal Research and Technology **27**, 121-125 (1992).
[17] W. Wołczyński, Crystal Research and Technology **27**, 195-200 (1992).

Received: 1 March 2004.

A R C H I V E S O F M E T A L L U R G Y A N D M A T E R I A L S
Volume 49 2004 Issue 2

M.A.J. SOMERS *

SELECTED TOPICS ON MASS TRANSPORT IN GAS-SOLID INTERACTIONS

WYBRANE ZAGADNIENIA Z DZIEDZINY TRANSPORTU MASY PODCZAS ODDZIAŁYWANIA GAZ-CIAŁO STAŁE

The present article is a short review containing examples of the role of mass transport in the solid state during gas-solid interactions. Examples are taken from the authors' research on the interaction of carbon and/or nitrogen with iron-based metals. Topics dealt with are diffusion-controlled dissolution of carbon in an austenite matrix, nucleation of nitrides at an iron surface, the competition between surface reaction and solid state diffusion during iron-nitride layer growth and the evolution of the morphology of a carbonitride layer during nitrocarburizing. The work presented focuses on the kinetics of phenomena in the solid state. Various experimental techniques were applied to investigate these phenomena; it is however beyond the scope of the present article to treat experimental conditions in detail. The interested reader is referred to the original work for in depth discussions of the experimental details.

Praca stanowi krótki, zilustrowany przykładami przegląd roli transportu masy w stanie stałym podczas oddziaływania gaz-ciało stałe. Przykłady pochodzą z badań autorów nad oddziaływaniem węgla i/lub azotu z materiałami na bazie żelaza. Poruszane zagadnienia to rozpuszczanie węgla w austenicie kontrolowane dyfuzją, zarodkowanie azotków na powierzchni żelaza, określenie który z mechanizmów (reakcja na granicy faz ciało stałe-gaz lub dyfuzja w stanie stałym) jest dominujący podczas wzrostu warstwy azotku żelaza, i dodatkowo rozwój morfologii warstwy azotku węgla podczas cyjanowania gazowego. Autorzy koncentrują uwagę na kinetyce zjawisk w ciele stałym. Do zbadania zjawiska zastosowano szereg technik badawczych.

1. Introduction

Gas-solid interactions can be both beneficial as well as harmful for materials properties and materials performance. The incorporation of carbon in a steel surface with the purpose of surface hardening (carburizing) is a classical example of intentional surface engineering

* DEPARTAMENT OF MANUFACTURING ENGINEERING AND MANAGEMENT, THE TECHNICAL UNIVERSITY OF DENMARK, KEMITORVET b. 204, DK-2800 DENMARK

to obtain improved wear and fatigue performance of steel components. On the other hand the interaction between iron and carbon as in metal dusting [1], an example of high temperature corrosion, is highly detrimental for continued materials performance. Often the boundary between beneficial and detrimental is very fine and, thus, thorough understanding of the interaction is essential for optimum materials processing or materials protection. In the present article a collection of, mostly, previously published work is given with the purpose of illustrating various aspects of the role of gas-solid interactions. In all cases described the solid state consists of an iron-based metal. The gas phase consists mainly of carbon and/or nitrogen containing components. Gas-solid interaction brings about a change of the solid state in the surface-adjacent region. Usually, for relatively low concentration of the species transferred from the gas to the solid, dissolution of this species is possible in the surface adjacent phase initially present, the so-called diffusion zone. As an example the dissolution of carbon in austenitic stainless steel (AISI 316) is discussed for a (low) temperature where, within the time of experimentation, carbide development in the austenite matrix does not occur, due to slow nucleation kinetics (chapter 2). Exceeding the (metastable) solubility of the dissolving species, a new phase may appear with a higher capacity for the dissolving species. As an example the nucleation of γ'-Fe_4N_{1-x} at an iron surface during nitriding in an ammonia/hydrogen mixture is discussed (chapter 3). Once the entire surface is covered by a continuous layer of a new phase (compound layer) continuous transfer of species to the substrate occurs through this layer. The case of growth of a continuous iron nitride double (dual phase) layer into an iron substrate is discussed in chapter 4. The concurrent incorporation of carbon and nitrogen in iron, and its effect on the evolution of the morphology of the compound layer are discussed in chapter 5.

1.1 Gas solid interactions [2]

The gas solid interactions to be discussed concern carburizing in CO, nitriding in NH_3/H_2 and nitrocarburizing in $NH_3/CO_2/H_2$. In all cases atmospheric pressure applies. Dissociation reactions at the surface provide atomic species at the surface, which subsequently may be incorporated into the solid state or leave the surface again. For carburizing in CO adsorbed carbon atoms diffuse into the solid phase ϕ:

$$CO \rightleftarrows C_{ad} + O_{ad} \tag{Ia}$$

$$C_{ad} \rightleftarrows [C]_{\phi}. \tag{Ib}$$

For nitriding in NH_3/H_2, adsorbed nitrogen atoms can diffuse into the solid phase ϕ:

$$NH_3 \rightleftarrows N_{ad} + \tfrac{3}{2} H_2 \tag{IIa}$$

$$N_{ad} \rightleftarrows [N]_{\phi} \tag{IIb}$$

or, upon development of molecular nitrogen, leave the surface:

$$N_{ad} + N_{ad} \rightleftarrows N_2 . \qquad \text{(IIc)}$$

For nitrocarburizing a competition between a carburizing and a nitriding reaction occurs. Because of the presence of hydrogen, carburizing according to the following scheme is kinetically preferred:

$$CO_2 + H_2 \rightleftarrows CO + H_2O \qquad \text{(IIIa)}$$

$$CO + H_2 \rightleftarrows C_{ad} + H_2O \qquad \text{(IIIb)}$$

$$C_{ad} \rightleftarrows [C]_\phi . \qquad \text{(IIIc)}$$

2. Carburizing of austenitic stainless steel [16]

A recent development in surface engineering of austenitic stainless steel is low temperature carburizing [3] (or nitriding). As a result a zone of expanded austenite [1] is obtained, which has a high hardness and is free of carbides (or nitrides). The zone of expanded austenite provides a considerable improvement of the wear performance of stainless steel. Important to note is that the corrosion properties are not impaired by this surface engineering, because no carbides/nitrides develop.

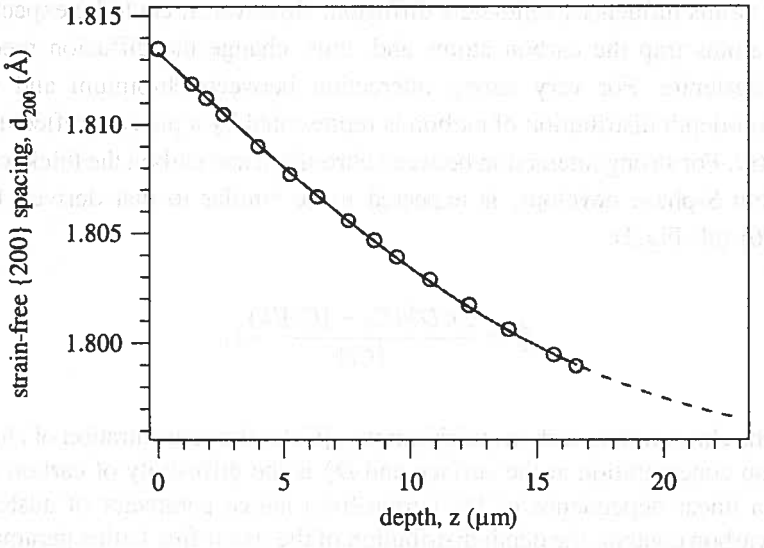

Fig. 1. Strain-free lattice parameter vs. depth for austenitic stainless steel AISI 316 carburized in CO for 25 hours at 761 K. The data were obtained from X-ray diffraction lattice strain determinations for measurement in the strain-free direction and correction for X-ray penetration. The drawn line was fitted to the data points assuming applicability of Eq.(1); the dashed part of the line is an extrapolation of the fitted line

[1] The name refers to the relatively high content of intersititally dissolved atoms. Expanded austenite is also referred to as S-phase

A sample of commercial AISI 316 was gaseously carburized at 761 K in pure CO for 25 hours. After carburizing the sample was investigated with X-ray diffraction analysis combined with successive layer removal for determination of the composition and lattice strains as a function of depth below the original surface. For an explanation of how to unravel the influences of composition and lattice strains on X-ray diffraction line profiles, and how to attribute X-ray results (which are a weighted average over the depth distribution) to a certain depth the reader is referred to Ref.4. The strain-free lattice parameter of expanded austenite is given as a function of depth in Fig.1.

For unidirectional solid-state diffusion in the direction z of a semi-infinite system, where the diffusion coefficient is independent of the concentration, the concentration-depth distribution $c(z,t)$ at time t is described by [5]:

$$\frac{c(z,t) - C_0}{C_s - C_0} = 1 - erf\left(\frac{z}{2\sqrt{Dt}}\right), \tag{1}$$

where C_0 is the initial concentration of the diffusing species in the solid state and C_s is the surface concentration, which is taken constant during diffusion. This well known solution of Fick's second law was applied to evaluate whether the interaction between chromium and carbon atoms influences solid-state diffusion. However, it could be expected that the chromium atoms trap the carbon atoms and, thus, change the diffusion mechanism of carbon in austenite. For very strong interaction between chromium and carbon the concentration-depth distribution of carbon is represented by a plateau, reflecting the Cr:C stoichiometry. For strong interaction between chromium and carbon the thickness, ξ, of the zone wherein S-phase develops, is expected to be similar to that derived for internal oxidation [6] (cf. Fig.2):

$$\xi^2 = \frac{2\kappa D_C^S (C_S - [Cr]/\kappa)}{[Cr]} t, \tag{2}$$

where κ is the chromium to carbon stoichiometry, [Cr] is the concentration of chromium, C_S is the carbon concentration at the surface and D_C^S is the diffusivity of carbon in S-phase. Assuming a linear dependence of the (strain-free) lattice parameter of austenite on the interstitial carbon content, the depth distribution of the strain-free lattice parameter reflects the carbon depth distribution. Evidently, Fig.1 does not show a plateau-like composition profile as in Fig.2, but is consistent with Eq.(1). Fitting Eq.(1) to the data in Fig.1, taking the lattice parameters corresponding to C_s and C_0 as well as the diffusion coefficient of carbon as fitting parameters, resulted in an excellent mathematical description of the data. The value for the diffusion coefficient thus obtained was $D_C^S = 1.03 \cdot 10^{-15}$ m^2.s^{-1}.

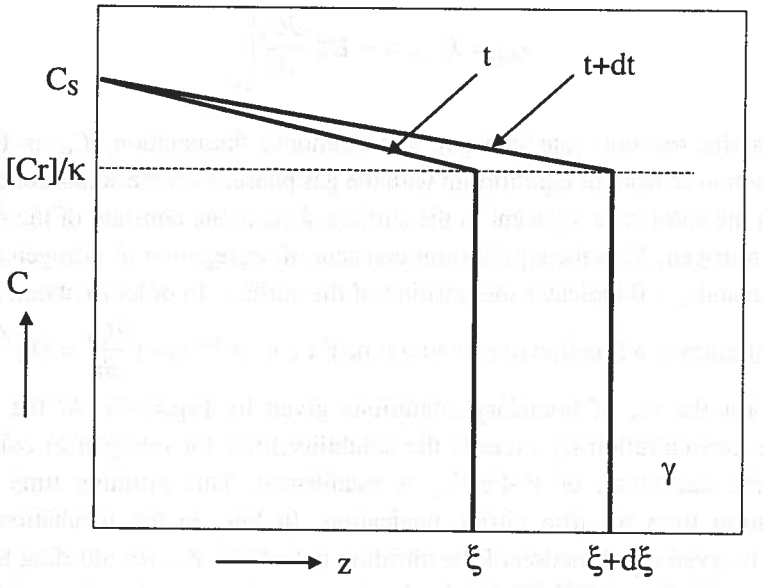

Fig. 2. Schematic composition depth profile for carbon dissolved in austenite under the presumption of strong interaction between carbon and chromium. For a time increment dt the carburized layer increases in thickness by $d\xi$. A linear concentration profile is assumed in the carburized layer

3. Nucleation of iron nitride at an iron surface during nitriding [7]

On gaseous nitriding of iron the first phase developing at the surface is γ' – Fe_4N_{1-x}, which nucleates upon exceeding the maximum solubility of nitrogen in iron in the region adjacent to the surface. The incubation time for the nucleation of γ' – nitride depends on the competition between the flux of nitrogen atoms arriving at the surface and the fluxes of nitrogen atoms leaving the surface. The flux of arriving nitrogen atoms is controlled by ammonia dissociation (reaction (IIa); the fluxes of nitrogen atoms leaving the surface are due to the development and desorption of N_2 (reaction(IIc) and diffusion of nitrogen atoms into the solid state (reaction (IIb)). For an iron plate of infinite length and width with finite thickness (L) and a uniform, initial nitrogen distribution (C_0), the fluxes of nitrogen atoms associated with the dissociation reaction of ammonia at the surface, J_{diss}, the desorption of molecular nitrogen from the surface, J_{des}, and solid state diffusion into the substrate, J_{diff}, are given by (cf. Refs. [7] and [8]):

$$J_{diss} = k \cdot (C_{eq} - C_S) \tag{3}$$

$$J_{des} = - k_2 \cdot \frac{K_S \cdot C_S^2}{1 + K_S \cdot C_S} \tag{4}$$

$$J_{diff} = J|_{z=0} = - D_N^{\alpha} \left. \frac{\partial C_N}{\partial z} \right|_{z=0}, \qquad (5)$$

where k is the reaction rate constant for ammonia dissociation, C_{eq} is the nitrogen concentration in α-iron for equilibrium with the gas phase, C_S is the actual concentration of nitrogen in the solid state adjacent to the surface, k_2 is a rate constant of the formation of molecular nitrogen, K_S is the equilibrium constant of segregation of nitrogen atoms at the iron surface and $z = 0$ indicates the position of the surface. In order to obtain the nitrogen depth distribution as a function of nitriding time F i c k ' s 2nd law ($\frac{\partial C_N}{\partial t} = D_N^{\alpha} \frac{\partial^2 C_N}{\partial z^2}$) has to be solved for the set of boundary conditions given by Eqs.(3-5). At the time where the surface concentration C_S exceeds the solubility limit for nitrogen in α-Fe a driving force for the nucleation of γ'-Fe_4N_{1-x} is established. This nitriding time is taken as the incubation time for iron nitride nucleation. In Fig. 3a the incubation time, thus calculated is given as a function of the nitriding potential [2], K_N, for nitriding temperatures ranging from 743 K to 863 K [7]. Evidently, the incubation time decreases with increasing nitriding potential. It follows from Fig. 3a that the formation of N_2 only affects the calculated incubation time for nitriding potentials just beyond the critical nitriding potential where ferrite can be stable. The effect of N_2 formation is a prolongation of the incubation period by maximally 10% (at 863 K) and decreases dramatically with decreasing temperature. The experimental investigation of the development of iron nitrides at a ferrite surface was carried out with light microscopy of the as-nitrided surface. Identification of the nitride phases was done with X-ray diffraction analysis. The surfaces of samples nitrided for 15 and 20 minutes at 833 K in a mixture of NH_3 and H_2 at $K_N = 1.2 \cdot 10^{-3}$ $Pa^{-1/2}$ ($=0.38$ $bar^{-1/2}$) are shown in Fig. 3c,d. After 15 minutes of nitriding, iron nitrides had developed occassionally at the ferrite grain boundaries. Prolonged nitriding led to the nucleation of iron nitrides on the surface of the α-iron grains away from the grain boundaries, as observed after 20 minutes of nitriding (Fig. 3d). Evidently, nucleation proceeds easier at grain boundaries than on grain surfaces. The experimental incubation times for γ'-Fe_4N_{1-x} nucleation are generally shorter than the times calculated for attaining the maximum lattice solubility of nitrogen in ferrite (Fig.3b). These systematic differences are attributed to differences in the surface conditions (composition and topography) of the samples used in the present experiments and those used in the experiments from which the rates of the surface reactions were assessed [7].

---

[2] Nitriding potential is proportional to the nitrogen activity in the solid state for equilibrium with the gas phase: $K_N = \frac{P_{NH_3}}{P_{H_2}^{3/2}}$

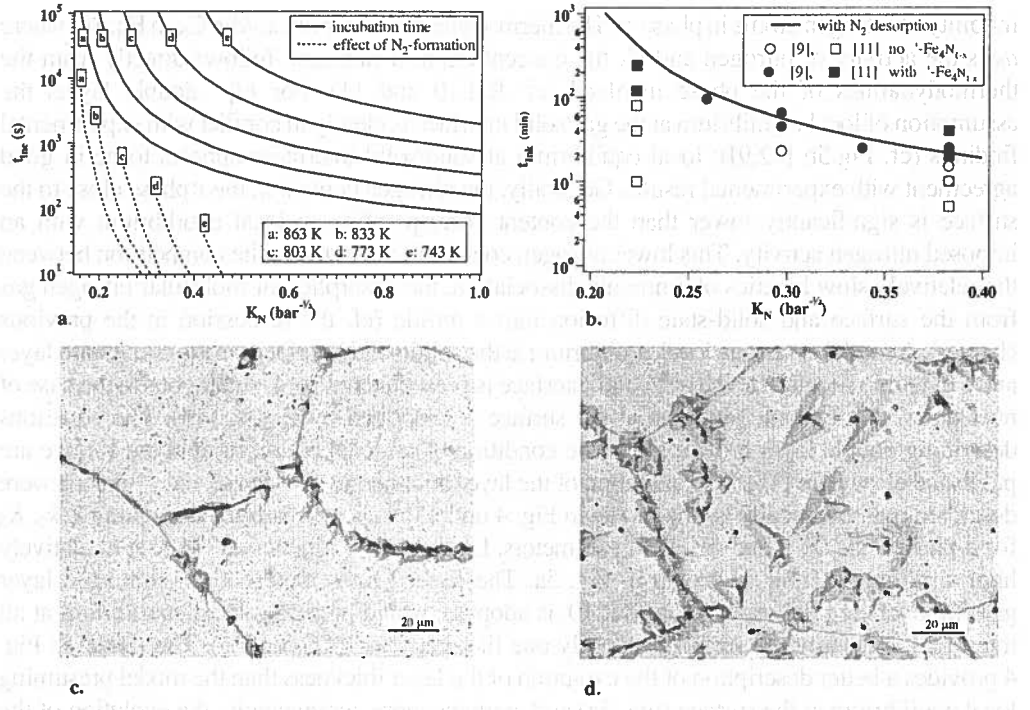

Fig. 3. a. Calculated incubation time for the nucleation of γ'-Fe_4N_{1-x} on pure iron in the temperature range 743 K to 863 K. The dashed curves represent the additional incubation time due to N_2 development at the surface.
b. Comparison of experimental and calculated incubation times at 833 K for γ'-Fe_4N_{1-x} nuclei at an iron surface
c. Light microscopy of polished surfaces H_2-reduced and nitrided. Nitriding was performed at 833 K at nitriding potential $K_N = 0.38$ bar$^{1/2}$ ($= 1.2 \cdot 10^{-3}$ Pa$^{-1/2}$) for 15 minutes d. As c. for nitriding time 20 minutes

4. Nitride layer growth under combined surface reaction and diffusion control [9]

On nitriding the growth kinetics of the compound layer during nitriding is usually assumed to be controlled by solid-state diffusion of nitrogen through the phases constituting the compound layer; the diffusion of Fe atoms can be neglected [10]. The growth of γ'-Fe_4N_{1-x} monolayers or the ε-Fe_2N_{1-z}/γ'-Fe_4N_{1-x} double layers on ferrite can be evaluated from considering the fluxes entering and leaving the sublayers (for mathematical descriptions see Ref.10). The assumptions usually made to arrive at a mathematical description of the growth kinetics involve local equilibrium at the solid/solid interfaces as well as at the surface. It can be assumed that the composition in each of the sublayers changes linearly with depth, provided that the composition dependent diffusion coefficients D_N^{φ} are replaced by the composition-weighted (effective) diffusion coefficient, $\langle D_N^{\varphi} \rangle$, for each of the sublayers [10]:

$$\langle D_N^{\varphi} \rangle = \int_{y_{N,\varphi}^{\min}}^{y_{N,\varphi}^{\max}} (D_N^{\varphi})^* \cdot \frac{d \ln a_N}{d \ln C_N} \cdot dy_{N \cdot \varphi} \quad \text{with} \quad (D_N^{\varphi})^* = RT(1 - y_{N,\varphi}) M_N^{\varphi}, \tag{6}$$

where $(D_N^{\varphi})^*$ is the tracer diffusion coefficient of nitrogen in phase φ, $y_{N,\varphi}^{\min}$ and $y_{N,\varphi}^{\max}$ are the minimum and maximum occupancies of the interstitial sublattice in phase φ and M_N^{φ} is the

mobility of nitrogen atoms in phase φ. The thermodynamic factor dln a_N/dln C_N in Eq.(6), where a_N is the activity of nitrogen and C_N the concentration of nitrogen, follows directly from the thermodynamics of the phase involved (cf. Ref.10 and 11). For ε/γ' double layers the assumption of local equilibrium at the gas/solid interface is clearly in conflict with experimental findings (cf. Fig.5b [12,9]); local equilibrium at solid/solid interfaces appears to be in good agreement with experimental results. Generally, the nitrogen content in the ε phase close to the surface is significantly lower than the content corresponding to local equilibrium with an imposed nitrogen activity. This lower nitrogen content is attributed to the competition between the relatively slow kinetics of ammonia dissociation, the desorption of molecular nitrogen gas from the surface and solid-state diffusion into ε nitride (cf. the discussion in the previous chapter). A model assuming local equilibrium at the solid/solid interfaces in the compound layer and a dynamic situation at the gas/solid interface is presented in Fig. 4. Analogous to the case of nucleation, the dynamic situation at the surface is described by Eqs. (3)-(5). The equations describing double layer growth under the condition of no local equilibrium at the surface are published elsewhere [13]. The evolution of the layer thicknesses of ε-phase and γ'-nitride were described mathematically by the model in Fig. 4 under the above conditions, adopting k, k_2, K_S for ε-phase and $(D_N^{\gamma'})^*$ and M_N^{ε} as fit parameters. Layer growth kinetics at 773 K at a relatively high nitriding potential is shown in Fig. 5a. The dashed lines represent the simulated layer growth kinetics if the model from Ref.10, is adopted, which presumes local equilibrium at all interfaces, including the surface, and only one fit parameter ($\langle D_N^{\varepsilon} \rangle$ or M_N^{ε}). The model in Fig. 4 provides a better description of the evolution of the layer thickness than the model presuming local equilibrium at the surface (Fig. 5a) and, perhaps more convincingly, the evolution of the nitrogen depth profile (Fig. 5b).

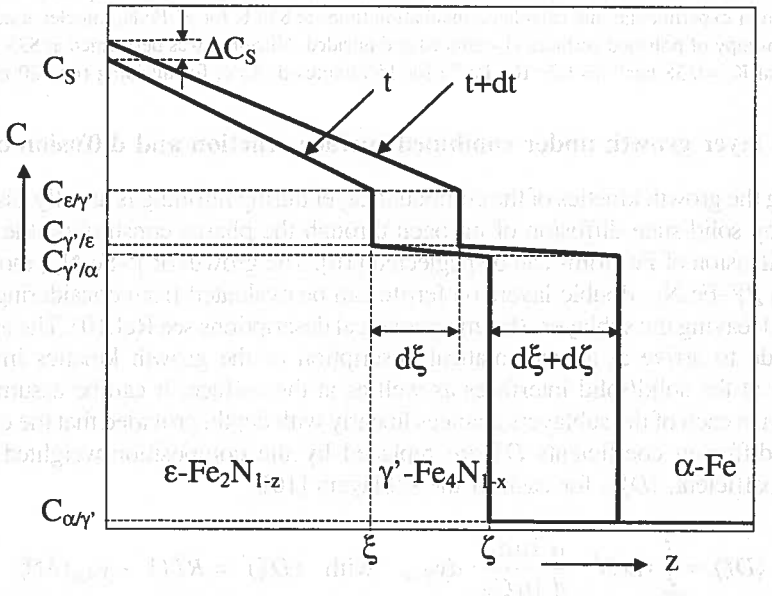

Fig. 4. Model for double layer growth. Local equilibrium prevails at all solid/solid phase boundaries, but not at the surface. For a time increment dt the sublayers increase in thickness by dξ and dζ, whilst the surface concentration increases by ΔC_S. Linear concentration profiles are assumed in the sublayers

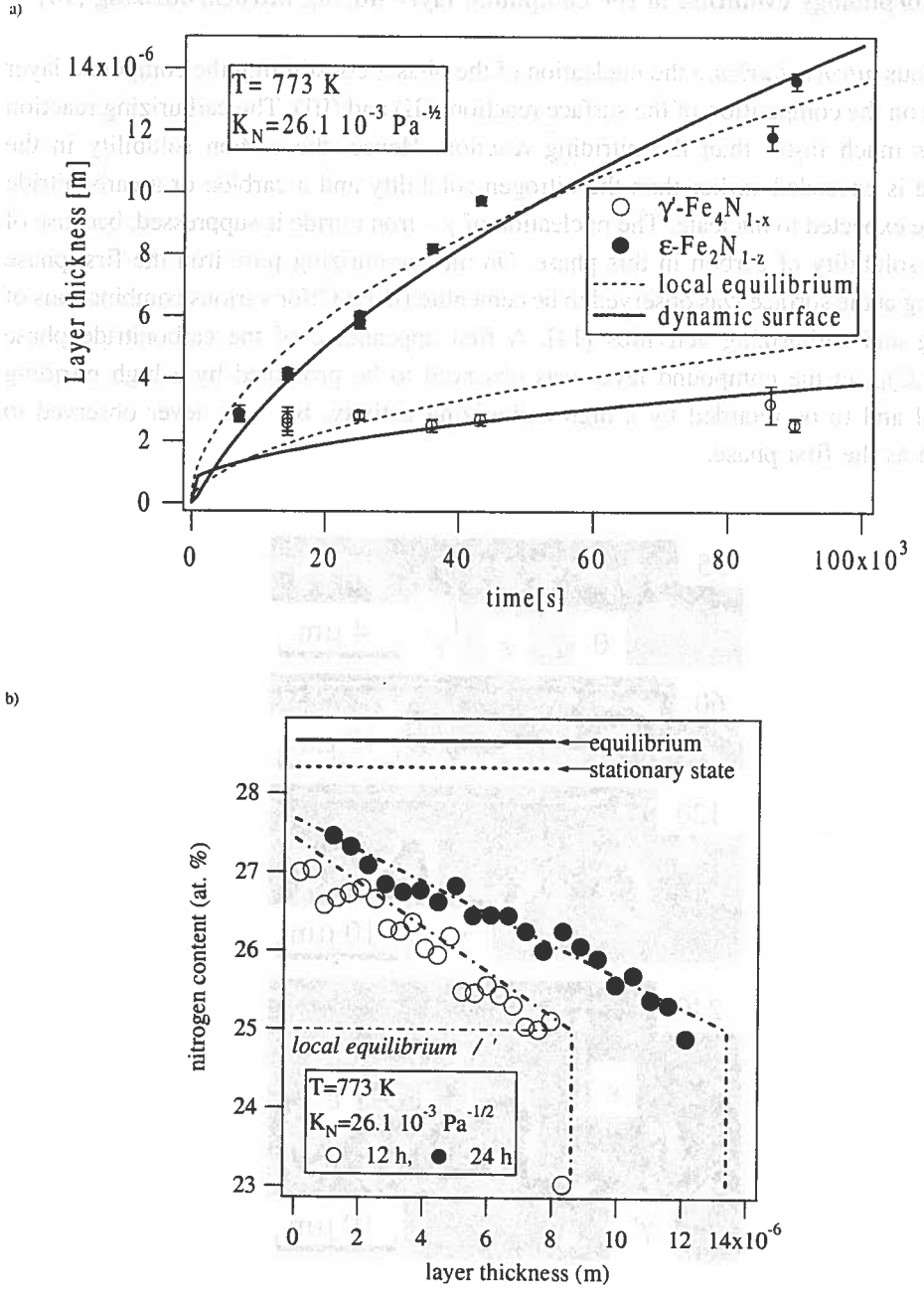

Fig. 5. a. Results of modelling double layer growth for the cases of local equilibrium (dashed lines) and a dynamic state (solid lines) at the surface, b. Comparison of experimental and modelled nitrogen profiles for the case of a dynamic state at the surface

5. Morphology evolution of the compound layer during nitrocarburizing [14]

On gaseous *nitrocarburizing* the nucleation of the phases constituting the compound layer depends on the competition of the surface reactions (II) and (III). The carburizing reaction proceeds much faster than the nitriding reaction. Hence, the carbon solubility in the substrate is exceeded earlier than the nitrogen solubility and a carbide or a carbonitride would be expected to nucleate. The nucleation of γ – iron nitride is suppressed, because of the low solubility of carbon in this phase. On nitrocarburizing pure iron the first phase appearing at the surface was observed to be cementite (θ-Fe_3C)for various combinations of nitriding and carburizing activities [14]. A first appearance of the carbonitride phase ε-$Fe_2(N,C)_{1-z}$ in the compound layer was observed to be promoted by a high nitriding potential and to be retarded by a high carburizing activity, but was never observed to nucleate as the first phase.

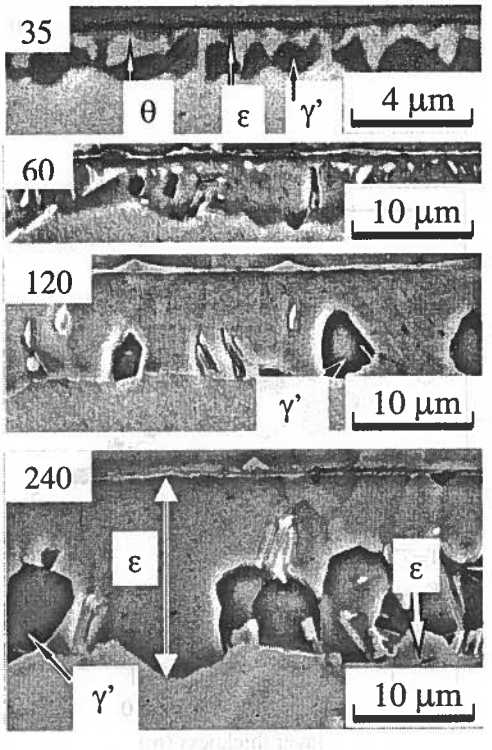

Fig. 6. a. Micrographs of cross sections of the compound layers formed in the NC1 series ($a_N = 753$, $a_C = 1.37$)) for times indicated in minutes in the upper left corner of each micrograph. Positive phase contrast microscopy: ε phase appears light grey, γ' phase appears dark; cementite (θ) appears white

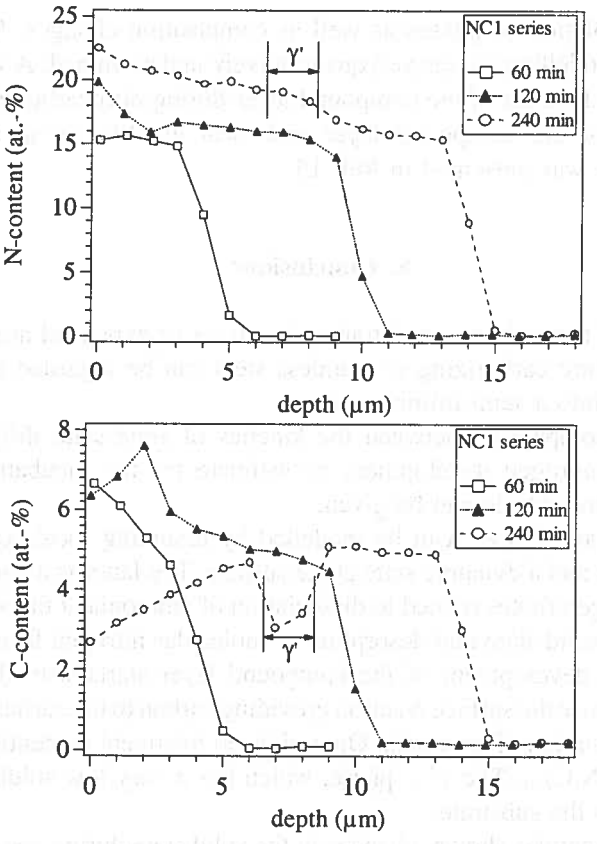

Fig. 6. b. EPMA nitrogen and carbon depth profiles for NC1 series after nitrocarburizing times (in minutes) indicated in the legend

In the sequel the microstructural evolution of the compound layer is discussed for the following combination of nitrogen and carbon activities: $a_N = 753$; $a_C = 1.37$. The morphological and compositional evolution of the compound layer on iron during nitrocarburizing under these conditions is presented in Fig. 6. After the initial development of cementite, the ε-phase becomes dominant in the compound layer on prolonged treatment. The content of cementite decreases and, eventually, becomes zero. Concurrently, the amount of γ' – phase increases (see Fig. 6a), particularly in the part of the compound layer adjacent to the substrate. The evolution of the composition depth profiles shows that the nitrogen content at the surface increases with time, while the carbon content at the surface decreases complementarily (Fig. 6b). This relatively slow increase of the nitrogen content is consistent with the observation of a continuously increasing nitrogen content in ε-phase on nitriding (cf. the previous chapter), due to the relatively slow kinetics of ammonia dissociation at (and nitrogen desorption from) the iron surface, which allowed an initially strong absorption of carbon. Needless to say that modelling of the microstructure evolution of the compound layer during nitrocarburizing is currently not possible, since it involves

nucleation and dissolution of phases as well as composition changes. Most parameters necessary for such modelling are (as yet) quantitatively undetermined. A very first attempt to model the growth kinetics of the compound layer during nitrocarburizing for a simple phase constitution of the compound layer and local equilibrium at the surface and solid/solid interfaces was presented in Ref. 15.

6. Conclusions

The development of the carbon concentration in a layer of expanded austenite (S-phase) during low temperature carburizing of stainless steel can be regarded as unidirectional diffusion of carbon into a semi-infinite system.
On the basis of a competition between the kinetics of solid-state diffusion, ammonia decomposition and nitrogen development an estimate for the incubation time for the nucleation of γ' – iron nitride can be given.
Growth of the compound layer can be modelled by assuming local equilibrium at the solid/solid interfaces and a dynamic state at the surface. The latter is a consequence of the competition of nitrogen fluxes related to dissociation of ammonia at the surface, diffusion of nitrogen into the solid state and desorption of molecular nitrogen from the surface.On nitrocarburizing the development of the compound layer starts with the nucleation of cementite Fe_3C, because the surface reaction providing carbon to the surface proceeds much faster than the dissociation of ammonia. On prolonged treatment cementite is dissolved at the favour of ε-$Fe_2(N,C)_{1-z}$. The γ' – phase, which has a very low solubility for carbon, develops adjacent to the substrate.
Generally, for the examples shown, changes in the solid state during gas-solid interaction can be understood on the basis of the kinetics of surface reactions and the kinetics of solid state diffusion.

Acknowledgement

The author wishes to acknowledge the following persons for their inspiring and fruitful collaboration on various parts of the work presented in this article: Thomas Christiansen, Hong Du, Peter B. Friehling, Leszek Maldzinski and Eric J. Mittemeijer.

REFERENCES

[1] H.J. Grabke, Materials and Corrosion **49**, 303-308 (1998).
[2] H.J. Grabke, Materials Science Forum. **154**, 69-85 (1994).
[3] Y. Sun, X. Li, T. Bell, Materials Science and Technology **15**, 1171-1178 (1999).
[4] M.A.J., Somers, E.J. Mittemeijer, Metallurgical Transactions A 21, 189-204 (1990).
[5] P. Shewmon, Diffusion in Solids, 2nd edition, TMS, 1989.
[6] J.L. Meijering, Advances in Materials Research **5**, 1 (1971).

[7] P.B. Friehling, F.W. Poulsen, M.A.J. Somers, Zeitschrift für Metallkunde **92**, 589-595 (2001).
[8] H.C.F. Rozendaal, E.J. Mittemeijer, P.F Colijn, P.J van der Schaaf, Metallurgical Transactions. **14**, 395-399 (1983).
[9] M.A.J. Somers, P.B. Friehling, Härterei-Technische Mitteilungen, **57**, 415-420 (2002).
[10] M.A.J. Somers, E.J. Mittemeijer, Metallurgical and Materials Transactions A **26**, 57-74 (1995).
[11] M.A.J. Somers, Heat treatment of Metals **27**, 92-102 (2000).
[12] E.J. Mittemeijer, M.A.J. Somers, Surface Engineering. **13**, 483-497 (1997).
[13] P.B. Friehling, L. Maldzinski, M.A.J. Somers, in preparation; see also P.B. Friehling- Ph.D. Thesis, Technical University of Denmark, 2000.
[14] H. Du, M.A.J. Somers, J. Ågren, Metallurgical and Materials Transactions A **31**, 195-211 (2000).
[15] H. Du, J. Ågren, Metallurgical and Materials Transactions A **27**, 1073-1080 (1996).
[16] T. Christiansen, M.A.J. Somers, in preparation.

Received: 1 March 2004.

A R C H I V E S O F M E T A L L U R G Y A N D M A T E R I A L S
Volume 49 2004 Issue 2

K. SIKORSKI *

ELECTRON PROBE MICROANALYSIS IN THE STUDY OF DIFFUSION IN SOLIDS

ILOŚCIOWA MIKROANALIZA RENTGENOWSKA W BADANIACH PROCESÓW DYFUZJI W CIAŁACH STAŁYCH

The paper illustrates the necessity of applying special corrections to concentration profiles determined on the cross-sections of the samples using an electron probe *x*-ray microanalyser when the thickness of diffusion zones are below tens of microns. The correction takes into account the influence of the width of the x-ray generation volume on the shape and width of the determined x-ray intensity profiles and consequently, on the value of diffusion coefficients calculated on their basis. The error increases with decreasing thickness of the analysed diffusion zones and inecreasing width of the x-ray generation volume. A method correcting the above effect is described and the examples of its application are given.

Methods of determining the concentration profiles formed as a result of diffusion processes in thin (below 1 micron) coatings are also described. They utilize the in-depth *x*-ray distribution function $\varphi(z)$ and need measurements of the x-ray intensities on the surface of the layers at various accelerating voltages. It was shown that the methods describe adequately the concentration profiles in the cases of multiphase diffusion when the profiles are of step-like shape. If the concentrations of elements in the diffusion zone change continuously, the profiles are described approximately as if they referred to 3-4 sub-layers of different but constant concentrations.

W pracy wykazano, że profile zmian stężeń pierwiastków w strefach dyfuzyjnych o grubości mniejszej od kilkudziesięciu mikrometrów, wyznaczone metodą mikroanalizy rentgenowskiej na przekrojach poprzecznych złącz, są obarczone błędem, którego wielkość rośnie, gdy grubość strefy dyfuzyjnej maleje, a szerokość obszaru emisji promieniowania X wzrasta. W pracy opisano metody korekcji profili zmian stężeń pierwiastków w strefach dyfuzyjnych. Wykazano, że wartości współczynników dyfuzji wyznaczone na podstawie nie skorygowanych profili są zawyżone i w przypadku stref o grubości kilku mikrometrów mogą osiągać wartości kilkakrotnie większe od rzeczywistych. Korekcja profili zmian stężeń może być pominięta jedynie w przypadku stref dyfuzyjnych o grubości większej niż 100 mikrometrów.

W pracy opisano również metody określania profili zmian stężeń pierwiastków w cienkich warstwach o grubości poniżej 1 mikrometra. Metody te wymagają wykonania pomiarów natężeń

* FACULTY OF MATERIALS SCIENCE AND ENGINEERING, WARSAW UNIVERSITY OF TECHNOLOGY, 02-507 WARSAW, WOŁOSKA STR. 141, POLAND

charakterystycznego promieniowania X przy kilku różnych energiach elektronów wzbudzających to promieniowanie w próbce, gdy wiązka elektronów pada prostopadle na powierzchnię warstwy. Wykazano, że metody te pozwalają na dokładny opis profili zmian stężeń pierwiastków w warstwach jedynie w przypadku dyfuzji reakcyjnej, gdy zmiany stężeń mają charakter skokowy. W przypadku dyfuzji jednofazowej, gdy stężenia pierwiastków w strefie dyfuzyjnej zmieniają się w sposób ciągły, metody cienkowarstwowe umożliwiają uzyskanie jedynie przybliżonych profili zmian stężeń pierwiastków w postaci 3-4 podwarstw o różnych, lecz stałych w obrębie każdej warstwy, stężeniach.

1. Introduction

Concentration profiles of all elements in the diffusion couple must be known to determine the values of the diffusion coefficients in the analysed system. For such a purpose the electron probe microanalysis (EPMA) is widely used due to its good lateral resolution (about 1 μm), high accuracy (relative error $1 \div 3\%$ for most elements and $5 \div 7\%$ for light ones ($Z < 10$)), good detectability limit ($0.001 \div 0.01\%$ for most elements and $0.05 \div 0.5\%$ for light ones), easy sample preparation and the advantage of being non-destructive. The element concentration profiles are usually determined on a sample cross-section perpendicular to the boundary between the diffusion couples. Because of the changes of the element concentrations inside the diffusion zone, the conventional methods of EPMA, which assume constant composition inside the *x*-ray generation volume, can cause significant errors in the determined concentration profiles. The errors increase with decreasing diffusion zone and with increasing width of the *x*-ray emission volume. In consequence, diffusion coefficients calculated on the basis of measured concentration profiles can significantly differ from the real ones.

The paper describes how the width of the diffusion zone and the width of the x-ray emission volume in the analysed sample influence the shape of diffusion profiles determined by the EPMA method and the value of diffusion coefficients obtained on their basis. A method of improving the EPMA results based on the experimentally determined instrumental window function of *x*-ray detection is described. The effects of fluorescence at the boundary of diffusion couples are also discussed.

EPMA can also be used for studying diffusion processes in thin films or/and coatings of thickness, lower than 1 μm, deposited on thick substrates. In such cases concentration profiles in the diffusion zone are determined using a special approach of the non-destructive in-depth microanalysis, based on the measurements performed at various accelerating voltages. This paper describes the EPMA procedure of in-depth profiling of element concentrations in the diffusion zone between two thin layers deposited on thick substrates. The accuracy of the method and its capabilities and limitations are discussed. Examples of applications of the method in studying the single-phase and multiphase diffusion processes that proceed in thin films are shown.

2. The effect of the width of x-ray emission volume on measured diffusion profiles

In *x*-ray microanalysis the x-rays characteristic of the elements in the analysed volume are generated by the electrons focused on the chosen sample micro-area (primary excitation) and by continuum and the characteristic *x*-rays generated by the electrons in the sample (secondary excitation). The primary *x*-ray generation volume depends on the chemical composition of the analysed micro-area, the critical excitation energy of the *x*-ray lines chosen for the analysis, the electron energy E_o and the incident beam diameter. This volume is defined by the maximum depth of *x*-ray generation $R_{(x)}$ and the width of the emission region D_y (Fig. 1).

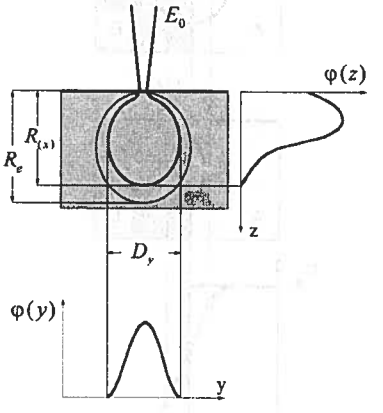

Fig. 1. *X*-ray production range (inner sphere) and electron penetration range (outer sphere)

The width D_y within which 68% of the x-rays are emitted is described by the Reed expression [1], based on the Bishop's Monte Carlo calculations [2, 3]:

$$D_y = \frac{0.077}{\rho}(E_o^{1.5} - E_c^{1.5}) \quad [\mu m], \tag{1}$$

where ρ is the material density [g/cm^3], E_0 is the energy of incident electrons [keV], and E_c is the critical excitation energy of the *x*-ray line chosen for analysis [keV].

The width within which 99% of x-rays are generated is three times as great as the above value.

The width of the excitation volume influences the measured concentration profiles in diffusion couples. Fig. 2 illustrates this effect in the A-B joint with step-like changes of the element concentrations C_A and C_B at the boundary. When the electron beam penetrates the

material A at a distance from the boundary shorter than $\frac{D_y}{2}$, the x-rays of element B are excited and the measured concentrations differ from their true values.

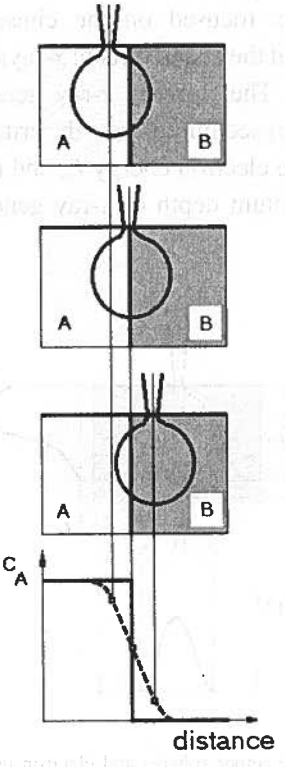

Fig. 2. The effect of the width of x-ray emission volume on the measured concentration profile of element A. Solid line – true concentration profile, dotted line – experimental profile

The difference between the measured and true concentrations increase with the decreasing distance to the joint boundary. The difference increases with the increasing width of the emission volume, which depends on the electron energy E_o, the incident beam diameter, the atomic number of the analysed material and the excitation energy of the x-rays chosen for the analysis. As a result, the measured concentration profiles obtained by moving the electron beam along the line perpendicular to the A-B boundary, become similar to the diffusion lines instead of being step-like.

If the true concentration profiles do not change as sharply as those in Fig. 2, the measured concentration profiles do not differ so much from the real ones, but the difference can significantly influence the value of the diffusion coefficient calculated on their basis even when the true diffusion zone is several tens of microns wide. For this reason, the measured concentration profile should be corrected.

3. A method of improving the EPMA results by using an instrumental window function of x-ray detection

In order to determine the real concentration profile in the diffusion zone the function $\varphi(y)$ must be known. The function $\varphi(y)$ describes the intensity distribution of the x-ray line emitted from the x-ray generation volume along the y axis perpendicular to the electron beam (Fig. 1). The function $\varphi(y)$ (known as the instrumental function) is a function of the analysed material, the excitation energy of the x-rays chosen for the analysis, the electron energy E_o, the incident beam diameter and the take-off angle of microanalyser. The shape and value of the instrumental function $\varphi(y)$ depend then on the structure of microanalyser used for experiments and must be determined under the same experimental conditions under which diffusion profiles are measured.

The function $\varphi(y)$ can be determined from the reference standard joint of the pair of analysed materials with step-like changes of element concentrations at the boundary (Fig. 3).

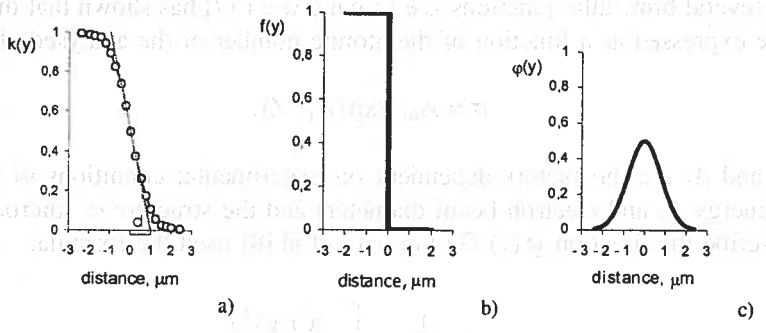

Fig. 3. Relative x-ray intensity profiles: a) measured on a standard joint; b) fitted to the real concentration changes in the joint; and c) a function $\varphi(y)$ calculated on their basis

In order to do this, the x-ray intensities should be measured at the points lying along the line perpendicular to the joint boundary and the k-ratio profile should be determined. The k-ratio (known as relative intensity) is the quotient of the intensity measured in the sample to the intensity from the standard of the analysed element. If the function chosen for describing the k-ratio profile obtained from intensity measurements at the standard joint is denoted as the $k(y)$ and the function chosen for describing the k-ratio profile fitted to the real concentration changes in the joint is the $f(y)$, then the x-ray distribution function $\varphi(y)$ can be determined by the deconvolution of the $k(y)$ and $f(y)$ functions, according to the following expression [4-6]:

$$k(y_o) = \int_{-\infty}^{+\infty} \varphi(y - y_o)\, f(y_o)\, d(y) \qquad (2)$$

where y_o is the co-ordinate of the $\varphi(y)$ maximum. The maximum corresponds to the position of the center of electron beam on the y axis.

For the instrumental function to be independent of the element concentration in the sample, we must assume that:

$$\int_{-\infty}^{+\infty} \varphi(y)\, d(y) = 1. \tag{3}$$

The shape of the $\varphi(y)$ function can be described by the G a u s s i a n-type function [1, 4]:

$$\varphi(y) = \frac{1}{\sigma\sqrt{2\pi}} \exp\left[-\frac{1}{2}\left(\frac{y}{\sigma}\right)^2\right]. \tag{4}$$

The parameter σ in this expression is chosen so as to obtain the best fitting to the shape of the function $\varphi(y)$ determined experimentally by using the least square method. By analysing several bimetallic junctions Ż e l e c h o w e r [7] has shown that the parameter σ could be expressed as a function of the atomic number of the analysed element Z:

$$\sigma = A_o \cdot \exp(A_1 \cdot Z), \tag{5}$$

where A_o and A_1 are the factors dependent on experimental conditions of the analysis (electron energy E_o and electron beam diameter) and the structure of microanalyser.

To describe the function $\varphi(y)$ G i l m o u r et al.[8] used the formula:

$$\varphi(y) = \frac{1}{d} \exp\left[-\frac{\pi}{4}\left(\frac{y}{d}\right)^2\right], \tag{6}$$

where d is the parameter defined as the intersection of the y axis by a tangent to the midpoint of the k(y) function measured on the standard joint (Fig. 3).

3.1. The effect of fluorescence at the boundary of standard diffusion couples

If the energy of the x-rays emitted from the material 1 being exposed to electron beam is greater than the excitation energy of the analysed line of the element A from the material 2 in the standard joint, then additional x-rays of element A are emitted. This effect, known as the fluorescence effect, changes the shape of the measured k-ratio profile and should be corrected before the instrumental function is determined. The fluorescence correction contains two components: the characteristic and the continuous correction factors. Both factors depend on the width of the material 2 (t) and the distance from the interface (y_b) between the materials 1 and 2 to the point of impact of electron beam in the material 1 (Fig.4).

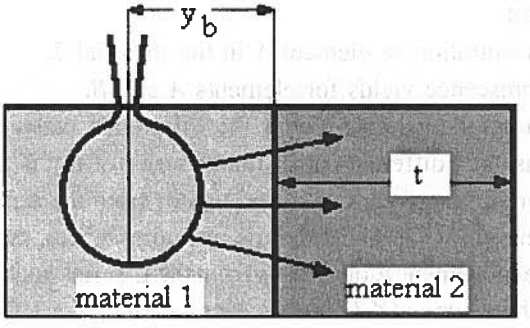

Fig. 4. Geometry used in the calculations of fluorescence effects in the material 2 by x-ray excited in the material 1

Characteristic fluorescence correction

The fluorescence correction factor for the excitation of the characteristic x-rays of element A in the material 2 of the thickness t by the characteristic x-rays of element B emitted in the material 1, can be written as [9]:

$$\frac{I^f_{A2}}{I_{A0}} = 0.25 \cdot C_{B1} \cdot C_{A2} \cdot \omega_B \cdot \frac{k_B}{k_A} \cdot \frac{r_{KA}-1}{r_{KA}} \cdot \frac{A_A}{A_B} \cdot \frac{\left(\mu/\rho\right)_{BA}}{\left(\mu/\rho\right)_{B2}} \cdot \left(\frac{\frac{E_o}{E_{cB}}-1}{\frac{E_o}{E_{cA}}-1}\right)^{1.67} \cdot \exp\left[-2.4\left(\mu/\rho\right)_{B1} \cdot \rho_1 y\right] \cdot$$

$$\cdot \left\{ \frac{\ln\left[1+\frac{\left(\mu/\rho\right)_{A2}}{\left(\mu/\rho\right)_{B2}} \cdot \cos ec\,\psi\right]}{\frac{\left(\mu/\rho\right)_{A2}}{\left(\mu/\rho\right)_{B2}} \cdot \cos ec\,\psi} + \frac{\ln\left[1+\frac{\sigma}{\left(\mu/\rho\right)_{B2}}\right]}{\frac{\sigma}{\left(\mu/\rho\right)_{B2}}} \right\} \cdot \left\{1-\exp\left[-2\left(\mu/\rho\right)_{B1} \cdot \rho_2 t\right]\right\} \tag{7}$$

where:

I^f_{A2} – intensity of the x-rays emitted by element *A* which are excited in material 2 as a result of fluorescence by the characteristic *x*-rays of element *B* from the phase 1,

I_{A0} – x-ray intensity of element *A* generated by the electrons in the pure element *A*,

C_{B1} – concentration of the element B in the material 1 exposed to electron beam,

C_{A2} – concentration of element A in the material 2,

ω_A, ω_B – fluorescence yields for elements A and B,

k_A/k_B – factor taking into account the difference between the proportionality constants, different for different series of the K and L lines. When the excited line of element A originates from the same series as the line of element B (K-K and L-L type of fluorescence), then $k_A/k_B = 1$. When the line of element A originates from the L-series and the line of element B is of the K series (K-L fluorescence), then $k_A/k_B = 0.24$. For L-K fluorescence $k_A/k_B = 4.2$,

E_{cA}, E_{cB} – critical excitation energies of the characteristic x-ray lines of element A and B,

r_{KA} – ratio of the mass absorption coefficients on the both sides of absorption edge K of the element A,

A_A, A_B – atomic weights of elements A and B,

$\left(\mu/\rho\right)_{BA}$ – mass attenuation coefficient representing absorption of the characteristic x-ray line of element B by the element A,

$\left(\mu/\rho\right)_{B1} \cdot \left(\mu/\rho\right)_{B2}$ – mass attenuation coefficients representing absorption of the characteristic x-ray line of element B by the materials 1 and 2,

$\left(\mu/\rho\right)_{A2}$ – mass attenuation coefficient representing absorption of the characteristic x-ray line of element A by material 2,

ψ – x-ray take-off angle of the spectrometer,

σ – Lenard's coefficient,

ρ_1, ρ_2 – densities of the phases 1 and 2.

When the excited line of element A originates from the L-series, the factor $\frac{r_{KA} - 1}{r_{KA}}$ should be replaced by the expression $\frac{r_{L_{III}A} - 1}{r_{L_{III}A} \cdot r_{L_{II}A} \cdot r_{L_IA}}$, where r_{L_IA}, $r_{L_{II}A}$, $r_{L_{III}A}$ are the ratios of the mass absorption coefficients on both sides of the element A absorption edges L_I, L_{II} and L_{III}.

Continuous fluorescence correction

The fluorescence correction factor for the excitation of the characteristic x-rays of element A in the material 2 of the thickness t by the continuum radiation emitted in the phase 1, can be written as [9]:

$$\frac{I_{A2}^{fc}}{I_{A0}} = 2.17 \cdot 10^{-6} \cdot C_{A2} \cdot \frac{r_{KA}-1}{r_{KA}} \cdot A_A \cdot \bar{Z}_1 \cdot E_{cA} \cdot \frac{\left(\frac{\mu}{\rho}\right)_{KA}}{\left(\frac{\mu}{\rho}\right)_{K2}} \cdot \frac{\ln\left[1 + \frac{\left(\mu/\rho\right)_{A2}}{\left(\mu/\rho\right)_{K2}} \cdot \operatorname{cosec}\psi \cdot \frac{E_o}{E_c}\right]}{\frac{\left(\mu/\rho\right)_{A2}}{\left(\mu/\rho\right)_{K2}} \cdot \operatorname{cosec}\psi \frac{E_o}{E_c}} \cdot$$

$$\cdot \exp\left[-2.4 \frac{E_{cA}}{E_o}\left(\mu/\rho\right)_{K1} \rho_1 y\right] \cdot \left\{1 - \exp\left[-2\left(\mu/\rho\right)_{B2} \rho_2 t\right]\right\}, \qquad (8)$$

where:

$\bar{Z}_1$ – mean atomic number of the phase 1,

$\left(\mu/\rho\right)_{KA}$ – mass attenuation coefficient of the element A on the high-energy side of K-absorption edge of element A,

$\left(\mu/\rho\right)_{K1}, \left(\mu/\rho\right)_{K2}$ – mass attenuation coefficients of the materials 1 and 2 on the high-energy side of the K-absorption edge of element A.

When the excited characteristic x-rays of element A originates from the L series, the factor $\frac{r_{KA}-1}{r_{KA}}$ should be replaced by the factor $\frac{r^i_{L_{III}A}-1}{r^i_{L_IA} r^i_{L_{II}A} r^i_{L_{III}A}}$, the mass attenuation coefficient $\left(\mu/\rho\right)_{KA}$ should be replaced by the mass attenuation of the element A on the high-energy side of the L_I absorption edge of element A $\left(\mu/\rho\right)_{L_IA}, \left(\mu/\rho\right)_{K1}$, should be replaced by mass attenuation coefficient of the material 1 on the high-energy side of the L_I-absorption edge of element A $\left(\mu/\rho\right)_{L_I1}, \left(\mu/\rho\right)_{K2}$ should be replaced by mass attenuation coefficient of the material 2 on the high-energy side of the L_I-absorption edge of element A $\left(\mu/\rho\right)_{L_I2}$ and the constant value $2.17 \cdot 10^{-6}$ should be replaced by the value $1.565 \cdot 10^{-6}$.

Equations (7) and (8) are obtained on the basis of R e e d ' s method [10] and give the same results for large thickness t.

In most cases, the continuum fluorescence correction can be neglected but it should be taken into account when the difference in mean atomic numbers is very high.

The graphs of fluorescence correction factors for Cr K_α radiation excited by Fe K_α radiation and by continuum, when the electron beam hits iron in the Fe-Cr joints of two

different thickness of Cr are shown in Fig. 5. The factors decrease with increasing distance of the electron beam from the boundary at the joint and decreasing Cr thickness.

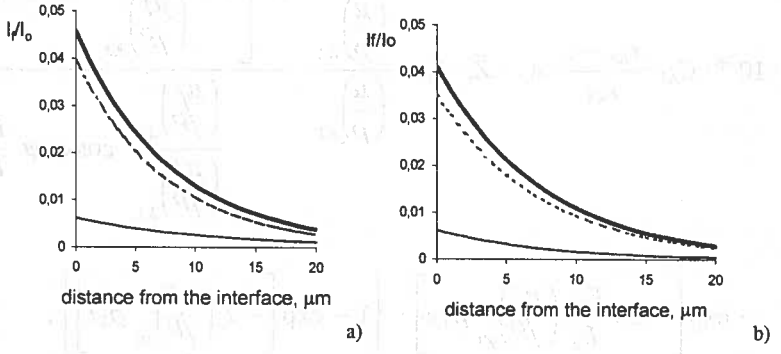

Fig. 5. X-ray fluorescence correction factors for Cr K_α radiation, when the electron beam hits iron in the Fe-Cr joint: a) semi infinite width of Cr, b) 10 µm width of Cr. Thin solid line – continuum fluorescence; dotted line – characteristic fluorescence; thick solid line – total fluorescence; E_O = 25 kV, take-off angle ψ = 62°

The profile $k(y)$ used to determine the instrumental function $\varphi(y)$ is obtained by subtraction the fluorescence correction factor profile from the as-measured profile (Fig. 6).

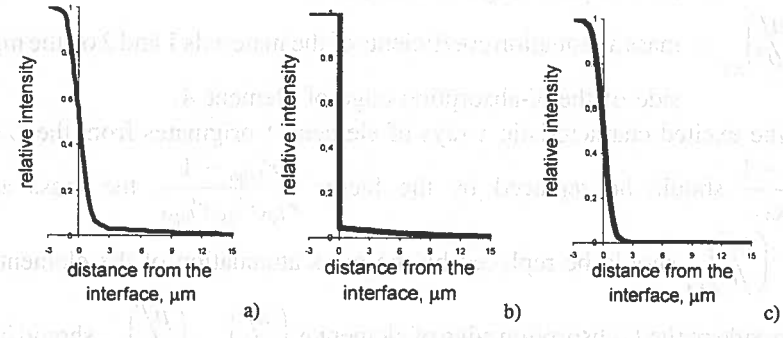

Fig. 6. Relative x-ray intensity profiles of Cr K_α-radiation in the reference standard Cr-Fe joint: a) – as-measured; b) – emitted by fluorescence; c) – after correction for fluorescence; E_o = 15 kV, take-off angle ψ = 62°

3.2. Determination of concentration profiles in diffusion zones

The experimental function $\varphi(y)$ is used to determine the k-ratio profile $f(y)$ fitted to the true concentration changes in the analysed diffusion zones. The profile is obtained by the deconvolution of the function $k(y)$ describing the measured k-ratio profile and the instrumental function $\varphi(y)$ by using the F o u r i e r transform [11] or the least square method [12]. The F o u r i e r transform method gives however satisfactory results only for the G a u s s i a n shaped profiles [11], and can be used to determine the $\varphi(y)$ function or k-ratio profiles in sandwich-like samples. In the least square method the requested function

that describes the profile $f(y)$ is determined by the convolution of an assumed function $f(y)$ and the instrumental function $\varphi(y)$. The parameters describing the function $f(y)$ are optimised by the least square method to obtain the best fitting to the measured profile $k(y)$.

The width of the x-ray emission volume D_y increases the size of the measured k-ratio profile in the diffusion zone and, in consequence, increases the value of the diffusion coefficient calculated on its basis. The difference between the value of the diffusion coefficient calculated from the as-measured concentration profile (D_m) and from the corrected profile (D_c) increases with decreasing of the width of diffusion zone. If the diffusion zone is wider than 100 microns, the influence of the correction for the width of the x-ray emission volume D_y is usually weak and can be omitted in most cases. For the example given in Fig. 7, the width of the diffusion zone is only 125 microns and the ratio $D_m/D_c = 1.07$. However, in the example shown in Fig. 8, the width of the diffusion zone is only 6 microns, so that the diffusion coefficients D_m/D_c reach the value of 2.5. In such cases, the values of diffusion coefficients obtained from the as-measured concentration profiles are worthless and need to be corrected according to the procedure mentioned above.

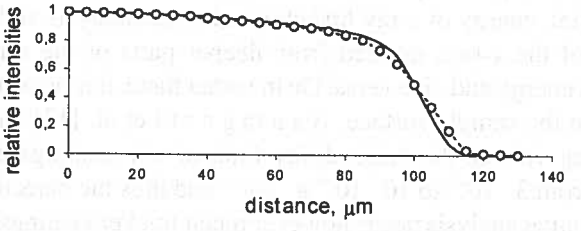

Fig. 7. Relative x-ray intensity profiles of Cu K_α radiation in the Cu-Ni diffusion couple heated for 23 h. at 900°C. Dotted line – experimental profile; solid line – corrected profile

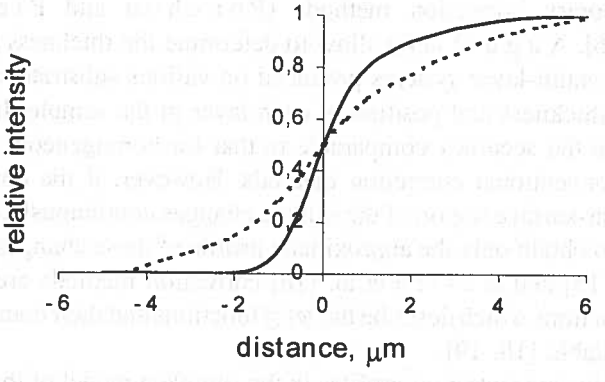

Fig. 8. Measured (dotted line) and corrected (solid line) relative intensity profiles of Cr K_α radiation in the diffusion zone between a high temperature creep resistant nickel-based alloy with the Cr-Mo-W-Co coating (after Żelechower [7])

To eliminate the error in the absorption correction caused by heterogeneity of the analysed sample within the diffusion zone, a special attention should be paid to the way in

which the specimen is mounted in a holder of microanalyser. To maintain the concentrations of the elements constant within the plane in which the x-rays are directed to the spectrometer, the plane should be parallel to the boundary between two analysed materials of the diffusion pair.

4. A study of diffusion processes in thin films

When the width of diffusion zone is below about 1 micrometer, the determination of the element concentration profiles on the cross-section of the joint is inaccurate. In such cases, special methods elaborated for quantitative analysis of thin coatings can be used.

In the analysis of thin coatings the measurements of the characteristic x-ray intensities are performed at various accelerating voltages. As can be seen in Fig. 1, the in-depth distribution of the *x*-rays generated in the sample (described by the function $\varphi(z)$) initially rises from the value $\varphi(0) > 1$ and then decreases exponentially to 0 at the maximum depth of the x-ray generation $R_{(x)}$. The position of the maximum of the function $\varphi(z)$ depends on the analysed material, energy of *x*-ray line chosen for the analysis and the electron energy E_o. The intensity of the *x*-rays emitted from deeper parts of the sample increases with increasing electron energy and vice versa. On the other hand, it is possible to detect very thin layers deposited on the sample surface. B a u m g a r t l et al. [13] have shown that at an optimal accelerating voltage the detectability limit of thin coatings deposited on various substrates ranges from $3 \cdot 10^{-8}$ to $10 \cdot 10^{-8}$ g $\cdot$ cm^{-2} and thus the detection of monolayers is possible. A quantitative analysis needs however much thicker coatings (at least 15 nm) and adequate correction methods to obtain reliable results.

By measuring the *x*-ray intensities at various accelerating voltages one can get information about the in-depth distributions of the element concentrations in the analyzed sample. Contemporary correction methods (P o u c h o u and P i c h o i r [14, 15], B a s t i n et al. [16], A u g u s t [17]) allow to determine the thickness and concentration of the elements in multi-layer systems produced on various substrates with the accuracy dependent on the thickness and position of each layer in the sample. In many cases it is possible to achieve the accuracy comparable to that for homogeneous samples analysed with the use of conventional correction methods. However, if the concentration of the elements in the near-surface region of the sample changes continuously, the "thin coatings methods" allows to obtain only the approximate profile of these changes. P o u c h o u and P u i c h o i r [14, 15] and B a s t i n et al. [16] correction methods are based upon their own analytical equations which describe the $\varphi(z)$ functions and their commercial correction programs are available [18, 19].

To determine the concentration profiles in the sample a model of the layered structure has to be chosen. Based on the assumed model the k-ratio for each of analysed elements is calculated by the correction program and displayed as a function of electron energy. Using the "trial and error" procedure the concentration profiles of the analysed elements can be obtained as a result of the agreement between the calculated and experimentally determined *k*-ratios.

The model have given very good results in determining the thickness and chemical composition of the layers formed by oxidation processes. An example of the aluminium oxide film formed by oxidation of pure aluminium sample is shown in Fig. 9. It can be seen that the best agreement with experimentally determined *k*-ratios was obtained when the mass thickness of the Al_2O_3 layer was equal to 130 $\mu g \cdot cm^{-2}$.

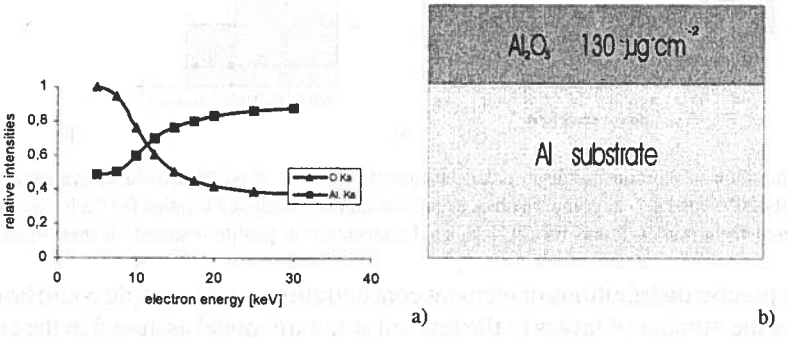

Fig. 9. Determination of the thickness of Al_2O_3 layer on Al substrate. a) comparison of experimental and calculated k-ratios for O K_α and Al K_α lines emitted from Al_2O_3 layer on Al; b) structure of the sample determined on their basis; take-off angle $\Psi = 62°$. Al_2O_3 and pure aluminium have been used as standards.

An analysis of diffusion processes in the Al/Cu/Al multi-layer system is shown in Fig. 10. The sample was prepared by depositing 58 nm Cu layer on Al substrate and then 52 nm Al layer on Cu surface. The sample was heated at 300°C for 40 min. and slightly eroded by thermal ionisation before the analysis. The best agreement with the measured Al K_α and Cu L_α *k*-ratios was obtained for the γ_2 phase of 65.8 $\mu g \cdot cm^{-2}$ thickness and 20 wt.% of Al and a very thin (4 nm) Al_2O_3 layer existed on the surface.

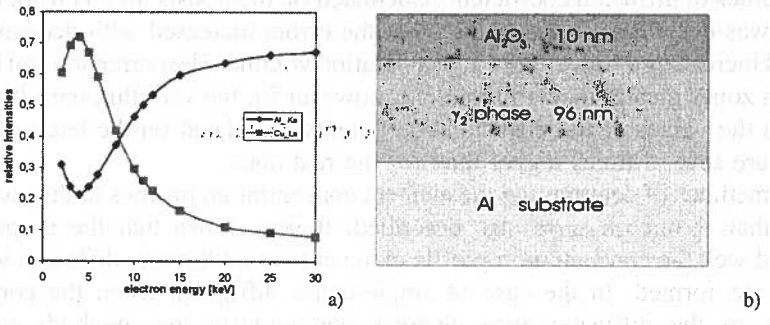

Fig. 10. Determination of the structure and chemical composition of the layers formed by heating of the Al/Cu/Al sample at 300°C for 40 min. a) comparison of experimental and calculated k-ratios for Al K_α and Cu L_α lines emitted from Al/Cu/Al after diffusion; b) structure of the sample restored on their basis (after P o u c h o u and P i c h o i r [13])

An example of the determination of Au concentration profile formed by heating of the Au/Ni two-layer system deposited on SiO_2 substrate at 850°C for 1 sec. is shown in Fig. 11.

The best agreement with the measured k-ratios was obtained for the sample contained three layers of thickness and Au concentration as shown in Fig. 11b.

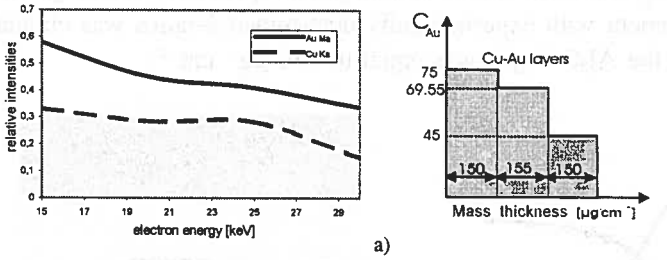

Fig. 11. Determination of Au concentration profile formed by heating of Au/Ni two-layer system deposited on SiO_2 substrate at 850°C for 1 sec. a) comparison of experimental and calculated k-ratios for Cu K_α and Au M_α lines emitted from Au/Cu layers on SiO_2; b) gold concentration profile restored on their basis

No more precise distributions of element concentrations in the sample could be obtained by increasing the number of layers in the layered structure model assumed in the correction procedure. The step-like profiles in the form of 3-4 bars, similar to those in Fig. 4b, is a typical result which can be expect in the case of single-phase diffusion, when the concentration of elements in the diffusion zone changes continuously.

5. Conclusions

It was shown that special correction is needed to determine the concentration profiles in the diffusion zones of thickness below tens of microns by use of EPMA in the cross-sections of the joints. The correction takes into account the influence of the width of *x*-ray generation volume on the size and shape of the determined *x*-ray intensity profiles and, in consequence on the values of diffusion coefficients calculated on their basis. In this work the correction method was described. It was shown that the errors increased with decreasing diffusion zone and increasing width of the *x*-ray generation volume. The correction can be omitted for diffusion zones greater than 100 microns, however for the very thin ones (thinner than 10 microns) the values of the diffusion coefficients calculated on the basis of as-measured profiles are several times higher than for the real ones.

The methods of determining the element concentration profiles in the coatings (layers) thinner than 1 micron were also described. It was shown that the proposed methods described well the concentration profile in the case of multiphase diffusion when step-like profiles are formed. In the case of single-phase diffusion, when the concentration of elements in the diffusion zone changes continuously, the methods can only give approximate diffusion profiles in the form of 3 to 4 bars of different element concentrations.

REFERENCES

[1] S.J.B. R e e d, X-Ray Optics and Microanalysis 1966 (eds. R. Castaing, P. Deschamps and J. Philibert), Hermann, Paris, 339 (1966).

[2] H.E. Bishop, Proc. Phys. Soc. **82**, 204 (1963).
[3] H.E. Bishop, Proc. Phys. Soc. **85**, 855 (1965).
[4] E.J. Rapperport, Advances in Electronics and Electron Physics, Supplement 6, Academic Press, New York, 117 (1969).
[5] J.I. Goldstein, J.W. Colby, Practical Scanning Electron Microscopy (eds. J.I. Goldstein and H. Yakowitz), Plenum Press, New York and London, 435 (1975).
[6] P.E. Best, in Spektrometria promieniowania rentgenowskiego (ed. V. Azaroff), PWN, Warszawa, 15 (1980).
[7] M. Żelechower, X-ray Optics and Microanalysis 1992 (eds. P.K. Kenway, P.J. Duke, G.W. Lorimer, W. Drummond, G. Love, A.G. Michette and M. Stedman), Institute of Physics Conference Series N°130, Institute of Physics, Bristol and Philadelphia, 157 (1992).
[8] J.B. Gilmour, G.R. Purdy, J.S. Kirkaldy, Met. Transactions **3**, 3213 (1972).
[9] D. Kowalczyk, K. Sikorski – to be published.
[10] S.J.B. Reed, Quantitative Electron-probe Microanalysis (eds. V.D. Scott and G. Love), Ellis Horwood Ltd, Chichester, 193 (1983).
[11] P.K. Gupta, J. Phys. D: Appl. Phys. **3**, 1919 (1970).
[12] M. Żelechower, Inżynieria Materiałowa **4**, 363 (1982).
[13] S. Baumgartl, P.L. Ryder, H.E. Büchler, Mikrochimica Acta, **Suppl.5**, 69 (1974).
[14] J.L. Pouchou, F. Pichoir, La Recherche Aerospatiale **5**, 47 (1984).
[15] J.L. Pouchou, F. Pichoir, Scanning **12**, 212 (1990).
[16] G.F. Bastin, J.M. Dijkstra, H.J.M. Heijligers, D. Klepper, Mikrochimica Acta, **Suppl.12**, 93 (1992).
[17] H.J. August, Mikrochimica Acta, **Suppl. 12**, 131 (1992).
[18] XTFML – Thin Film Multi-Layered software, CAMECA, Courbevoie 1993.
[19] TFA/MLA – Thin film analysis program, TECHAN, Eindhoven 1991.

Received: 1 March 2004.

ARCHIVES OF METALLURGY AND MATERIALS
Volume 49 2004 Issue 2

P. ZIĘBA *

ATOMIC TRANSPORT MEASURED BY ANALYTICAL ELECTRON MICROSCOPY TECHNIQUE

POMIARY TRANSPORTU ATOMÓW PRZY ZASTOSOWANIU TECHNIKI ANALITYCZNEJ MIKROSKOPII ELEKTRONOWEJ

Most of the changes in the structure occurs by thermally activated mass and charge transport through the matter, called diffusion. The most important information concerning the rate controlling factor can be determined from the solute partitioning, which accompanies the changes in the microstructure. In many cases, the solute redistribution occurs within a narrow area of nanometer order. Such highly localised changes in chemistry can be detected using an analytical electron microscopy (AEM). The present paper reviews the capabilities of AEM showing the following examples:

- diffusion couples and precipitation of grain boundary allotriomorphs (determination of intediffusion coefficient),
- discontinuous precipitation (determination of grain boundary diffusivity),
- austenite to intragranular ferrite and bainitic transformation (determination of transformation mechanism).

Większość zmian strukturalnych następuje w wyniku termicznie aktywowanego transportu masy lub ładunki nazywanego dyfuzją. Najważniejszą informację dotyczącą czynnika kontrolującego szybkości dyfuzji można uzyskać z rozkładu dodatku drugiego pierwiastka wynikającego ze zmian w mikrostrukturze.

W wielu przypadkach rozkład drugiego pierwiastka ma miejsce w bardzo wąskim zakresie ograniczonym często do kilku nanometrów. Tak subtelne zmiany w składzie chemicznym można jedynie analizować przy zastosowaniu analitycznej mikroskopii elektronowej (AEM).

W pracy przedstawiono syntetyczne ujęcie aktualnych możliwości AEM na przykładzie:

- złączy dyfuzyjnych oraz tworzenia wydzieleń aliotriomorficznych na granicach ziaren (wyznaczenie współczynnika dyfuzji wzajemnej-objętościowej),
- wydzielania nieciągłego (wyznaczanie dyfuzyjności na granicy ziarna),
- przemiany austenitu w ferryt oraz przemiany bainitycznej (określenie mechanizmu przemiany fazowej).

* INSTYTUT METALURGII I INŻYNIERII MATERIAŁOWEJ IM. A. KRUPOWSKIEGO, PAN, 30-059 KRAKÓW, UL. REYMONTA 25
* POLISH ACADEMY OF SCIENCES, INSTITUTE OF METALLURGY AND MATERIALS SCIENCE, 30-059 CRACOW, 25 REYMONTA STR., POLAND

1. Introduction

Most of the changes in the structure occur by thermally activated mass and charge transport through the matter. This process, called diffusion, plays a key role in the kinetics of many microstructural changes, which take place during processing of materials. Typical examples are: nucleation of new phases, diffusive phase transformations, precipitation and dissolution of a second phase, recrystallization and grain growth, high-temperature creep, annealing of radiation damage, and thermal oxidation.

The most important information concerning the rate controlling factor can be determined from the solute partitioning accompanying the changes in the microstructure. In many cases the solute redistribution occurs within a very narrow area of nanometer order, which is far beyond the spatial resolution limit offered by a conventional energy probe *X*-ray microanalysis. Such highly localised changes in chemistry can be detected using an analytical electron microscopy (AEM).

In the present paper, the potential and capabilities of AEM will be shown by the measurement of the variation of chemical composition resulting from interdiffusion process both in the bulk and at the interfaces.

2. Analytical electron microscopy

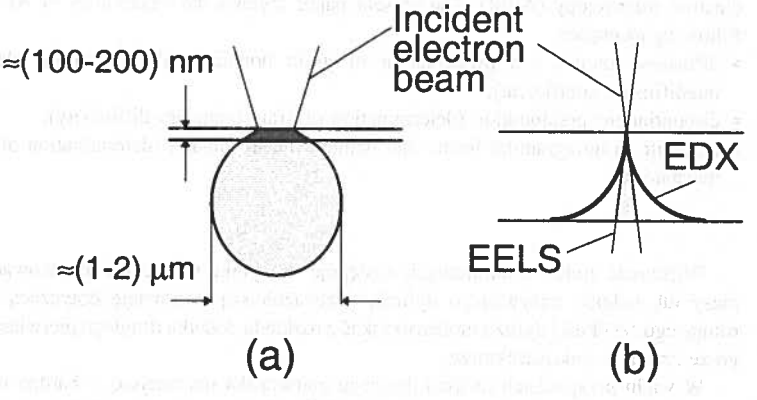

Fig. 1. Schematic representation of the activated volume in a bulk specimen (a) and thin foil (b)

The technique of AEM consists in the examination of a thin foil in a (scanning) transmission electron microscope ((S)TEM) equipped with an analyser of chemical composition. The incident electron beam focused down to tens of nanometers leads to the limitation of the analysed volume of the material by a factor of 10^5 and the beam broadening within the specimen by factor 10^2 in comparison with a conventional electron probe microanalysis (EPMA). This is schematically presented in Fig. 1 together with the geometry of the electron distribution for the energy dispersive X ray analysis (EDX) and electron energy-loss analysis (EELS). As can be seen, the broadening of electron beam within the

thin foil is comparable for both techniques, provided the foil thickness is less than 100 nm. The very complex quantification for the EELS is the reason that all the analytical electron microscopes are equipped with an EDX system while EELS system remains only an option.

The crucial parameter in measurements of chemical composition using the EDX system is spatial resolution, which is a measure of the smallest distance, R, between the centres of two analysed volumes, from which independent X-ray microanalysis can be obtained (Fig. 2). The parameter R comprises a combination of the incident electron beam diameter, d, and the beam broadening within the specimen, b. A recent definition of the spatial resolution, considered as the average broadening at the mid-plane of the foil, has been given by M i c h a e l al. [1] in the following form:

$$R = \frac{d + \sqrt{(d^2 + b^2)}}{2\sqrt{2}} \tag{1}$$

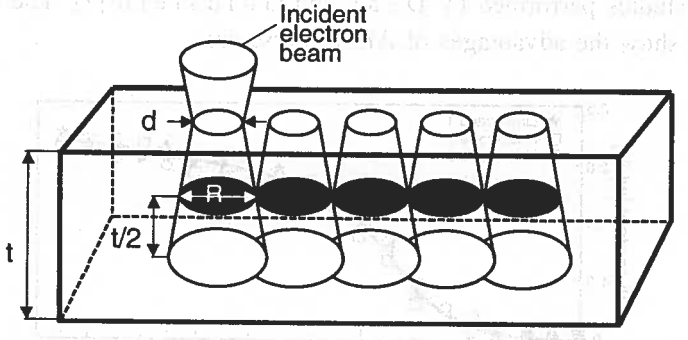

Fig. 2. Schematic diagram of the interaction volume for a series of electron probes scanned the specimen showing the definition of the spatial resolution in a thin foil

where the beam broadening in a single-scattering approximation is given by:

$$b = 625 \frac{Z}{E_o}\left(\frac{\rho}{A}\right)^{0.5} (10^{-7} t)^{1.5}. \tag{2}$$

Here, Z is the atomic number, A is the atomic weight, E_o is the beam energy in kV, ρ is the specimen density in g/cm^3, and t is the specimen thickness in cm.

This definition assumes that the electron distribution in the incident electron beam and within the thin foil are given by a G a u s s i a n function. To minimize R, it is necessary to reduce the diameter of the electron probe and sample thickness and to increase the accelerating voltage. However, the thinner the sample, the smaller the activation volume and the lower the intensity of the X-ray signal, which makes the detection and quantification of the elements much more difficult. Therefore, the parameters used during the analysis must be a compromise between the maximum attainable spatial resolution and the minimum detectability limit.

3. Determination of interdiffusion coefficient

3.1. Diffusion couple

Chemical or interdiffusion coefficient can be determined from a classical experiment by means of a diffusion couple. The experiment consists in clamping two pieces of solid material (pure metal or alloy) to each other. Annealing of such couple results in the diffusion manifested by a formation of a characteristic profile. Figure 3 shows the variation of Ni content for Fe/Fe-2 wt.% Ni couple. The good reproducibility of results for three line scans makes possible to use the Boltzmann-Matano analysis for determination of interdiffusion coefficient. The resulting value $D = 4.3 \times 10^{-14}$ cm^2/s corresponds very well with similar studies performed by D e a n and G o l d s t e i n [2]. The obtained results convincingly show the advantages of AEM. These are:

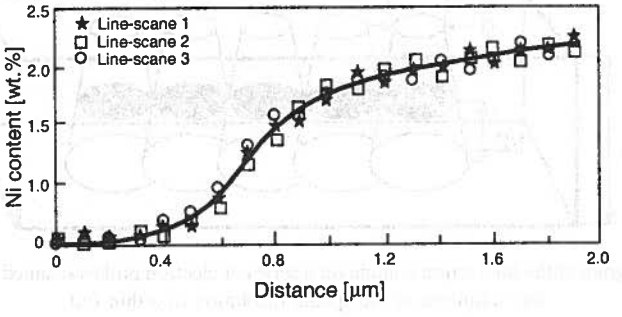

Fig. 3. Ni concentration profile for Fe/Fe-2Nu wt.% diffusion couple annealed at 925 K for 30 h

- very short diffusion field, usually less than 2 μm but in principle only limited by the spatial resolution (typically 10 nm) and the need to acquire a sufficient number of data points (10-20),
- annealing time of diffusion couple is up to ten times shorter than for the EPMA study. This enables interdiffusion experiment at $T < 0.3\ T_m$ (T_m- melting temperature),
- possibility of microstructural observations and determination of crystallography using selected area electron diffraction analysis.

However, applying analytical electron microscope it is necessary to asses carefully the possible effect of foil thickness on the quality of the resulting concentration profile. This is especially crucial in heavily absorbed system as Ni-Al. Figure 4 presents variations of Al content measured across Ni/Ni- 25 at.% Al diffusion couple annealed at 1100 K for 20 h. One can see that the results are seriously underestimated without applying correction procedure.

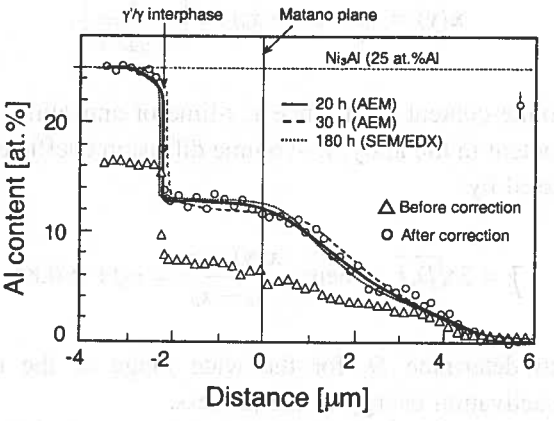

Fig. 4. Variations of Al content measured across Ni/Ni- 25 at.% Al diffusion couple annealed at 1100 K for 20 h

3.2. Precipitation of GB allotriomorphs

Precipitation of grain boundary (GB) allotriomorphs involves the volume diffusion of solute to the GB and then the diffusion of this solute along it to the growing edge of precipitate (Fig. 5a). The mechanism is called collector-plate [3] and the volume diffusion to the GB rate is the controlling step. The measurements of solute distribution near the grain boundary are the method to obtain the reliable diffusion data at relatively low temperature. Figure 5b shows the result of the EDX analysis recorded for Al-4.5 wt.% Cu alloy aged at 500 K for 6 hours. One can notice that the width of the profiles is less than 1 μm, which makes impossible to apply the conventional EPMA. The obtained profile is well described by the G r u b b e relationship:

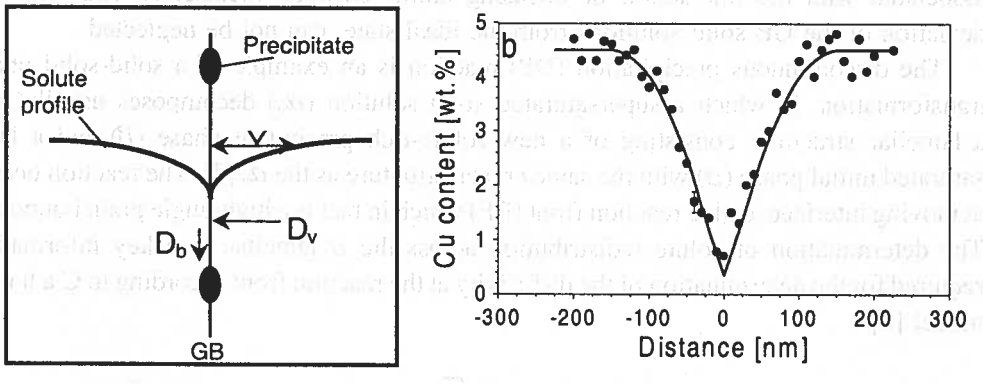

Fig. 5. a) Schematic diagram showing processes occurring during the growth of allotriomorphs, b) Cu distribution for the specimen aged at 500K for 6h. Solid line is the solution of Eq. 3

$$\mathbf{x}(y) = x_o + (x_e - x_o)\, erf\left(\frac{y}{2\sqrt{D_v t}}\right). \tag{3}$$

where $x(y)$ is the solute content at distance y, t-time of annealing, x_e-equilibrium solute content, x_o-solute content in the alloy, D_v-volume diffusion coefficient. The half-width of the profile is expressed by:

$$z = 2\sqrt{D_v t} \quad \text{where} \quad \frac{x(y) - x_o}{x_e - x_o} = erf1 \cong 0.84 \tag{4}$$

which allows us to determine D_v for the wide range of the temperatures and, in a consequence, the activation energy of the process.
The measurements performed in the temperature range from 460 K to 580 K resulted in the following equation for interdiffusion coeffcient:

$$D_v = 0.115 \exp\left(\frac{-32 kcal/mol}{RT}\right)$$

3.3. Grain boundary diffusivity

Diffusion along grain boundaries (GBs), being orders of magnitude faster than that through the bulk of crystal, plays a key role in a large number of metallurgical and technological processes. Most of the information gathered so far has been from experiments on stationary GBs [4-6]. Much less attention has been paid to the diffusion along GBs accompanied with simultaneous GB migration, which better reflects the real circumstances during service of the materials. For example, the concentration gradient created is larger and all the effects, associated with the interaction of diffusing atoms between themselves and with the deviation of the GB solid solutions from the ideal state, can not be neglected.

The discontinuous precipitation (DP) reaction is an example of a solid-solid phase transformation, in which a supersaturated solid solution (α_o) decomposes usually into a lamellar structure, consisting of a new solute-rich precipitate phase (β) and a less-saturated initial phase (α) with the same crystal structure as the α_o [7]. The reaction occurs at moving interface, called reaction front (RF) which in fact is a high-angle grain boundary. The determination of solute redistribution across the α lamellae is a key information required for the determination of the diffusivity at the reaction front according to C a h n ' s model [8]:

$$x(y) = (x_e - x_o)\frac{\cosh\left[(y - 0.5)\sqrt{C}\right]}{\cosh\left(\sqrt{C/2}\right)} + x_o \quad \text{with} \quad s\delta D_b = \frac{v_{DP}\lambda^2}{C}. \tag{5, 6}$$

Here, x_o is the solute content in the alloy, x_e is the equilibrium solute concentration in the α phase lamellae at the α/β interfaces, $s\delta D_b$ is the diffusivity at the grain boundary, v_{DP} is the growth velocity of the DP reaction, λ_α is the thickness of the α lamellae, and y is the normalised co-ordinate measured from the edge of the β lamella perpendicular to the α lamella.

Figure 6a shows several alternating α and Ni_3Sn lamellae of a colony moving into the supersaturated solid solution in an Ni-4 at.% Sn alloy. The corresponding result of the EDX analysis (Fig. 6b) shows that there is still an excess of the solute atoms within the α lamellae. The solid line represents the best fit to the Eq. 5 and allows the calculation of the parameter C in Eq. 6. Having v_{Dp} and λ_α from independent experiments, it is possible to determine the diffusivity at the reaction front of the DP. Such systematic investigation was performed for other alloy systems like Al-Zn, Cu-In and Co-Al [9-11]. The obtained diffusivities and the activation energy data were very similar to the relevant parameters for stationary GBs. This yields the conclusion that there was no significant difference in the rate of the diffusion process along the migrating and stationary GBs in the systems investigated. Therefore, it is believed that the diffusivity values of the moving reaction front of the DP reaction can be a source of reliable information about the diffusion rate, especially in systems and/or at temperatures, in which the radiotracer data are not available.

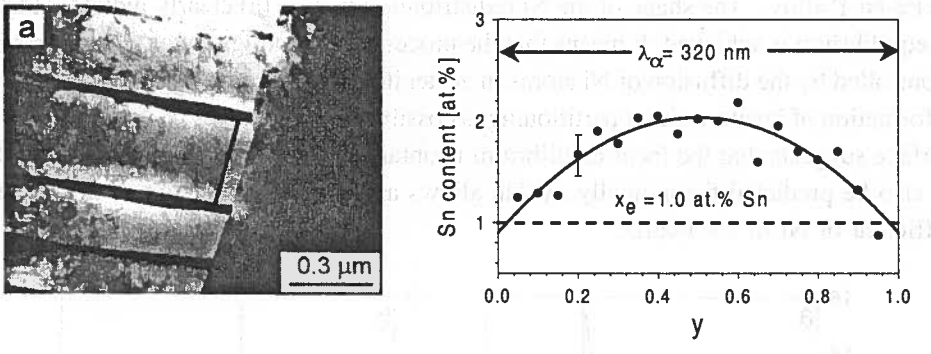

Fig. 6. Ni-4 at.% Sn alloy aged for 250 h at 725 K followed by 60 h at 775K. (a) TEM micrograph, and (b) example of a tin concentration profile measured across the α lamella. The location of the EDX line-scan is shown in Fig. 6a

4. Determination of growth mechanism

4.1. Solute partitioning in intragranular ferrite

There are three models describing the partitioning behaviour of the alloying elements during austenite (γ) to ferrite (α) transformation in the A-B-X ternary systems [12]. The equilibrium is characterized by complete partitioning at the α/γ interface and growth is controlled by the diffusion of alloying element B (Fig. 7a). In the case of local equilibrium ferrite forms without the partitioning of the alloying element (Fig. 7b). The situation, in

which ferrite inherits the alloy content of the parent phase is attributed to the para-equilibrium (Fig. 7c). For local- and para-equilibrium the growth is controlled by the diffusion of element *X*. Therefore, the determination of the solute redistribution across the α/γ interface will clearly indicate, which mode of the partitioning is dominant.

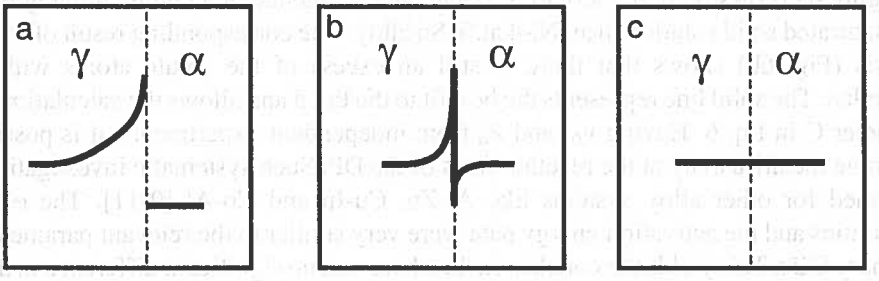

Fig. 7. Models describing the distribution of solute, which diffuses slower than others in a ternary system. Dashed line is the α/γ interface

Figure 8 shows the typical results of the EDX analysis made across the α/γ interface in two Fe-Ni-P alloys. The shape of the Ni redistribution in case (a) clearly indicates that the full equilibrium is achieved. It means that the process of the intragranular ferrite formation is controlled by the diffusion of Ni atoms in austenite. However, the case (b) indicates that the formation of ferrite without partitioning is possible. The pile-up of Ni content at the α/γ interface suggests that the local-equilibrium is obtained. One should note that Ni-profiles can also be predicted theoretically, which allows also the determination of the diffusion coefficient of Ni in the matrix.

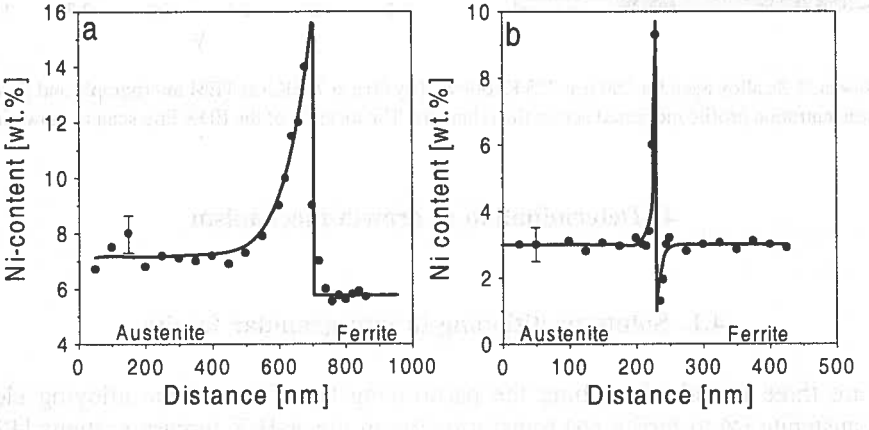

Fig. 8. Ni concentration measured across the α/γ interface for the Fe-7.2Ni-0.55P (wt.%) alloy cooled from 1170 K to 925 K at the rate of 5 K/day (a), and Fe-3Ni-0.6P (wt.%) annealed at 1075 K for 3 months (b). The solid line is the profile predicted by the theoretical model developed by Narayan and Goldstein [13]

4.2. Bainitic transformation in CuZnAl aloys

It is generally accepted [14] that bainitic transformation in non – ferrous alloys requires both, martensitic shear and diffusion-controlled mechanisms. The high spatial *X*-ray microanalysis can provide us with the information, which mechanism prevails in the nucleation and growth stage of the transformation.

Figure 9 presents the results of the EDX analysis performed in the various section of the growing bainite plate in a Cu-30Zn-6.5Al alloy. No change in solute content detected along the plate indicates that the lengthening takes place due to crystallographic-shear mechanism. However, the plate is simultaneously Zn-depleted in comparison with the matrix, which supports the idea that some kind of diffusion must be involved even in the early stage of bainite formation. The well-pronounced Zn profiles observed in the matrix in the case of the analyses across the plate show that the thickening is governed by volume diffusion process.

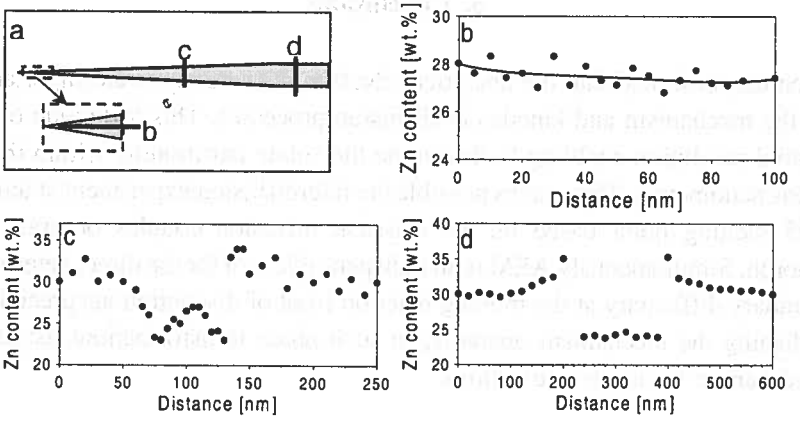

Fig. 9. Schematic representation of bainite plate in the Cu-30Zn-6.5Al (wt.%) alloy after ageing at 500 K for 600 s and the corresponding results of EDX analyses performed along the plate (b) and across the plate (c-d)

Figure 10 shows three different possibilities of the solute redistribution accompanying the bainitic transformation, which have been observed so far [15]. In case (a) bainite forms as an equilibrium phase in a diffusion controlled process. In case (b) pure shear mechanism is involved in the formation of the bainite plate (no change in the solute content) followed by diffusion mechanism until the equilibrium state is obtained. Case (c) takes into account the nucleation of the bainite plate by shearing at the defects, where the solute concentration is reduced due to stress induced diffusion. Since the nucleus was formed, the diffusion from the compression (-) to tension (+) side in the stress field activates faster growth in (+) direction. As a consequence, the asymmetric solute profiles on opposite sides of the bainite plate is observed. This explains the asymmetry of the Zn distribution in the matrix, which was shown in Fig. 9.

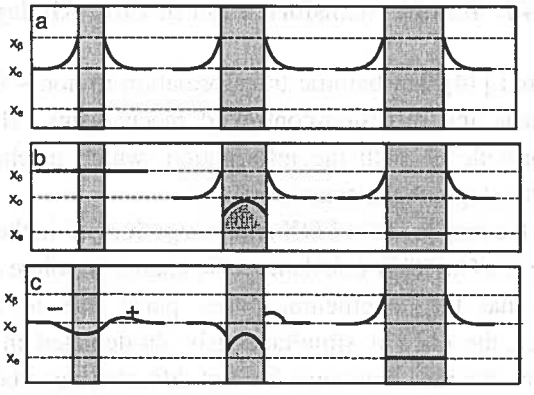

Fig. 10. Redistribution of solute content accompanying the bainitic transformation [15]

5. Conclusions

It has been demonstrated that the analytical electron microscopy is an important tool for studying the mechanism and kinetics of diffusion processes. This technique offers much better spatial resolution enabling to determine the solute partitioning within the range of several tens nanometers. This makes possible the interdiffusion experiment at temperatures below 0.3 melting point based on the classical diffusion couples or grain boundary allotriomorph. Simultaneously AEM is an indispensable tool for the direct determination of grain boundary diffusivity at the moving reaction front of discontinuous precipitation and for establishing the mechanism operating in such phase transformations as: austenite to ferrite and banitic in non-ferrous alloys.

REFERENCES

[1] J.R. Michael, D.B. Williams, J.I. Goldstein, C.F. Klein, R. Ayer, J. Microsc. **160,** 41 (1990).
[2] D.C. Dean, J.I. Goldstein, Metall. Trans. **17A**, 1131 (1986).
[3] H.B. Aaron, H.I. Aaronson, Acta Metall. 16, 789 (1968).
[4] I. Kaur, W. Gust, L. Kozma, Handbook of Grain and Interphase Boundary Diffusion, (Ziegler, 397 Stuttgart, 1989.
[5] I. Kaur, Y. Mishin, W. Gust, Fundamentals of Grain and Interphase Boundary Diffusion, John Wiley & Sons, Chichester, 1995.
[6] Y. Mishin, Chr. Herzig, J. Bernardini, W. Gust, Int. Mater. Rev. **42**, 155 (1997).
[7] P. Zięba, W. Gust, Int. Mater. Rev. **43**, 70 (1998).
[8] J.W. Cahn, Acta Metall. **7**, 18 (1959).
[9] P. Zięba, Local Characterization of the Chemistry and Kinetics in Discontinuous Solid State Reactions, Polish Academy of Sciences, Cracow, Ed. Orekop Ltd., 2001.

[10] P. Zięba, W. Gust, Z. Metallkd. **92**, 645 (2001).
[11] P. Zięba, Interface Sci. **11**, 51-58 (2003).
[12] J.R. Bradley, H.I. Aaronson, Metall. Trans. **12A**, 1729 (1981).
[13] C. Narayan, J.I. Goldstein, Metall. Trans. **15A**, 867 (1984).
[14] Z. Nishiyama, Martensitic Transformations (Application), Maruzen, p. 71 Tokyo 1974.
[15] K. Takezawa, S. Sato, Metall. Trans. **21A**, 1541 (1990).

Received: 1 March 2004.

A R C H I V E S O F M E T A L L U R G Y A N D M A T E R I A L S
Volume 49 2004 Issue 2

E. RABKIN *, Y. AMOUYAL*

APPLICATIONS OF SCANNING PROBE MICROSCOPY FOR STUDYING OF INTERFACIAL THERMODYNAMICS AND KINETICS

ZASTOSOWANIE MIKROSKOPII SIŁ ATOMOWYCH W BADANIACH TERMODYNAMIKI I KINETYKI ZJAWISK NA GRANICY FAZ

We illustrate how the quantitative information on interfacial thermodynamics and kinetics can be obtained from the *post-mortem* scanning probe microscopy studies of surface topography in the vicinity of grain boundary grooves formed during high-temperature annealing. The examples include the magnetic effect in surface diffusion in pure Fe and Fe-Pb alloys, the measurements of grain boundary energy in Ni-rich NiAl intermetallics, the effect of strong anisotropy in surface energy and diffusivity on the morphology of grain boundary grooves, and the recovery of grain boundary migration kinetics from the topography of new and abandoned grooves.

Autorzy zilustrowali sposób w jaki badania topografii powierzchni w strefie rowków powstałych na granicy ziaren podczas wysokotemperaturowego wygrzewania, metodą mikroskopii sił atomowych, mogą dostarczyć ilościowych informacji z zakresu termodynamiki i kinetyki zjawisk na granicy faz. Przedstawione przykłady to efekt magnetyczny w dyfuzji powierzchniowej w czystym Fe i w stopach Fe-Pb, pomiary energii granic ziaren w bogatych w Ni związkach miedzymetalicznych NiAl, wpływ silnej anizotropii energii powierzchniowej i dyfuzyjności na morfologię rowków granic ziaren oraz wnioskowanie o kinetyce migracji granic ziaren z topografii dwóch typów rowków.

1. Introduction

Temporal evolution of the surface topography driven by capillary forces is often controlled by surface diffusion and is closely related with the surface energy. A great deal of data on surface diffusivities and surface energies in a large variety of materials was obtained using the methods of healing of the periodic surface perturbations and of thermal grain boundary grooving. Scanning probe microscopy (SPM) allows the measurements of surface topography with high accuracy that was unattainable by the previous experimental

* DEPARTAMENT OF MATERIALS ENGINEERING, TECHNION-ISRAEL INSTITUTE OF TECHNOLOGY, 32000 HAIFA, ISRAEL

techniques. In this review we will show several examples of the use of SPM for determining interfacial diffusivities, energies and migration kinetics. Most of the results were obtained from the analysis of the thermal grooves formed at the intersection of a grain boundary (GB) with the free surface (Fig. 1). In the now classical treatment of W. W. Mullins [1] it was assumed that both surface energy and diffusivity are isotropic and that the equilibrium dihedral angle θ at the root of GB groove is instantly attained. High initial curvature at the root of the groove is relaxed by the surface diffusion bringing the near-root atoms to more remote regions and causing the growth of the groove. Assuming the local thermodynamic equilibrium at the surface and using the Nernst-Einstein equation for atomic mobility, Mullins obtained the equation relating the volume flux at the surface, J, with the surface chemical potential, μ_s:

$$J = \frac{D_s \delta}{kT} V_a \nabla_s \mu_s , \tag{1}$$

where D_s and V_a are the surface self-diffusion coefficient and atomic volume, respectively. kT has its usual meaning and ∇_s denotes the gradient of taken along the curved surface. From Eq. (1) the shape change of the surface can be determined using the mass conservation law:

$$\frac{\partial n}{\partial t} + \nabla_s J = 0 , \tag{2}$$

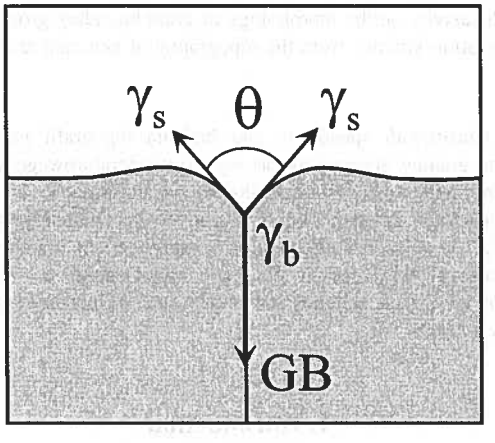

Fig. 1. Schematic of symmetrical GB groove

where the first term in the left hand side of Eq. (2) represents the rate of advance of the surface along the outward pointing normal. For the isotropic surfaces the chemical potential is proportional to surface curvature, K:

$$\mu_s = \gamma_s K , \tag{3}$$

where γ_s is the surface energy. For small surface slopes $\frac{\partial y}{\partial x} << 1$ the following

simplifications can be made: $K \approx -\frac{\partial^2 y}{\partial x^2}$ and $\frac{\partial n}{\partial t} \approx \frac{\partial y}{\partial t}$. Then the Eqs. (1), (2) and (3) yield together

$$\frac{\partial y}{\partial t} + B\frac{\partial^4 y}{\partial x^4} = 0, \tag{4}$$

where $B = \frac{\delta D_s \gamma_s}{kT} V_a$ is the M u l l i n s coefficient. In the context of the present paper two solutions of Eq. (4) are of particular interest. The first one describes the temporal evolution of artificially produced sinusoidal perturbation with the wave number $k_p = 2\pi/\lambda$, where λ is the perturbation wavelength:

$$y(x,t) = y(x,0)\exp[-Bk_p^4 t]\sin(k_p x). \tag{5}$$

The second solution describes thermal GB grooving. The formal boundary conditions for Eq. (4) in this case are:

$$y(\infty, t) = 0 \tag{6a}$$

$$\left.\frac{\partial y(x,t)}{\partial x}\right|_{x\to\infty} = 0 \tag{6b}$$

$$\left.\frac{\partial y(x,t)}{\partial x}\right|_{x=0} = \tan^{-1}\left(\frac{\theta}{2}\right) \equiv m \tag{6c}$$

$$\left.\frac{\partial^3 y(x,t)}{\partial x^3}\right|_{x=0} = 0. \tag{6d}$$

The Eq. (6d) follows from the symmetry of the problem (see Fig. 1) that requires zero surface diffusion flux at the root of GB groove ($x = 0$) and it can be obtained by combining Eqs (1) and (3). The solution of problem described by Eqs (4) and (6) was found to be [1]

$$y(x,t) = m(Bt)^{1/4} Z(u), \tag{7}$$

where $Z(u)$ is an even function of $u = \frac{x}{(Bt)^{1/4}}$ that was expressed by M u l l i n s as power series. An important property of this solution is that it describes a time-independent shape of GB groove growing self-similarly with the linear dimensions proportional to the fourth root of time. The width w between the maxima of the groove is given by

$$w \approx 4.6(Bt)^{1/4}. \tag{8}$$

Equation (8) provides a basis for calculation of surface diffusivity D_s from experimentally measured GB groove profile: once the width w is known the M u l l i n s coefficient can be determined and with the knowledge of γ_s the diffusivity D_s can be calculated [2]. In addition, the condition of mechanical equilibrium applied to the groove root requires the following equation to be fulfilled:

$$\gamma_b = 2\gamma_s \cos\left(\frac{\theta}{2}\right), \tag{9}$$

where γ_b is the energy of a GB. Equation (9) is the basis for determining the relative GB energy γ_b/γ_s, from the known surface slope at the root of GB groove. It is straightforward to use the advantages of SPM for determining the surface diffusivities and relative GB energies [2, 3]. Moreover, the unprecedented vertical resolution of SPM allowed us to uncover the fine features of GB grooves that urged further development and extension of original M u l l i n s model [4]. In addition, the fine details of dynamic behavior of the GBs could be recovered from surface topography in the vicinity of GB grooves [5, 6]. The new experimental data along with the developed theoretical models are reviewed below.

2. Surface diffusion in Fe and Fe-Pb

Fine grain samples of pure Fe and Fe-5 wt.% Pb alloys were prepared by cold compaction of pure Fe or a mixture of Fe and Pb elemental powders (99.9 wt.% nominal purity and 5 mm initial particle size) with the intermediate reduction of the green body at 600 °C in the flow of dry hydrogen for removal of surface oxides. The details of experimental procedure can be found in Ref. [2]. The samples were subsequently annealed in the flow of hydrogen in the temperature range of 650-900 °C. In the Fe-Pb alloy partial extraction of Pb to the surface of the sample and formation of droplets of liquid Pb occurred during annealing. These droplets were then partly evaporated either *in-situ* (during high-temperature annealings) or, after the long low-temperature annealing, by a short exposure of the sample at high temperatures in dynamic vacuum. Figure 2 shows an optical microscopy (OM) micrograph of imprints left by the evaporating droplets, and a SPM micrograph of the border region of one of these imprints. A difference in surface morphology between the former solid-liquid (S-L) and solid-Pb vapor (S-V) interfaces is clearly visible. In both cases the GB grooves are formed but they are deeper and wider at the S-L interface than at the *S-V* interface. Examples of the GB groove profiles at the S-L interface for two different temperatures are given in Fig. 3. It can be seen that the groove formed at 800 °C is considerably wider than its counterpart formed at 650 °C.

The A r r h e n i u s plot of the diffusion coefficients derived from the measured values of w with the aid of Eq. (8) is shown in Fig. 4. It is known that for pure Fe in dry hydrogen (S-H_2 interface) the GB grooving proceeds by the surface diffusion mechanism [7]. Assuming the same mechanism for the *S-V* interface, one finds that the values of D_s in these two cases are very close to each other, thus supporting the hypothesis of the surface diffusion mechanism of GB grooving at the *S-V* interface. The D_s dependences exhibit two

linear regions on either side of the C u r i e temperature T_C. Above T_C, the activation energy, Q, is low (Q = 110 ± 70 kJ mol^{-1}), whereas below T_C the activation energy is much higher (Q = 550 ± 150 kJ mol^{-1}). For the *S-L* interface the GB grooving mechanism is unknown. Both the surface self-diffusion and the diffusion of Fe in the liquid phase represent feasible mechanisms of GB grooving in this range of temperatures (self-diffusion in the bulk of solid Fe is excluded because it is too slow). Therefore, the experimental data were processed with the help of Eq. (8) (D_s, surface diffusion mechanism, filled triangles in Fig. 4) and with the help of a model assuming that bulk diffusion in liquid controls the process of GB grooving (D_l, diffusion in the liquid phase, filled squares in Fig. 4). It can be seen that the temperature dependences of D_s and D_l are not affected by the C u r i e transformation. At lower temperatures (650-680°C) the grooves dimensions at the *S-L* interface change abruptly and approach those at the S-H_2 interface, thus suggesting that the grooving mechanisms for these two interfaces are identical in this range of temperatures.

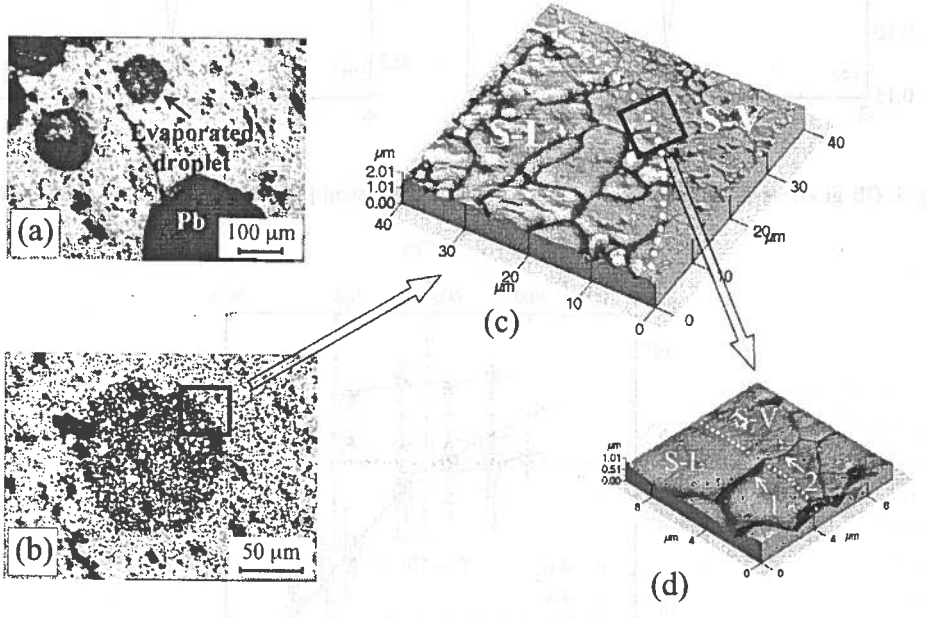

Fig. 2. OM (a, b) and SPM (c, d) micrographs of the surface of an Fe-Pb sample annealed at 700°C for 4 h. Note in (a) the presence of Pb droplets of 50-100 μm in diameter and of imprints of evaporated droplets. The micrograph (b) is a zoom on the evaporated droplet of the micrograph (a). The SPM images (c, d) were taken at the border between the S-L and S-V interfaces [marked by a rectangle in (b)]. A difference in morphology of the S-L and S-V interfaces is clearly seen [2]

The change of the activation energy for D_s at the C u r i e temperature T_C for pure Fe and for *S-V* interface of the Fe-Pb alloy can be interpreted in terms of the effect of ferromagnetism on diffusion. For volume diffusion, the anomaly of the diffusion coefficient below T_C was explained by the effect of spin ordering on the vacancy formation and motion [8]. A drastic change of the GB diffusion coefficient below T_C has also been reported [9]. But to our knowledge, the data obtained in Ref. [2] represents the first direct observation of

magnetic effect in surface self-diffusion. The physical reason for this effect may be similar to that for the magnetic effect for bulk diffusion. However, the C u r i e transition can also increase the amount of segregated residual impurities at the surface, as was the case for GB segregation [10]. Segregated impurities can diminish drastically the rate of surface self-diffusion [11]. Therefore, it is possible that the observed magnetic effect is the result of an increased surface segregation of impurities below the C u r i e temperature.

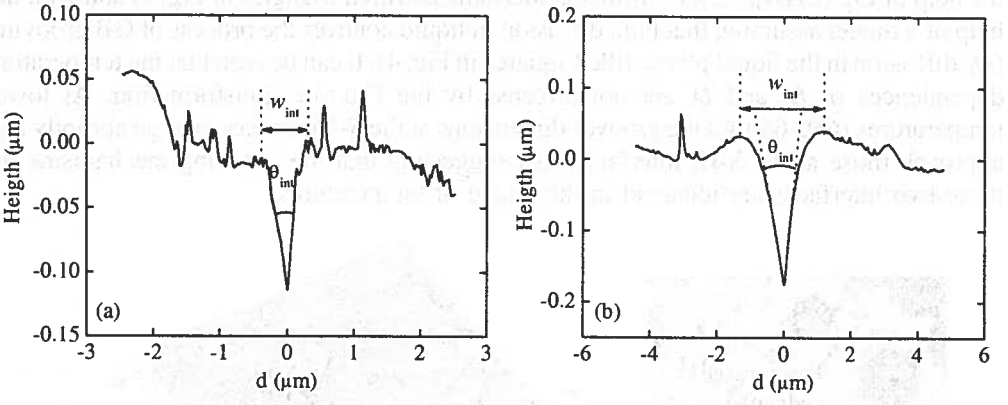

Fig. 3. GB groove profiles at the S-L interface in the Fe-Pb system [2]. (a) 8h at 650°C; (b) 2h at 800°C

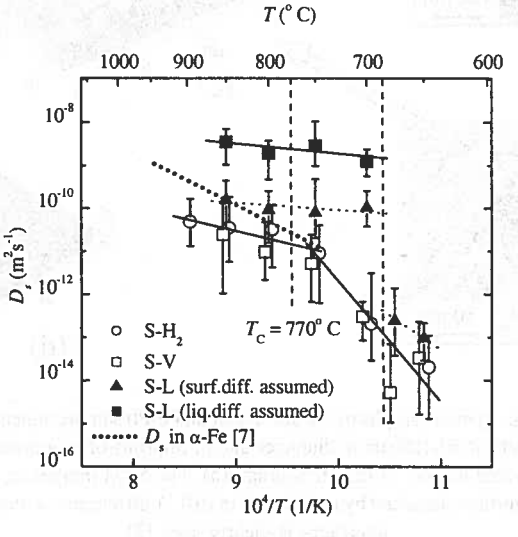

Fig. 4. Temperature dependence of the interfacial diffusion coefficients for pure Fe and for S-V and S-L interfaces in Fe-Pb [2]. For the S-L interface, the diffusion coefficients were derived from w assuming interface (filled triangles) and liquid (filled squares) diffusion mechanisms. The temperature dependence of D_s for pure Fe from Ref. [7] is given for comparison

The striking feature of Fig. 4 is that the C u r i e transformation has no effect whatsoever on the temperature dependence of the coefficient of Fe self-diffusion along the *S-L* interface, an abrupt decrease of the diffusivity being observed only 100°C below the Curie

point. It is very unlikely that the presence of liquid Pb shifts the Curie temperature at the interface by more than 100°C, since it follows from Fig. 4 that the Curie temperature for the *S*-H_2 and *S*-*V* interfaces is very close to the bulk one. Therefore, the bulk diffusion of Fe atoms in the liquid Pb seems to be the only GB grooving mechanism consistent with the temperature dependence of the diffusion coefficient. Indeed, the data on the temperature dependence of the GB groove width, w processed under the assumption of liquid bulk diffusion mechanism yield the bulk diffusivities in the range of $10^{-8} - 10^{-9}$ m^2s^{-1}, which are typical values for bulk diffusivity in many metallic melts. Moreover, no magnetic effect should be observed for diffusion in paramagnetic liquid Pb, and the activation energy for diffusion in a liquid should be lower than that for surface diffusion. This is consistent with the experimental results (see Fig. 4), which unequivocally prove that the GB grooving at the *S*-*L* interface in the Fe-Pb system occurs by diffusion of Fe through the liquid phase. This mechanism is dominant for GB grooving at the S-L interface for the majority of solid-liquid metallic couples.

3. GB energy in NiAl

Figure 5 represents a typical GB groove formed in polycrystalline Ni-45.6 at.% Al alloy after annealing at 1400 °C for 30 min. The details of experimental procedure can be found in Refs [3] and [6]. Our aim was to determine the relative GB energy and to correlate is with geometrical degrees of freedom (DOFs) of the boundaries. The macroscopic geometrical DOFs of a GB are associated with the misorientation parameters of two adjacent grains and with the inclination of GB plane. Geometrical DOFs of the GBs in bulk polycrystalline sample were determined by a combination of electron backscattering diffraction (EBSD) in scanning electron microscope (SEM) and metallographic serial sectioning technique. A common difficulty in presenting the dependence of GB energy on macroscopic geometrical DOFs is that it requires 6-dimensional space. To avoid this, we convoluted all five DOFs into two parameters: the disorientation angle and the dimensionless parameter η that describes the tilt/twist character of GB. η is defined as a scalar product of the normal to the GB plane and the unit vector directed along the disorientation axis. The cases $\eta = 0$ and $\eta = 1$ correspond to pure tilt and twist GBs, respectively, while any $0 < \eta < 1$ describes a general GB of a mixed type. The three-dimensional presentation of GB properties as a function of disorientation angle and parameter η was firstly suggested by Seidman and Krakauer [12]. The dependence of relative GB energy in Ni-rich NiAl on GB disorientation and on parameter η is shown in Fig. 6. It can be seen that the ratio γ_b/γ_s can exceed 1 which is unusually high for metallic materials but rather common for ceramics. It can be concluded, therefore, that from the point of view of interfacial energies NiAl intermetallic is intermediate between pure metals (where $0.3 < \gamma_b/\gamma_s < 0.5$ for large angle random GBs) and brittle ceramics. In this respect the intergranular brittleness may be an intrinsic property of NiAl. Another interesting conclusion that can be drawn from Fig. 6 is that the twist GBs generally exhibit higher energies than their tilt counterparts. His is in agreement with the results of Seidman and Krakauer that found higher impurity segregation at twist boundaries in Fe-Si alloy [12].

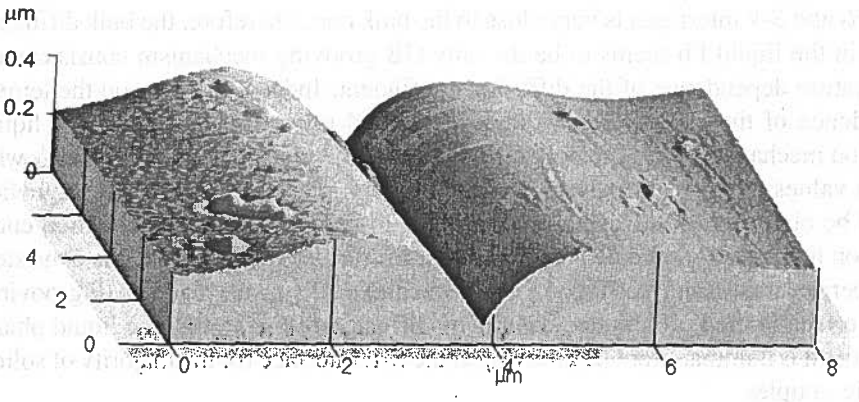

Fig. 5. A SPM image (composed of 256×256 pixels) of a typical GB groove in Ni-rich NiAl [3]

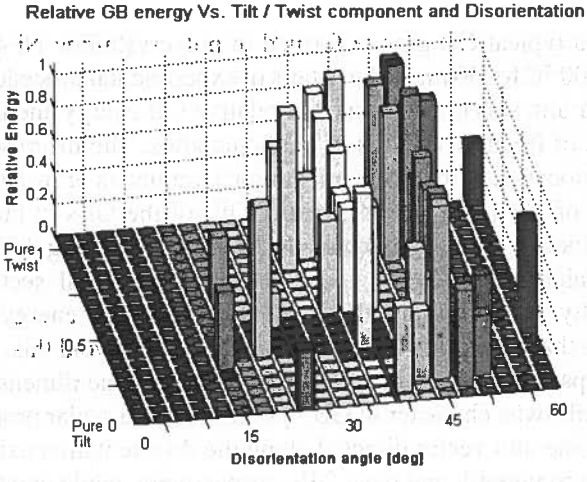

Fig. 6. The dependence of relative GB energy in Ni-rich NiAl on the Tilt/Twist component (h) and disorientation angle

4. The effect of faceting on GB grooving

Some of the GB grooves in Ni-rich NiAl exhibited unusual morphology that is in apparent contradiction with the main concept of the M u l l i n s model [1]. One example is shown in Fig. 7 [4]. The root region of this groove exhibits apparent negative curvature which means that surface diffusion flux should be directed from the remote surface regions to the root of the groove. In this case, however, the healing instead of growth of the GB groove should occur. Closer inspection of the root reveals that apparent concave curvature is caused by a flat facet joined by curved convex surfaces. This faceting is related with the surface energy

anisotropy, and such faceted grooves were not considered in determining GB energy in Ref. [3]. One way to deal with the problem of GB grooving for anisotropic surface energy was suggested in Ref. [13]. In this approach, the expression (3) is modified by adding to γ_s an appropriately chosen second derivative of γ_s with respect to surface inclination, and Eqs (4) and (6) are solved numerically. In our approach developed in Ref. [4] we assumed from the beginning that otherwise isotropic surface γ-plot exhibits a sharp cusp at singular orientation that results in surface faceting. The Mullins' problem can be solved in this case without any specific knowledge of the dependence of surface energy on inclination in the cusp region. The new geometry of the groove, in addition to the usual Mullins' parameters, is determined by the inclination α of the singular surface to the original sample surface, by the energy γ_0 of the singular surface, and by the ratio $d = D_0/D_s$, where D_0 is the self-diffusion coefficient along the singular surface (see Fig. 8).

The examples of the calculated self-similar GB groove shapes are shown in Fig. 9. It can be seen that with decreasing d the length of the facet at the root of the groove decreases, such that for $d \to 0$ the grooves converges to symmetric, M u l l i n s-type shape. However, the apparent slope of non-singular surface at the GB root $m_1 = \tan(\alpha + \delta\theta)$ is different from the slope m of classical isotropic groove determined by Eqs (6c) and (9). This difference is caused by finite rate of free energy dissipation caused by diffusion along short, but highly immobile facet. This is an instructive example showing how the kinetic anisotropy may affect the apparent values of energetic parameters determined from the study of surface topography.

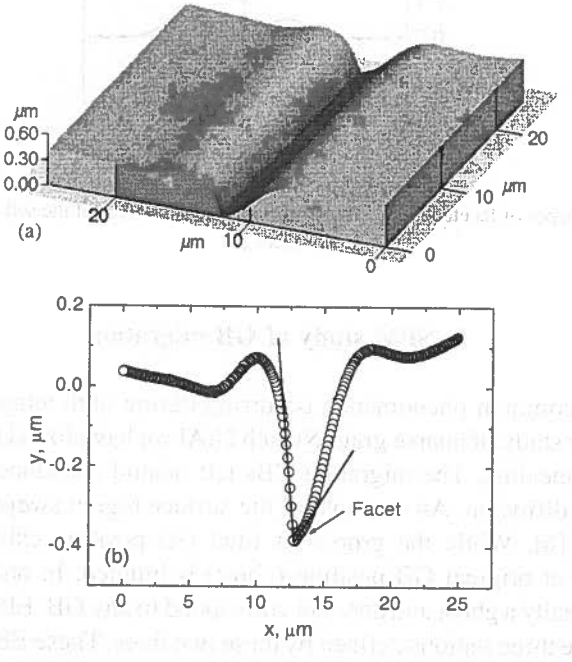

Fig. 7. A SPM image of anisotropic GB groove exhibiting an apparent concave surface curvature at the groove root (a) and a corresponding topography line profile taken perpendicular to the GB (b)

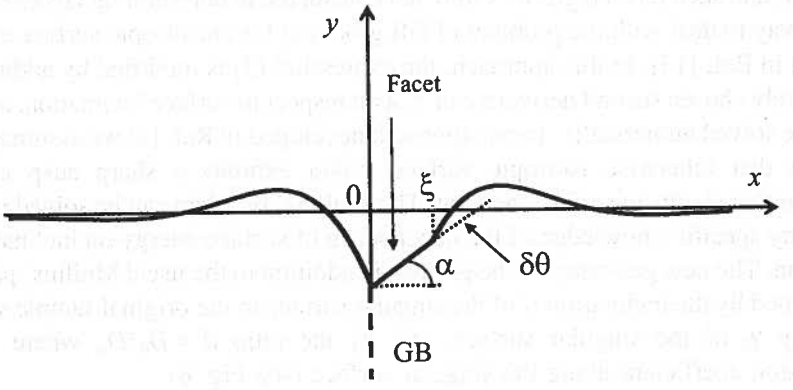

Fig. 8. The geometry of of faceted GB groove [4]

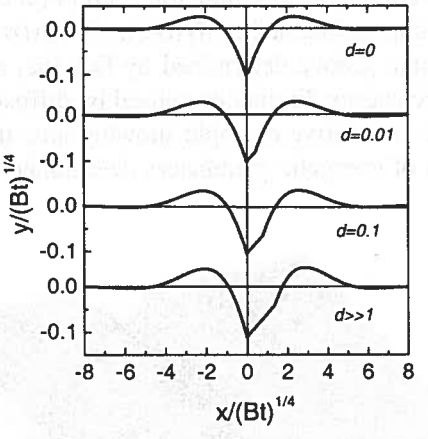

Fig. 9. The calculated shapes of faceted GB grooves different relative values of the self-diffuson coeficient along the facet [4]

5. SPM study of GB migration

Grain growth is a common phenomenon occurring during high temperature annealing of polycrystals. In our study of coarse grain Ni-rich NiAl we have found that some of the GBs migrated during annealing. The migrating GBs left behind abandoned groves that begun healing by surface diffusion. An example of the surface region swept by migrating GB is shown in Fig. 10 [6]. While the groove at final GB position exhibits sharp root, the abandoned groove at original GB position (ghost) is blunted. In order to verify that the blunted groove is really a ghost and does not correspond to any GB, EBSD patterns (EBSPs) were taken from the three regions defined by these two lines. These EBSPs shown in Fig. 10 indicate that two crystallographically identical regions straddle the ghost line, while the actual change of orientation occurs across the narrow sharp groove.

The migration time of the GB can be calculated as a difference between the formation time of the new groove at the final GB position and the healing time of the abandoned groove. Since the blunting of the groove root occurs in the close vicinity of the triple line, the initial conditions for this problem can be approximated by the symmetrical sharp wedge formed by two surfaces with the slopes $\pm m$:

$$y(x,0) = mx \tag{10a}$$

$$\left.\frac{\partial y(x,t)}{\partial x}\right|_{x\to\infty} = m \tag{10b}$$

$$\left.\frac{\partial y(x,t)}{\partial x}\right|_{x=0} = 0 \tag{10c}$$

$$\left.\frac{\partial^3 y(x,t)}{\partial x^3}\right|_{x=0} = 0\,. \tag{10d}$$

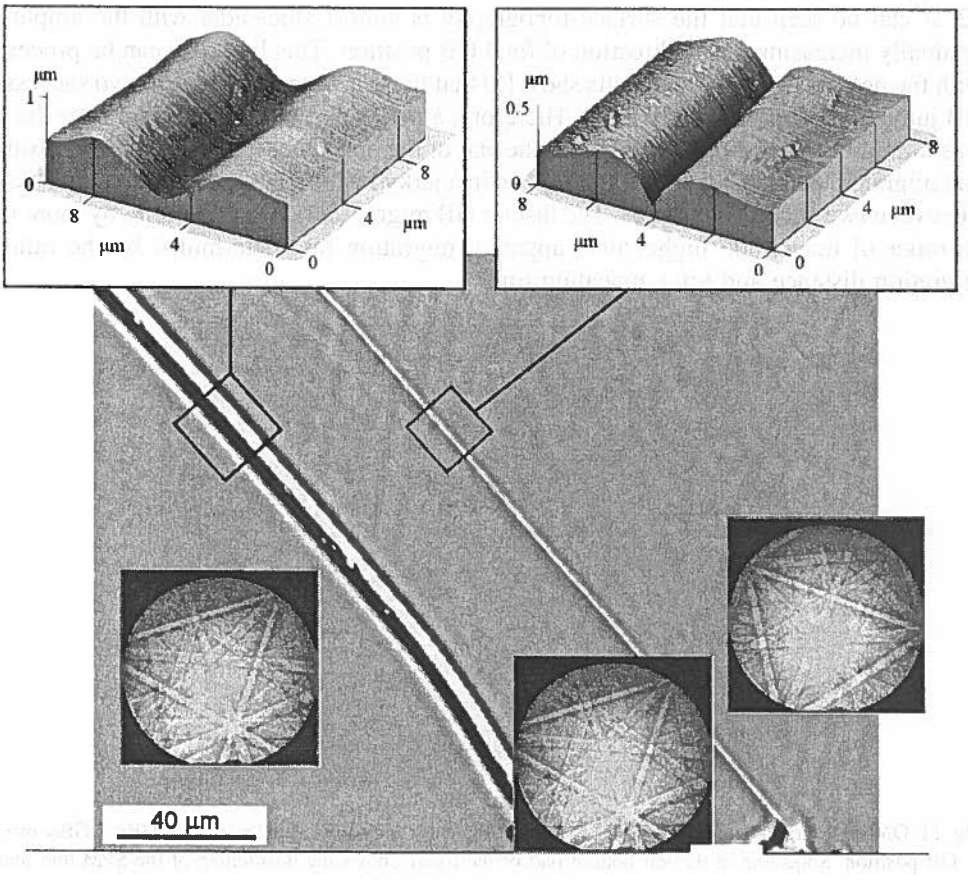

Fig. 10. SEM image of migrated GB together with the SPM images of the abandoned (left) and new (right) grooves

It is easy to show (by simple substitution) that the function

$$y(x,t) = mx - m(Bt)^{1/4} Z(u) \qquad (11)$$

represents a solution of Eqs (4) and (10). We fitted the shape of the blunted root of abandoned GB grooves by Eq. (11) and determined using such fitting the time of groove blunting. In all cases this time turned out to be approximately equal to the formation time of the new groove determined using Eq. (8). This means that at the late stages of grain growth in coarse grain NiAl most of the time the GBs are immobile and all changes of microstructure occur by very fast migration of few GBs. Similar conclusions were drawn from the study of the morphologies of the "ghost lines" [5] and of migrated triple junctions [6].

In Fig. 11 the characteristic surface morphology of the family of "ghost lines" left behind migrating GB in Ni-43.0 at.%Al alloy after 1 h annealing at 1400 °C is shown. This kind of surface perturbation occurs in the course of spasmodic GB migration: tiny GB groves are formed during short "stop" phase of the migration process, and their decay begins immediately after the GB abandon them during "go" phase of the migration process. The typical SPM line scan of the area in the middle of the ghost line region is shown in Fig. 12. It can be seen that the surface topography is almost sinusoidal with the amplitude gradually increasing in the direction of final GB position. This line scan can be processed with the help of Eq. (5). The results show [5] that the time interval between two successive GB jumps was approximately 3.5 s. Therefore, a major part of the annealing time the GB was immobile, then about 100 s before the end of the annealing it left the original position and migrated the distance of approx. 52 μm in a jerky fashion, with the time interval of 3.5 s between two successive jumps. The instant GB migration rate is, therefore, by more than an order of magnitude higher than apparent migration rate determined by the ratio of migration distance and total annealing time.

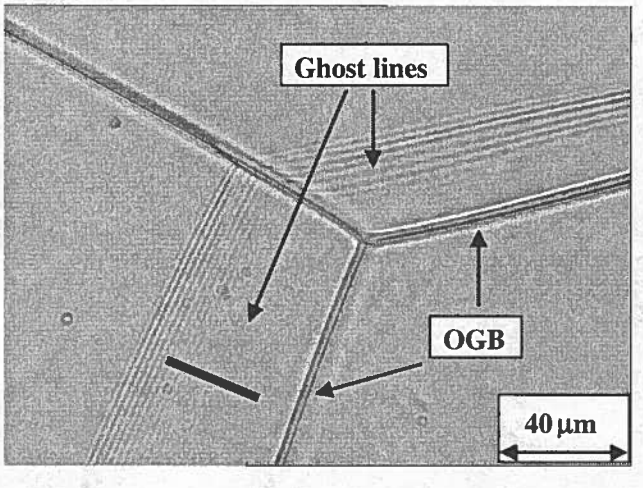

Fig. 11. OM micrograph demonstrating the regions of the ghost lines left behind migrating GBs. OGB = original GB position. Solid line in the left bottom part of the figure shows the positioning of the SPM line scan presented in Fig. 12 [5]

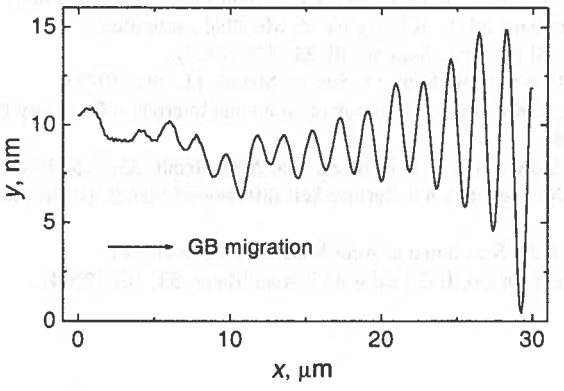

Fig. 12. SPM line scan along the solid line in Fig. 11 in the region of the ghost lines

6. Conclusions

We have shown that the quantitative and precise measurements of surface topography with the help of SPM provide valuable information on surface diffusion and GB energy. In comparison with other techniques used previously for these purposes (i.e. OM, SEM, and laser surface interferometry) the SPM is unique since it combines the possibility to scan large surface areas with the atomic resolution in the vertical direction. Beyond the increased accuracy in determining of thermodynamic and kinetic parameters, the use of SPM allowed us to reveal phenomena that were largely overlooked in the past, such as faceting in the vicinity of GB groove root. This urged an appropriate revision and extension of the original Mullins' model of GB grooving. Moreover, the possibility of quantitative characterization of the dynamics of GB migration during high-temperature annealing from the fine features of surface topography determined in post-mortem SPM study was demonstrated.

Acknowledgement

This research was partly supported by the US-Israel Binational Science Foundation under the Grant No. 2000066. Helpful discussions with Prof. Y. Mishin, Dr. L. Klinger, Dr. J.-P. Monchoux and Dr. V. Semenov are heartily appreciated.

REFERENCES

[1] W.W. Mullins, J. Appl. Phys. **28**, 333 (1957).
[2] J.-P. Monchoux, E. Rabkin, Acta Mater. **50**, 3159 (2002).
[3] Y. Amouyal, Y. Mishin, E. Rabkin, Acta Mater., in preparation.
[4] L. Klinger, E. Rabkin, Interface Sci. **9**, 55 (2001).

[5] E. Rabkin, V. Semenov, T. Izyumova, Scripta Mater. **42**, 359 (2000).
[6] E. Rabkin, Y. Amouyal, L. Klinger, Z. Metallkd., submitted.
[7] J. M. Blakely, H. Mykura, Acta metall. **11**, 399 (1963).
[8] G. Hettich, H. Mehrer, K. Maier, Scripta Metall. **11**, 795 (1977).
[9] I. Kaur, W. Gust, L. Kozma, Handbook of Grain and Interphase Boundary Diffusion Data **1**, Ziegler Press, Stuttgart (1989).
[10] K. Ishida, S. Yokoyama, T. Nishizawa, Acta Metall. **33**, 255 (1985).
[11] G. Neumann, G. M. Neumann, Surface Self-diffusion of Metals, Diffusion Information Center, Bay Village (1972).
[12] B.W. Krakauer, D.N. Seidman: Acta Mater. **46**, 6145 (1998).
[13] W. Zhang, P. Sachenko, I. Gladwell, Acta Mater. **52**, 107 (2004).

Received: 1 March 2004.

A R C H I V E S O F M E T A L L U R G Y A N D M A T E R I A L S
Volume 49 2004 Issue 2

B. SEPIOŁ *, M. SLADECEK*, L.M. STADLER*, D. KMIEĆ*, M. RENNHOFER*,
G. VOGL*, M. HAJDUGA**

SYNCHROTRON RADIATION – A VERSATILE TOOL FOR DIFFUSION STUDIES

PROMIENIOWANIE SYNCHROTRONOWE – UNIWERSALNE NARZĘDZIE DO BADAŃ DYFUZJI

Due to the finite size, dynamical effects become more pronounced but also more complex in nanostructured materials compared to bulk solids. The progress in synchrotron methods and the access to X-rays of third generation synchrotron radiation sources enables studies of dynamics in surfaces and nanostructures. Especially nuclear resonant scattering of synchrotron radiation, which has gained the sensitivity required to study ultra thin films in the last years, can explore nearly the whole field of dynamical effects. Combining X-ray reflexion with nuclear resonant scattering of synchrotron radiation results in the depth-selective investigation of hyperfine parameters of the resonant atoms, allowing study their motion in near-surface layers. The availability of coherent X-rays enabled photon correlation spectroscopy studies of coarsening mechanisms in phase-separating alloys otherwise inaccessible with any other experimental method.
The manuscript is intended as compact but extensive introduction into theoretical principles of synchrotron radiation methods applied for diffusion studies, illustrated with most recent experimental results.

W materiałach nanostrukturalnych efekty dynamiczne są wyraźniejsze aniżeli w materiałach masywnych. Rozwój metod synchrotronowych i dostęp do trzeciej generacji źródeł promieniowania synchrotronowego umożliwia prowadzenie badań dynamiki zjawisk zachodzących w warstwach powierzchniowych i nanostrukturach. Specjalne zastosowanie znajduje tutaj rezonansowe rozpraszanie jądrowe promieniowania synchrotronowego, gdyż wysoka czułość tej metody umożliwiająca badania nawet ultra cienkich warstw sprawia, że pokrywa ona prawie cały zakres efektów dynamicznych. Połączenie metod odbicia promieniowania X i rezonansowego rozpraszania jądrowego promieniowania synchrotronowego umożliwia badanie ruchu atomów w warstwach przypowierzchniowych. Dostępność spójnego promieniowania X umożliwiła badania spektroskopowe korelacji fotonów w zastosowaniu do mechanizmów koagulacji w stopach. Prezentowana publikacja jest pomyślana jako zwięzłe przedstawienie podstaw teoretycznych metod badawczych wykorzystujących promieniowanie synchrotronowe do badań dyfuzji, zilustrowane najnowszymi wynikami eksperymentalnymi.

* INSTITUT FÜR MATERIALPHYSIK DER UNIVERSITÄT WIEN, A- 1090 WIEN, AUSTRIA
** INSTITUTE OF MATERIALS ENGINEERING, UNIVERSITY OF BIELSKO BIAŁA 43-309 BIELSKO-BIAŁA, POLAND

1. Introduction

It is hard to overestimate the role of diffusion, an important and fundamental phenomenon responsible for the properties and behaviour of metals, alloys, semiconductors, ceramics, glasses and polymers at higher temperatures and playing an essential role in the kinetics of microstructural changes in materials. Diffusion is a driving force for nucleation of new phases, recrystallisation and phase transformations with a wide use in current technology, e.g., surface hardening, changing of deformation behaviour by nucleation, diffusion doping or sintering. Particularly important is the role of diffusion in nanostructures. The term "nanostructure" has various interpretations in materials science, e.g., nanocrystals embedded in a matrix, thin layers, multilayers, clusters or even molecules. All of these terms describe objects with different shapes but there is a common peculiarity – the high fraction of surfaces and interfaces, respectively. These determine the modification of mechanical and magnetic properties of nanostructures that provide interesting perspectives of mechanical (composite materials, solid lubricants, filters), magnetic (ultrahigh density recording) and electronic applications (nanotransistors, field emitters). Self-organised nanostructures on single crystalline substrates, embedded into single crystalline matrices or even intermetallic phases that can also be considered as self-organised structures on the atomic level play a special role in experimental results discussed in this paper, while they represent different model systems, easy to prepare and representative for a wide class of materials.

The intermetallics attracted attention as suitable materials for high-temperature applications. The knowledge of the diffusion behaviour of the intermetallics is, therefore, of interest for basic materials science and for their use in technological applications. On the other hand, processes in or near surfaces represent another main focus of our scientific interest and will be discussed in detail here.

To achieve a thorough understanding of diffusion in the solid state, where both the collective (phonons) and single-particle (usually called diffusion) dynamics shall be understand, a detailed characterisation of the structure of the system on an atomic scale must be achieved. In most cases this requires the combination of different experimental techniques. Diffusion in solids is typically investigated on a macroscopic scale following the interpenetration of two atomic species across an interface, which is related to the chemical diffusion coefficient. The self-diffusion coefficient can be measured, on the other hand, by labelling atoms with radioactive isotopes. This technique, also known as tracer or macroscopic method of diffusion investigation and thoroughly discussed through other contributions of this band, deduces atomic events from macroscopic effects as, for instance, the concentration gradient of diffusing isotopes. Diffusion can also be studied at the microscopic level, i.e., by revealing the jump vector and the jump rate of the atoms. The study of the microscopic jump diffusion mechanism, i.e., jump vectors and residence times on different lattice sites, is the topic of this paper. Different scattering methods can be used to resolve the atomic dynamics on various time scales: *Mössbauer* spectroscopy, quasielastic neutron scattering and neutron spin echo, nuclear resonant scattering, quasielastic scattering of helium atoms or *X*-ray photon correlation spectroscopy.

A considerable part of our investigations was performed in recent years with synchrotron radiation (SR), which turns out to be an exceptionally versatile tool for diffusion studies. There are several textbooks on synchrotron radiation but we recommend a book written by A l s - N i e l s e n and M c M o r r o w [1], which has been used in the preparation of this article. In this contribution special consideration has been given to the peculiarities of SR, e.g., high coherence and spectral density, facilitating diffusion studies. Two methods utilising SR, nuclear resonant scattering (NRS) in bulk and on the surface in grazing-incidence geometry and *X*-ray photon correlation spectroscopy (XPCS), will be treated in this paper. Other methods are thoroughly discussed in the literature, see Refs. [2-6] and citations hither.

2. Photon sources and their application for diffusion studies

Since the discovery of X-rays by W.C. Röntgen in 1895, their application range has progressively increased. Progress was steady to the mid 1970s and limited only by the available X-ray sources that were simply based on the principle of fluorescent lines superimposed on the continuous spectrum of bremsstrahlung. In the 1970s it was realised that the synchrotron radiation emitted from charged particles accumulated in storage rings constructed for high energy physics was a much more powerful source of X-rays. A lot of devices especially dedicated to produce X-rays have been constructed since that time. One of the most compact parameter describing the quality of synchrotron radiation is the brilliance. It is defined as the number of X-ray photons lying in the 0.1% wide relative energy bandwidth emitted per second into solid angle (stays for the beam collimation and is given in *mrad*) and is inverse proportional to the source area (given in mm^2)

$$\text{brilliance} = \frac{\text{photons}/s}{(mrad^2)(mm^2 \text{ source area})(0.1\% \text{ bandwidth})}. \quad (1)$$

So-called third generation synchrotron radiation sources are now of a factor of approximately 10^{12} times more brilliant than X-ray tubes available in a laboratory, and there are still no signs of a saturation effect, i.e., this factor will be increased with next generation synchrotrons. Such new devices are constructed and planned, respectively, like the high-energy accelerator PETRA III, which will start operation 2007 then being the world strongest, i.e., most brilliant, SR source, or the free-electron X-ray laser XFEL, which is planned for 2011 (both are projects of DESY in Hamburg).

2.1. Mössbauer spectroscopy at the synchrotron – nuclear resonant scattering (NRS)

It took some time before physicists recognised that SR could be used for M ö s s b a u e r spectroscopy experiments, substituting radioactive sources of γ–radiation. M ö s s b a u -

e r spectroscopy is a nuclear fluorescence method, which is, basically, similar to the atomic fluorescence, however, with the recoil energy orders of magnitude higher than that involved in the emission or absorption of a photon by electronic shells. For nuclei the recoil energy is very high since the energies of the emitted quanta are very high, typically between 10 and 100 *keV* for M ö s s b a u e r isotopes in use. This causes such a shift between the energy of the emitted γ–quantum and the energy difference between the ground state and the excited level of the nucleus, that resonant absorption of the emitted γ–quantum cannot take place. It was R u d o l f M ö s s b a u e r ' s discovery that, for nuclei placed *in solids* at low temperature, there is, however, a finite probability that emission or absorption of the γ-ray photon will take place without absorption or emission of a phonon. This means that the solid will be in the same internal state before and after the event, so that, in effect, the recoil is taken up by the crystal as a whole and not by an individual atom. This makes the recoil energy immeasurably small. The result is a spectroscopy having the resolution of the lifetime uncertainty of the excited nuclear state, which is usually in the 10^{-9} *eV* range. In practice, the energy is scanned by repetitively moving a radioactive source towards and away from an absorber. Due to the corresponding Doppler shift, the energy of the γ-rays arriving at the absorber is varied causing a varying count rate at the detector behind the absorber. The effect of diffusion on the M ö s s b a u e r spectrum, namely a broadening of the detected M ö s s b a u e r line, was soon exploited in experiments (for a review see [8]). Theoretical principles of nuclear resonant scattering (NRS) of M ö s s b a u e r radiation were worked out just after the discovery of the M ö s s b a u e r effect, but until 1974 when R u b y [9] suggested that SR could be used for a resonant excitation of nuclei, it was not considered for applications. But 11 years later G e r d a u *et al.* [10] observed the resonant effect with SR for the first time. The next step was the experimental observation of the time structure of the scattered SR in the forward direction, which, primarily, opened the vast field of hyperfine structure for the investigation. Finally, S m i r n o v and K o h n [11] proposed a theory of NRS in the presence of diffusive motion of nuclei.

The NRS technique combines the properties of a small and intense synchrotron beam with the spatial and energetic resolution of conventional M ö s s b a u e r spectroscopy and can be regarded as its time-based analogue. The first experiment showing the applicability of synchrotron radiation (SR) to diffusion studies was performed at the synchrotron radiation source ESRF in Grenoble [12]. NRS allows the determination of the diffusion mechanism on an atomic scale in space and time (see Ref. [13] for a systematic discussion of theoretical and experimental aspects of NRS).

An efficient way to produce an *X*-ray beam from electrons circulating in a storage ring is to insert into that beam a device, which forces electrons to execute oscillations in the horizontal plane. This is achieved by a periodic arrangement of magnets, which produces a field that alternates between up and down along the electron path. Such an "insertion device", which produces *X*-rays with the highest brilliance, is a so-called undulator. The enormous brilliance of SR produced by an undulator specially designed for the energy required to excite the resonant level of a M ö s s b a u e r atom (which is 14.4. *keV* for the ^{57}Fe isotope) enables to extract a very narrow band in the range of few *meV* from the energy spectrum. This is achieved with so-called nested monochromators that are especially

designed for NRS and an object of intensive work of X-ray optics groups over the last decade. To collect photon counts with good time-resolution usually an avalanche photodiode (APD) is used as a detector. A schematic of the NRS beamline ID18 at the ESRF, Grenoble is shown in Fig. 1.

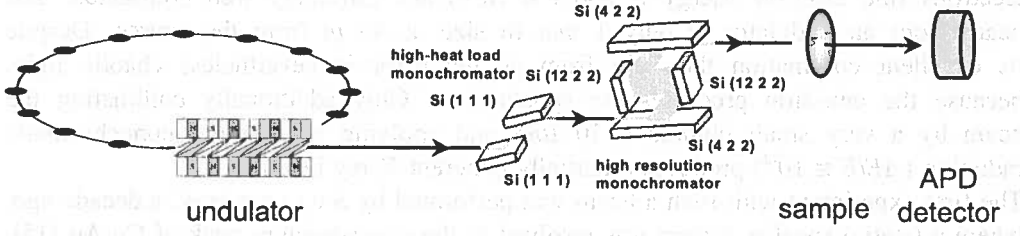

Fig. 1. Typical experimental set-up for nuclear resonant scattering (NRS) experiments. The essential components and optical elements are discussed in the text

While first studies of diffusion with SR were feasibility tests in bulky materials, the field where all unique properties of SR are exploited, is, in our opinion, the application of NRS to surface studies. These measurements are performed in grazing-incidence conditions, i.e., the technique of NRS and grazing-incidence reflexion are combined for studying the structure, hyperfine parameters and the dynamics of thin films [14]. It is known that NRS in grazing-incidence geometry provides depth selectivity, thus it can also be utilised to investigate diffusion phenomena on the surface or in near-surface regions of metallic films containing iron (or other M ö s s b a u e r isotopes). Measurements in the grazing-incidence geometry can only be performed if: (i) the beam divergence is very low, (ii) the energetic resolution is in the *meV* range. Both conditions are fulfilled by the beamline in Fig. 1.

2.2. X-ray photon correlation spectroscopy

X-ray photon correlation spectroscopy (XPCS) relies on the fact that scattering of coherent radiation from a disordered sample produces a highly modulated diffraction pattern, commonly referred to as a speckle pattern [15]. This interference pattern is in direct relation to the positions of all scattering centres in the illuminated sample volume. If their positions change, the corresponding speckle pattern will also be modified, and the speckle intensities will fluctuate in time. By analysing the temporal correlations of these intensity fluctuations, which is usually done by calculating (auto) correlation functions, XPCS yields information about the dynamics in the material. Using coherent (visible) laser light, this technique is well known as dynamic light scattering (DLS) and photon correlation spectroscopy (PCS), respectively, in the soft-condensed matter community for not less than three decades. Applied for measurements of particle sizes in colloids etc., PCS became even a standard industrial gauge. However, all applications hitherto were limited to optically transparent media and to relatively large sub-μm dimensions. Only with the advent of highly brilliant SR sources coherent *X*-rays with sufficient intensity became available and thus the method of XPCS became feasible.

By using coherent X-rays instead of visible light an almost atomic resolution can be achieved. Moreover dynamics in metallic systems can be investigated now [16].
As stated above, the brilliance of the advanced photon sources is 12 orders of magnitude higher than that of X-ray tubes and the photons emitted by highly relativistic electrons (the electron energy is about 6 *GeV*) are extremely well collimated. The beam from an undulator is only 1 *mm* in size at 40 *m* from the source. Despite its excellent collimation the light from an undulator is nevertheless chaotic light, because the emission processes are spontaneous. Only additionally collimating the beam by a very small pinhole ($\sim 10\ \mu m$) and applying moderately monochromatic radiation ($\Delta E/E \cong 10^{-4}$) produces a partially coherent X-ray beam.
The first experiment with such a beam was performed by S u t t o n *et al.* a decade ago, where a (static) speckle pattern was resolved in the superstructure peak of Cu_3Au [15]. Meanwhile the available flux of coherent *X*-rays could be increased and dynamical measurements (and not only static ones) are possible.
Our *X*-ray measurements were performed at the undulator beamline ID10A at the ESRF, Grenoble. The beamline design is similar to that of the resonance beamline ID18 shown in Fig. 1, except that instead of the high-load and high-resolution monochromators only one Si (111) reflexion is used and in place of an APD a CCD camera is used as detector. A circular pinhole aperture approximately 20 *cm* upstream of the sample was used to generate a spatially coherent *X*-ray beam. The diameter of a speckle in a distance of ~ 2 *m* of the sample is about 30 μm. Consequently, the CCD camera pixels must be of the same dimension or smaller to enable the resolution of single speckles, which was fulfilled for our measurements (pixel size of the used CCD camera: $22.5 \times 22.5\ \mu m^2$).

3. Introduction to diffusion studies with synchrotron radiation

In order to verify which diffusion mechanism operates in a specific material it is necessary to develop a mathematical model of the diffusion process. This mathematical idea is developed from the knowledge of the system or it is simply an educated guess. The mathematical model is a system of differential equations. In some cases, it can be solved analytically and yields the function describing the atomic motion. The free parameters in the model are adjusted in such a way that the best possible agreement with the experiment is achieved.
The simple-minded picture of atoms jumping on the lattice can be precisely formulated using the van Hove correlation function $G(\boldsymbol{r},t)$. If we know the function $G(\boldsymbol{r},t)$, we have the full information about the diffusing system. The van Hove correlation function (*pair correlation function*) has the following classical meaning:

$G(\boldsymbol{r},t)d^3\boldsymbol{r}$ is the probability to find a nucleus in the volume element $\boldsymbol{r}....\boldsymbol{r}+d^3\boldsymbol{r}$ for a given time *t*, if *this or another nucleus* has been at the position $\boldsymbol{r}=0$ at time $t=0$. Its self-part $G_S(\boldsymbol{r},t)\ d^3\boldsymbol{r}$ is the probability of finding a nucleus in the volume element $\boldsymbol{r}....\boldsymbol{r}+d^3\boldsymbol{r}$ for a given time *t* if *the same particle* was at the origin $\boldsymbol{r}=0$ at $t=0$, averaged over all starting positions of the nucleus.

The particular case of diffusion jumps on an empty lattice, which is the simplest model compared to other more complicated systems, was first considered by C h u d l e y and E l l i o t t [17]. One can describe this standard problem as a random walk of a particle on a translation-invariant lattice (i.e., a *Bravais* lattice), where the transition between the nearest-neighbour sites is a Poisson process. The last postulate is fulfilled if the present state of the system is determined only by the past state at a particular time (*Markov* process = uncorrelated diffusion). If we denote a jump rate of the particle from one site to any nearest neighbour site by τ^{-1} and the number of neighbouring sites (coordination number) by N, then the probability of finding this particle at position $\boldsymbol{r}$ at time $t+\Delta t$ is

$$G_S(\boldsymbol{r},t+\Delta t) = \sum_{i=1}^{N} \frac{1}{N\tau} G_S(\boldsymbol{r}+\boldsymbol{l}_i,t)\,\Delta t + G_S(\boldsymbol{r},t)\left(1-\frac{1}{\tau}\Delta t\right), \tag{2}$$

i.e., two probability terms are contained: the first term describing particles that were at the neighbouring site i in a distance l_i from $\boldsymbol{r}$ and jump into $\boldsymbol{r}$ during the time interval Δt; the second term describing particles that stay at the site $\boldsymbol{r}$. In the limit of infinitesimally small Δt the following *master equation* is found

$$\frac{\partial}{\partial t} G_S(\boldsymbol{r},t+\Delta t) = \frac{1}{N\tau} \sum_{i=1}^{N} \{G_S(\boldsymbol{r}+\boldsymbol{l}_i,t) - G_S(\boldsymbol{r},t)\} \tag{3}$$

Eq. (3) is usually solved by a F o u r i e r transform in space leading to the differential equation for the so-called intermediate scattering function $I_S(\boldsymbol{k},t)$

$$\frac{\partial}{\partial t} I_s(\boldsymbol{k},t) = -\frac{1}{N\tau} \sum_{i=1}^{N} [1 - \exp(-i\boldsymbol{k}\cdot\boldsymbol{l}_j)]\, I_s(\boldsymbol{k},t)\,. \tag{4}$$

The solution of eq. (4) with the boundary condition corresponding to $G_S(\boldsymbol{r},0)=\delta(\boldsymbol{r}) \Rightarrow I_S(\boldsymbol{k},0)=1$ is an exponential function of time

$$I_s(\boldsymbol{k},t) = I_s(\boldsymbol{k},0)\exp[-\gamma(\boldsymbol{k})t/\tau], \quad \gamma(\boldsymbol{k}) = N^{-1}\sum_{j=1}^{N}[1-\exp(-i\boldsymbol{k}\cdot\boldsymbol{l}_j)]\,. \tag{5}$$

$I_S(\boldsymbol{k},t)$ transformed into the energy domain by a F o u r i e r transform in time yields the scattering function $S(\boldsymbol{k},\omega)$ which is a Lorentzian function and can be measured experimentally by M ö s s b a u e r spectroscopy or quasielastic neutron scattering. The line width of this L o r e n t z i a n scattering function is $\Gamma(\boldsymbol{k})=(2\hbar/\tau)\,\gamma(\boldsymbol{k})$.
We can explicitly calculate the line broadening using eq. (5) for different lattices, e.g., for a cubic b.c.c. lattice with a lattice constant a, the coordinate number $N=8$ and k_x, k_y, and k_z the components of the outgoing wavevector $\boldsymbol{k}$ referred to the crystal axes. The eight possible jump vectors l_i are: $\pm(a/2, a/2, a/2), \pm(a/2, -a/2, a/2), \pm(-a/2, a/2, a/2)$ and $\pm(-a/2, -a/2, a/2)$. The function $\gamma(\boldsymbol{k})$ calculated due to eq.(5) reads

$$\gamma(\boldsymbol{k}) = 1 - \cos\left(k_x \frac{a}{2}\right) \cos\left(k_y \frac{a}{2}\right) \cos\left(k_z \frac{a}{2}\right). \tag{6}$$

One should notice that for calculating the function $I_S(\boldsymbol{kk}, t)$ or $\Gamma(\boldsymbol{k})$ only the jump rate τ^{-1} and the explicit directions of atomic jumps l_i, must be applied. However, in order to get a function from eq. (5) which can be applied for calculating NRS spectra, further transformation, discussed in Section 3.1, is required.

The problem of diffusion in non-Bravais lattices can also be solved analytically and has been treated in details by R a n d l *et al.* [18]. If the jump mechanism and jump frequencies are known, we can in any case calculate the macroscopic diffusion coefficient and compare with the tracer diffusion result. The diffusion coefficient in a non-Bravais lattice with i non-equivalent sublattices is a sum of partial diffusion coefficients

$$\mathrm{D} = \frac{1}{6} \sum_{i,j} (\boldsymbol{l}_i - \boldsymbol{l}_j)^2 \, \tau_{ij}^{-1} \, c_i \,. \tag{7}$$

where τ_{ij}^{-1} are the jump rates from a site of symmetry i to any nearest-neighbour site of symmetry j and c_i is the probability of the occupation of the ith sublattice ($\Sigma c_i = 1$).

3.1. Nuclear resonant scattering in grazing-incidence direction

The idea of nuclear resonant scattering, which is the time-based analogue of classical M ö s s b a u e r spectroscopy, will be discussed in this section for the case of X-ray scattering in grazing-incidence geometry. This approach will be in a simple way extended onto forward scattering measurements [19].

The simultaneous excitation of the nuclear energy levels of M ö s s b a u e r isotope (e.g., ^{57}Fe) by a radiation pulse (length some tens of picoseconds, monochromatic within a few *meV* around 14.4 *keV* and following each other after 176 *ns*) leads to interference effects of re-emitted X-ray photons. The interference effects manifest as a modified temporal evolution of the intensity decay after the short excitation pulse. The analysis of the time evolution of the re-emitted intensity allows the determination of hyperfine fields in the sample [1] and of the dynamics of the re-emitting nuclei. In our case we are interested in effects caused by diffusion that are usually investigated at increased temperatures (higher than the C u r i e temperature), where all materials are paramagnetic. Thus, polarisation effects will be disregarded, which seriously simplifies our notation. For the extended theory of resonant reflectivity, see [19], for the pure electronic reflectivity, see [1].

Let us consider the electronic reflectivity from a slab of finite thickness d. This is schematically shown in Fig. 2. For X-ray wavelengths the refractive index can be expressed as $n = 1 - \delta + i\beta$ where δ is a complex decrement of the index of refraction of the material from one and is of order of 10^{-5}, while the imaginary part β is usually much smaller than δ.

[1] Magnetic fields, electric-field gradients and their magnitudes and directions can be measured because of perfect polarisation of the SR beam.

one shall note that for *X*-rays the real part n of the refraction index is always smaller than unity, thus $\alpha_1 < \alpha_0$ (note that angles are measured parallel to the sample surface), see Fig. 2. Snell's law, resulting from the wave continuity at the interface, relates the incident grazing angle α to the refracted grazing angle α_1 via $\cos\alpha = n\cos\alpha_1$. An index of refraction less than unity, implies that below a certain angle α_c X-rays are totally reflected. The critical angle depends on the material, e.g., $\alpha_c \cong 3.8\ mrad$ for 14.4 *keV* photons in iron. From the continuity of perpendicular wave components one can derive Fresnel's equations for amplitude reflexion and transmission

$$r_{ij} = \frac{\mathbf{A}^R}{\mathbf{A}^0} = \frac{\alpha_i - \alpha_j}{\alpha_i + \alpha_j}, \quad t_{ij} = \frac{\mathbf{A}^T}{\mathbf{A}^0} = \frac{2\alpha}{\alpha_i + \alpha_j}, \tag{8}$$

where the amplitude reflectivity r_{ij} and transmittivity t_{ij} are shown for the interface between two media i and j. The corresponding intensity reflectivity (transmittivity) is calculated as modulus squared of the corresponding amplitude value.

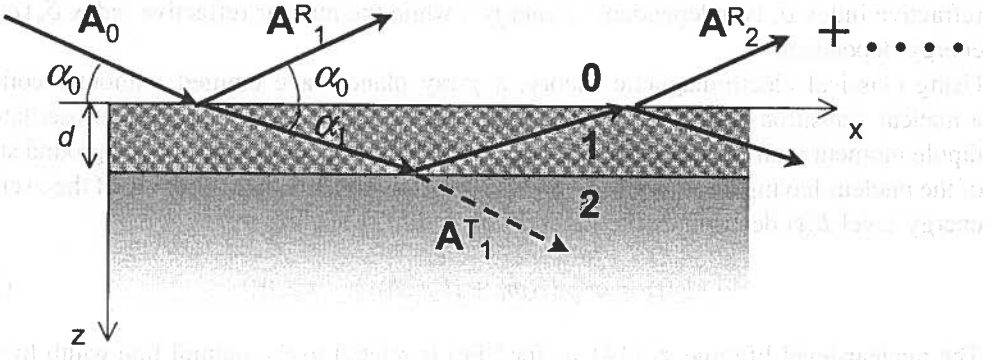

Fig. 2. A wave scattered at a thin film. The layers labelled 0, 1, and 2 denote vacuum, film, and substrate, Orespectively

Considering a slab of thickness d on a semi-infinite substrate shown in Fig. 2, one has to consider an infinite series of possible reflexions. The first two are drawn in the figure:

i. Reflexion at interface 0 to 1 (vacuum to thin film) with amplitude r_{01}.
ii. Transmission at interface 0 to 1, t_{01}, then reflexion at interface 1 to 2 (thin film to semi-infinite substrate), r_{12} and finally transmission at interface 1 to 0, t_{10}. When adding this amplitude to the first one it is necessary to include the phase-shift factor (the wave propagates in a medium with refractive index n) $\exp(iQ_1 d)$, where Q_1 is the wavevector transfer in the layer. Because the x component does not change through the layer(s) (grazing incidence condition), the value of $Q_1 = 2k_1 \sin\alpha_1 \cong 2\ k_1\alpha_1 = 2k_{1z}$. The wavevector k_1 of *X*-ray photons in medium "1" has to be calculated from the wavevector of incoming radiation k_0 in vacuum (7.3 Å^{-1} for 14.4 *keV* radiation) and from the refractive index of the medium. [2]

[2] A good approximation for the z-component of the wavevector in the jth layer is $2k_{jz} = (2k_{0z}^2 - 8k_0^2\delta_j + i8\ k_0^2\beta_j)^{1/2}$, see Ref. [1].

iii. Next steps that are not shown in Fig. 2 include infinite series of $t_{01}\, r_{12}\, r_{10}\, r_{12}\, t_{10}$ followed by $t_{01}\, r_{12}\, r_{10}\, r_{12}\, r_{10}\, r_{12}\, t_{10}$, etc..

The total amplitude reflectivity is therefore a geometrical series of reflectivities, which can be in a straightforward manner summed and simplified by the use of Fresnel's eq. (8) giving

$$r_{\text{slab}}(\alpha) = \frac{r_{01} + r_{12}\exp(i\,2k_{1z}d)}{1 + r_{01}r_{12}\exp(i\,2k_{1z}d)}. \tag{9}$$

The expression above is known as Parratt formula and is widely used in reflectivity of X-rays. It can be easily extended to the case of an arbitrary number of multilayers using recursive methods [1].

The refractive index reflects the resonant behaviour of the matter at frequencies corresponding to the electronic and nuclear transitions. The effect of the nuclear resonance is included by adding a frequency-dependent nuclear contribution to the complex index of refraction δ, yielding $\delta = \delta(\omega) = \delta_e + \delta_n(\omega)$. In the resonant range, the electronic refractive index δ_e is independent of energy[3], while the nuclear refractive index $\delta_n(\omega)$ is energy dependent.

Using classical electromagnetic theory, a γ-ray plane wave emitted without recoil in a nuclear transition (Mössbauer effect, see Section 2.1) is described as oscillating dipole moment with the frequency $\omega_0 = (E_1 - E_0)/\hbar$ between the excited and the ground state of the nucleus having the energies E_1 and E_0, respectively. The mean lifetime of the excited energy level $E(t)$ determines the natural line width Γ_0 leading to

$$E(t) \propto \exp\{i(\omega_0 + i\Gamma_0/2\hbar)t\}, \quad t \geq 0. \tag{10}$$

The nuclear-level lifetime τ_0 (141 *n*s for ^{57}Fe) is related to the natural line width by the uncertainty relation $\Gamma_0\tau_0 \approx \hbar$. The nuclear contribution to the refractive index, $\delta_n(\omega)$, can be found by decomposing the γ-ray plane wave packet from eq. (10) into spectral/frequency components by means of a Fourier expansion [20]

$$\exp\{i(\omega_0 + i\Gamma_0/2\hbar)t\} = \text{const}\int_{-\infty}^{+\infty} d\omega\, \delta_n(\omega)\exp(i\omega t), \quad t \geq 0. \tag{11}$$

Solving the problem of scattering first for an elementary component of light and then integrating the solutions for all constituents is a widely used approach in optics. Eq. (11) is solved by multiplying with $\exp(-i\omega t)$ and integrating over time from 0 to $+\infty$ ($t = 0$ is the time of formation of the excited state), yielding

[3] Exactly speaking it is a slowly varying function of energy, but it can be completely neglected in the nuclear resonant range of 4.6 *neV* for ^{57}Fe.

$$\delta_n(\omega) \propto \frac{1}{\omega - \omega_0 - iq\Gamma_0/2\hbar}. \qquad (12)$$

Thus, for an isolated resonant nuclei, the nuclear contribution $\delta_n(\omega)$ has a complex Lorentzian frequency dependence. More generally, $\delta_n(\omega)$ is a sum over all hyperfine components of a transition. We have inserted a dimensionless factor $q(\boldsymbol{k})\Gamma_0 = \Gamma_0(1 + \Delta\Gamma(\boldsymbol{k})/\Gamma_0)$ in eq. (12) which describes the broadening $\Delta\Gamma$ of the resonance line width due to diffusion ($q(\boldsymbol{k}) \geq 1$)[4]. The broadening factor is calculated from eqs. (5) and (6).

The time response to an impulse excitation is the F o u r i e r transform, i.e., the integration of the frequency/energy solution, as commented on eq. (11)

$$I_{SC}(\alpha, t) = |E_\alpha(t)|^2 \propto \left| \int_{-\infty}^{+\infty} d\omega\, r_{\text{slab}}(\alpha) \exp(i\omega t) \right|^2, \qquad (13)$$

where the scattered intensity after the SR-pulse excitation is calculated as modulus squared of the amplitude $E_\alpha(t)$.

3.2. Nuclear resonant scattering in forward direction

In this section we want to show how to simulate NRS spectra measured in forward direction (see, e.g., Ref. [20]).

For the sake of simplicity we consider transmission of a SR pulse through a thin layer containing resonant nuclei. If the thickness of the layer, d, is very small, the amplitude of the wave scattered in forward direction after excitation by a short pulse of SR can be found by summing the waves re-emitted by the individual nuclei[5]. In this case the radiation amplitude E_{TR} transmitted through the target is a superposition of the incident E_i and the forward scattered radiation

$$E_{\text{TR}}(\omega) = E_{\text{i}}\left(1 - i\frac{k}{2} f_0 nd\right), \quad f_0(\omega) = \sigma_0 \frac{q(\boldsymbol{k})\Gamma/\hbar}{\omega - \omega_0 - iq(\boldsymbol{k})\Gamma_0/2\hbar} f_{LM}\chi, \qquad (14)$$

where $f_0(\omega)$ is the amplitude of scattering in the forward direction. The energy dependence of $f_0(\omega)$ is the same as for the refractive index $\delta_n(\omega)$, see eq. (12). The other constants are: the resonance-cross section σ_0, the L a m b - M ö s s b a u e r recoilless fraction f_{LM} and the isotopic enrichment χ (these factors were not explicitly written in eq. (12)). It is a general convention in M ö s s b a u e r spectroscopy to write these constant factors together as a dimensionless effective resonance absorber thickness $L = \sigma_0 f_{\text{LM}} \chi nd$. The factor of ($-i$) is due to the phase shift of ($-\pi/2$) of the resonantly scattered wave. As in eq. (12), we have inserted the diffusional broadening factor $q(\boldsymbol{k})$ ($q \geq 1$) in eq. (14)[6].

---

[4] In this case $\boldsymbol{k}$ denotes the outgoing wavevector.

[5] This approximation is called kinematical approximation – only interaction with the primary radiation is taken into account.

[6] The forward scattered wave is in antiphase with the incident wave resulting in the strongest attenuation of the transmitted intensity.

The SR amplitude in the time-domain transmitted through a thin absorber can be obtained integrating components of $E_{TR}(\omega)$ in the same way as in eq. (13). The integral of the left part of eq. (14) yields the δ-function (fast response) and is not interesting for us. The delayed forward scattering intensity is

$$I_{FS}(\boldsymbol{k},t) = |E_{TR}(t)|^2 \propto L^2 \exp(-q\,t/\tau_0), \tag{15}$$

i.e., it consists of an exponentially decaying part representing the delayed forward scattering radiation. The decay rate is increased by the diffusional line broadening $q(\boldsymbol{k})$ of the resonance, thus the determination of the diffusion mechanism is possible applying eqs. (5) and (6).

One should note that the scattering intensity is proportional to the square of the number of resonant nuclei (i.e., the effective thickness) L^2, whereas in the conventional Mössbauer spectroscopy the effect is only a linear function of L.

Resonant scattering in grazing incidence geometry can also be simplified for very thin layers (in the kinematical approximation) [19], yielding an expression similar to eq. (15) but for the thickness which is $1/\sin\alpha \cong 1/\alpha$ outsized than in transmission through an absorber. The factor of $1/\alpha$, increasing the effective layer thickness [7], enables measurements of very thin resonant layers. It was even possible to measure dynamics in a monolayer of ^{57}Fe on the surface of tungsten [21].

In the general case of a thick absorber the intensity of the forward NRS intensity must be calculated using general dynamic theory of resonant scattering, where also multiple scattering effects are included. This problem lies, however, beyond the scope of this contribution

3.3. X-ray photon correlation spectroscopy (XPCS)

Making use of the coherence of SR for dynamic X-ray speckle measurements would liberate diffusion research from the serious limitation to rather high diffusivities and of being selective to resonant atoms only. We always place emphasis on studies of the diffusion mechanism in a wider range of metallic and/or organic systems.

When coherent light/X-rays are scattered by an assembly of N atoms, the instantaneous far field of the scattered radiation constitutes a random diffraction or "speckle" pattern consisting of bright and dark regions. The instantaneous amplitude $E(\boldsymbol{k},t)$ of the scattered radiation is

$$E(\boldsymbol{k},t) = \sum_{j=1}^{N} f_j \exp[i\boldsymbol{k}\cdot\boldsymbol{r}_j(t)], \tag{16}$$

[7] The path length of the radiation travelling under very small angles α through a film is increased by a factor of $1/\alpha$.

where f_i is the atomic scattering factor of the atom at position $\boldsymbol{r}_i$ and time t. The instantaneous scattered intensity of a speckle is $I_{sc}(\boldsymbol{k},t) \equiv E(\boldsymbol{k},t)E^*(\boldsymbol{k},t)$. Therefore the speckle pattern consists of a section of the structure in reciprocal space corresponding to the instantaneous configuration of particles in real space. As the atomic positions $\boldsymbol{r}_i$ change by diffusion jumps the phase relationships determining the speckle pattern change and the pattern evolves through a sequence of random configurations.

A detector having a sensitive area roughly equal to the size of one speckle is placed in the far field. The signal proportional to the fluctuating scattering intensity $I_{sc}(\boldsymbol{k},t)$ is fed to the computer (a photon correlator) which constructs its time correlation function $\rho(\boldsymbol{k},t)$

$$\rho(\boldsymbol{k},t) \propto \frac{\langle I_{SC}(\boldsymbol{k},0)\, I_{SC}(\boldsymbol{k},t)\rangle}{\langle I_{SC}(\boldsymbol{k})\rangle^2}, \tag{17}$$

where $\langle ... \rangle$ represents an ensemble average. Using eq. (16) we get

$$\rho(\boldsymbol{k},t) \propto \sum_{i=1}^{N}\sum_{j=1}^{N}\langle \exp\{i\boldsymbol{k}\cdot[\boldsymbol{r}_i(0) - \boldsymbol{r}_j(t)]\}\rangle^2 \quad \propto |I(\boldsymbol{k},t)|^2, \tag{18}$$

which is nothing else than the familiar intermediate scattering function $I(\boldsymbol{k},t)$ squared, see eq. (5). Thus the XPCS experiment directly measures the *intermediate scattering function*, which is a fundamental quantity in each study of the elementary diffusion mechanism. Notice, however, that $I(\boldsymbol{k},t)$ measured by the XPCS method is not a self- but a pair-scattering function. The consequence of this feature is that XPCS is not very specific in the resolution of elements with similar atomic numbers.

The analysis of the temporal correlation of intensity fluctuations at different wavevector transfers is a delicate issue. For fast dynamics with exponential decaying correlations, the classical (auto-) correlation function method is appropriate. The situation changes, however, if very slow dynamics and long-term correlations, respectively, are present. "Long-term correlations" denotes a power-law correlation behaviour, i.e., the autocorrelation function $\rho(k,t)$ is proportional to $t^{-\gamma}$ with $0 < \gamma < 1$. Especially on longer time scales it becomes very difficult to resolve the correlation behaviour unambiguously by calculating the autocorrelation function $\rho(k,t)$ directly. The latter attempt is even more delicate in the presence of statistical noise. These problems can be overcome by applying the fluctuation analysis (FA) technique, which was used as "DNA walk analysis" when spatial long-range correlations in nucleotide sequences were detected [22]. For this we calculate the so-called fluctuation function $F(t)$

$$\mathrm{F}^2(t) = \langle (Y(j+t) - Y(j))^2\rangle \quad \text{with} \quad Y(j) = \sum_{k=1}^{j} \Delta I_{SC}. \tag{19}$$

Here, $\Delta I_k = I_k - \langle I\rangle$ where I_k is the intensity in a pixel in the kth time bin and $\langle \mathrm{I}\rangle = (1/N)\,\Sigma I_k$ is the mean intensity. The angular brackets in eq. (19) represent the average over all pairs with

the same time lag t. Repeating this procedure for all t between 1 and N-1, the squared fluctuation function $F^2(t)$ is obtained. Statistics is improved by averaging the FA results over all pixels with the same $\boldsymbol{k}$ (as written in 2.2 we use a CCD camera as detector, where each pixel corresponds to one speckle, roughly). In general $F^2(t)$ can be well fitted by a power law $F^2(t) \propto t^{2\alpha}$. The so-called fluctuation exponent α is related to the correlation exponent γ via $\gamma = 2\text{-}2\alpha$ [23]. Without diffusional motion and dynamics, respectively, in the sample $\alpha = {}^1/_2$, with slow dynamics $\alpha > {}^1/_2$. Such correlation behaviour was indeed observed in an XPCS experiment, when coarsening dynamics in phase-separating alloys was investigated [16], see section 5.

4. Experiments with nuclear resonant scattering

The first example of NRS measurements of diffusion is dedicated to the "textbook" example of diffusion of iron atoms in the $B2$ ordered (b.c.c. structure where one sort of atoms occupies the cube corners whereas the other sort occupies the cube centre) intermetallic phase FeAl near stoichiometric composition [24]. The sample enriched in ^{57}Fe was measured at different temperatures and orientations vs. the SR beam. Fig. 3 shows the temperature dependence of the intensity decay rate described by eq. (15). At 800°C the thin sample approximation is insufficient for describing the measured spectrum (the curvature of the intensity decay curve is well visible) and full dynamical theory [20], must be applied. Experimental spectra at higher temperatures are simple exponential functions. By use of eq. (7) the diffusion coefficient of iron can be calculated in agreement with the tracer results (see Ref. [25]). However, one should be aware that the diffusion coefficient is not the most interesting parameter for a microscopic method like NRS [8]. From the angular dependence of the time-integrated decay rate, see Fig. 4, the microscopic model of the effective jump of Fe on its own lattice was established. With relatively small uncertainty we found that Fe jumps are performed via an antistructure Al-site with the estimated proportion between face diagonal [110] and [100] jumps $P_{110}/P_{100} = 1.9(1)$.

A preference of effective jumps to third-nearest-neighbour sites over second-nearest-neighbour sites could also be simulated via Monte Carlo method with interaction energies between atoms and vacancies [26]. In the simulations we chose ordering energies that ensured a phase diagram close to that of the real Fe-Al system. Allowing the vacancy to exchange with nearest-neighbour atoms exclusively, we obtained a perfect agreement between simulation and experiment when an interaction between the vacancy and the atoms was included. We suggest that the remarkable features of Fe diffusion arise from highly correlated vacancy paths, which are due to an interaction of the vacancy with locally disordered areas in the B2 lattice created by the vacancy movement itself.

[8] Radiotracer methods measure much slower diffusivities than NRS or other microscopic methods, therefore cover an extremely broad temperature range.

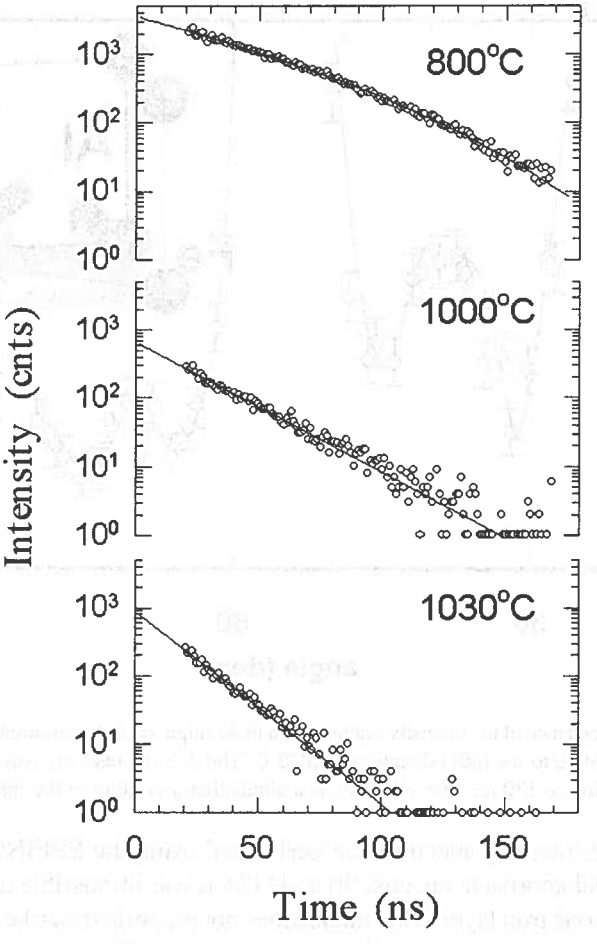

Fig. 3. Intensity decay (logarithmic scale) is accelerated at 1030°C. Measurement performed at a FeAl single crystal, synchrotron beam parallel to the [110] crystal direction

The second example refers to an experiment in grazing incidence geometry [14], see Fig. 5. We exploited the depth selectivity of NRS for investigating diffusion phenomena in near-surface regions of metallic films of iron. The sample was grown by molecular beam epitaxy under UHV conditions. The substrate was an MgO (001) polished single crystal. The iron grows with the [001] normal parallel to the [001] normal of the MgO substrate. A small lattice mismatch causes a 45° rotation of the iron unit cell relative to the MgO cell. The evaluation of the X-ray reflectivity beats, also known as K i e s s i g beats, of SR yielded an iron layer thickness of 270 *nm*.

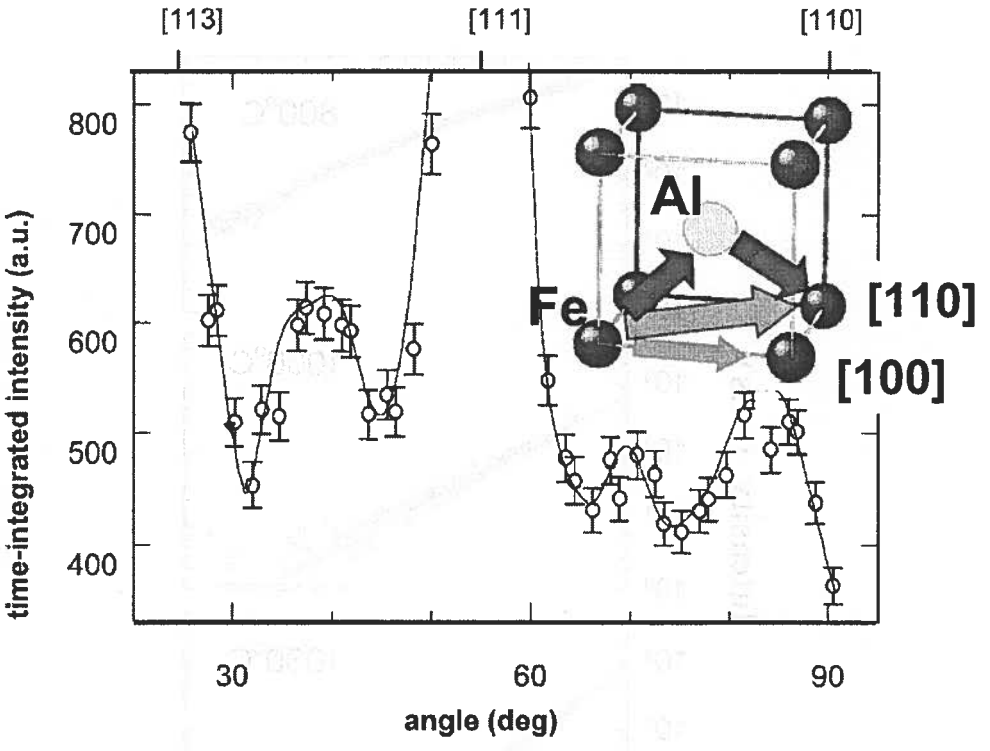

Fig. 4. Orientation dependence of the intensity scattered at a FeAl single crystal, measured with the SR beam in the (110) crystal plane relative to the [001] direction at 1030°C. The delayed intensity was intergrated for the time from the SR excitation to 170 *ns*. The solid line is a simulation according to the jump model in the inset

Fits to the delayed intensity spectra were performed using the EFFINO [27] routine with a general theoretical approach, cp. eqs. (9) and (13). It was impossible to achieve satisfying fits assuming only one iron layer. This model does not properly describe the curvature of the experimental spectrum (see dashed line in the inset of Fig. 5). In contrast, excellent agreement was achieved using a two-layer model. There, the upper layer is a 2 *nm* thick near-surface layer with measurable diffusion, the rest is bulk iron without a noticeable diffusion. The attempts to fit the thickness of the near-surface layer led at all three temperatures and for all orientations of the sample to the same value of 2 *nm*. As shown in eqs. (5) and (6) the accelerated intensity decay depends on the relative orientation of the jump vectors l_i and the wavevector $\boldsymbol{k}$. Rotating the sample around the axis normal to the sample surface varies the position of $\boldsymbol{k}$ relative to l_i. Surprisingly, the best match with the experimental decay rate was achieved with a 2D square-lattice diffusion model in the (001) iron planes. The diffusion coefficients calculated according to the described model and using eq. (7) show almost two orders of magnitude faster diffusion of iron in the near-surface layer than in the bulk iron. Additional calculations of the phonon density of states as well as using ab-initio computer simulation methods shall shed light on the origin of the experimentally observed behaviour in the near-surface layer of iron.

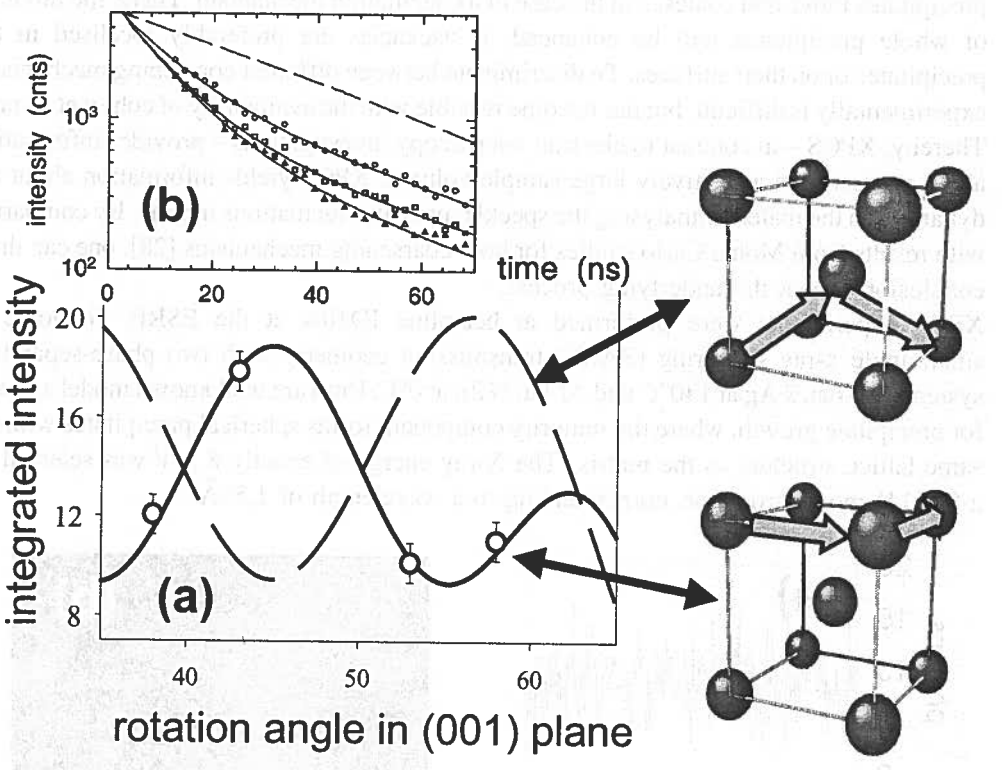

Fig. 5. (a) Angular dependence of the intensity decay (cp. eq. (15), Section 3.2) at 930°C and an angle of incidence of $\alpha = 1.66$ *mrad*. The solid line is calculated for a 2D square-lattice jump diffusion mechanism in the (001) plane of the α-iron phase. The dashed line is calculated for NN jumps on a b.c.c. lattice in bulk α-iron. The inset (b) shows the delayed intensity for various temperatures: 820°C upper curve; 930°C middle and 960°C lower. The dashed line is an *incorrect* fit using the bulk iron model only

5. XPCS experiment

Es an exemplary application of the XPCS method to diffusion studies and the study of diffusion mediated processes, respectively, the problem of precipitate coarsening in phase-separating alloys is presented. This problem, an object of a long-standing debate, is of great importance for the understanding of precipitation hardening of aluminium-based alloys like Al-4%Cu (duraluminium), Al-1%Li etc.. Recent Monte Carlo simulations showed different predominant coarsening mechanisms depending on the preferred location of vacancies. If vacancies are preferably found in the matrix, coarsening will proceed via diffusion of individual atoms from smaller precipitates to larger ones, which is the classical Lifshitz-Slyozov-Wagner (LSW) mechanism. In contrast to that, whole

precipitates move and coalesce in the case of a coagulation mechanism. There, the mobility of whole precipitates will be enhanced, if vacancies are preferably localised in the precipitates or on their surfaces. To discriminate between different coarsening mechanisms experimentally is difficult, but has become feasible with the availability of coherent X-rays. Thereby, XPCS – in contrast to electron microscopy investigations – provides information about processes in a relatively large sample volume. XPCS yields information about the dynamics in the material analysing the speckle intensity fluctuations in time. By comparing with results from Monte Carlo studies for both coarsening mechanisms [28], one can draw conclusions about the underlying process.

XPCS experiments were performed at beamline ID10A at the ESRF, Grenoble in small-angle x-ray scattering (SAXS) transmission geometry with two phase-separating systems, Al-6at.%Ag at 140°C and Al-9at.%Zn at 0°C. Both are well known model systems for precipitate growth, where the minority component forms spherical precipitates with the same lattice structure as the matrix. The X-ray energy of exactly 8 *keV* was selected by a Si(111) monochromator, corresponding to a wavelength of 1.55Å.

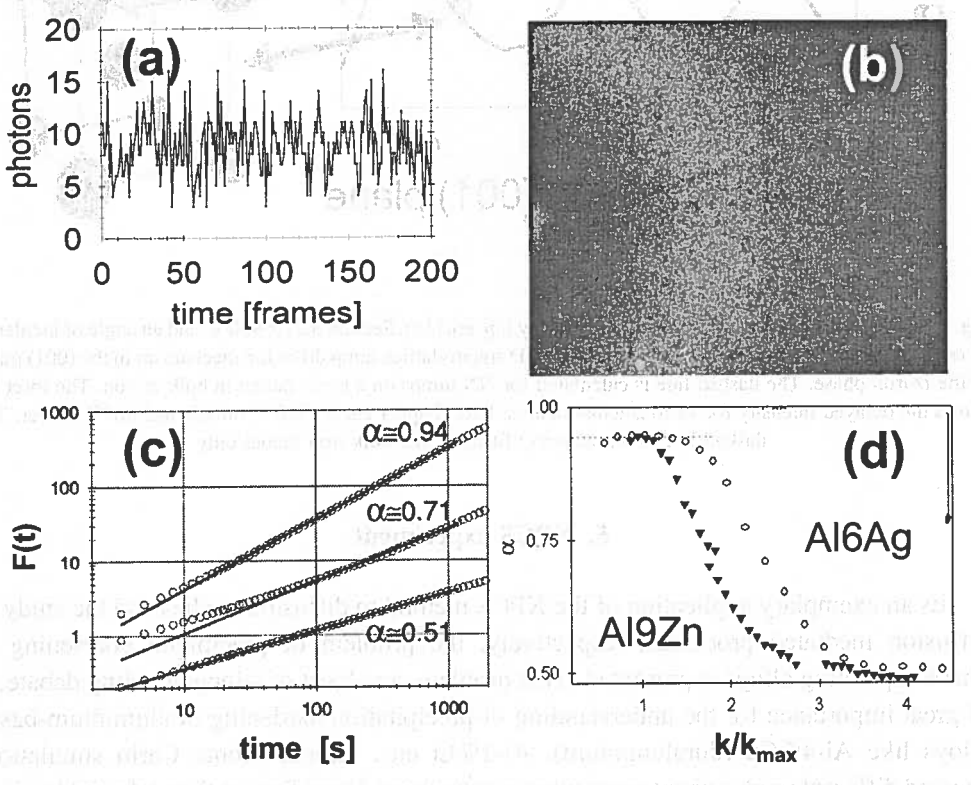

Fig. 6. Radiation scattered at a Al-6at.%Ag sample at 140°C forms a characteristic ring structure, (b). The (a) shows the fluctuating intensity in one single pixel for 200 consecutively measured frames; (c) double-logarithmic plot of typical $F(t)$ curves at different wavevectors k and fitted curves $\propto t^{\alpha}$, (d) α for Al-6at.%Ag sample at 140°C and Al-9at.%Zn at 0°C normalised to the same maximum value of α vs. the normalised scattering vector k/k_{max}

Fig. 6(b) shows a CCD picture of the SAXS diffraction pattern of the Al-6at.%Ag sample with a well visible ring structure caused by the spherical shape and isotropic arrangement of the precipitates. Fig. 6(a) demonstrates the intensity fluctuations in one pixel of the CCD camera – corresponding to a single speckle – during 200 consecutive frames, each of about 1 *sec.* exposure time. Figure 6(c) shows typical results of the fluctuation analysis of the Al-6at.%Ag data for a small, a medium, and a large value of the wavevector transfer k, normalised to k_{max} where the maximum scattering intensity was found. As can be seen a power law over several decades is observed for $F(t)$. Fig. 6(d) shows the extracted fluctuation exponent a versus k/k_{max} for both samples. Note the clearly different curve characteristics, which is in a good, qualitative agreement with the Monte Carlo results. It appears that in Al-6at.%Ag at 140°C the LSW mechanism dominates the coarsening. In case of Al-9at.%Zn at 0°C results indicate coarsening via the coagulation mechanism.

6. Summary

The progress in synchrotron methods and the access to X-rays of third generation synchrotron radiation sources enable studies of dynamics in surfaces and nanostructures. Nuclear resonant scattering of synchrotron radiation, which has gained in the last years the sensitivity required for studying ultra thin films, and X-ray photon correlation spectroscopy can explore a wide field of dynamical effects. X-ray reflection combined with nuclear resonant scattering of synchrotron radiation results in the depth-selective study of atomic motion in near-surface layers. Coherent X-rays enable correlation spectroscopy studies of coarsening mechanisms in phase-separating alloys.

A distinct advantage of the technique of nuclear resonant scattering is that it is isotope-specific. Compared to other methods, the signal is essentially free of contributions from surrounding materials. Moreover, probe layers can be selectively deposited to study the dynamic properties with atomic resolution.

In contrast, the strength of X-ray photon correlation spectroscopy is that it can measure practically all kinds of atoms. Up to now the resolution of the method is limited to objects not smaller than about *nm* in size but rapid progress in the synchrotron sources of the next generation opens perspectives for the achievement of an atomic resolution in the studies of diffusion mechanisms.

Acknowledgements

We would like to express our thanks to R. Rüffer, O. Leupold (both at ESRF), and G. Grübel (before also at ESRF, now at DESY), and to H. Thiess and M. Kaisermayr (our former PhD students) for their help with measurements. Investigations were financially supported by the Austrian Fonds zur Förderung der wissenschaftlichen Forschung (FWF), contract No. P15421, by the Austrian Federal Ministry for Education, Science and Culture (project GZ 45.529/2-VI/B/7a/2002), and by the Hahn-Meitner-Institut Berlin in cooperation with the University of Potsdam. XPCS data were evaluated using the Schrödinger II cluster of the Vienna University Computer Centre.

REFERENCES

[1] J. Als-Nielsen, D. McMorrow, Elements of Modern X-ray Physics, John Willey & Sons (2001).

[2] M. Kaisermayr, J. Combet, C. Pappas, R. Rüffer, G. Vogl, J. Synchrotron Rad. **9**, 210-214 (2002).

[3] M. Kaisermayr, C. Pappas, B. Sepiol, G. Vogl, Phys. Rev. Lett. **87**, 175901 (2001).

[4] G. Grübel, G. Vogl, Synchr. Rad. News **15**, 14-17 (2002).

[5] G. Vogl, B. Sepiol, M. Sladecek, L-M. Stadler, M. Kaisermayr, Hyperfine Interactions **144/145**, 93-101 (2002).

[6] G. Vogl, R. Feldwisch, in Diffusion in Condensed Matter, Eds J. Kärger, P. Heitjas and R. Haberlandt, Vieweg Verlag p. 40 (1998).

[7] R. Hempelmann, Quasielastic Neutron Scattering and Solid State Diffusion, Oxford University Press (2000).

[8] G. Vogl, Hyperfine Interact. **53**, 197 (1990); G. Vogl in Mössbauer Spectroscopy Appl. to Magn. and Mat. Sci **2**, eds. G.J. Long and F. Grandjean, Plenum Press (1996).

[9] S.L. Ruby, J. Phys **35**, C6-209 (1974).

[10] E. Gerdau, R. Rüffer, H. Winkler, W. Tolksdorf, C.P. Klages, J.P. Hannon, Phys. Rev. Lett. **54**, 835 (1985).

[11] G.V. Smirnov, V.G. Kohn, Phys. Rev. B **52**, 3356 (1995).

[12] B. Sepiol, A. Meyer, G. Vogl, R. Rüffer, A.I. Chumakov, A.Q.R. Baron, Phys. Rev. Lett. **76**, 3220-3223 (1996).

[13] G. Vogl, B. Sepiol in Nuclear Resonant Scattering of Synchrotron Radiation, Eds G. Langouche and H. de Waard, Hyperfine Interactions **123/124**, (1999) 595.

[14] M. Sladecek, B. Sepiol, M. Kaisermayr, J. Korecki, B. Handke, H. Thiess, O. Leupold, R. Rüffer, G. Vogl, Surface Science **507-510C**, 124 (2002).

[15] M. Sutton, E.E. Nagler, S.G. Mochrie, T. Greytak, L.E. Bermann, G. Held, G.B. Stephenson, Nature **352**, 608 (1991).

[16] L.-M. Stadler, B. Sepiol, R. Weinkamer, M. Hartmann, P. Fratzl, J.W. Kantelhardt, F. Zontone, G. Grübel, G. Vogl, Phys. Rev. B **68**, 180101(R) (2003).

[17] C.T. Chudley, R.J. Elliott, Proc. Phys. Soc. **77**, 353 (1961).

[18] O.G. Randl, B. Sepiol, G. Vogl, R. Feldwisch, K. Schroeder, Phys. Rev. B **49**, 8768 (1994).

[19] R. Röhlsberger, J. Bansmann, V. Senz, K.L. Jonas, A. Bettac, K.H. Meiwes-Broer, Phys. Rev. B **67**, 245412 (2003).

[20] G.V. Smirnov, V.G. Kohn in Nuclear Resonant Scattering of Synchrotron Radiation, Eds G. Langouche and H. de Waard, Hyperfine Interactions **123/124**, 31 (1999).

[21] M. Sladecek, B. Sepiol, J. Korecki, O. Leupold, R. Rüffer, G. Vogl, Surface Science (2004) in press.

[22] C.-K. Peng, S.V. Buldyrev, A.L. Goldberger, S. Havlin, F. Sciortino, M. Simons, H.E. Stanley, Nature (London) **356**, 168 (1992).

[23] J.W. Kantelhardt, E. Koscielny-Bunde, H.H.A. Rego, S. Havlin, A. Bunde, Physica A **295**, 441 (2001).

[24] G. Vogl, B. Sepiol, C. Czichak, R. Rüffer, R. Weinkamer, P. Fratzl, M. Fähnle, M. Meyer, Mat. Res. Soc. Symp. Proc. **527**, 197 (1998).

[25] M. Eggersmann, H. Mehrer, Phil. Mag. A **80**, 1219 (2000).

[26] R. Weinkamer, P. Fratzl, B. Sepiol, G. Vogl, Phys. Rev. B **59**, 8622 (1999).

[27] H. Spiering, L. Deak, L. Bottyán, Hyperfine Interact. **125**, 197 (2000).

[28] R. Weinkamer, P. Fratzl, Europhys. Lett. **61**, 261 (2003).

Received: 1 March 2004.

ARCHIVES OF METALLURGY AND MATERIALS
Volume 49 2004 Issue 2

R.A. De SOUZA *, M. MARTIN*

SECONDARY ION MASS SPECTROMETRY: A POWERFUL TOOL FOR DIFFUSION STUDIES IN SOLIDS

SIMS – DOSKONAŁE NARZĘDZIE DO BADAŃ DYFUZJI W CIELE STAŁYM

We disuss the use of secondary ion mass spectrometry (SIMS) as a powerful tool for diffusion studies in solids. The basic principles of SIMS are introduced and examples for oxygen diffusion and cation diffusion in oxides are given. It is shown that SIMS is capable of analysing diffusion profiles on a broad length scale, from some tens of nanometres to several hundred micrometres, which makes it possible to measure diffusion coefficients from ab out 10^{-22} m^2s^{-1} to 10^{-10} m^2s^{-1}.

W pracy przedstawiono zalety spektrometrii mas jonów wtórnych (SIMS) jako narzędzia badania dyfuzji w ciałach stałych. Omówiono zasady metody SIMS oraz przykłady dyfuzji tlenu i kationów w tlenkach. Wykazano, że metodą tą można analizować profile dyfuzji w szerokim zakresie odległości, od dziesiątek nanometrów do setek mikrometrów, co sprowadza się do możliwości pomiaru współczynnika dyfuzji w zakresie od $10^{-18}cm^2s^{-1}$ do 10^{-6} cm^2s^{-1}.

1. Introduction

In the analysis of diffusion processes in solids, tracer diffusion is an important method [1,2,3,4,5]. Tracers of component A, denoted A^*, are by definition chemically identical to A and have a very low concentration. Since one can distinguish between A^* and A, the motion of the indistinguishable A particles can be followed with the help of the tracers, A^*. The analysis of tracer concentration profiles in a chemically homogeneous solid yields the tracer diffusion coefficient, D_A^* (or the mean square displacement of tracers). As ideal tracers we can use either radioactive isotopes or stable isotopes of an element. Radiotracers are analyzed by means of their emitted radiation (mostly γ-radiation, sometimes β-emitters). The detection of stable isotopes is most widely accomplished by ion beam analysis techniques, because they combine the ability to distinguish between isotopes with

* INSTITUTE OF PHYSICAL CHEMISTRY, RWTH AACHEN UNIVERSITY. TEMPLERGABEN 59, D–52056 AACHEN, GERMANY

good spatial resolution. Of these techniques Secondary Ion Mass Spectrometry (SIMS) is the most widely applicable [6] and has been used for some years to study diffusion in metals and ceramics (see, *e.g.*, [7,8,9,10,11]). The aim of this article is to explain the basic principle of SIMS (section 2) and to demonstrate the capability of this modern analytical technique as a tool for diffusion studies in solids. Two examples of diffusion in oxides will be discussed: section 3 deals with oxygen diffusion, and in section 4 cation diffusion is discussed. Together, the examples demonstrate that SIMS is capable of analysing diffusion profiles over a broad length scale, from some tens of nanometres to several hundred micrometres, and can, as a consequence, determine diffusion coefficients in the range of 10^{-22} $m^2 s^{-1}$ to 10^{-10} $m^2 s^{-1}$ with high precision.

2. SIMS

The principle of SIMS is illustrated in Fig. 1. The solid sample to be analysed is bombarded with ions of keV energy. These ions undergo elastic collisions with the atoms of the target, which in turn collide with other target atoms. In this way a cascade of collisions is initiated between the target atoms. Collision cascades that reach the surface with sufficient energy and momentum result in the ejection of target material in the forms of atoms, molecules and larger clusters, a process known as sputtering. Most of these species are neutral, but a small fraction is charged: these are the secondary ions. Some of these ions can be collected by means of a suitable electrical potential. They are then separated according to their mass to charge ratio and counted.

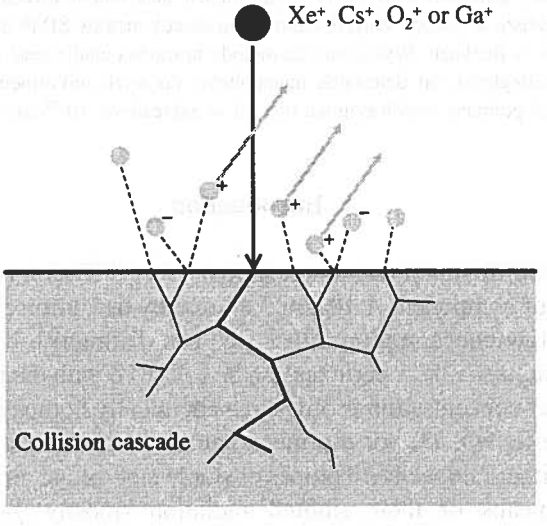

Fig. 1. The SIMS principle

SIMS offers an excellent combination of properties for the analysis of vacuum compatible solids. It is capable of detecting all elements from H to U; differentiating

between isotopes; determining concentrations from the matrix level down to the ppm level, and in favourable cases, down to the ppb level; and of providing such information as a function of spatial co-ordinate. The depth resolution is typically of the order of nanometres, whereas the lateral resolution is in the micrometer range.

Sputter bombardment of a solid does have its drawbacks. The most trivial of these is that it is obviously impossible to analyse the same place twice. Far more relevant for the SIMS analyst is the fact that ion bombardment changes the sample. The chemical composition of the bombarded region will be altered; at the very least this region will be enriched with the primary ion (although this is sometimes put to good use – see below). In multicomponent targets, preferential sputtering of one component may take place. An initially flat surface may, in certain cases, develop severe topographical features [12].

It is quantification, however, that is the main weakness of the SIMS technique. The measured secondary ion intensity i_X^s is related to the atomic fraction of element X, c_X, via

$$i_X^s = I^p \, Y \, \alpha_X \, \eta_X \, \theta_X \, c_X \qquad (1)$$

where I^p is the primary ion intensity [ions / s]; Y, the sputter yield [ejected target atoms / incident primary ion]; α_X, the ionisation probability (α_X^+ for positive secondary ions, α_X^- for negative secondary ions); η_X, the combined efficiency of the extraction optics, the transmission of the mass spectrometer and the detector; and θ_X, the isotope abundance. I^p and Y can be easily measured, and values of θ_X are, of course, known. This leaves α_X and η_X, of which the former is the more important: it varies by several orders of magnitude, and depends on both the secondary ion and the matrix under consideration. With regard to ionisation probabilities, it is worth noting that they can be enhanced by bombarding with an appropriate primary ion. The use of electropositive Cs^+, for example, increases α_X^-, whereas O_2^+ primaries are often employed in positive ion SIMS (improved α_X^+).

Fortunately, quantification does not, in general, present a problem in diffusion studies. If one employs a stable tracer (*e.g.* ^{18}O for oxygen diffusion), then use of the isotope fraction in analysis means that the unknown terms in Eq. (1) cancel, as the tracer is chemically identical to the host. In other cases, for instance, impurity diffusion, it is the diffusion distance that is the key parameter, rather than the absolute amount of the diffusant. If quantification is necessary, then it is best achieved by analysing, under the same SIMS conditions, an ion-implanted standard. Each diffusion problem requires, therefore, a separate standard for each ion in each matrix.

One last point that needs to be mentioned with regard to SIMS data is the possibility of mass interferences, that is, the appearance of two different secondary ions at the same nominal mass, *e.g.*, at mass 56, $^{28}Si_2$ (55.954 amu) and ^{56}Fe (55.935 amu).

2.1. Operational modes

a. Static SIMS

This operational mode refers to the use of primary ion beam currents low enough, that secondary ions are emitted from regions of the surface that have not yet been bombarded. It thus makes true *surface* analysis possible. As the mass spectrum contains clusters ions, in addition to the atomic and molecular ions, this technique provides information, not only on the elemental composition, but also on the chemical structure of surfaces.

b. Depth profiling

Bombarding the surface with a high current beam of primary ions results in the surface being rapidly eroded away (dynamic SIMS). By recording the intensities of various secondary ions as a function of time, one can monitor changes in the chemical composition and in this way obtain a depth profile. Converting sputter time to depth is usually performed post-analysis by surface profilometry or interference microscopy.

The ultimate depth resolution is determined by a process known as ion-beam mixing. This process concerns the redistribution of target atoms, as a result of the collision cascades, prior to their emission as secondary ions. Hence, the depth resolution is of the order of the penetration depth of the primary ions (in the nm range), even though secondary ions are emitted from the topmost atomic layers of a solid.

Since primary beams usually exhibits Gaussian-type intensity profiles, the use of stationary beams would lead to a secondary ions being collected from a variety of depths. One way of avoiding this crater-wall effect is to raster scan the beam, typically over an area of 300 μm × 300 μm, but to record secondary ion intensities only from the central area of the crater (*e.g.* 150 μm × 150 μm). This is known as gating.

c. SIMS imaging

By scanning the primary beam, just as in a scanning electron microscope, and collecting secondary ions at each point, chemical images can be generated. At present, the best SIMS machines deliver a lateral resolution in the sub μm range, and this is determined by how well the primary ion beam can be focussed.

2.2. Types of SIMS machine

There are three types of SIMS machines: magnetic sector, quadrupole and time-of flight (ToF). Essentially, the machines differ according to the methods they use to produce and

analyse secondary ions. They all have, however, the same basic components (see Fig. 2): an ion gun to produce primary ions, an ultra-high vacuum sample chamber, an extraction electrode to collect as many secondary ions of given polarity as possible, a mass spectrometer, and finally a detector. Most machines also have an electron-flood gun, in order to compensate the charge that builds up during ion bombardment of insulators.

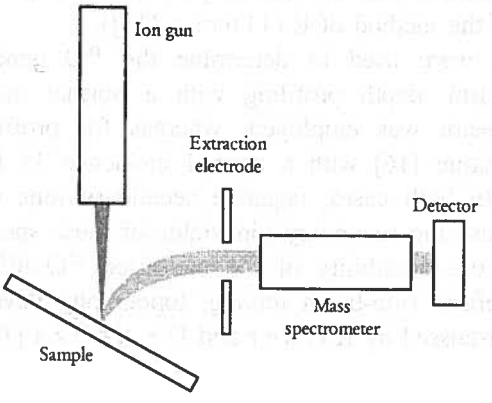

Fig. 2. Schematic diagram of the main components of a SIMS machine. Adapted from Ref. [6]

3. Oxygen diffusion

Perovskite oxides with the general formula $La_{1-x}Sr_xMn_{1-y}Co_yO_{3\pm\delta}$ have attracted much attention as mixed ionic and electronic conducting ceramics, with possible application as permeation membranes and as the cathode material in a Solid Oxide Fuel Cell (SOFC). The determination of the ionic conductivity of these materials is far from simple on account of the electronic conductivity being many orders of magnitude greater than the ionic component. If one determines the tracer diffusion coefficient of oxygen, however, one can subsequently calculate the ionic conductivity via the Nernst – Einstein equation.

3.1. Experimental

In the case of tracer introduction from the gas phase, one should use ceramic samples of greater than 95% theoretical density (open pores are eliminated, and thus gas tightness ensured, when the porosity is less than 5% [13]), or better, single crystals, if available.

The fabrication of high quality ceramic samples and their preparation (polishing, etc) for the diffusion experiments are detailed in Ref. [14]. An $^{18}O/^{16}O$ exchange experiment consisted of annealing, first of all, a sample in research grade oxygen (99.996%) of normal isotopic abundance for a period of time approximately one order of magnitude greater then the tracer anneal time. This was carried out to ensure that the material was in chemical equilibrium at the desired temperature and oxygen partial pressure. The sample was then

quenched to room temperature, the research grade oxygen removed, and labelled oxygen (97% enriched $^{18}O_2$) introduced. As before, the sample was rapidly heated to the anneal temperature, annealed for the required time t, and quenched. During both anneals the temperature was monitored by a thermocouple situated close to the sample. The duration of the isotope anneal was calculated from the temperature–time profile by means of a computer program, which takes into account the periods required to heat up and cool down the specimen (based on the method of K i l l o r a n [15]).

Two SIMS modes were used to determine the ^{18}O penetration profiles. For profiles less than 10 μm, depth profiling with a normal incidence 10 keV Xe^+ or Cs^+ primary ion beam was employed, whereas for profiles greater than 100 μm, the linescan technique [16] with a normal incidence 15 keV Cs^+ primary ion beam was employed. In both cases, negative secondary ions were monitored ($^{16}O^-$ and $^{18}O^-$), mainly because the secondary ion yields of these species are high. Special attention was paid to the possibility of the measured ^{18}O diffusion profiles being distorted by SIMS artefacts (ion-beam mixing, topography development, insufficient lateral resolution), as discussed by K i l n e r and D e S o u z a [17].

3.2. Mathematical description

During the isotope anneal, the rate of isotope exchange across the gas/solid interface is assumed to be directly proportional to the difference in isotope concentration between the gas and the solid. This leads to the boundary condition

$$-D^* \left.\frac{\partial c}{\partial x}\right|_{x=0} = k^*(c_g - c_s), \tag{2}$$

where D^* is the oxygen tracer diffusion coefficient, k^* is the surface tracer exchange coefficient, and c_g and c_s refer to the ^{18}O isotope fraction in the gas phase and at the sample surface respectively. The solution for a semi-infinite medium with the above boundary condition, assuming a constant isotope concentration in the gas phase, is given by C r a n k [18] as

$$c'(x,t) = \frac{c(x,t) - c_{bg}}{c_g - c_{bg}} = erfc\left[\frac{x}{2\sqrt{D^* t}}\right] - \left[\exp\left(\frac{k^* x}{D^*} + \frac{k^{*2} t}{D^*}\right) \times erfc\left(\frac{x}{2\sqrt{D^* t}} + k^* \sqrt{\frac{t}{D^*}}\right)\right], \tag{3}$$

where $c'(x,t)$ is the ^{18}O isotope fraction corrected for the natural isotopic background level of ^{18}O (c_{bg} = 0.002) and for the isotope enrichment of the gas (c_g). t is the corrected time of the isotope anneal. The parameters D^* and k^* were obtained by a non-linear least squares fit (employing the simplex search algorithm in MATLAB [19]) of the experimental data to Equation (3).

3.3. Results

Data of extremely high quality can be obtained from ^{18}O tracer diffusion experiments. This is illustrated in Fig. 3 (a) and (b), typical ^{18}O diffusion profiles determined by SIMS depth profiling and SIMS linescanning, respectively. In both cases it is clear that the experimental data fit very well to Eq. (3). The experimental precision for this set of measurements was estimated by performing a number of runs (more than four) on a variety of samples. It was found that the experimental precision was ~ 10% for both D^* and k^* obtained from either depth profiles or linescans [20,21].

In some depth profiles, "tails" were observed at large depths. This is usually taken as evidence of an operative short circuit diffusion path, *e.g.*, grain boundaries or dislocations. It should be noted, however, that such tails were only observed, though not exclusively, in cases where the bulk diffusivity was low (less than ~ 10^{-14} m^2/s). A detailed analysis of grain boundary diffusion of oxygen in $La_{0.8}Sr_{0.2}MnO_{3+\delta}$ is given in Ref. [22]).

Oxygen tracer diffusion coefficients obtained for the $La_{0.8}Sr_{0.2}Mn_{1-y}Co_yO_{3\pm\delta}$ series are plotted in Fig. 4. Examination of the isothermal values indicates that D^* generally increases with increasing Co site fraction. From y = 0 to y = 1, *i.e.*, for the end members, the increase is almost five orders of magnitude.

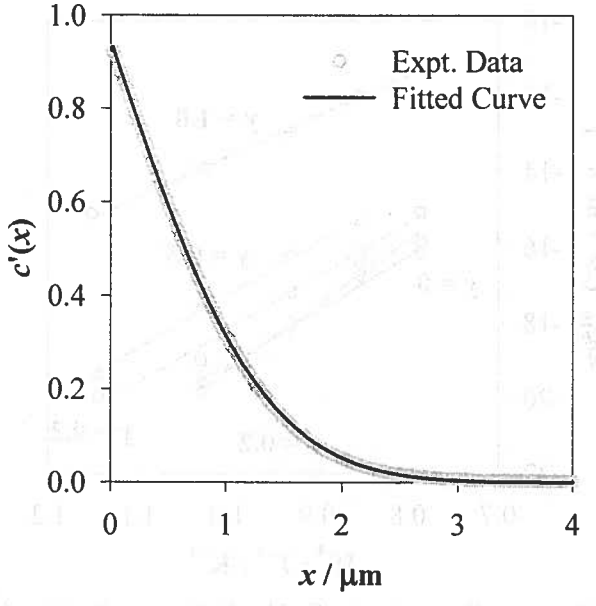

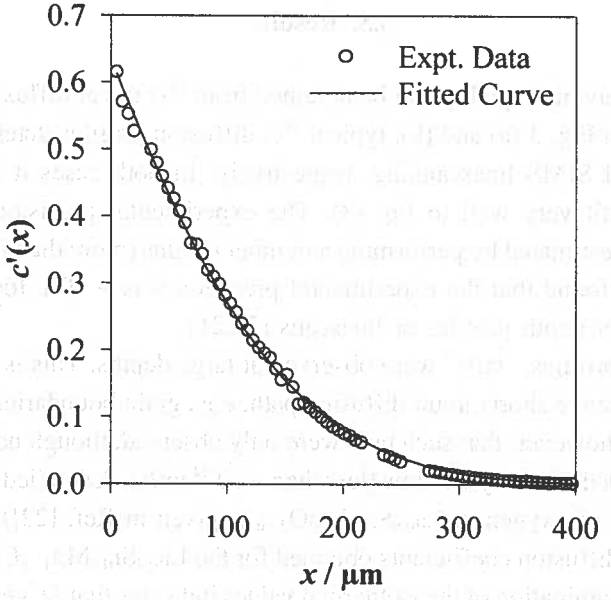

Fig. 3. Typical ^{18}O diffusion profiles, showing the corrected isotope fraction, $c'(x)$, against depth, together with the fitted curves. **(a)** determined by SIMS depth profiling of a $La_{0.8}Sr_{0.2}Mn_{0.8}Co_{0.2}O_{3\pm\delta}$ sample (^{18O} anneal at 1000°C for 3840 s). **(b)** determined by SIMS linescanning of a $La_{0.8}Sr_{0.2}CoO_{3-\delta}$ sample (^{18}O anneal at 1000°C for 1675 s)

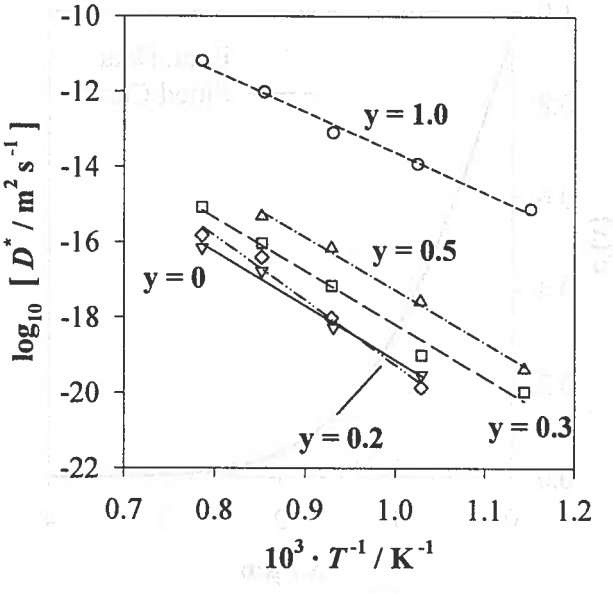

Fig. 4.Oxygen tracer diffusion coefficients for $La_{0.8}Sr_{0.2}Mn_{1-y}Co_yO_{3\pm\delta}$ as a function of inverse temperature at a nominal pressure of 1 atm O_2. Lines are least squares fits to r r h e n i u s behaviour

The bulk oxygen tracer diffusivity of ABO_3 perovskite oxides can be expressed as the product of the oxygen vacancy diffusivity, D_V; the site fraction of oxygen vacancies, n_V; and

the tracer correlation factor, f^*, which is assumed to be independent of n_V and equal to 0.69 [23]. It was demonstrated previously [24,25] that isothermal values of D_v are almost independent of the type of B cation for B = Mn, Co, Cr, Fe. This consequently implies that the isothermal changes observed for D^* as a function of Co site fraction are predominantly due to increases in the oxygen vacancy concentration [20]. Lastly we note that the ionic conductivities at 900 °C calculated from these data via the Nernst–Einstein equation are, for example, 8×10^{-8} S cm^{-1} for $La_{0.8}Sr_{0.2}MnO_{3+\delta}$ and 4×10^{-3} S cm^{-1} for $La_{0.8}Sr_{0.2}CoO_{3-\delta}$.

4. Cation diffusion in LSGM

The perovskite oxide lanthanum gallate, $LaGaO_3$, doped with strontium on the A site and magnesium on the B site, $La_{1-x}Sr_xGa_{1-y}Mg_yO_{3-(x+y)/2}$ (LSGM), exhibits higher oxygen-ion conductivities [26,27] than yttria-doped zirconia (YSZ). LSGM thus represents a promising alternative to YSZ as the electrolyte material in an SOFC [28]. Cells using LSGM as the electrolyte are expected to operate at intermediate temperatures around 700°C for more than 30000 hours, and very thin electrolyte layers (down to some microns) are desired to reduce the cell resistance.

Although cation diffusion in perovskites is known to be very slow (as shown, *e.g.*, for $(La_{1-x}Ca_x)CrO_3$ [29]), there are several important processes that are determined by the slowest moving species such as sintering or creep [30,31]. If the cations exhibit different diffusivities kinetic demixing of the electrolyte [32,33] can be an additional origin of long term degradation. It is therefore important to obtain data for the cation diffusion coefficients in LSGM. First diffusion experiments were performed with radiotracers at a temperature of 1400°C [34]. However, due to the small bulk diffusion coefficients and the low depth resolution (some μm) of the radiotracer section method, it was only possible to determine the upper limits of the bulk diffusion coefficients. Using SIMS, with its superior depth resolution (some nm), cation impurity diffusion of Y, Fe and Cr in LSGM was investigated [35,36,37].

In this chapter we summarize some recent results for tracer self-diffusion of lanthanum, strontium and magnesium in $La_{0.9}Sr_{0.1}Ga_{0.9}Mg_{0.1}O_{2.9}$ (LSGM1010) [38]. The diffusion experiments were performed with stable, strongly enriched isotopes of La, Sr and Mg, and the diffusion profiles were measured with SIMS.

4.1. Experimental

A modified Pechini method [34,39], that ensures homogeneous mixing of all cations, was chosen to prepare the samples. The resulting powders were uniaxially pressed yielding dense, mechanically stable samples to meet the requirements of diffusion experiments. All samples were annealed in air at 1400°C for 160 hours for two reasons: first, to achieve a grain size distribution that was suitable to the carrying out of well defined diffusion experiments in the so-called *B*-regime, following the Harrison classification

[40], that is, simultaneous bulk and grain boundary diffusion in polycrystalline materials; and second, to establish at 1400°C the equilibrium defect structure in the material. This is of particular importance for the cation vacancies, which are the minority defects in LSGM, but are fundamental for cation diffusion. Finally all samples were polished using 80 nm grade polishing media to achieve smooth sample surfaces, which are required for the diffusion experiments and the subsequent SIMS analysis.

To measure the cation tracer diffusion coefficients of lanthanum, strontium and magnesium the stable, enriched isotopes ^{138}La (7.8%), ^{84}Sr (77%) and ^{25}Mg (94.5%) (Isotec) were applied simultaneously as aqueous nitrate solutions onto the polished LSGM surfaces. Subsequently the solvent was evaporated. Assuming a homogenous distribution of the remaining precipitate the estimated thickness, h, of the resulting layer is in the range of 30 nm. The samples were annealed at six temperatures between 900 and 1400°C (steps of 100°C) for defined diffusion times, t_{diff}. These were estimated in such a way, that the typical penetration depth of a tracer concentration profile, $\Delta x_{diff} = (2 \cdot D(T) \cdot _{diff}$, is small compared to the thickness of the surface layer which was equilibrated during the high temperature treatment at 1400°C for 160h. It was the aim of this procedure to freeze in the concentrations of the minority defects (established at 1400°C) at lower temperatures and to separate in this way defect formation and migration energies. After the diffusion anneal the samples were coated with a gold layer (thickness about 30 nm) to prevent charging during the subsequent SIMS analysis. Measurements were made on a Cameca ims5f. An O_2^+ primary beam of *ca.* 100 nA was used for sputtering material off from an area of $200 \times 200\ \mu m^2$; by means of optical gating only secondary ions from the central 40% of the total sputtered area were recorded. An electron beam was employed for charge compensation. All measured profiles were corrected by one matrix element (La or Ga) to suppress minor instabilities of the primary ion beam. In addition, the natural background contents of ^{138}La, ^{84}Sr and ^{25}Mg in the matrix were measured at large sputter depths and subtracted from the corresponding profiles.

The experimental SIMS depth resolution is mainly determined by ion beam mixing during sputtering and the surface roughness of the sample. To estimate these effects experiments with well defined tracer layers consisting of the impurity metals Y, Fe and Cr were performed. In comparison with enriched isotopes, impurities have the advantage of a very low background signal. The layers were prepared using molecular beam epitaxy (MBE) [37]. Fig. 5 shows a typical SIMS profile of an as prepared MBE layer on an LSGM1010 sample, *i.e.*, before the annealing process. The thickness of the MBE layer according to the SIMS profile in Fig. 5 is 27 nm. It agrees well with the thickness of 30 nm, measured by a quarz crystal oscillator in the MBE chamber. The SIMS sputter rate of the metal layer was determined independently in a MBE-layer of a thickness of about 600 nm. As can be seen from Fig. 5, ion beam mixing and surface roughness result in an interfacial region between the layer and the sample with a finite width, σ, of about 20 nm. This has to be considered during profile processing (see Eq. (4)). Fig. 6 shows SIMS profiles of the impurity Fe in LSGM1010 as a function of diffusion time. Each profile consists of a bulk part at small penetration depths and a grain boundary part at larger penetration depths. In this article only bulk diffusion will be discussed. The thickness, h, of the tracer source is of the same order as the typical penetration depths of the profiles. Thus, the solution of the diffusion equation for a source of finite thickness must be used [18]. The SIMS intensity, I, corresponding to bulk diffusion is then given by

$$I(x,t) = \alpha \cdot \left(\mathrm{erf}\left(\frac{x+h}{\sqrt{4D^*t + 4\sigma^2}} \right) - \mathrm{erf}\left(\frac{x}{\sqrt{4D^*t + 4\sigma^2}} \right) \right) \quad (4)$$

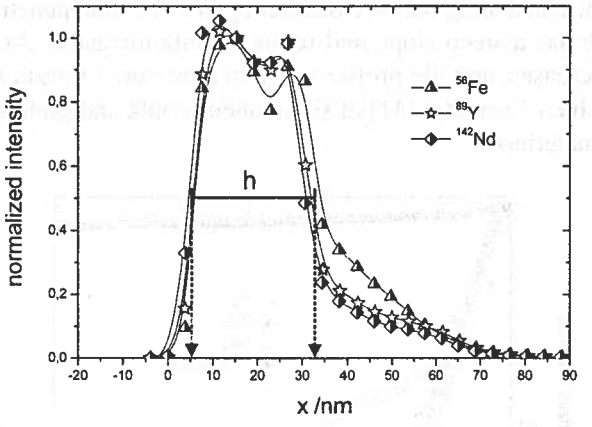

Fig. 5. SIMS profile of an as prepared MBE layer on a LSGM1010 sample, i.e. before the annealing process. The thickness of the MBE layer is 27 nm (x > 32 nm: LSGM sample)

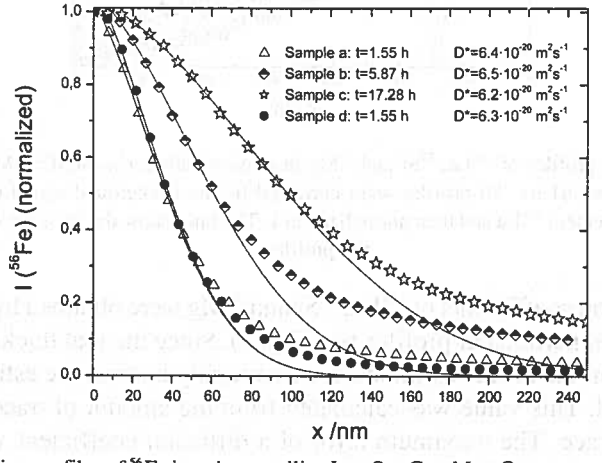

Fig. 6. Typical diffusion profiles of ^{56}Fe in polycrystalline $La_{0.9}Sr_{0.1}Ga_{0.9}Mg_{0.1}O_{2.9}$ measured by SIMS as function of diffusion time (T = 1400°C). The lines show the fit of Eq. (4) to the bulk part of the profiles

where x is the penetration depth and t the diffusion time. α is a constant containing the parameters of Eq. (1), D^* the tracer diffusion coefficient of the corresponding cation, and σ the width of the initial profile (t = 0) determined by SIMS analysis. Eq. (4) was then fitted to the bulk part of the profiles in Fig. 6 using σ= 20 nm and h = 27 nm. For all three diffusion times the same bulk diffusion coefficients were obtained, which indicates that the profiles *a*, *b* and *c* correspond to bulk diffusion. To exclude the influence of mechanical damage during polishing one sample (profile *d*) was annealed again after final polishing and before applying the tracers. The bulk diffusion coefficients of samples a and d are identical, showing that the influence of mechanical damage due to polishing is negligible.

4.2. Results and discussion

Typical penetration profiles for ^{138}La, ^{84}Sr and ^{25}Mg obtained by SIMS are shown in Fig. 7. In each profile one can distinguish two different parts. At small penetration depths (up to 100 nm) the profile has a steep slope and refers to bulk diffusion. At larger penetration depths the slope decreases, and the profile refers to a mixture of grain boundary and bulk diffusion after F i s h e r ' s model [41] of simultaneous bulk and grain boundary diffusion in polycrystalline materials.

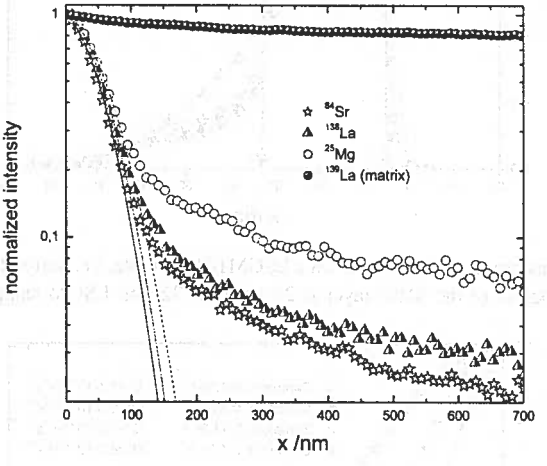

Fig. 7. Typical diffusion profiles of ^{138}La, ^{84}Sr and ^{25}Mg in polycrystalline $La_{0.9}Sr_{0.1}Ga_{0.9}Mg_{0.1}O_{2.9}$ measured by SIMS (T = 1400°C, t_{diff} = 1.61 h). All profiles were corrected by the background signal of the corresponding isotope and the matrix-element ^{139}La and then normalized to 1. The lines show the fit of Eq. (4) to the bulk part of the profiles

The bulk diffusion coefficients of ^{138}La, ^{84}Sr and ^{25}Mg were obtained by fitting Eq. (4) to the bulk part of the experimental profiles (see Fig. 7). Since the real thickness of the tracer source prepared from the nitrate solutions is only roughly known, the estimated thickness, h = 30 nm, was used. This value was calculated from the amount of tracer in the solution applied to each surface. The maximum error of a diffusion coefficient was estimated by considering the two possible limiting cases, a much thicker tracer layer, $h >> 30$ nm, and a very thin tracer layer, $h << 30$ nm. In the former case, the tracer profile in Eq. (4) becomes identical to the constant source solution and in the latter case it transforms to the thin film solution.

The resulting cation tracer diffusion coefficients in $La_{0.9}Sr_{0.1}Ga_{0.9}Mg_{0.1}O_{2.9}$ are shown in Fig. 8 as a function of the inverse temperature. The data points were then fitted by purely mathematical functions without physical meaning (lines in Fig 8), and the apparent activation energies, E_a, were calculated from the local slope of these curves, $E_a = -R \cdot (d\ lnD/d(1/T))$. It was found that the apparent activation energies of the tracer diffusion coefficients of ^{138}La, ^{84}Sr and ^{25}Mg change from about 1.5 eV at 900°C to about 4.5 eV at 1400°C.

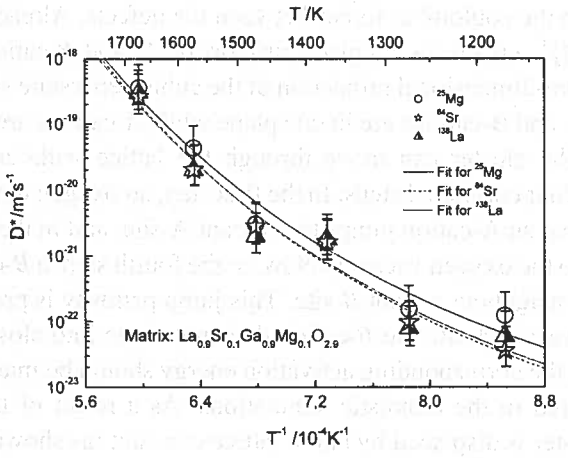

Fig. 8. Bulk diffusion coefficients of ^{138}La, ^{84}Sr and ^{25}Mg in $La_{0.9}Sr_{0.1}Ga_{0.9}Mg_{0.1}O_{2.9}$ as a function of the inverse temperature

The grain boundary diffusion coefficients which can be obtained from the tails of the diffusion profiles [42,43] are about three to four orders of magnitude higher than the bulk diffusion coefficients. These results will be discussed in detail in a forthcoming paper.

In LSGM, oxygen vacancies, $V_O^{\bullet\bullet}$, and acceptors, Sr'_{La} and Mg'_{Ga}, are the majority defects, $2[V_O^{\bullet\bullet}] = [Sr'_{La}] + [Mg'_{Ga}]$, while cation vacancies, V_{La}^{III} and V_{Ga}^{III}, are only minority defects (K r ö g e r - V i n k notation). As a result, the cation diffusivities are very small, and at low temperatures it is nearly impossible to equilibrate LSGM samples (concerning their minority defect structure). This means that the defect structure which was established at high temperatures will be frozen in at an intermediate temperature when the samples are cooled. Thus, the apparent activation energies of the diffusion coefficients should increase with increasing temperature, as observed experimentally. At low temperatures the values correspond to the migration energy of the cations (about 1.5-2 eV), whereas at high temperatures they correspond to the sum of the migration energy and the formation energy (2.5-3 eV) of the defects by which the cations are mobile.

The nearly identical cation migration energies and diffusion coefficients found in our experiments are in contradiction to the expectations for cation diffusion in a perovskite structure. Assuming a simple vacancy mechanism, diffusion of *B* cations should be much slower than diffusion of *A* cations, because *B* cations cannot perform direct nearest neighbour jumps, in contrast to *A* cations. Theoretical calculations of the cation migration energies support this expectation. K h a n *et al.* [44] have obtained $E_{mig}(La_A) = 4.6$ eV and $E_{mig}(Ga_B) = 16.9$ eV, and recently D e S o u z a a n d M a i e r [45] have calculated $E_{mig}(Sr_A) = 2.8$ eV, $E_{mig}(La_A) = 4.7$ eV and $E_{mig}(Ga_B) = 14.7$ eV. The large migration energy for *B* cations is caused by the fact that during that jump the B cation comes into close contact with the large *A* cation, which results in strong coulombic repulsion [45,46].

To explain our experimental observations we have proposed a more complicated diffusion mechanism [38]. Cation vacancies in the *A*- and *B*-sublattices, V_A^m and V_B^m, and oxygen vacancies, $V_O^{\bullet\bullet}$, (K r ö g e r - V i n k notation) can form defect clusters which are

strongly bound due to the coulombic forces between the defects. Already the most simple cluster, $\{V_A'''', V_B''', V_O^{\bullet\bullet}\}^{4'}$, enables a coupled transport of *A*- and *B*-cations. The cluster is shown in Fig. 9 in a two-dimensional projection of the cubic perovskite structure of LSGM. Note that oxygen ions and B-cations are in one plane while *A*-cations are located above (or below) that plane. The cluster can move through the lattice without dissociating into individual defects in four correlated steps. In the first step, an oxygen ion jumps to a vacant oxygen site, in step two an A-cation jumps to a vacant A-site, and in the third step another oxygen ion jumps into the oxygen vacancy. Now, in the fourth step, a *B*-cation can perform a jump to the nearest neighbour vacant *B*-site. This jump pathway is probably curved, but due to the adjacent, vacant *A*-site the *B*-cation does not come into close contact with the large A-cation. Thus, the corresponding activation energy should be much smaller than for the B-jumps considered in the atomistic simulations. As a result of the four correlated jumps, the whole cluster is displaced by half a lattice constant (as shown in the last part of Fig. 9), and both an *A*-cation and a *B*-cation have moved simultaneously. The activation energy of the whole process is determined by the step with the highest activation energy. Since the activation energy for a jump of an oxygen ion is only 0.6 eV [47] steps two or four must be rate determining (considering our experimental value of about 2 eV for the migration energy).

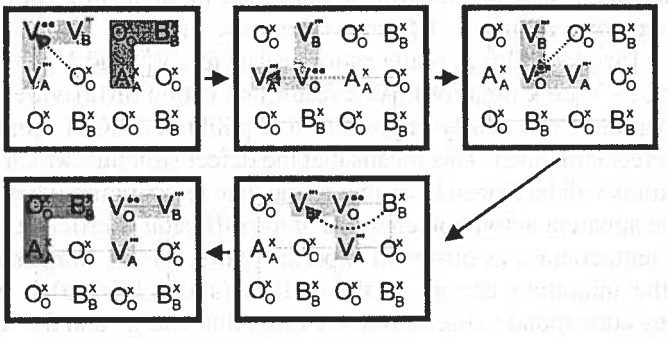

Fig. 9. Defect cluster, $\{V_A'''', V_B''', V_O^{\bullet\bullet}\}^{4'}$, in cubic, perovskite-type LSGM and four-step jump mechanism by which the cluster is mobile without dissociation (two-dimensional projection of the cubic perovskite structure; oxygen ions and B-cations are in one plane while A-cations are located above or below that plane)

A comparison of our experimental results for the cation tracer diffusion coefficients in LSGM with the values in YSZ [48] shows that the cation diffusion coefficients are of the same order in both electrolyte materials. However, concerning kinetic demixing of an electrolyte in a SOFC, which is driven by the difference in the diffusion coefficients of the respective cations [32,33] YSZ and LSGM should behave differently. In YSZ we expect long term kinetic demixing because Y moves three times faster than Zr [48]. In LSGM, however, there should be no kinetic demixing as long as cation diffusion is determined by our proposed cluster mechanism where all cations have the same diffusion coefficient.

4.5. Conclusions

Secondary ion mass spectrometry has been discussed as a powerful tool for diffusion studies in solids. The experimental techniques which are available were shortly introduced and examples for oxygen diffusion and cation diffusion in oxides were discussed.

Oxygen tracer measurements were used to determine the ionic conductivity and to provide information on defect process in selected $La_{1-x}Sr_xMn_{1-y}Co_yO_{3\pm\delta}$ perovskite compositions. It was found that the variations in isothermal tracer diffusivities are predominantly due to changes in the site fraction of oxygen vacancies.

Cation tracer diffusion coefficients of La, Sr and Mg have been measured in Sr- and Mg-doped lanthanum gallate, $La_{1-x}Sr_xGa_{1-y}Mg_yO_{3-(x+y)/2}$. The bulk diffusion coefficients are similar for all cations with apparent activation energies which are strongly dependent on temperature. To explain these findings the formation a defect cluster was proposed which consists of vacancies in the A-, B- and O sublattices, $\{V_A'''', V_B'''', V_O^{\bullet\bullet}\}^{4'}$. The cluster is strongly bound and can move through the perovskite lattice by a postulated four-jump diffusion mechanism without dissociation. In this way *A*- and *B*-cations are moved simultaneously resulting in identical diffusion coefficients. The observed increase of the apparent activation energy of the diffusion coefficients with increasing temperature is explained by a non-equilibrated defect structure of the minority defects at lower temperatures.

Acknowledgements

Financial support by the Deutsche Forschungsgemeinschaft is gratefully acknowledged.

REFERENCES

[1] W. Jost, K. Hauffe, Diffusion (Steinkopff, Darmstadt, 1957).
[2] R.E. Howard, A.B. Lidiard, Rep. Prog. Phys. **27**, 161 (1964).
[3] J.R. Manning, Diffusion Kinetics for Atoms in Crystals (Van Nostrand, Princeton, 1968).
[4] A.D. Le Claire, in Physical Chemistry – An Advanced Treatise **X**, eds. H. Eyring, D. Henderson, W. Jost (Academic Press, New York), 261-330, (1970).
[5] J. Philibert, Diffusion et Transport de Matiére dans les Solides (Les Ulis, Editions de Physique, 1985).
[6] R.G. Wilson, F.A. Stevie, C.W. Magee, Secondary Ion Mass Spectrometry: A practi cal handbook for depth profiling and bulk impurity analysis (Wiley, New York, (1989).
[7] W. Gust, M.B. Hintz, A. Lodding, H. Odelius, B. Predel, Physica Status Solidi A **64**, 187 (1981).
[8] F. Degreve, N.A. Thorne, J.M. Lang, J. Mat. Sci. **23**, 4181 (1988).
[9] J.L. Routbort, S.J. Rothman, N. Chen, J.N. Mundy, J.E. Baker, Phys. Rev. B **43**, 5489 (1991).
[10] S.V. Divinski, S. Frank, U. Sodervall, C. Herzig, Acta Materialia **46**, 4369 (1998).
[11] T. Horita, M. Ishikawa, K. Yamaji, N. Sakai, H. Yokokawa, M. Dokiya, Solid State Ionics **108**, 383 (1998).
[12] Secondary Ion Mass Spectrometry, eds. J. C. Vickerman, A. Brown and N. M. Reed, Clarendon Press Oxford (1989).
[13] W.D. Kingery, H.K. Bowen, D.R. Uhlmann, "Introduction to Ceramics", John Wiley, New York, 521, (1976).
[14] R.A. De Souza, Ph.D. Thesis, University of London (1996).

[15] D.R. Killoran, J. Electrochem. Soc. **109**, 170 (1963).
[16] S. Carter, A. Selcuk, R.J. Chater, J. Kajda, J.A. Kilner, B.C.H. Steele, Solid State Ionics, **53-56**, 597 (1992).
[17] J.A. Kilner, R.A. De Souza, in: Proc. 17th Intnl. Risø Symp. on Mater. Sci., eds. F.W. Poulsen, N. Bonanos, S. Linderoth, M. Mogensen, B. Zachau-Christiansen, Risø National Laboratory, Roskilde, Denmark, 41, (1996).
[18] J. Crank, The Mathematics of Diffusion, Oxford University Press, Oxford, (1975).
[19] MATLAB® 4.0, The MathWorks, Inc., Natick, MA.
[20] R.A. De Souza, J.A. Kilner, Solid State Ionics **106** (3-4), 175-187 (1998).
[21] R.A. De Souza, J.A. Kilner, Solid State Ionics **126** (1-2), 153-161 (1999).
[22] R.A. De Souza, J.A. Kilner, J.F. Walker, Materials Letters **43** (1-2), 43-52 (2000).
[23] T. Ishigaki, S. Yamauchi, K. Kishio, J. Mizusaki, K. Fueki, J. Sol. St. Chem. **73**, 179 (1988).
[24] J. Mizusaki, I. Yasuda, J. Shimoyama, S. Yamauchi, F. Fueki, J. Electrochem. Soc **140** 467, (1993).
[25] J.A. Kilner, R.A. De Souza, I.C. Fullarton, Solid State Ionics **86-88**, 703 (1996).
[26] T. Ishihara, H. Matsuda, Y. Takita, J. Am. Chem. Soc. **116**, 3801 (1994).
[27] M. Feng, J.B. Goodenough, Eur. J. Solid State Inorg. Chem. **31**, 663 (1994).
[28] M. Feng, J. B. Goodenough, K. Huang, C. Milliken, Jounal of Power Sources **63**, 47 (1996).
[29] T. Horita, M. Ishikawa, K. Yamaji, N. Sakai, H. Yokokawa, M. Dokiya, Solid State Ionics **108**, 383 (1998).
[30] J. Wolfenstine, Solid State Ionics **126**, 293 (1999).
[31] J. Wolfenstine, P. Huang, A. Petric, Journal of Solid State Chemistry **118**, 257 (1999).
[32] M. Martin, The Electrochemical Society Proceedings Series: SOFC-VI, ed. S. C. Singhal and M. Dokiya, PV 99-19, p. 308, (1999).
[33] M. Martin, Solid State Ionics **136-137**, 331 (2000).
[34] O. Schulz, M. Martin, Solid State Ionics **135**, 549 (2000).
[35] O. Schulz, M. Martin, Advances in Sciences and Technology: Mass and Charge Transport in Inorganic Materials, ed. P. Vincenzini and V. Buscaglia **29**, 83, (2000).
[36] A. Matraszek, D. Kobertz, L. Singheiser, K. Hilpert, W. Kuncewicz-Kupczyk, M. Miller, O. Schulz, M. Martin, Materialwiss. und Werkstofftechn. **33**, 355 (2002).
[37] O. Schulz, S. Flege, M. Martin, The Electrochemical Society Proceedings Series: SOFC-VIII, ed. S. C. Singhal and M. Dokiya, PV 2003-07, 304, (2003).
[38] O. Schulz, M. Martin, C. Argirusis, G. Borchardt, Phys. Chem. Chem. Phys. **5**, 2308 (2003).
[39] M.P. Pechini, in U.S. Pat. **3** 330 697 (1967).
[40] L.G. Harrison, Trans. Faraday Soc. **57**, 1191 (1961).
[41] J.C. Fisher, J. Appl. Phys. **22**, 74 (1951).
[42] A.D. Le Claire, Brit. J. Appl. Phys. **14**, 351 (1963).
[43] Y.C. Chung, B.J. Wuensch, Materials Letters **28**, 47 (1996).
[44] M.S. Khan, M.S. Islam, D.R. Bates, J. Phys. Chem. **102**, 3099 (1998).
[45] R.A. De Souza, J. Maier, Phys. Chem. Chem. Phys. **2003**, 5, 740 (2003).
[46] R.A. De Souza, M.S. Islam, E. Ivers-Tiffée, J. Mater. Chem. **9** (7), 1621-1627 (1999).
[47] T. Ishihara, J.A. Kilner, M. Honda, Solid State Ionics **113-115**, 593 (1998).
[48] M. Kilo, G. Borchardt, B. Lesage, S. Weber, S. Scherrer, M. Martin, M. Schroeder, The Electrochemical Society Proceedings Series: SOFC-VII, ed. H. Yokokawa and S. C. Singhal, PV 2001-16, p. 275, (2001).

Received: 1 March 2004.